# Development of Electrode Materials for Lithium-ion Batteries and Sodium-ion Batteries

A thesis presented for the award of the degree of

**Doctor of Philosophy**

from

**University of Technology, Sydney**

By

**Xiuqiang Xie, B. Sc., M.Sc.**

December, 2016

# CERTIFICATE OF ORIGINAL AUTHORSHIP

I, Xiuqiang Xie, certify that the work presented in this thesis has not previously been submitted for a degree nor has been submitted as part of requirements for a degree except as fully acknowledged within the text.

I also certify that the thesis has been written by me. Any help that I have received in my research work and the preparation of the thesis itself has been acknowledged. In addition, I certify that all information sources and literature used are indicated in the thesis.

Xiuqiang Xie

Sydney, Australia

October, 2016

# DEDICATION

This thesis is dedicated to my family. Thank you for all of your love and support.

# ACKNOWLEDGEMENTS

Firstly, I am grateful to my supervisor, Professor Guoxiu Wang, for his kind and continuous support and invaluable advice throughout my Ph.D. study. I would also like to thank Professor Yury Gogotsi for his valuable guidance during my visit to Drexel University in Philadelphia.

I would like to acknowledge Dr. Jane Yao. Her kind help and support is essential to my laboratory work.

Special thanks are given to my colleagues at UTS, Dr. Dawei Su, Dr. Zhimin Ao, Dr. Bing Sun, Dr. Hao Liu, Dr. Shuangqiang Chen, Dr. Anjon Kumar Mondal, Mr. Jinqiang Zhang, Miss Yufei Zhao, Miss Katja Kretschmer, Mr. Xin Guo, Mr. Jianjun Song, Mr. Kefei Li, Miss Jing Xu, and Mr. Weizhai Bao. Their kind collaboration and assistance were helpful. Also, I want to thank my friends in Philadelphia, Dr. Taron Makaryan, Dr. Babak Anasori, Dr. Meng-Qiang Zhao, Chang (Evelyn) Ren, Miss Kathleen Maleski, Miss Katie Van Aken, Mr. Tyler Mathis, Mr. Patrick Urbankowski, Mr. Chi Chen, Mr. Xin-Bing Cheng, Professor Jianguang Xu, Professor Jun Yan, Professor Fayan Meng, Mr. Mohamed Alhabeb, Mr. Muhammad Boota, Dr. Narendra Kurra, Miss. Adriana Navarro Suarez, and Miss Christine Hatter. We have a lot of good memories in Philadelphia.

In addition, I appreciate the administrative and technical support I received from Dr. Ronald Shimmon, Dr. Linda Xiao, Miss Sarah King, and Miss Emaly Black. I would also like to thank Danielle and Wendy at Drexel University for the help in many aspects.

The financial support from UTS and AutoCRC 2020 to help finish my Ph.D. study are highly appreciated.

Last but not the least, I would like to thank my parents, my wife and sisters for supporting me spiritually throughout writing this thesis and my life in general.

Xiuqiang Xie

## RESEARCH PUBLICATIONS

1. ***Xiuqiang Xie***, Shijian Wang, Katja Kretschmer, Guoxiu Wang, Two-dimensional Layered Compound Based Anode Materials for Lithium-ion Batteries and Sodium-ion Batteries, ***J. Colloid Interf. Sci.***, 2017, 499, 17-32.
2. ***Xiuqiang Xie***, Meng-Qiang Zhao, Babak Anasori, Kathleen Maleski, Chang E. Ren, Jingwen Li, Bryan W. Byles, Ekaterina Pomerantseva, Guoxiu Wang and Yury Gogotsi, Porous heterostructured MXene/carbon nanotube composite paper with high volumetric capacity for sodium-based energy storage devices, ***Nano Energy***, 2016, 26, 513–523.
3. ***Xiuqiang Xie***, Taron Makaryan, Mengqiang Zhao, Katherine L. Van Aken, Yury Gogotsi and Guoxiu Wang, $MoS_2$ nanosheets vertically aligned on carbon paper: A freestanding electrode for highly reversible sodium-ion batteries, ***Adv. Energy Mater***, 2016, 6, 1502161. **(One of the Top 10 most read articles of Advanced Energy Materials in March 2016)**
4. ***Xiuqiang Xie***, Zhimin Ao, Dawei Su, Jinqiang Zhang, and Guoxiu Wang, $MoS_2$/graphene composite anodes with enhanced performance for sodium ion batteries: the role of the two-dimensional heterointerface, ***Adv. Funct. Mater.***, 2015, 25, 1393-1403. **(Web of Science ESI Highly Cited Paper; one of the most accessed papers between 03/2015 to 02/2016, Most Accessed 04/2015 to 03/2016)**
5. ***Xiuqiang Xie***, Katja Kretschmer, Jinqiang Zhang, Bing Sun, Dawei Su, and Guoxiu Wang, Sn@CNT nanopillars grown perpendicularly on carbon paper: A novel free-standing anode for sodium ion batteries, ***Nano Energy***, 2015, 13, 208-217. **(One of the most downloaded Nano Energy articles)**
6. ***Xiuqiang Xie***, Katja Kretschmer and Guoxiu Wang, Advances in graphene-based semiconductor photocatalysts for solar energy conversion: fundamentals and materials engineering, ***Nanoscale***, 2015, 7, 13278-13292.
7. ***Xiuqiang Xie***, Shuangqiang Chen, Bing Sun, Chengyin Wang, and Guoxiu Wang*, 3D networked $SnO_2$/graphene aerogel with hierarchically porous architecture for high-rate performance sodium-ion batteries, ***ChemSusChem***, 2015, 8, 2948-2955.
8. ***Xiuqiang Xie***, Dawei Su, Jinqiang Zhang, Shuangqiang Chen, Anjon Kumar Mondal, and Guoxiu Wang, A comparative investigation on the effects of nitrogen-doping into graphene on enhancing the electrochemical performance of $SnO_2$/graphene for sodium-ion batteries, ***Nanoscale***, 2015, 7, 3164-3172. **(Web of Science ESI Highly Cited Paper)**
9. ***Xiuqiang Xie***, Dawei Su, Bing Sun, Jinqiang Zhang, Chengyin Wang, and Guoxiu Wang, Synthesis of single-crystalline spinel $LiMn_2O_4$ nanorods for lithium-ion batteries with high rate capability and long cycle life, ***Chem. - Eur. J.***, 2014, 20, 17125-17131.

10. ***Xiuqiang Xie***, Dawei Su, Shuangqiang Chen, Jinqiang Zhang, Shixue Dou, and Guoxiu Wang, $SnS_2$ nanoplatelet@graphene nanocomposites as high-capacity anode materials for sodium-ion batteries, ***Chem. - Asian J.***, 2014, 9, 1611-1617. **(One of the most frequently cited papers published in 2013 and 2014 according to Web of Science)**
11. Yufei Zhao, ***Xiuqiang Xie***, Jinqiang Zhang, Hao Liu, Hyo-Jun Ahn, Kening Sun and Guoxiu Wang, $MoS_2$ nanosheets supported on 3D graphene aerogel as a highly efficient catalyst for hydrogen evolution, ***Chem. - Eur. J.***, 2015, 21, 15908-15913.
12. Dawei Su, ***Xiuqiang Xie***, and Guoxiu Wang, Hierarchical mesoporous SnO microspheres as high capacity anode materials for sodium-ion batteries, ***Chem. - Eur. J.***, 2014, 20, 3192-3197.
13. Dawei Su, ***Xiuqiang Xie***, Paul Munroe, Shixue Dou, and Guoxiu Wang, Mesoporous hexagonal $Co_3O_4$ for high performance lithium ion batteries, ***Sci. Rep.***, 2014, 4, 6519.
14. Dawei Su, ***Xiuqiang Xie***, Shixue Dou, and Guoxiu Wang, CuO single crystal with exposed {001} facets-A highly efficient material for gas sensing and Li-ion battery applications, ***Sci. Rep.***, 2014, 4, 5753.
15. Bing Sun, Katja Kretschmer, ***Xiuqiang Xie***, Paul Munroe, Zhangquan Peng and Guoxiu Wang, Hierarchical Porous Carbon Spheres for High-Performance Na–$O_2$ Batteries, ***Adv. Mater.***, 2017, DOI: 10.1002/adma.201606816.
16. Chi Chen, Muhammad Boota, ***Xiuqiang Xie***, Mengqiang Zhao, Babak Anasori, Chang E. Ren, Ling Miao, Jianjun Jiang and Yury Gogotsi, Charge transfer induced polymerization of EDOT confined between 2D titanium carbide layers, ***J. Mater. Chem. A***, 2017, 5, 5260-5265.
17. Jianjun Song, Dawei Su, ***Xiuqiang Xie***, Xin Guo, Weizhai Bao, Guangjie Shao, and Guoxiu Wang, Immobilizing polysulfides with MXene-functionalized separators for stable lithium-sulfur batteries, ***ACS Appl. Mater. Interfaces***, 2016, 8, 29427–29433.
18. Katja Kretschmer, Bing Sun, ***Xiuqiang Xie***, Shuangqiang Chen and Guoxiu Wang, A free-standing $LiFePO_4$–carbon paper hybrid cathode for flexible lithium-ion batteries, ***Green Chem.***, 2016, 18, 2691-2698.
19. Anjon Kumar Mondal, Hao Liu, ***Xiuqiang Xie***, Katja Kretschmer and Guoxiu Wang, Hydrothermal synthesis of multiwalled carbon nanotubes/zinc manganate nanoparticles as anode materials for lithium ion batteries. ***ChemPlusChem***, 2016, 81, 399-405.
20. Jinqiang Zhang, Bing Sun, ***Xiuqiang Xie***, Yufei Zhao and Guoxiu Wang, A bifunctional organic redox catalyst for rechargeable lithium–oxygen batteries with enhanced performances, ***Advanced Science***, 2016, 3, 1500285.
21. Shuangqiang Chen, Bing Sun, ***Xiuqiang Xie***, Anjon Kumar Mondal, Xiaodan Huang and Guoxiu Wang, Multi-chambered micro/mesoporous carbon nanocubes as new

polysulfides reserviors for lithium–sulfur batteries with long cycle life, ***Nano Energy***, 2015, 16, 268-280.

**22.** Jinqiang Zhang, Bing Sun, ***Xiuqiang Xie***, Katja Kretschmer, and Guoxiu Wang, Enhancement of stability for lithium oxygen batteries by employing electrolytes gelled by poly(vinylidene fluoride-co-hexafluoropropylene) and tetraethylene glycol dimethyl ether, ***Electrochim. Acta***, 2015, 183, 56-62.

**23.** Jinqiang Zhang, Shuangqiang Chen, ***Xiuqiang Xie***, Katja Kretschmer, Xiaodan Huang, Bing Sun, and Guoxiu Wang, Porous poly(vinylidene fluoride-co-hexafluoropropylene) polymer membrane with sandwich-like architecture for highly safe lithium ion batteries, ***J. Membr. Sci.***, 2014, 472, 133-140.

**24.** Katja Kretschmer, Bing Sun, Jinqiang Zhang, ***Xiuqiang Xie***, Hao Liu and Guoxiu Wang, 3D Interconnected Carbon Fiber Network-Enabled Ultralong Life $Na_3V_2(PO_4)_3$@Carbon Paper Cathode for Sodium-Ion Batteries, ***Small***, 2017, 13, 1603318.

**25.** Shuangqiang Chen, Zhimin Ao, Bin Sun, ***Xiuqiang Xie***, and Guoxiu Wang, Porous carbon nanocages encapsulated with tin nanoparticles for high performance sodium-ion batteries, ***Energy Storage Materials***, 2016, 5, 180-190.

**26.** Anjon Kumar Mondal, Dawei Su, Shuangqiang Chen, ***Xiuqiang Xie***, and Guoxiu Wang, Highly porous $NiCo_2O_4$ nanoflakes and nanobelts as anode materials for lithium-ion batteries with excellent rate capability, ***ACS Appl. Mater. Interfaces***, 2014, 6, 14827-14835.

**27.** Jing Xu, Dawei Su, Weizhai Bao, Yufei Zhao, Xiuqiang Xie, Guoxiu Wang, Rose flower-like $NiCo_2O_4$ with hierarchically porous structures for highly reversible lithium storage, ***Journal of Alloys and Compounds***, 2016, 684, 691-698.

**28.** Shuangqiang Chen, Yufei Zhao, Bing Sun, Zhimin Ao, ***Xiuqiang Xie***, Yiying Wei, and Guoxiu Wang, Microwave-assisted synthesis of mesoporous $Co_3O_4$ nanoflakes for applications in lithium ion batteries and oxygen evolution reactions, ***ACS Appl. Mater. Interfaces***, 2015, 7, 3306-3313. **(Web of Science ESI Highly Cited Paper)**

**29.** Anjon Kumar Mondal, Dawei Su, Shuangqiang Chen, Katja Kretschmer, ***Xiuqiang Xie***, Hyo-Jun Ahn, and Guoxiu Wang, A microwave synthesis of mesoporous $NiCo_2O_4$ nanosheets as electrode materials for lithium-ion batteries and supercapacitors, ***ChemPhysChem***, 2015, 16, 169-175. **(Web of Science ESI Highly Cited Paper)**

## TABLE OF CONTENTS

CERTIFICATE OF ORIGINAL AUTHORSHIP ..... I

DEDICATION ..... II

ACKNOWLEDGEMENTS ..... III

RESEARCH PUBLICATIONS ..... V

TABLE OF CONTENTS ..... VIII

LIST OF TABLES ..... XIII

LIST OF FIGURES ..... XIV

ABSTRACT ..... XXVIII

INTRODUCTION ..... XXXI

Chapter 1 Literature Review ..... XXXI

1.1 Lithium-ion Batteries ..... 1

1.1.1 Electrochemistry of Lithium-ion Batteries ..... 2

1.1.2 Cathode materials for LIBs ..... 4

1.1.3 Anode materials for LIBs ..... 15

1.2 Sodium-ion Batteries ..... 20

1.2.1 Cathode materials for SIBs ..... 22

1.2.2 Anode materials for SIBs ..... 27

Chapter 2 Experimental ..... 38

2.1 Overview ..... 38

2.2 Materials preparation ..... 40

2.2.1 Solid state reaction ..... 40

2.2.2 Hydrothermal method ..... 41

2.3 Materials characterization ..... 42

2.3.1 X-ray Diffraction (XRD) ..... 42
2.3.2 Raman Spectroscopy ..... 42
2.3.3 X-ray photoelectron spectroscopy (XPS) ..... 43
2.3.4 $N_2$ sorption/desorption measurement ..... 44
2.3.5 Thermogravimetric Analysis (TGA) ..... 44
2.3.6 Scanning Electron Microscopy (SEM) ..... 44
2.3.7 Transmission Electron Microscopy (TEM) ..... 45
2.4 Electrode preparation and batteries assembly ..... 45
2.4.1 Electrode preparation ..... 45
2.4.2 Cell assembly ..... 46
2.5 Electrochemical measurements ..... 46
2.5.1 Galvanostatic charge-discharge ..... 47
2.5.2 Cyclic voltammetry ..... 47
2.5.3 Electrochemical Impedance Spectroscopy ..... 48
Chapter 3 Synthesis of Single Crystalline Spinel $LiMn_2O_4$ Nanorods for Li-ion Batteries with High Rate Capability and Long Cycle Life ..... 50
3.1 Introduction ..... 50
3.2 Experimental ..... 53
3.2.1 Synthesis of $MnO_2$ nanorods ..... 53
3.2.2 Synthesis of porous $Mn_3O_4$ nanorods ..... 53
3.2.3 Synthesis of $LiMn_2O_4$ nanorods ..... 53
3.2.4 Characterization ..... 54
3.2.5 Cell assembly and electrochemical testing ..... 54
3.3 Results and Discussion ..... 55
3.4 Conclusions ..... 74

Chapter 4 A Comparative Investigation on the Effects of Nitrogen-doping into Graphene on Enhancing the Electrochemical Performance of $SnO_2$/graphene for Sodium-ion Batteries 76

4.1 Introduction ..... 76

4.2 Experimental ..... 78

4.2.1 Materials ..... 78

4.2.2 Structural and physical characterization ..... 79

4.2.3 Cell assembly and electrochemical testing ..... 80

4.3 Results and Discussion ..... 80

4.4 Conclusions ..... 99

Chapter 5 $MoS_2$/Graphene Composite Anodes with Enhanced Performance for Sodium Ion Batteries: the Role of the Two-dimensional Heterointerface ..... 100

5.1 Introduction ..... 100

5.2 Experimental Section ..... 102

5.2.1 Sample preparation ..... 102

5.2.2 Structural and physical characterization ..... 103

5.2.3 Cell assembly and electrochemical testing ..... 103

5.2.4 DFT calculations ..... 104

5.3 Results and Discussions ..... 106

5.4 Conclusions ..... 134

Chapter 6 $SnS_2$ Nanoplatelet/Graphene Nanocomposites as High Capacity Anode Materials for Sodium Ion Batteries ..... 135

6.1 Introduction ..... 135

6.2 Experimental Section ..... 136

6.2.1 Sample preparation ..... 136

6.2.2 Structural and physical characterization ..... 136

6.2.3 Cell assembly and electrochemical testing ..... 137

6.3 Results and Discussion .....138
6.4 Conclusion .....150
Chapter 7 Three-dimensional Networked $SnO_2$/Graphene Aerogel with Hierarchically Porous Architecture for High-Rate Performance Sodium-Ion Batteries .....152
7.1 Introduction .....152
7.2 Experimental .....153
7.2.1 Materials preparation .....153
7.2.2 Structural and physical characterization .....154
7.2.3 Cell assembly and electrochemical testing .....154
7.3 Results and Discussion .....155
7.4 Conclusions .....173
Chapter 8 Sn@CNT Nanopillars Grown Perpendicularly on Carbon Paper: a Novel Free-standing Anode for Sodium Ion Batteries .....174
8.1 Introduction .....174
8.2 Experimental .....177
8.2.1 Sample preparation .....177
8.2.2 Structural and physical characterization .....178
8.2.3 Electrochemical testing .....178
8.2.4 Full Na-ion cell assembly .....179
8.3 Results and Discussions .....180
8.4 Conclusions .....200
Chapter 9 $MoS_2$ Nanosheets Vertically Aligned on Carbon Paper: a Freestanding Electrode for Highly Reversible Sodium Ion Batteries .....202
9.1 Introduction .....202
9.2 Experimental Section .....204
9.2.1 Sample preparation .....204

9.2.2 Structural and physical characterization....204
9.2.3 Electrochemical testing....205
9.2.4 *In situ* Raman measurements....205
9.3 Results and Discussions....206
9.4 Conclusions....222
Chapter 10 Porous Heterostructured MXene/Carbon Nanotube Composite Paper with High Volumetric Capacity for Sodium-Based Energy Storage Devices....223
10.1 Introduction....223
10.2 Experimental Section....225
10.2.1 Preparation of delaminated $Ti_3C_2T_x$ suspension....225
10.2.2 Fabrication of freestanding $Ti_3C_2T_x$ and its composite films....226
10.2.3 Characterizations....226
10.2.4 Electrochemical tests....227
10.2.5 Assembly of $Na_{0.44}MnO_2$//$Ti_3C_2T_x$/CNT-SA full cells....228
10.3 Results and Discussions....229
10.4 Conclusions....253
Chapter 11 Conclusions and Future Perspective....254
11.1 Conclusions....254
11.1.1 $LiMn_2O_4$ nanorods as cathode materials for lithium-ion batteries....254
11.1.2 Nanostructured electrode materials for sodium-ion batteries....254
11.2 Future Perspective....257
APPENDIX: NOMENCLATURE....260
REFERENCES....263

## LIST OF TABLES

Table 1.1 Characteristics of sodium and lithium ..... 21

Table 1.2 Some of the MAX phases reported ..... 30

Table 1.3 Summary of properties of typical metal or metalloid materials for Na-ion batteries ..... 35

Table 2.1 Chemicals used in the research project ..... 39

Table 3.1 Summary of $LiMn_2O_4$ nanorods as cathode materials for lithium-ion batteries.. 52

Table 3.2 Electrochemical data derived from potentiostatic differential capacity curves of $LiMn_2O_4$ samples prepared at different temperatures..... 65

Table 4.1 Kinetic parameters of $SnO_2$/G and $SnO_2$/NG electrodes..... 97

Table 5.1 Elemental composition obtained by EDX analysis of the MG-3 composites before and after post-treatment.....109

Table 5.2 Elemental composition obtained by EDX analysis of the MG-x composites ....113

Table 5.3 The total energy of $MoS_2$ and the $MoS_2$/graphene heterostructure with a Na atom adsorbed at representative positions, the corresponding adsorption energy of the Na atom and the charge transferred from Na atom to $MoS_2$ or $MoS_2$/graphene bilayer system are also provided.....122

Table 7.1 Elemental analysis of GO and graphene obtained by hydrothermal reduction...157

Table 7.2 Survey of the BET surface area and pore volume of the as-prepared SGA-1, SGA-2, SGA-3, and SGA-4 .....160

Table 7.3 Kinetic parameters of the $SnO_2$ and SGA-2 electrode .....166

## LIST OF FIGURES

Figure 1.1 (a) Relative energy diagram of electrode potentials and electrolyte energy gap in LIBs; (b) schematic diagram of the lithium intercalation–de-intercalation reaction mechanism in a rechargeable LIB containing solid electrodes and a liquid electrolyte. ..... 2

Figure 1.2 Schematic illustration of rechargeable LIBs. ..... 3

Figure 1.3 Diagram illustrating the capacities and electrochemical potentials of important cathode and anode materials with respect to Li metal and the cell voltage of LIBs. ..... 4

Figure 1.4 Lamellar structure of $LiCoO_2$. ..... 5

Figure 1.5 (a) Crystal structure of $LiFePO_4$. (b) Schematic representation of the processes during charge/discharge of $LiFePO_4$..... 8

Figure 1.6 Crystal structure of spinel $LiMn_2O_4$..... 10

Figure 1.7 Schematic representation showing insertion/extraction of $Li^+$ during discharge/charge. ..... 16

Figure 1.8 Schematic illustration of the conversion reaction of a transition metal oxide in LIBs..... 17

Figure 1.9 Operation voltages versus specific capacities of various cathode materials for SIBs..... 22

Figure 1.10 Classification of Na-Me-O layered materials with sheets of edge-sharing $MeO_6$ octahedra and phase transition processes induced by sodium extraction. ..... 23

Figure 1.11 Framework of Prussian blue analogues..... 27

Figure 1.12 Operation voltages vs. specific capacities of various anode materials for SIBs.[158] ..... 28

Figure 2.1 Framework of the experiments. ..... 38

Figure 2.2 Modified coin cell design for *in situ* Raman spectroscopy. ..... 43

Figure 2.3 Schematic impedance spectrum in a Nyquist plot for lithium/sodium-ion cells. 48

Figure 3.1 A schematic illustration of the procedure for preparing the porous $Mn_3O_4$ nanorods and spinel $LiMn_2O_4$ nanorods. ..... 55

Figure 3.2 XRD pattern of $MnO_2$. ..... 57

Figure 3.3 Low-magnification and high-magnification SEM images of $MnO_2$ (a and b), $Mn_3O_4$ (c and d), illustrating the nanostructure of the as-synthesized products. ..... 57

Figure 3.4 XRD pattern of $Mn_3O_4$. ..... 58

Figure 3.5 $N_2$ adsorption-desorption analysis results for the as-synthesized porous $Mn_3O_4$ nanorods, the inset gives the pore size distribution of the $Mn_3O_4$ sample. ..... 59

Figure 3.6 $N_2$ adsorption-desorption analysis results of $LiOH/Mn_3O_4$ mixture prepared by vacuum-assisted impregnation method. ..... 59

Figure 3.7 XRD patterns of the product obtained at different calcination temperatures, all patterns agree well with the standard pattern of spinel $LiMn_2O_4$ (JCPDS 35-0782). ..... 61

Figure 3.8 (a) Medium- and (b) high-magnification FESEM images of $LiMn_2O_4$ nanorods. ..... 61

Figure 3.9 (a) Low-magnification, (b) medium-magnification and (c) lattice-resolved high resolution TEM images of $LiMn_2O_4$ nanorods, (d) SAED pattern of a single crystalline $LiMn_2O_4$ nanorod. ..... 62

Figure 3.10 Electrochemical characterization of $LiMn_2O_4$ nanorods. (a) Cyclic voltammetry curve between 3.0 and 4.5 V *vs.* $Li/Li^+$ at a scanning rate of 0.1 mV $s^{-1}$. (b) Galvanostatic charge/discharge curve and potentiostatic differential capacity *vs.* voltage (dQ/dV). ..... 63

Figure 3.11 Potentiostatic differential capacity *vs.* voltage (dQ/dV) of $LiMn_2O_4$ obtained at different calcination temperature at 0.2 C. ..... 64

Figure 3.12. Cycling performance of LMO-650 at 1C and 2C. ..... 66

Figure 3.13. Cycling performance of LMO-700 at 1C and 2C. ..... 66

Figure 3.14 Cycling performance of LMO-750 at 1C and 2C (1C = 148 mA $g^{-1}$). ..... 67

Figure 3.15 Cycling performance of $LiMn_2O_4$ obtained from a precursor ratio (Li:Mn) of 1.05:2 at a rate of 1C. ..... 69

Figure 3.16 Cycling performance of $LiMn_2O_4$ obtained from a precursor ratio (Li:Mn) of 1.10:2 at different rates. ..... 70

Figure 3.17 Cycling performance of $LiMn_2O_4$ obtained from a precursor ratio (Li:Mn) of 1.15:2 at different rates. ..... 70

Figure 3.18 (a) Cycling performance of $LiMn_2O_4$ nanorods obtained from a precursor ratio (Li:Mn) of 1.2:2 at the 3C rate. (b) The Coulombic efficiency as a function of cycle number. (c) Discharge capacity retention as a function of cycle number at 3C rate. (d) Capacity retention comparison with other $LiMn_2O_4$ nanoarchitectures reported recently. . 71

Figure 3.19. SEM images of $LiMn_2O_4$ obtained at a calcination temperature of 800 ºC (a and b) at a Li:Mn ratio of 1.20:2 and the corresponding cycling performance at 3C at room temperature. ..... 72

Figure 3.20 (a) Charge-discharge profiles of $LiMn_2O_4$ nanorods at different C rates between 3.0 and 4.3 V in coin-type half cells (1C = 148 mA $g^{-1}$). (b) Rate capability of $LiMn_2O_4$ electrode at varied C rates. ..... 73

Figure 3.21 SEM image of $LiMn_2O_4$ electrode after 1000 cycles. ..... 74

Figure 4.1 Schematic illustration for the preparation of $SnO_2$/NG nanohybrids. ..... 81

Figure 4.2 TGA curves of the $SnO_2$/G and $SnO_2$/NG. ..... 82

Figure 4.3 (a) XRD patterns of $SnO_2$/NG and $SnO_2$/G composites. (b) Raman spectra of $SnO_2$/NG and $SnO_2$/G composites in the range of 800-2000 $cm^{-1}$. ..... 82

Figure 4.4 Medium-magnification TEM image, high-resolution TEM image, $SnO_2$ particle size distribution of $SnO_2$/NG nanohybrids (a, c, and e) and $SnO_2$/G composites (b, d, and f). ..... 84

Figure 4.5 $N_2$ sorption isotherms of the $SnO_2$/G (a) and $SnO_2$/NG composites (b). Pore size distribution of the $SnO_2$/G (c) and $SnO_2$/NG composites (d). ..... 85

Figure 4.6 XPS analysis of $SnO_2$/NG and $SnO_2$/G composites: (a) the survey spectrum, (b) high-resolution spectrum of C 1s, (c) N 1s spectrum, (d) XPS Sn 3d spectra, and (e) O 1s spectra. (f) Schematic illustration of different nitrogen species in NG. ..... 86

Figure 4.7 CV profiles of the $SnO_2$/NG composites at a scan rate of 0.1 mV $s^{-1}$ between 0.01 and 3.0 V..... 88

Figure 4.8 CV profiles of NG at a scan rate of 0.1 mV $s^{-1}$ between 0.01 and 3.0 V..... 89

Figure 4.9 Chare-discharge curves of bare $SnO_2$ at a current density of 20 mA $g^{-1}$. ..... 90

Figure 4.10 (a) Galvanostatic charge-discharge profiles of the $SnO_2$/NG and $SnO_2$/G composites. (b) Cycling performance of $SnO_2$/NG and $SnO_2$/G composites at a current density of 20 mA $g^{-1}$ from the second cycle..... 91

Figure 4.11 Galvanostatic charge-discharge profiles of the $SnO_2$/NG and $SnO_2$/G composites of the $50^{th}$ cycle (a) and $100^{th}$ cycle (b) at 20 mA $g^{-1}$..... 93

Figure 4.12 (a) Cycling performance of $SnO_2$/NG composites at current densities of 40 and 80 mA $g^{-1}$ from the second cycle. (b) Rate performance of $SnO_2$/NG at different current densities..... 94

Figure 4.13 (a) Cycling performance of graphene and NG at a current of 20 mA $g^{-1}$. (b) The Nyquist plots of the $SnO_2$/G and $SnO_2$/NG electrode, the inset shows the modeled equivalent circuit. (c) Contribution of different nitrogen-doping effects to the overall electrochemical performance enhancement of $SnO_2$/NG nanohybrids for SIBs compared to $SnO_2$/G, where Effect 1 is the increased electro-active sites within graphene matrix due to the nitrogen-doping and Effect 2 is the improved electron transfer efficiency within the $SnO_2$/NG electrode benefiting from nitrogen-dopants. ..... 95

Figure 4.14 $SnO_2$/NG nanohybrids as anode materials for SIBs..... 98

Figure 4.15 SEM images of $SnO_2$/NG electrode after 100 cycles..... 98

Figure 5.1 Schematic illustration for the preparation of $MoS_2$/RGO heterostructures. As shown in (d), there are two possible stacking configurations: MC (Mo on top of C atoms) and SC (S on top of C atoms) configurations. The yellow, green and grey atoms represent S, Mo and C atoms, respectively. .....107

Figure 5.2 Molecular structure of phosphomolybdic acid (PMA). .....107

Figure 5.3 XRD patterns of MG-3 composites before and after post-treatment. .....108

Figure 5.4 TGA curves of $MoS_2$, MG-1, MG-2, and MG-3. .....110

Figure 5.5 XRD patterns of RGO, MG-1, MG-2, MG-3, and $MoS_2$.....110

Figure 5.6 (a) Raman spectra of $MoS_2$, RGO and MG-3, showing a set of $MoS_2$ Raman peaks together with D band and G band of RGO. (b) Schematic illustration of $E^1_{2g}$ and $A_{1g}$ vibration models. .....112

Figure 5.7 SEM images of MG-1 (a and b), MG-2 (c and d), and MG-3 (e and f), showing the microstructural features of the nanocomposites, the inserts show the corresponding schematic illustrations of the composites.....114

Figure 5.8 SEM image of bare $MoS_2$.....115

Figure 5.9 SEM image and the corresponding EDX map of carbon, oxygen, molybdenum and of sulfur MG-1 (a), MG-2 (b), and MG-3 (c). .....116

Figure 5.10 TEM images of MG-x composites. (a, b) MG-1, (c, d) MG-2, and (e, f) MG-3. .....117

Figure 5.11 CV curves of MG-3.....118

Figure 5.12 Galvanostatic charge-discharge profiles of MG-1 (a), MG-2 (b), and MG-3 (c). (d) Initial reversible capacities of RGO, MG-x, and $MoS_2$ at a current density of 20 mA $g^{-1}$, and the nominal capacities based on experimental values. The blue bars indicate the increased capacities due to the intimate $MoS_2$/RGO heterointerface. (e) Cycling performance of MG-3, $MoS_2$, and graphene at a current density of 20 mA $g^{-1}$. .....119

Figure 5.13 (a) Atomic structure of monolayer $MoS_2$ supercell in the simulation, the numbers denote the possible adsorption position of Na atom. (b) The favorite structure of monolayer $MoS_2$ with a Na atom adsorbed. Configuration of MC bilayer (c) and SC bilayer (d). The energy minimum diffusion pathway of a Na atom on the monolayer $MoS_2$ (e), in MC bilayer (f), and in SC bilayer (g). The inserts in (e, f, and g) show the atomic structure of initial state (IS), transition state (TS) and final state (FS). .....123

Figure 5.14 Six representative configurations for a Na atom adsorbed on $MoS_2$/graphene bilayer structure. (a) Na adsorbed on the hallow site of a hexagon ring over $MoS_2$ layer, (b) Na adsorbed on the top of a Mo atom over $MoS_2$ layer, (c) Na adsorbed on the top of a S atom over $MoS_2$ layer, (d) Na adsorbed on the top of a C atom over graphene, (e) Na

adsorbed on the top of the hallow site of a C ring over graphene, (f) Na adsorbed between graphene and $MoS_2$ layers. ....124

Figure 5.15 The band structures of monolayer $MoS_2$ (a), $MoS_2$/graphene bilayer with MC structure (c), and $MoS_2$/graphene bilayer with SC structure (e). (b), (d), and (f) show the corresponding band structure after the adsorption of Na. The blue dash lines are the band structure of pristine graphene and red dash line denotes the Fermi level. ....127

Figure 5.16 Atomic structure of a Na atom adsorbed on $MoS_2$/RGO (MC configuration) with epoxy (a) and hydroxyl (b) groups in RGO, respectively. The corresponding energy minimum diffusion pathways of a Na atom on $MoS_2$/RGO with epoxy and hydroxyl groups in RGO are shown in (c) and (d) respectively. ....129

Figure 5.17 The band structure of $MoS_2$/RGO (MC configuration) with epoxy (a) and hydroxyl (c) groups in RGO. After the Na atom adsorption, the corresponding band structures are shown in (b) and (d), respectively. ....131

Figure 5.18 (a) Nyquist plots of MG-3 and $MoS_2$ as anode materials in the charged state (3.0 V *vs.* $Na^+$/Na). (b) Rate performance of MG-3 and $MoS_2$ electrodes. (c) Discharge capacity as a function of cycle number of MG-3 electrode from the second cycle at high current densities of 80 mA $g^{-1}$ and 320 mA $g^{-1}$. The first 20 cycles were tested at a current density of 20 mA $g^{-1}$. ....132

Figure 6.1 XRD pattern of the as-prepared $SnS_2$/graphene composites. *I* = Intensity. .....138

Figure 6.2 (a) Low-magnification SEM image of $SnS_2$/graphene nanocomposites. (b) Enlarged view of the area marked by a white square in (a), showing the morphological features of graphene and $SnS_2$. ....139

Figure 6.3 SEM images of $SnS_2$ nanoplatelets. ....140

Figure 6.4 (a) and (b) Low and high magnification TEM images of the $SnS_2$/graphene composites, respectively. (c) HRTEM image of an individual $SnS_2$ nanoplatelet oriented along the [001] direction, taken from the rectangular region in (b). (d) Structural simulation of layered $SnS_2$, with an interlayer distance of 0.59 nm. ....140

Figure 6.5 Raman spectrum of $SnS_2$/graphene nanocomposites in the range of 130-2400 $cm^{-1}$. *I* = Intensity. ....141

Figure 6.6 TGA curve of $SnS_2$/graphene nanocomposites. *W* = Weight percentage, *T* = Temperature.....142

Figure 6.7 CV curves for selected cycles of $SnS_2$/graphene composites at a scan rate of 0.1 mV $s^{-1}$ in the range of 0.01-3 V *vs.* $Na^+$/Na. *I* = Current, *E* = Potential. .....143

Figure 6.8 (a) The initial discharge profile of $SnS_2$/graphene at a current density of 20 mA $g^{-1}$. (b), (c) Ex-situ XRD patterns of $SnS_2$/graphene electrode discharged to different state as marked in the profile, in which the standard diffraction peaks of different products are located at the bottom. *E* = Potential, $C_a$ = Capacity, *I* = Intensity.....144

Figure 6.9 (a) The 1st, 2nd, and 10th charge-discharge profiles of $SnS_2$/graphene at a rate of 20 mA $g^{-1}$. (b) Cycling performance of $SnS_2$/graphene, $SnS_2$, and graphene at a rate of 20 mA $g^{-1}$. *E* = Potential, $C_a$ = Capacity, *N* = Cycle number.....145

Figure 6.10 The 1st, 2nd and 10th cycle charge-discharge profiles of $SnS_2$ at a rate of 20 mA $g^{-1}$. .....146

Figure 6.11 Discharge curves of $SnS_2$ (a) and $SnS_2$/graphene nanocomposites (b) at current densities of 40, 80, 160, 320, and 640 mA $g^{-1}$, respectively. (c) Comparison of discharge capacities of $SnS_2$ and $SnS_2$/graphene nanocomposites at current densities of 40, 80, 160, 320, and 640 mA $g^{-1}$, respectively. (d) Rate performance of $SnS_2$ and $SnS_2$/graphene nanocomposites at currents of 20, 40, 80, 160, 320, 640, 320, 160, and 80 mA $g^{-1}$, respectively. *E* = Potential, $C_a$ = Capacity, *N* = Cycle number, $C_d$ = Current density. .....147

Figure 6.12 (a) Nyquist plots of $SnS_2$ and $SnS_2$/graphene nanocomposites. (b) The corresponding equivalent circuit ($R_\Omega$: Ohm resistance; $R_{ct}$: Charge transfer resistance; $Z_w$: Warburg diffusion process; *CPE*: constant-phase element).....148

Figure 6.13 SEM images of $SnS_2$ electrode (a and b) and $SnS_2$/graphene electrode (c and d) after cycling. .....150

Figure 7.1 Schematic illustration for the preparation of $SnO_2$/graphene aerogels. .....155

Figure 7.2 XRD patterns (a) and TGA curves (b) of SGA-1, SGA-2, SGA-3, and SGA-4. The TGA measurement was conducted at a heating rate of 10 °C $min^{-1}$ in air from room temperature to 800 ºC.....157

Figure 7.3 Low, medium, and high magnification SEM images of SGA-1 (a, b, c), SGA-2 (d, e, f), SGA-3 (g, h, i), and SGA-4 (j, k, l). The scale bars in a, b, d, e, g, h, j, and k are 10, 2, 10, 1, 10, 1, 10, and 2 μm, respectively, and the scale bars in c, f, i, and l are 200, 100, 200, and 100 nm, respectively. .....158

Figure 7.4 $N_2$ isotherms of SGA-1 (a), SGA-2 (b), SGA-3(c), and SGA-4(d). .....160

Figure 7.5 TEM images of SGA-1 (a), SGA-2 (b), SGA-3 (c), and SGA-4 (d). Lattice-resolved high-resolution TEM image of a single $SnO_2$ nanoparticle (e), showing a neighboring interplanar distance of 0.33 nm, which can be indexed to the (110) plane of $SnO_2$. SAED pattern of $SnO_2$ (f). .....162

Figure 7.6. SEM images of bare $SnO_2$. .....163

Figure 7.7 CV curves of the as-prepared SGA-2.....163

Figure 7.8 Charge-discharge curves of SGA-2 at a current density of 20 mA $g^{-1}$. The insert shows the derivative curve (dQ/dV *vs.* V) of the 1st discharge process. .....164

Figure 7.9 (a) Rate performance of the as-prepared SGA-1, SGA-2, SGA-3, and SGA-4. (b) A comparison between the SGA-2 electrode and a variety of recently reported $SnO_2$/graphene anode materials for SIBs. The capacities were estimated based on the total mass of the composite. .....165

Figure 7.10 The Nyquist plots of the $SnO_2$, SGA-2 and SGA-3 electrode, the inset shows the modeled equivalent circuit. $R_e$ is the electrolyte resistance, CPE represents constant phase element, $R_{ct}$ is the charge-transfer resistance, and $Z_w$ is the Warburg impedance. ...166

Figure 7.11 (a) Cycling performance of SGA-2, $SnO_2$, and graphene electrode at a current density of 20 mA $g^{-1}$ (22.2 μA $cm^{-2}$). (b) Cycling performances of SGA-2 at current densities of 320, 640, and 1000 mA $g^{-1}$. .....168

Figure 7.12 Cycling performance and the Coulombic efficiency of the SGA-1 electrode at a current density of 20 mA $g^{-1}$.....170

Figure 7.13 Cycling performance the Coulombic efficiency of the SGA-3 electrode at a current density of 20 mA $g^{-1}$.....170

Figure 7.14 Cycling performance the Coulombic efficiency of the SGA-4 electrode at a current density of 20 mA $g^{-1}$.....171

Figure 7.15 Schematic illustration of the charge transfer within $SnO_2$/graphene aerogel electrode, showing that the 3D hierarchically porous architecture favors both fast $Na^+$ diffusion and efficient electron transfer. .....172

Figure 8.1 The schematic illustration of the 3D free-standing electrode consisting of core-sheath structured Sn@CNT nanopillars grown vertically on carbon paper. .....176

Figure 8.2 A schematic illustration for the preparation procedure of 3D Sn@CNT-CP free-standing electrode. (a) $SnCl_4$/FT. (b) Sn/carbon paper. (c) Sn@CNT-CP electrode with 3D nanoarchitecture. (d) Structural details of the 3D Sn@CNT-CP. .....180

Figure 8.3 TGA curves of FT in $N_2$ atmosphere. .....181

Figure 8.4 SEM images of the carbon paper. .....182

Figure 8.5 (a) XRD pattern and (b) Raman spectrum of the Sn@CNT-CP electrode.....182

Figure 8.6 Raman spectrum of the bare carbon paper (CP) obtained from the carbonization of facial tissue (FT). .....183

Figure 8.7 TGA curves of Sn@CNT-CP (in air atmosphere). .....184

Figure 8.8 (a) Digital photograph of a rectangular Sn@CNT-CP free-standing electrode, the insert shows “UTS” shaped Sn@CNT-CP. (b) Low- and (c, d) medium- magnification SEM images of Sn@CNT-CP. (e and f) High-magnification SEM images of Sn@CNT-CP with a hierarchical structure. .....185

Figure 8.9 SEM images of the products prepared by the same procedure without $C_2H_2$. ..186

Figure 8.10 SEM energy dispersive spectroscopic (EDS) characterization of Sn@CNT-CP (a-d). (a) SEM image, (b and c) C and Sn elemental mapping of the region shown in the marked area in (a), (d) an integrated C- and Sn-elemental mapping image. (e) EDX spectrum of the Sn@CNT-CP. .....187

Figure 8.11 (a) TEM image of a single Sn@CNT nanopillar. (b) HRTEM image, showing the thickness of the CNT layer. (c) Lattice-resolved high-resolution TEM image. (d) SAED pattern of (a), demonstrating the single crystalline nature of Sn nanopillar. .....188

Figure 8.12 The photograph of the separator-supported Sn@CNT-CP electrode being bent (a) and released (b). .....189

Figure 8.13 (a) CV curves of Sn@CNT-CP composite at a scan rate of 0.1 mV $s^{-1}$ in the range of 0.01-2.6 V *vs.* $Na/Na^+$. (b) Charge-discharge curves of Sn@CNT-CP electrode at a current density of 50 μA $cm^{-2}$.....190

Figure 8.14 XRD pattern of Sn@CNT-C electrode discharged to 0.01 V.....190

Figure 8.15 Cycling performances of (a) Sn@CNT-CP electrode and (b) carbon electrode prepared by the traditional dispersion technique. .....191

Figure 8.16 (a) Cycling performance of the Sn@CNT-CP and the carbon paper electrode at a current density of 50 μA $cm^{-2}$, and the corresponding Coulombic efficiency of the free-standing Sn@CNT-CP electrode. (b) Cycling performance of Sn@CNT-CP at 250 μA $cm^{-2}$ and 500 μA $cm^{-2}$. .....194

Figure 8.17 Cycling performance of bare Sn electrode prepared by the traditional dispersion technique at a current density of 80 mA $g^{-1}$. .....195

Figure 8.18 Rate performance of the Sn@CNT-CP free-standing electrode.....196

Figure 8.19 (a) Schematic illustration of a full Na-ion battery with $Na_{0.80}Li_{0.12}Ni_{0.22}Mn_{0.66}O_2$ as cathode and free-standing Sn@CNT-CP as anode. (b) Cycling performance and Coulombic efficiency of the full Na-ion battery. (c) Discharge curves of the 1st, 10th, 20th, 30th, and 40th cycle. (d) A photograph shows that a full Na-ion battery can store the electrical energy to light up a LED.....198

Figure 8.20 Cycling performance of $Na_{0.80}Li_{0.12}Ni_{0.22}Mn_{0.66}O_2$ cathode in a half cell.....199

Figure 9.1 (a) Schematic illustration for the preparation of $MoS_2$ vertically aligned on carbon paper, which includes $MoS_2$-loading by hydrothermal deposition followed by annealing under Ar. (b) XRD patterns of the as-prepared $MoS_2$@C, indicating the 2H phase of $MoS_2$. (c) The simulated structure of 2H-$MoS_2$. (d) TGA curves of bare $MoS_2$ and $MoS_2$@C in air. .....206

Figure 9.2 Energy dispersive X-ray (EDX) spectrum of the purified paper towel. .....208

Figure 9.3 Digital photo of a $MoS_2$ loaded paper towel. .....208

Figure 9.4 Digital photo of a freestanding $MoS_2$@C paper. .....209

Figure 9.5 SEM images of carbon paper derived from paper towel. .....209

Figure 9.6 (a-d) SEM images of the as-prepared freestanding $MoS_2$@C. (e) High-magnification TEM image and (f) SAED pattern of $MoS_2$@C.....210

Figure 9.7 (a) CV curve of the as-prepared $MoS_2$@C anode for sodium-ion batteries. *In situ* Raman spectra of the $MoS_2$@C electrode at different cut-off voltages during discharge (b) and charge (c) processes. (d) Schematic of the phase transition between 2H-$MoS_2$ and 1T-$MoS_2$ during sodium intercalation/de-intercalation.....212

Figure 9.8 CV curves of the as-prepared $MoS_2$@C anode for sodium-ion batteries in the first 4 cycles at a scan rate of 0.1 mV $s^{-1}$. .....214

Figure 9.9 *Ex situ* SEM images of $MoS_2$@C-CMC electrode discharged to 0.5 V (a and b), 0.01 V (c and d) and charged to 3.0 V (e and f). .....215

Figure 9.10 (a) Charge-discharge curves of the as-prepared $MoS_2$@C paper electrode at a current density of 80 mA $g^{-1}$. (b) Cycling performance and the corresponding Coulombic efficiencies of the $MoS_2$@C paper electrode at 80 mA $g^{-1}$. The cycling performance of bare carbon paper is also presented for comparison. (c) Charge-discharge curves of CMC coated $MoS_2$@C electrode ($MoS_2$@C-CMC) at a current density of 80 mA $g^{-1}$. (d) Cycling performance and the corresponding Coulombic efficiencies of the $MoS_2$@C-CMC paper electrode at 80 mA $g^{-1}$ and the cycling performance of the CMC-coated carbon paper electrode (C-CMC). (e) Charge-discharge curves of $MoS_2$@C-CMC at different current densities. (f) Rate-performance of the $MoS_2$@C-CMC electrode.....216

Figure 9.11 Coulombic efficiency of bare carbon paper electrode as a function of cycle number at a current density of 80 mA $g^{-1}$. .....217

Figure 9.12 Change of impedance spectra of $MoS_2$@C-CMC electrode during cycling. The inset shows the modeled equivalent circuit. $R_\Omega$ is the electrolyte resistance, Q represents constant phase element, $R_{ct}$ is the charge-transfer resistance, and $Z_w$ is the Warburg impedance.....218

Figure 9.13 Cycling performance of the $MoS_2$@C-CMC electrode and carbon paper-CMC electrode at a current density of 160 mA $g^{-1}$. .....219

Figure 9.14 Schematic illustration showing paths for sodium-ion diffusion and electron conduction in the $MoS_2$@C electrode.....221

Figure 10.1 (a) Schematic showing preparation of the porous MXene/CNT electrode by the self-assembly method. The MXene nanosheets are negatively charged due to their functional groups, and the CTAB-grafted CNTs are positively charged. (b) Zeta potential of $Ti_3C_2T_x$ nanosheets, CTAB-grafted CNTs (CNT-CTAB), and self-assembled $Ti_3C_2T_x$/CNT-CTAB ($Ti_3C_2T_x$/CNT-SA). (c) Digital photographs of $Ti_3C_2T_x$ suspension, CNT-CTAB in water, and $Ti_3C_2T_x$/CNT-SA composites. .....229

Figure 10.2 Digital photographs of the as-prepared freestanding $Ti_3C_2T_x$/CNT-SA film. .231

Figure 10.3 (a) Zeta potential of a colloidal solution of CNT-SDS. (b) Digital photographs of $Ti_3C_2T_x$ suspension, CNT-SDS, and a $Ti_3C_2T_x$/CNT-SDS mixture. .....231

Figure 10.4 TEM images of $Ti_3C_2T_x$ nanosheet. (a) in plane, (b) cross-section. .....231

Figure 10.5 Top view (left panels) and cross-sectional (right panels) SEM images of pure $Ti_3C_2T_x$ (a and b), $Ti_3C_2T_x$/CNT-SDS (c and d) and porous $Ti_3C_2T_x$/CNT-SA (e and f). Scale bars: 1 μm. .....232

Figure 10.6 $N_2$ adsorption-desorption isotherms (a) and pore size distribution curves (b) of $Ti_3C_2T_x$/CNT-SDS and porous $Ti_3C_2T_x$/CNT-SA. .....234

Figure 10.7 XRD pattern of the as-prepared $Ti_3C_2T_x$/CNT-SA film. .....235

Figure 10.8 The electrochemical properties of the $Ti_3C_2T_x$/CNT-SA electrode in a two electrode $Ti_3C_2T_x$/CNT-SA//Na cell, where Na foil was used as the counter and reference electrode: (a) cyclic voltammetry (CV) curves of the porous $Ti_3C_2T_x$/CNT-SA electrode at different scan rates from 0.1 to 3 mV $s^{-1}$; (b) the relationship between peak current and scan rate; (c) separation of the non-diffusion limited currents ($k_1\nu$) in the $Ti_3C_2T_x$/CNT-SA electrode at 0.1 mV $s^{-1}$. Three-electrode tests (overcapacitive activated carbon films and Na work as counter and reference electrodes, respectively): (d) CV curves at different scan rates collected from 0.5 to 100 mV $s^{-1}$; (e) volumetric and gravimetric rate performances; (f) galvanostatic charge-discharge profiles at different current densities. .....236

Figure 10.9 Electrochemical performance of electrodes in a two-electrode cell with Na foil as the counter and reference electrode: (a) charge/discharge curves of $Ti_3C_2T_x$/CNT-SA at 20 mA $g^{-1}$ in the voltage window of 0.01-3.0 V. (b) Cycling performance of pure $Ti_3C_2T_x$, $Ti_3C_2T_x$/CNT-SA, and $Ti_3C_2T_x$/CNT-SDS papers at a current density of 20 mA $g^{-1}$ from the

second cycle, the Coulombic efficiencies of $Ti_3C_2T_x$/CNT-SA electrode are also shown. (c) Linear fit of the Warburg impedance of $Ti_3C_2T_x$, $Ti_3C_2T_x$/CNT-SA, and $Ti_3C_2T_x$/CNT-SDS electrodes. (d) Volumetric capacities of $Ti_3C_2T_x$/CNT-SA (this work), carbon, $MoS_2$/graphene paper, multilayered $Ti_2CT_x$ powder, porous carbon nanofiber film, and N-doped carbon nanofiber film. (e) Reversible capacities and Coulombic efficiencies of $Ti_3C_2T_x$/CNT-SA electrodes at 100 mA $g^{-1}$ from the second cycle. ..... 238

Figure 10.10 XRD patterns of $Ti_3C_2T_x$/CNT-SA electrodes after different cycles. ..... 239

Figure 10.11 (a) Nyquist plots of pure $Ti_3C_2T_x$, $Ti_3C_2T_x$/CNT-SA and $Ti_3C_2T_x$/CNT-SDS electrodes, the inset is the enlarged Nyquist plots of $Ti_3C_2T_x$/CNT-SA electrode. ..... 241

Figure 10.12 SEM images of the as-produced $Ti_3C_2T_x$/rGO-SA film. (a) Top view, (b) cross-sectional view. Scale bars: 1 μm. ..... 242

Figure 10.13 $N_2$ adsorption-desorption isotherm and pore size distribution curve (inset) of $Ti_3C_2T_x$/rGO. ..... 242

Figure 10.14 Cycling performances of $Ti_3C_2T_x$/CNT-SA and $Ti_3C_2T_x$/rGO-SA films at a current density of 100 mA $g^{-1}$. ..... 243

Figure 10.15 Linear fit of the Warburg impedance of $Ti_3C_2T_x$/CNT-SA and $Ti_3C_2T_x$/rGO-SA electrodes. ..... 243

Figure 10.16 XRD pattern of $Na_{0.44}MnO_2$ powder. ..... 245

Figure 10.17 SEM image of $Na_{0.44}MnO_2$ powder. ..... 245

Figure 10.18 Galvanostatic charge/discharge curves of the $Na_{0.44}MnO_2$ electrode at a current density of 14 mA $g^{-1}$. ..... 246

Figure 10.19 Extended cycling performance of $Na_{0.44}MnO_2$ in a Na-ion half cell at a current density of 14 mA $g^{-1}$. ..... 246

Figure 10.20 Electrochemical performance of a $Na_{0.44}MnO_2$//$Ti_3C_2T_x$/CNT-SA cell. Charge-discharge curves (a) and cycling performance (b) at a current density of 50 mA $(g\text{-}Ti_3C_2T_x/CNT\text{-}SA)^{-1}$. The inset in b shows that the as-assembled full sodium-ion cell can light up a LED. ..... 247

Figure 10.21 $Na^+$ diffusion and electron transfer within porous MXene/CNT-SA electrodes. .....249

Figure 10.22 Zeta potential of $Mo_2CT_x$ nanosheets.....250

Figure 10.23 SEM images of pure $Mo_2CT_x$ paper (a and b) and $Mo_2CT_x$/CNT-SA paper (c and d).....250

Figure 10.24 Charge/discharge curves of the $Mo_2CT_x$/CNT-SA//Na cell at 50 mA $g^{-1}$.....251

Figure 10.25 Cycling performance of pure $Mo_2CT_x$ and self-assembled $Mo_2CT_x$/CNTs paper electrodes at 50 mA $g^{-1}$. The Coulombic efficiencies of $Mo_2CT_x$/CNT-SA electrode are also presented.....251

Figure 10.26 Rate performance of the $Mo_2CT_x$/CNT-SA//Na cell.....252

## ABSTRACT

Electrode materials are vital to the performance of lithium-ion batteries and sodium-ion batteries. A rational design of electrode materials depends critically on understanding of their electrochemical processes, which is highly desirable for the development of high performance electroactive materials towards different applications. The composition, morphology, structure and preparation method can affect the electrochemical performance. In this doctoral work, a series of electrode materials were designed and fabricated and their electrochemical properties for lithium-ion batteries and sodium-ion batteries were investigated.

Single crystalline spinel $LiMn_2O_4$ nanorods were prepared as stable cathode materials for lithium-ion batteries. The preparation involves infiltration of LiOH into porous $Mn_3O_4$ nanorods by a vacuum-assisted impregnation route, which facilitates the homogeneous reaction to prepare $LiMn_2O_4$. The reaction parameters were optimized and Li-rich single crystalline $LiMn_2O_4$ nanorods were prepared, which retained 95.6 % of its initial capacity after 1000 cycles at 3C rate as cathode material for lithium-ion batteries.

Considering the concerns of the increasing cost of lithium salts, the development of low-cost sodium-ion batteries is becoming a hot topic. In this doctoral work, a series of anode materials were explored for sodium-ion storage. The electrochemical performances of $SnO_2$/nitrogen-doped graphene and $SnO_2$/graphene were compared to investigate the effects of nitrogen-doping into graphene on enhancing the electrochemical performance for sodium-ion batteries. In contrast to the previous reports which often ascribe the enhanced electro-activity of nitrogen-doped graphene based composites to two nitrogen-doping effects (improving the electron transfer efficiency and increasing electro-active sites within the graphene network)

in one single declaration, it was demonstrated that the improved electron transfer efficiency of $SnO_2$/nitrogen-doped graphene due to nitrogen-doping plays a more important role than the increased electro-active sites within graphene network in enhancing the electro-activity of $SnO_2$/nitrogen-doped graphene nanohybrids compared to the $SnO_2$/graphene counterpart.

$MoS_2$/reduced graphene oxide (RGO) nanocomposites with intimate two-dimensional heterointerfaces were prepared by a facile one-pot hydrothermal method. The synergistic effect between $MoS_2$ and graphene contributing to the enhanced reversible capacity of $MoS_2$/RGO nanocomposites was investigated by experimental and computational studies. It was revealed that Na prefers to be adsorbed on $MoS_2$ in the $MoS_2$/RGO heterostructure rather than intercalate into the $MoS_2$/RGO heterointerface. Interestingly, the $MoS_2$/RGO heterointerfaces can significantly increase the electronic conductivity of $MoS_2$, and store more Na ions, while maintaining the high diffusion mobility of Na atoms on $MoS_2$ surface and high electron transfer efficiency from Na to $MoS_2$.

$SnS_2$ nanoplatelet@graphene nanocomposites were prepared by using a morphology-controlled hydrothermal method. The as-prepared materials achieved a high reversible specific sodium-ion storage capacity of 725 mA h $g^{-1}$, stable cyclability, and an enhanced high-rate capability as anode materials for sodium-ion batteries.

Three dimensional interconnected $SnO_2$/graphene aerogels with a hierarchically porous structure were constructed by a facile *in situ* process. Such a functional architecture not only facilitates the electrode–electrolyte interaction but also provides an efficient electron pathway within the graphene networks. The as-prepared $SnO_2$/graphene aerogels exhibited an initial reversible capacity of 451 mA h $g^{-1}$ with a stable cycling performance at a current

density of 20 mA $g^{-1}$. Even at a high current density of 1000 mA $g^{-1}$, the electrode achieved a capacity of 168 mA h $g^{-1}$ after 500 cycles.

A series of freestanding electrodes with distinct architectures and promising electrochemical performance for sodium-ion storage were prepared, including:

1) Three dimensional freestanding electrodes consisting of Sn@CNT nanopillar arrays grown on carbon paper, which achieved a reversible capacity of 887 μA h $cm^{-2}$ in the first cycle and good cyclability extending to 100 cycles.

2) Vertically aligned $MoS_2$ nanosheets/carbon paper electrodes as highly reversible anode materials. Coating with carboxy methyl cellulose sodium salt improved the cycling performance and a high reversible capacity of 286 mA h $g^{-1}$ was achieved after 100 cycles at a current density of 80 mA $g^{-1}$. The as-prepared electrodes delivered a high initial Coulombic efficiency of 79.5% and promising rate capability. Even at a high current density of 1000 mA $g^{-1}$, a reversible capacity of 205 mA h $g^{-1}$ was maintained.

3) Heterostructured $Ti_3C_2$ MXene/CNTs porous films with high volumetric capacity for sodium-ion storage. The open structure facilitates electrolyte transport and access of ions to the electrode and produces functional MXene-based electrodes for sodium-ion storage. When applied as freestanding electrodes for sodium-ion storage, the built-to-order $Ti_3C_2$ MXene/CNTs porous films showed a volumetric capacity of 421 mA h $cm^{-3}$ at 20 mA $g^{-1}$, good rate performances, and excellent cycling stability.

## INTRODUCTION

Human flourishing relies critically on the exploration and utilization of energies. With the ever-increasing concerns about the depletion of fossil fuels and the environmental pollution resulting from their combustion for energies, developing and utilizing renewable energy sources such as solar, wind, geothermal and tidal energy is of great significance for a sustainable future. In order to support the application of renewable energies, energy storage and conversion technologies need to be implemented to store the intermittently available energy and supply power when required. Lithium-ion batteries now surpass other battery systems (for example, lead–acid batteries, nickel metal hydride batteries) in terms of energy density. Their applications range from electric vehicles (EV) and hybrid electric vehicles (HEV) to portable devices. Although there have been advances in lithium-ion batteries in recent decades, significant improvements of lithium-ion battery performances, such as energy density, cost and cyclability, are still required. The performance of lithium-ion batteries critically depends on the electrode materials used, especially on the cathode side. In this doctoral work, the focus is directed towards a low-cost spinel $LiMn_2O_4$ cathode material.

On the other hand, sodium-ion batteries have attracted attentions as a low-cost alternative to lithium-ion batteries because sodium is the fourth most abundant element in the earth's crust and the distribution of sodium mineral salts is widespread. Although working similarly to lithium-ion batteries, sodium-ion batteries are in the early stage of development. The development of electrode materials that can satisfy criteria for commercialization of sodium-ion batteries is one of the key issues. Compared to widely investigated cathode materials, anode materials that can host sodium-ions with decent electrochemical performances are facing challenges, including low initial Coulombic efficiency, low specific capacity, poor

cycling performance and rate capability. In this doctoral work, the development of anode materials with enhanced electrochemical performance for sodium-ion batteries is the research interest.

For both lithium-ion batteries and sodium-ion batteries, the electrode reaction occurs at the surface and requires transport of ions into the electrode material. Consequently, the design of electrode materials plays a vital role to achieve high performance batteries. In this doctoral work, electrode materials were constructed based on the understanding of structure-electrochemical performance interplay for better utilization of electroactive materials and achieving prolonged cyclability and enhanced rate capability. Methodologies such as optimization of preparations, tuning the composition and morphology of electroactive materials as well as the harmonious hybridization between each component were applied to fabricate advanced electrode materials for lithium-ion batteries and sodium-ion batteries.

Each chapter of this doctoral thesis is outlined as follows:

1) Chapter 1 reviews the research development of lithium-ion batteries and sodium-ion batteries. The working principle, the development of cathode materials, especially spinel $LiMn_2O_4$ cathodes, and anode materials are presented in this chapter. For sodium-ion batteries, the comparison to lithium-ion batteries is given and advances in cathode materials and anodes are summarized.

2) The experimental section is Chapter 2, which includes material preparations, physiochemical characterizations as well as the electrochemical investigations. In detail, solid state reaction and hydrothermal synthesis were mainly applied to prepare different electrode materials in this doctoral work. The structure and morphology of the prepared

materials were characterized by X-ray diffraction (XRD), field emission scanning electron microscopy (FESEM), transmission electron microscopy (TEM), nitrogen adsorption-desorption, Raman Spectroscopy, X-ray photoelectron spectroscopy (XPS), and thermogravimetric analysis. Cell assembly and electrochemical testing techniques were also presented.

3) Chapter 3 shows the preparation of single-crystalline spinel $LiMn_2O_4$ nanorods by a novel template-engaged reaction method. Using porous $Mn_3O_4$ nanorods and vacuum assisted impregnation, Mn- and Li-precursors can be mixed homogeneously. By optimizing the sintering temperature and the precursor ratio, stable $LiMn_2O_4$ cathode materials were prepared. The post-mortem FESEM analysis demonstrates that the single-crystalline $LiMn_2O_4$ nanorods exhibited ultrahigh structural stability. It shows that single crystalline spinel $LiMn_2O_4$ nanorods could be promising cathode materials for LIBs with long cycle life.

4) Chapter 4 elucidates the nitrogen-doping effect on enhanced electrochemical performance of $SnO_2$/nitrogen-doped graphene compared to $SnO_2$/graphene. For a reasonable comparison, $SnO_2$/nitrogen-doped graphene and $SnO_2$/graphene with the same $SnO_2$ ratio, similar $SnO_2$ crystallinity and particle size, comparable surface area and pore size were prepared.

5) The focus of Chapter 5 is to investigate the interfacial interactions between layered transition metal sulfides (TMSs) and graphene. $MoS_2$ in the family of TMSs was selected as a typical example. A series of $MoS_2$/graphene composites with tuned heterointerfacial areas were prepared and the electrochemical performances were tested. In combination with computational investigations, the synergistic effect contributing to the enhanced reversible capacity of $MoS_2$/graphene nanocomposites was studied.

6) Research findings in Chapter 5 inspired the preparation of two-dimensional platelet-on-sheet nanoarchitectured $SnS_2$/graphene composites for sodium-ion storage, as shown in Chapter 6. The $SnS_2$/graphene composites exhibited high capacity and long cycling performance as anode materials for sodium-ion batteries.

7) To support the high-rate applications of sodium-ion batteries, Chapter 7 presented the preparation of 3D $SnO_2$/graphene composite anode materials by a facile *in-situ* process, during which cross-linked 3D conductive graphene networks with macro-/meso-sized hierarchical pores were formed and $SnO_2$ nanoparticles were dispersed uniformly on the graphene surface simultaneously. The mass transport and electron transfer were optimized within the 3D architecture, which affords high-rate sodium-ion storage.

8) To eliminate electrode preparation by traditional slurry methods, a series of freestanding electrodes were fabricated, as shown from Chapter 8 to Chapter 10. These freestanding electrodes include Sn@CNT arrays on carbon paper (Chapter 8), vertically aligned $MoS_2$ nanosheets on carbon paper (Chapter 9) and heterostructured MXene/carbon nanotube composite paper (Chapter 10). The electrode preparations, physiochemical properties, sodium-ion storage mechanisms and other electrochemical characterizations are shown in detail.

9) The last chapter of this doctoral thesis (Chapter 11) briefly summarizes the research outcomes of this doctoral work and future scope of related research is also presented.

## Chapter 1 Literature Review

Adopted on 12 December 2015, the Paris agreement by 195 countries in the twenty-first Conference of the Parties (COP21) of the United Nations Framework Convention on Climate Change (UNFCCC) sets the goal of limiting the rise in the global average temperature to well below 2 °C by 2100. To achieve this goal, the use of renewable energy sources will offer a key support by reducing the combustion of fossil fuels and, hence, by reducing emissions of greenhouse gases, such as carbon dioxide, and nitrous oxide. The main sources of renewable energy include solar energy, wind energy, hydroelectricity, biomass energy, geothermal energy, hydrogen, etc. The development of energy-storage technologies that can be combined with the use of these renewable energies is needed. In this context, new and advanced rechargeable battery systems are currently being pursued and in this doctoral study, the focus is directed towards lithium-ion battery (LIBs) and sodium-ion battery (SIBs) technologies.

### 1.1 Lithium-ion Batteries

Among all metals, lithium is the lightest and has the greatest electrochemical potential and provides the largest energy density for weight. However, attempts to develop rechargeable lithium batteries failed because of poor lithium metal rechargeability due to the formation of dendrites and the consequent safety concerns. Research then shifted to a non-metallic lithium battery using lithium ions. In 1991, the first commercialized LIB appeared.[1] Besides the improved safety, LIBs have merits such as high energy density, low maintenance, long cycle life, no memory effect and low self-discharge. LIBs have been attracting R&D investment from all corners of the world, with wide applications for portable devices, power tools, and electric vehicles.

### 1.1.1 Electrochemistry of Lithium-ion Batteries

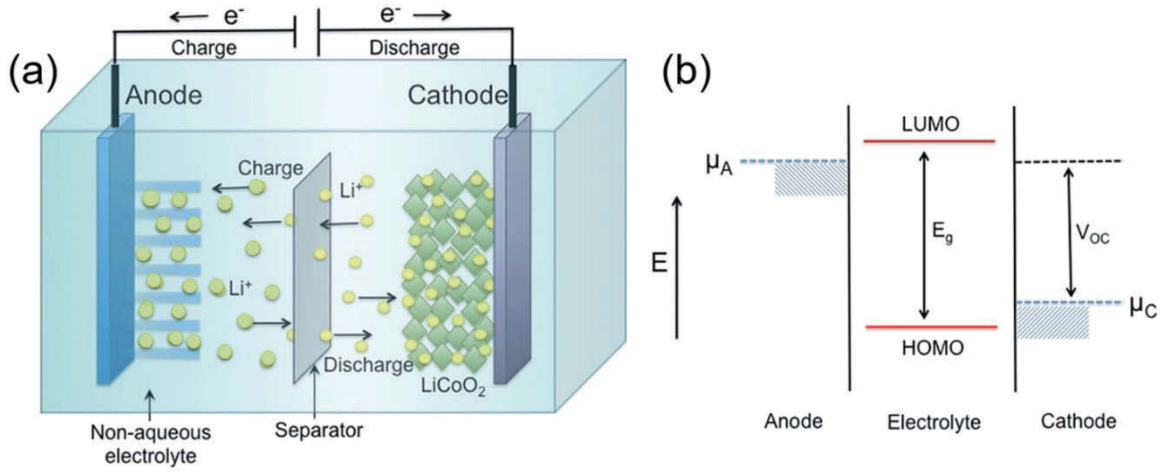


**Figure 1.1** (a) Relative energy diagram of electrode potentials and electrolyte energy gap in LIBs; (b) schematic diagram of the lithium intercalation–de-intercalation reaction mechanism in rechargeable LIBs containing solid electrodes and a liquid electrolyte.[2]

LIBs work by storing electricity in the form of chemical energy during charging while converting chemical energy into electrical energy during discharge. As shown in **Figure 1.1a**, a LIB consists of four components, including anode (negative electrode), separator, cathode (positive electrode), and a $Li^+$ conducting medium as electrolyte. The insulating separator allows the penetration of $Li^+$ while preventing direct contact between anode and cathode. Importantly, the electrolyte solvent should be able to withstand the potentials of electrodes without decomposing, i.e., LUMO of the electrolyte should be higher than the potential of anode while HOMO of the electrolyte should be lower than the potential of cathode, which otherwise will result in cell failure upon the long-term cycling.

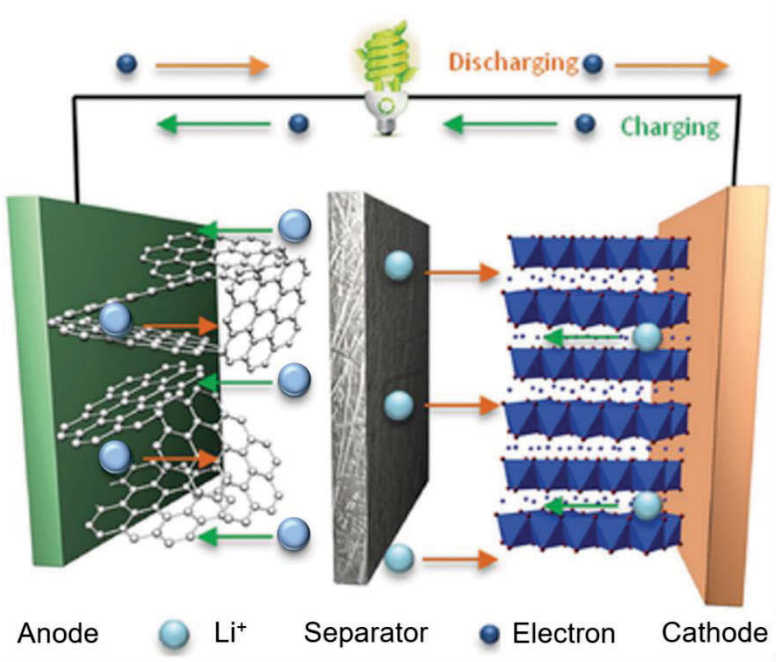


**Figure 1.2** Schematic illustration of rechargeable LIBs.[3]

A typical operation of LIBs is shown in **Figure 1.2**. During the charge-discharge cycles, Li-ions are shuttled between the cathode and anode electrodes. Taking the typical $LiCoO_2$//C cell as example, during the charging process, electrons transfer via the external circuit from the cathode to the anode. Meanwhile, Li-ions are extracted from the layered $LiCoO_2$ cathode, move within the electrolyte and intercalate into the anode electrode, storing electrochemical energy within the battery in the form of chemical energy. When the cell is discharged, the reverse occurs and the electrons flow in the opposite direction through the external circuit powering electrical devices.

Characteristics of LIBs, such as energy and power density, safety, cycle life, cost, environmental impact, depend crucially on the chosen electrode materials. Tremendous efforts have been devoted to developing cathode and anode materials for LIBs. **Figure 1.3** summarizes some of these electrode materials and it can be seen that their potential and

specific capacity varies with the chemical compositions. In the following part, recent advancements of electrode materials for LIBs will be reviewed.

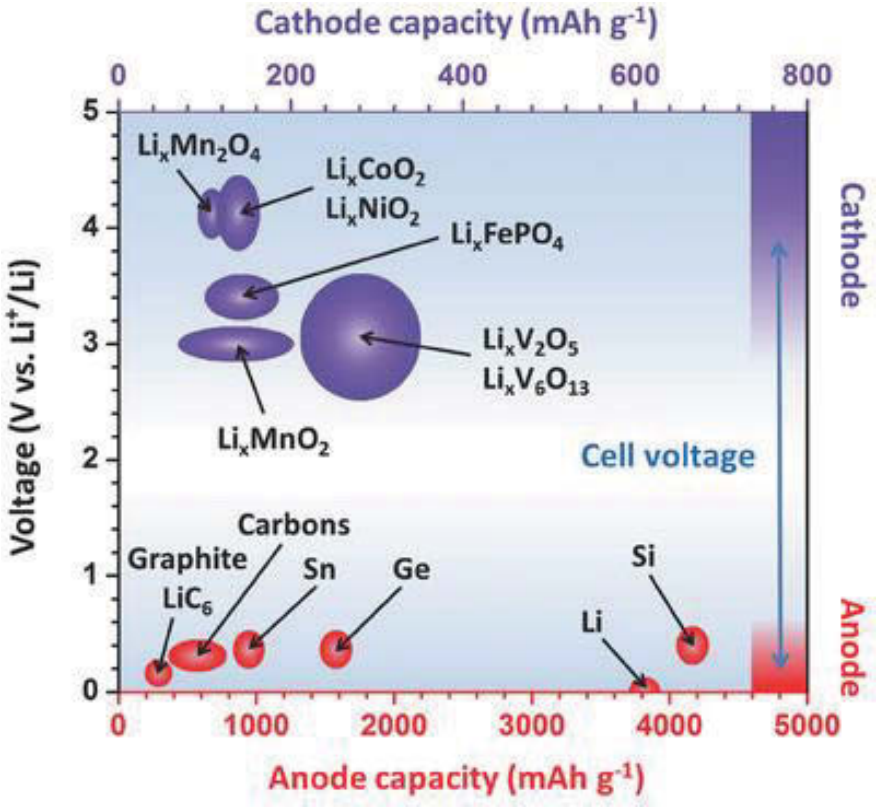


**Figure 1.3** Diagram illustrating the capacities and electrochemical potentials of important cathode and anode materials with respect to Li metal and the cell voltage of LIBs.[3]

### 1.1.2 Cathode materials for LIBs

Although numerous cathode materials have been investigated, the most promising ones for practical applications include $LiCoO_2$, $Li(Ni_{1/3}Co_{1/3}Mn_{1/3})O_2$, olivine $LiFePO_4$, and spinel $LiMn_2O_4$.

#### 1.1.2.1 $LiCoO_2$

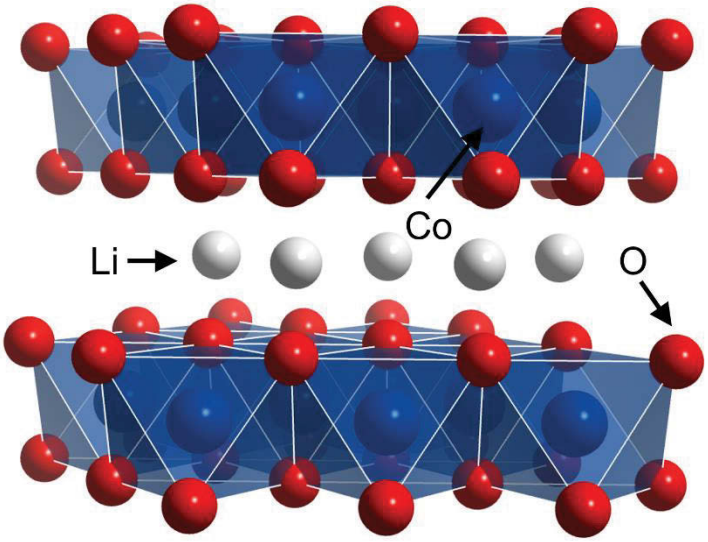


**Figure 1.4** Lamellar structure of $LiCoO_2$.

$LiCoO_2$ has been popularly used as cathode materials since the launch of commercial LIBs in 1991. It has an α-$NaFeO_2$ structure with the oxygen in a cubic close-packed arrangement as shown in **Figure 1.4**. The theoretical capacity of $LiCoO_2$ is 270 mA h $g^{-1}$ when all $Li^+$ ions are extracted from the crystal. Experimentally, a practical capacity of 130-150 mA h $g^{-1}$ can be achieved, indicating that only half of the Li atoms can be used during the charge/discharge process. A voltage plateau at around 3.9 V vs. $Li^+$/Li can be clearly seen at this stage due to the phase change in $LiCoO_2$ from a rhombohedral to monoclinic structure.[4] Although $LiCoO_2$ is identified as a successful cathode material, intrinsic disadvantages exist, including[5]:

1) Cobalt is less available, and thus more costly, than other transition metals, such as manganese, nickel and iron.

2) $LiCoO_2$ is not as stable as other potential electrode materials and can undergo performance degradation or failure when overcharged. One reason is that Co is dissolved in the electrolyte when the electrode is delithiated during charging, leading to the loss of cobalt in the lattice.[6]

Another reason is that at the end of charging, $CoO_2$ layers form, which shear from the electrode surface and create barriers for lithiation.[7] Additionally, there is a dramatic change in lattice parameters with the change in lithium content, which can lead to stresses and micro-cracking of the cathode particles.[8, 9]

3) High voltage charging of the material is harmful to the safety of $LiCoO_2$-based battery, because $O_2$ gas will be released from the lattice upon high voltage charging, which then reacts with the electrolyte.

Tremendous efforts have been devoted to improving the electrochemical performance of $LiCoO_2$. One effective strategy is surface coating.[10] Various metal oxide coatings, such as $Li_2CO_3$,[11] MgO,[12-15] $Al_2O_3$,[16-21] $AlPO_4$,[22-25] $LiMn_2O_4$,[26] $SnO_2$,[27] $ZrO_2$,[28-30] and carbon,[31] have been shown to improve both the cycle life (especially at high-voltage charging) and the rate capability of the $LiCoO_2$ cathode. Besides these, nanostructured $LiCoO_2$ including 1D nanowires,[32] nanotubes,[33] and 3D mesoporous structures[34] have been prepared to improve the electrode/electrolyte interaction, and thus, increase the power density of the battery,

#### 1.1.2.2 $Li(Ni_{1/3}Co_{1/3}Mn_{1/3})O_2$

Apart from $LiCoO_2$, other layered oxides, such as $LiNiO_2$ and $LiMnO_2$, have also been intensively investigated. However, complex synthesis methods and unstable structures during the charging state made it difficult to commercialize these materials. Interestingly, the addition of Ni and Mn to $LiCoO_2$ can maintain its $\alpha$-$NaFeO_2$ layered structure. The most commonly used $Li(Ni,Mn,Co)O_2$ composition contains equal amounts of the three transition metals, i.e. $Li(Ni_{1/3}Mn_{1/3}Co_{1/3})O_2$. The valence states of Ni, Mn, and Co are +2, +4, and +3, respectively.[35] The advantages of the $Li(Ni_{1/3}Mn_{1/3}Co_{1/3})O_2$ cathode are that it provides high

capacity, good rate capability and can operate at high voltages. It was reported that $Li(Ni_{1/3}Mn_{1/3}Co_{1/3})O_2$ can operate at voltage of 4.5 V with a capacity of around 200 mA h $g^{-1}$.[36] The reversible capacity of $Li(Ni_{1/3}Mn_{1/3}Co_{1/3})O_2$ involves the oxidation of $Ni^{2+}$ to $Ni^{4+}$ (a two-electron transfer process) during the initial stage and $Co^{3+}$ to $Co^{4+}$ in the later stage.[37-39] Thus, the higher capacity of layered $LiNi_{1/3}Co_{1/3}Mn_{1/3}O_2$ could be due to the improved chemical stability associated the $Ni^{2+/3+}$ and $Ni^{3+/4+}$ redox couple compared to $Co^{3+/4+}$ redox couple. Unfortunately, $Li(Ni_{1/3}Mn_{1/3}Co_{1/3})O_2$ suffers from poor electrochemical properties at high voltage due to the polarization effect and electrolyte decomposition.[40] Moreover, even at upper voltage limits (4.4-4.5 V), capacity fading was still observed upon cycling. As reported by Shaju and coworkers, this may originate from the gradual decaying of electroactive Co.[41]

#### 1.1.2.3 Olivine $LiFePO_4$

The crystal structure of $LiFePO_4$ is shown in **Figure 1.5a** in which P occupies tetrahedral sites, Fe occupies octahedral sites and Li forms one-dimensional chains along the [010] direction. $LiFePO_4$ delithiates to $FePO_4$ as $Fe^{2+}$ is oxidized to $Fe^{3+}$ and a miscibility gap exists between $FePO_4$ and $LiFePO_4$, as schematically shown in **Figure 1.5b**. During the lithiation process, $FePO_4$ is reversed back to $LiFePO_4$ upon lithiation. Electrochemically, $LiFePO_4$ has a theoretical capacity of 170 mA h $g^{-1}$ and a flat discharge voltage of 3.4 V vs. $Li^+/Li$.

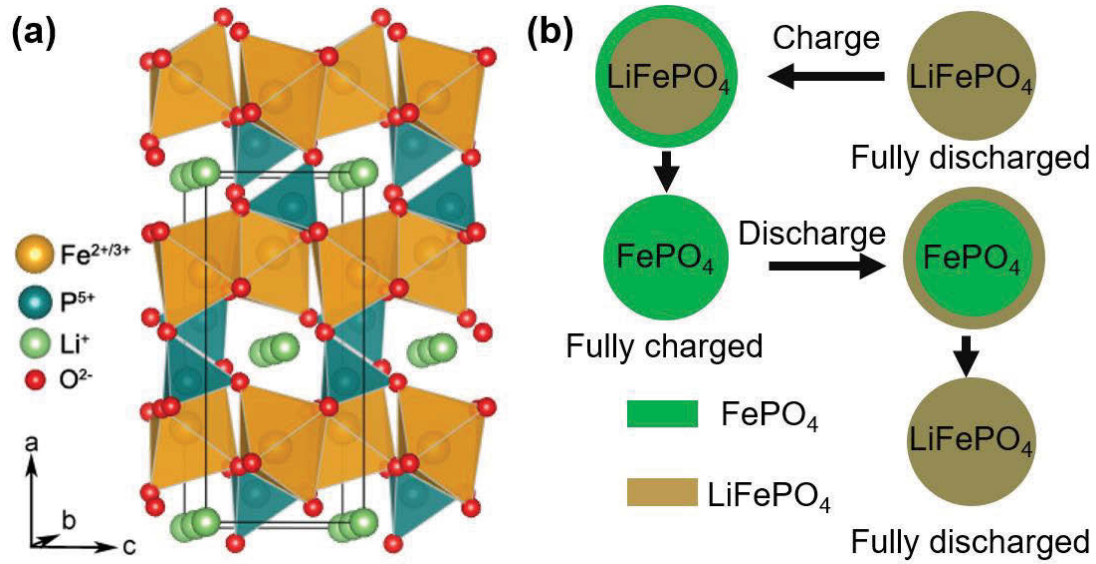


**Figure 1.5** (a) Crystal structure of $LiFePO_4$. (b) Schematic representation of the processes during charge/discharge of $LiFePO_4$.[42]

Furthermore, the electronic conduction of pure $LiFePO_4$ is low ($10^{-9}$ S $cm^{-1}$) and it shows limited ionic conductivity due to the one-dimensional lithium diffusion. The poor electronic and ionic conductivity result in poor rate capability.[43] However, it is reported that the conductivity can be improved by heat treatment.[44] Moreover, the impurity phase $Fe_2P$ that is formed during preparation and/or use as one conductive phase, can improve the electrochemical performance.[45, 46] Coating of a conductive layer on $LiFePO_4$ has proved to be a promising way to improve the electronic conductivity. The conductive ingredients include carbon,[47] and conductive polymers.[48-50] To alleviate the low ionic conductivity, constructing nanostructured $LiFePO_4$ to shorten the diffusion distances and increase the electrode/electrolyte interaction has been intensively investigated. For example, $LiFePO_4$ with an average size of 140 nm has been prepared, which delivered a specific capacity of

147 mA h $g^{-1}$ at 5 C rate and a good cycle stability with no significant capacity loss after more than 400 cycles at 0.5 C rate.[51]

#### 1.1.2.4 Spinel $LiMn_2O_4$

It has been reported that several Mn-oxide crystal types can store Li ions to reasonable levels. These materials can therefore be applied on the cathode side. Reversibility of Li insertion into the manganese oxide host and extraction from manganese oxide electrodes is required in order to ensure multiple charge and discharge cycles. As a very promising substitute to $LiCoO_2$ as a cathode material of choice in rechargeable batteries, spinel lithium manganese oxide ($LiMn_2O_4$) with an open framework that allows insertion of lithium ions from any angle has attracted great technological and research interest because of its low cost, limited environmental impact, and high safety.[52-54]

The crystal structure of spinel $LiMn_2O_4$ is shown in **Figure 1.6**. In the $LiMn_2O_4$ spinel structure (space-group: Fd3m), a cubic close-packed (ccp) array of oxygen ions occupy the 32e position, Mn-ions are located in the octahedral sites (16d sites), and Li in the tetrahedral sites (8a site). The Mn-ions have an octahedral coordination to the oxygen atoms, and the $MnO_6$ octahedra share edges in a three-dimensional host for the Li guest ions (**Figure 1.6**). The 8a tetrahedral site is situated furthest away from the 16d site of all the interstitial tetrahedral sites (8a, 8b and 48f) and octahedral site (16c). Each of the 8a-tetrahedron faces is shared with an adjacent, vacant 16c site. This combination of structural features in the stoichiometric spinel compound constitutes a very stable structure.

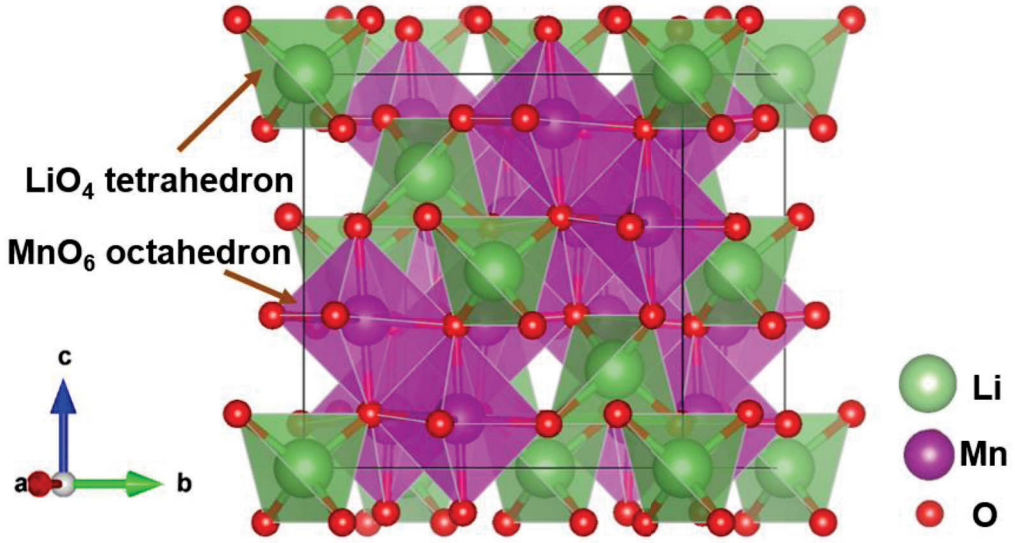


**Figure 1.6** Crystal structure of spinel $LiMn_2O_4$.

The discharge proceeds in predominantly two steps, one around 4 V and the other around 3 V. Usually only the 4 V plateau is used, so that the cell is constructed in the discharged state and must be charged before use just as for $LiCoO_2$.

During the charge process, the removal of Li from $LiMn_2O_4$ occurs through a two-step reaction around 4V; two potential plateaus can be discerned in the charge curve, separated by 100-150 mV. Rigorous studies have also shown that the material goes through at least one two-phase region during charge/discharge:[55]

$$\text{one-phase reaction: } LiMn_2O_4 - (1\text{-}x)\ Li^+ \rightarrow Li_xMn_2O_4\ (0.4< x <1.0) \qquad (1\text{-}1)$$

$$\text{two-phase reaction: } LiMn_2O_4 - (1\text{-}x)\ Li^+ \rightarrow Li_xMn_2O_4\ (0.1< x <0.4) \qquad (1\text{-}2)$$

Although $LiMn_2O_4$ has been demonstrated as the most promising cathode for LIBs, there is still a critical problem prohibiting its wider applications, that is, its unstable rechargeability. This capacity fading was attributed to several possible factors:

1) Mn dissolution. Thackeray *et al.* reported that the capacity fading during cycling was ascribed to Mn dissolution into the electrolyte for the first time.[56] Supervening on this work, Tarascon and co-workers detected the presence of Mn in the surface of the negative electrode by Rutherford backscattering spectroscopy (RBS), in which the deposited Mn on the negative electrode was caused by the reduction of dissolved Mn originating from the spinel.[57] The dissolution of Mn results in the gradual conversion of active electrode materials to a lower voltage defect spinel phase, which results in the capacity loss.

Mn dissolution into the electrolyte has always been linked to the disproportional reaction: $2Mn^{3+} \rightarrow Mn^{4+} + Mn^{2+}$. However, this simple mechanism of Mn dissolution, that is, the disproportional dissolution of $Mn^{3+}$ into the electrolyte, seems to be in conflict with observations since the capacity fading depends on the charge-limited voltage and it is predominant at the end of the charge process. In this high-voltage region, the $Mn^{3+}$ content in the spinel matrix is minimal.[58]

Another plausible Mn dissolution mechanism is related to the electrolyte solution decomposition in high voltage ranges. It was believed that the $LiClO_4$-propylene carbonate (PC)/dimethoxyethane (DMC) electrolyte system could be oxidized on the carbon surface (conductive material) and the as-generated species promoted the manganese dissolution.[59]

2) Structural instability in the high-voltage region. The high-voltage charging of spinel $LiMn_2O_4$ not only may induce oxidation of the electrolyte, but may also lead to the formation of an unstable two-phase structure. The two-phase structure is unstable for lithium insertion/extraction and is transformed to a more stable, one phase structure, such as the structure of “lithium-rich” or “oxygen-rich” spinels. The capacity loss upon cycling for the

stoichiometric spinel is due to the removal of lithium from deep charge depths after many cycles.

3) Jahn-Teller distortion at the end of discharge. The onset of Jahn-Teller distortion in the 4 V range has also been suggested to take place at the surface of the spinel particle due to lithium-ion accumulation at the surface. It was speculated that under dynamic, nonequilibrium conditions during discharging, some crystallites "at the surface" are more lithiated than others in the bulk, thereby driving the composition of the electrode surface into a $Mn^{3+}$-rich region. This might induce a Jahn-Teller effect and transform the surface of the $LiMn_2O_4$ particles from a cubic to a tetragonal phase. As the lattice parameter of the tetragonal phase differs greatly from that of the cubic phase, there is a misfit between the phases, and some of the tetragonal phases might dissociate from the bulk electrode.[60-63]

Many efforts have been devoted to improve the cycle life of spinel $LiMn_2O_4$, with the aim to substitute for $LiCoO_2$ in commercial use. Many strategies have been taken into account and the partial replacement of Mn with other cations has been proved to be an effective one. Mono-cation doped $LiMn_2O_4$ cathodes have been widely investigated using dopants including Al,[64-69] Co,[70-73] Cr,[74-84], Fe,[85] *etc*. The Al-doping enhanced $Li^+$ storage performance is attributed to the factor that the substitution of $Mn^{3+}$ for $Al^{3+}$ increased Mn-O bonding strength in the spinel framework and suppressed the two-phase behavior of the unsubstituted spinel during the intercalation/deintercalation which is the origin of the failure mechanism in the 4 V region.[64]

The development of LIBs is known to suffer from kinetic problems associated with the solid-state diffusion of $Li^+$ in intercalation electrode materials. As mentioned previously, spinel

$LiMn_2O_4$ has a 3D open frame for lithium insertion and extraction. In order to maximize the kinetic properties to obtain satisfactory charge/discharge capacity, morphology engineering has been successfully applied with the aim to design nanostructured electrode materials that facilitate $Li^+$ diffusion.

3D assembled structured $LiAl_{0.02}Mn_{1.98}O_4$ with randomly aligned nanorods on a microsphere were designed not only to increase the $Li^+$ sites on the nanoscaled large surface area to improve the kinetic properties, but also to increase the volumetric energy density and prevent the separator from tearing, which may cause electrical short circuits and safety problems.[69] The nanothorn sphere structured $LiAl_{0.02}Mn_{1.98}O_4$ produces high discharge capacity of 129.8 mA h $g^{-1}$, excellent rate capability (94.6 mA h $g^{-1}$ at 20 C, 72 % of 0.2 C rate discharge capacity) and stable cyclic retention for 50 cycles.

One-dimensional (1D) nanostructures are also particularly attractive because they not only have a large surface-to-volume ratios that allows efficient active mass-electrolyte contact, but also provides 1D electron transport pathways. Among all of the nanostructures, a single crystalline nanowire is an attractive morphology because the nonwoven fabric morphology constructed by the single crystalline nanowire suppresses the aggregation and grain growth at high temperature. Thus, the potential barriers among the nanosize grains can be ignored to decrease the electronic resistance among the nanosize grains. Zhou et al. prepared high-quality single crystalline cubic spinel $LiMn_2O_4$ nanowires based on a novel reaction method using $Na_{0.44}MnO_2$ nanowires as a self-template. These single crystalline spinel $LiMn_2O_4$ nanowires show high thermal stability because the nanowire structure is maintained after heating to 800 °C for 12 h and have excellent performance at high charge-discharge rates, such as 20 A $g^{-1}$, with both a relative flat charge-discharge plateau and excellent cycle

stability.[86] Cui et al. reported that ultrathin $LiMn_2O_4$ nanowires with a cubic spinel structure, which were synthesized by using a solvothermal reaction to produce α-$MnO_2$ nanowires followed by solid-state lithiation, deliver 100 and 78 mA h $g^{-1}$ at very high rates (60C and 150C, respectively) in a larger potential window with very good capacity retention and outstanding structural stability. Such performances are due to both the favorable morphology and the high crystallinity of nanowires.[87] 1D $LiMn_2O_4$ nanorods have also been investigated as advanced cathode materials for LIBs. Cui et al. reported the hydrothermal synthesis of single-crystalline β-$MnO_2$ nanorods and their chemical conversion into freestanding single-crystalline $LiMn_2O_4$ nanorods using a simple solid-state reaction. Galvanostatic battery testing showed that $LiMn_2O_4$ nanorods have a high charge storage capacity at high power rates compared with commercially available powders. More than 85% of the initial charge storage capacity was maintained for over 100 cycles. The structural transformation studies showed that the Li-ions are intercalated into the cubic phase of the $LiMn_2O_4$ with a small change of lattice parameter, followed by the coexistence of two nearly identical cubic phases in the potential range of 3.5 to 4.3 V.[88]

Porous $LiMn_2O_4$ nanorods cathode material was prepared by using porous $Mn_2O_3$ nanorods as the self-supported template, which was obtained from the thermal decomposition of manganese oxalate precursor.[53] Without surface modification, the as-synthesized porous nanorods exhibited superior high-rate capability and cyclability compared to the counterpart nonporous nanorods and nanoparticles. An initial discharge capacity of 105 mA h $g^{-1}$ could be delivered at 10 C rate, and a capacity retention of about 90% was obtained after 500 cycles at this high rate. Using polystyrene as a solid template, Wu et al. successfully fabricated porous $LiMn_2O_4$ consisting of nanograins.[89] $VO_x$-coated $LiMn_2O_4$ spinel nanorod clusters as

a lithium battery cathode material are prepared by mixing $VO(CH_3H_7)_3$ dissolved in ethanol and $LiMn_2O_4$ powder consisting of nanorod clusters and firing this mixture at 700 °C. A significantly decreased amount of Mn dissolution (60 ppm) is observed, in contrast to that of an uncoated counterpart (5000 ppm).[90]

Ordered mesoporous materials have a relatively large surface area, which decreases the current density per unit surface area; thin walls can reduce the length of the diffusion path. Moreover, well-ordered mesoporous materials can facilitate ionic motion more easily compared with conventional mesoporous materials in which the pores are randomly connected. Generally, a hard templating route with post-template treatment is applied to generate highly ordered mesoporous Li-Mn-O spinel. Xia et al. developed a soft-chemical process to fabricate ordered mesoporous $LiMn_2O_4$ as a cathode material for LIBs, in which mesoporous $LiMn_2O_4$ was obtained by chemical lithiation of LiI with mesoporous $MnO_2$ at a low temperature of 350 °C.[91] The as-prepared mesoporous $LiMn_2O_4$ maintains 94% of its initial capacity after 500 cycles at 0.1 C rate and keeps 80% of its reversible capacity, even at 5 C rate. Bruce's group reported the preparation of ordered mesoporous $Li_{1.12}Mn_{1.88}O_4$ as a positive electrode for rechargeable lithium batteries using mesoporous silica (KIT-6) as a hard template.[52] By combining a mesoporous structure with the composition $Li_{1.12}Mn_{1.88}O_4$, superior rate capability at ambient temperature compared with the corresponding bulk material have been demonstrated.

### 1.1.3 Anode materials for LIBs

To support the large-scale applications of LIBs, the development of anode materials with high electrochemical performances has received extensive attention in the past decades.

Basically, there are three types of anode reactions for LIBs: intercalation, conversion, and alloying. In the following section, a brief review of the development of anode materials for LIBs will be discussed.

### 1.1.2.1 Anode materials based on intercalation reaction

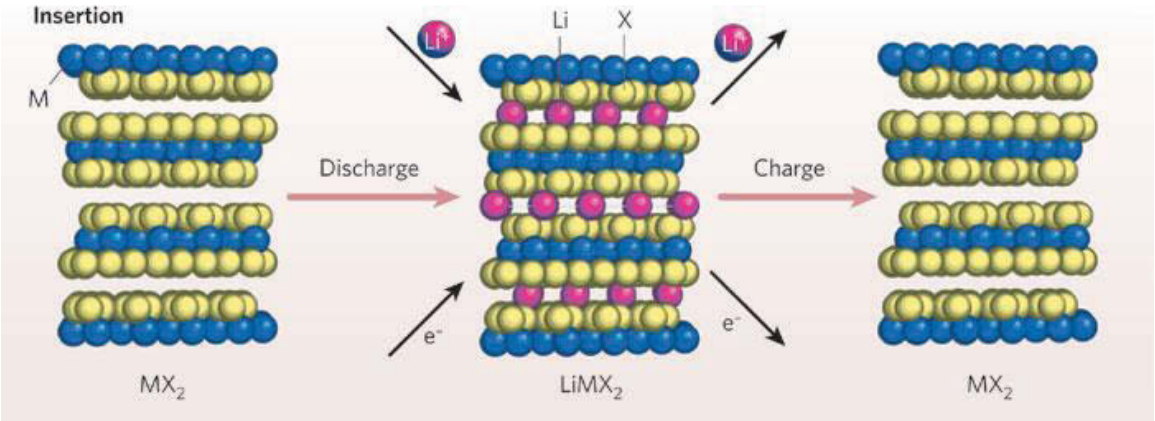


**Figure 1.7** Schematic representation showing insertion/extraction of $Li^+$ during discharge/charge.[93]

The most important anode intercalation materials are carbon and $Li_4Ti_5O_{12}$ (LTO). Carbon anode materials for LIBs have been widely investigated and commercialized since the launch of the first commercial LIBs. The theoretical capacity of graphite is 372 mA h $g^{-1}$ based on that one lithium ion reacts with six C-atoms in a completely reversible intercalation/de-intercalation process ($Li^+ + C_6 + e^- \rightarrow LiC_6$).[94] The potential at which lithium insertion/extraction is at around 0.05 V vs. $Li^+/Li$. Apart from graphite, carbon nanostructures have been extensively investigated, including one-dimensional (1D) carbon nanotubes (CNTs)[95, 96] and carbon nanofibers (CNFs),[97] two-dimensional (2D) graphene,[98, 99] and porous carbonaceous materials.

Spinel lithium titanate ($Li_4Ti_5O_{12}$, LTO) has attracted great interest as an anode material for LIBs. The lithiation of LTO results in a capacity of 150-160 mA h $g^{-1}$ at 1.5 V vs. $Li^+/Li$.[100] Although LTO is inferior to carbon in both its low capacity and high voltage, it is regarded as one promising alternative to graphite anodes due to: i) long and stable cycle life because of zero-strain lithiation/delithiation during the charge/discharge process; ii) the suppression of electrolyte reduction on the surface of the electrode because of the high insertion potential of 1.55 V; and iii) fast charge/discharge rate and excellent low temperature performance due to a high $Li^+$ diffusion coefficient ranging between $10^{-15}$ and $10^{-16}$ $cm^2$ $s^{-1}$.[101, 102] Tremendous efforts have been devoted to alleviate the low electronic conductivity of LTO, including the partial substitution of $Li^+$ or $Ti^{4+}$ by multi-valent metal ions ($V^{5+}$, $Mn^{4+}$, $Fe^{3+}$, $Ni^{2+}$, $Cr^{3+}$, and $Mg^{2+}$)[103-106] and surface coating by metallic grains or carbon.[107-109]

### 1.1.2.2 Anode materials based on conversion reaction

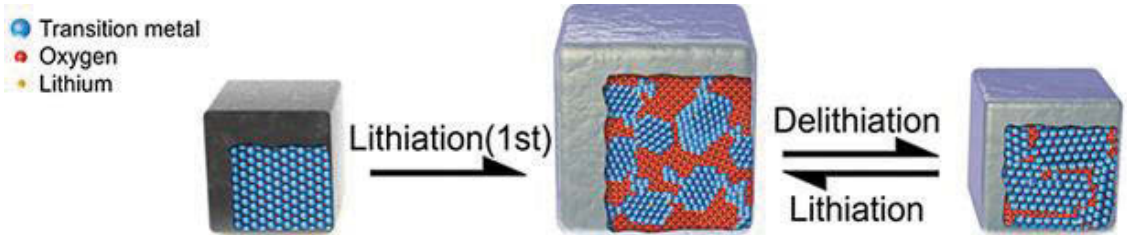


**Figure 1.8** Schematic illustration of the conversion reaction of a transition metal oxide in LIBs.[110]

In 2000, Tarascon and co-workers discovered that transition metal oxides nanoparticles (TMOs NPs) such as CoO, CuO and $Fe_2O_3$, undergo reversible reduction, named as "conversion reaction", in the presence of $Li^+$.[111] The general equation of conversion reactions can be described as follows:

$$M_xO_y + 2yLi^+ + 2ye^- \leftrightarrow xM^0 + yLi_2O \text{ (M = transition metals)} \qquad (1\text{-}3)$$

Conversion reaction-based TMOs are attractive candidates for LIB anodes because of their high theoretical capacities in the range of 600-1000 mA h $g^{-1}$, which is 2-3 times higher than that of graphite (372 mA h $g^{-1}$). After an intensive research for more than one decade, the family of conversion reaction-based TMOs has been dramatically expanded, which includes oxides of iron,[112] manganese,[113, 114] cobalt,[115-118] copper,[119, 120] nickel,[121] molybdenum,[122, 123] zinc,[124] ruthenium,[125-127] chromium,[128, 129] and tungsten,[130-132] and mixed metal oxides.[110]

**Figure 1.8** shows a schematic illustration of the conversion reaction of TMOs as anode materials for LIBs. There is a structural change and amorphization of transition metal oxides that involves large volume expansion. At the end of lithiation, nanoscale transition metal clusters are embedded in the lithium oxide ($Li_2O$) matrix. During delithiation, these transition metal clusters are oxidized to form amorphous transition metal oxides.[110] It should be noted that the conversion reaction involves a complete change in structure and chemical composition of the reactants. The development of nanostructured TMOs anode materials with different morphologies has been intensively investigated to effectively alleviate the strain derived from the volume change. Moreover, nanostructured TMOs anode materials can provide improved electrode-electrolyte contact areas and shorten diffusion lengths for $Li^+$ in the active materials, leading to a high rate capability.[42, 114, 133-135]

Besides TMOs, it was demonstrated that transition metal sulfides,[136-139] phosphides[140-142], and fluorides[143, 144] can also undergo similar reversible, high-capacity conversion reactions.

#### 1.1.2.3 Anode materials based on alloying reaction

Lithium has abundant physiochemical properties, and can alloy with a variety of metals such as Si, Sn, Sb, Al, Mg, Bi, In, Zn, Pb, Ag, Pt, Au, Cd, As, Ga and Ge.[145, 146, 92] Alloy anodes

are known for their high specific capacity and safety characteristics. Generally, they exhibit theoretical specific gravimetric capacities 2-10 times higher than that of graphite while their volumetric capacities are still 2-5 times higher than those of graphite and LTO (considering full volume expansion of lithiated products). While avoiding the energy loss of batteries, the moderate increased operation potential of alloy anodes compared to graphite anodes can suppress lithium deposition, thereby increasing safety of batteries.

However, alloy anodes are still facing challenges for practical applications. The first issue is related to the large irreversible capacity in the first cycle. The large irreversible capacity requires a larger mass of corresponding cathode material in full cells, thereby increasing the total weight and cost. The large irreversible capacity can be ascribed to[92]:

1) Loss of active material;

2) Formation of solid–electrolyte interface (SEI) films on the surface of electrodes;

3) Trapping of lithium in the host alloy;

4) Surface reaction with oxide layers;

5) Aggregation of alloy particles.

Another limitation that hinders the implementation of alloy anodes for practical applications is the huge volumetric change, which results in pulverization of the active alloy particles and poor cycle stability of batteries.

To reduce the first-cycle capacity loss and improve the lifetime of alloy anodes, several strategies have been proved to be effective, including:

1) Dispersing alloy anodes in matrices such as carbonaceous materials,[147, 148] intermetallics[149-151];

2) Preparation of nanostructured alloy anodes, such as 0D nanoparticles;[152, 153]

3) Controlling the operating voltage by restricting either the upper or lower cutoff voltage, which reduces the amount of volume change, the tendency for particle aggregation and the extent of structural change;[154, 155]

4) Optimization of binder and electrolyte.[156]

### 1.2 Sodium-ion Batteries

Recent years have witnessed a significant growth of electric vehicles and energy storage systems. On one hand, the distribution of lithium resources is uneven, being limited to North and South America, China, Australia, Portugal, and Zimbabwe.[157] On the other hand, it is predicted that the size of the global rechargeable battery market will increase from $10 billion in 2010 to over $30 billion in 2020.[158] However, the limited Li resources in the earth's crust could be a bottleneck for LIBs to support the expanded market. These factors will increase the cost of LIBs. Consequently, the development of alternative battery technologies with lower costs is highly desired. Sodium (Na) sits below Li in the periodic table. The similarities and differences between Li and Na are summarized in **Table 1.1**. Na is highly abundant (4$^{th}$ most abundant element in the Earth crust) and low in cost, which makes sodium-ion batteries (SIBs) attractive as alternatives to LIBs. Moreover, unlike in LIBs, Al does not form a binary alloy with sodium at a low voltage, which enables the use of aluminum as a current collector for anodes of SIBs, leading to further reduced cost.

**Table 1.1** Characteristics of sodium and lithium[159, 160]

| Category | Sodium | Lithium |
|---|---|---|
| Cation radius, Å | 1.06 | 0.76 |
| Atomic weight | 23 g $mol^{-1}$ | 6.9 g $mol^{-1}$ |
| $E°$ (vs. SHE) | -2.7 V | -3.04 V |
| Melting point | 97.7 °C | 180.5 °C |
| Cost, carbonates | $150 per ton | $5000 per ton |
| Cost, current collectors at the anode | At $2000–2500 per ton | Cu $7000–8500 per ton |
| Capacity (mA h $g^{-1}$), metal | 1165 | 3829 |
| A–O coordination preference | Octahedral and prismatic | Octahedral and tetrahedral |

The fundamentals of SIBs are identical to LIBs, in which $Na^+$ ions shuttle between cathode and anode as charge carriers. Important criteria of batteries, such as specific capacity and operation voltage, are mainly determined by the electrochemical properties of the electrode material. However, the larger ionic radius of $Na^+$ (1.02 Å) than that of $Li^+$ (0.76 Å) makes it difficult to search for proper electrode materials for SIBs. Successful reversible intercalation hosts must possess channels and interstitial sites large enough to accept the larger $Na^+$ cations.

### 1.2.1 Cathode materials for SIBs

A summary of operation voltages as well as specific capacities of some cathode materials for SIBs is shown in **Figure 1.9**. The identified cathode materials can be categorized into three types: layered sodium transition-metal oxides, sodium polyanions (phosphates, fluorophosphates, pyrophosphates, fluorosulfates, and sulfates) and Prussian blue cathodes.

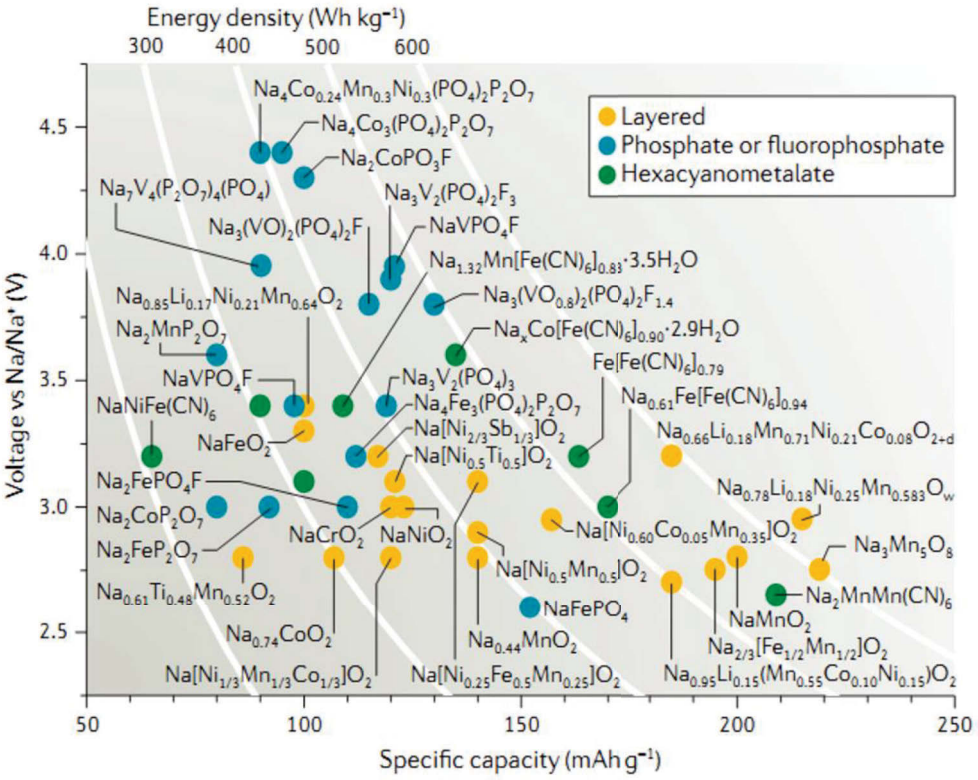


**Figure 1.9** Operation voltages versus specific capacities of various cathode materials for SIBs.[158]

#### 1.2.1.1 Layered sodium transition-metal oxides

The most common layered structures are composed of a sheet of edge-sharing $MeO_6$ octahedra (Me = 3d transition metals). The $MeO_2$ layers are stacked along the *c*-axis direction and $Na^+$ are accommodated in between the $MeO_2$ motifs. As shown in **Figure 1.10**, there are

two types of sodium-based layered materials, i.e., O3-type or P2-type, where O and P represent octahedral or trigonal prismatic coordinations of the sodium ions and 3 or 2 represents the number of distinguishable sodium layers.

In general, sodium extraction from O3- and P2-type phases induces phase transitions. For example, when $Na^+$ are extracted from the O3-type phase, vacancies form and Na ions become energetically stable at prismatic sites, which are formed by gliding of $MeO_2$ slabs.[161, 162] As a results, oxygen packing changes from "AB CA BC" to "AB BC CA", and this phase is classified as a P3-type phase as shown in **Figure 1.10**.[163] When $Na^+$ are extracted from the P2-type phase, the layered oxides are transformed from P2-type phases to O2-type phases. For example, as one of the first materials investigated, α-$NaMnO_2$ with an O3-type structure has voltage profiles exhibiting pronounced stepwise processes, suggesting structural transitions. It can deliver a capacity of 200 mA h $g^{-1}$ with good capacity retention.[164]

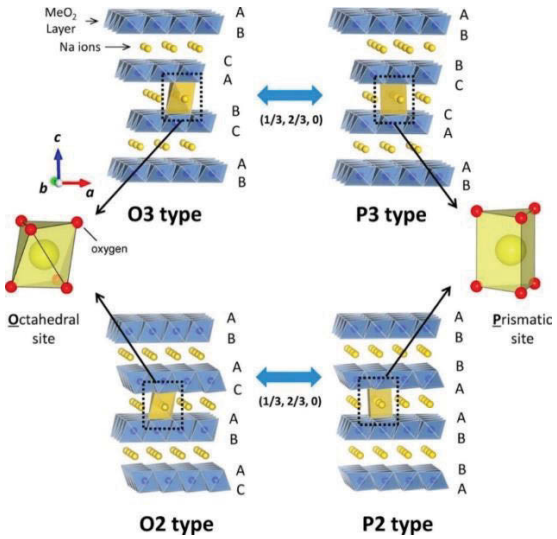


**Figure 1.10** Classification of Na-Me-O layered materials with sheets of edge-sharing $MeO_6$ octahedra and phase transition processes induced by sodium extraction.[163]

P2-$Na_{2/3}Mn_{1/2}Fe_{1/2}O_2$, is among the most promising cathode materials for SIBs in terms of both sustainability and electrochemical performance.[165] P2-$Na_{2/3}Mn_{1/2}Fe_{1/2}O_2$ delivers 190 mA h $g^{-1}$ of reversible capacity in sodium cells with the electrochemically active $Fe^{3+}/Fe^{4+}$ redox couple. However, only 75% of its initial capacity can be retained after 30 cycles. Cation doped layered materials such as P2-$Na_{0.8}[Li_{0.12}Ni_{0.22}Mn_{0.66}]O_2$,[166] P2-$Na_{0.67}Mn_{1-y}Mg_yO_2$ (y=0, 0.05, 0.1, 0.2),[167] and $NaFe_{1-y}Ni_yO_2$ (0.5< y <0.7),[168] have been proved to improve capacity retention.

Although layered cathode materials have been intensively investigated, some of them have been demonstrated to be sensitive to atmosphere. For example, intercalation of water has been observed in P2-$Na_{2/3}[Co_xNi_{1/3-x}Mn_{2/3}]$ (x = 1/6, 1/3) and mixed P2/P3 structured $Na_xNi_{0}.22Co_{0.11}Mn_{0.66}O_2$.[169, 170] Their atmosphere sensitivity leads to concerns over storage and handling, which could bottleneck large-scale applications.

**1.2.1.2 Sodium polyanions**

Parallel to layered oxide materials, a plethora of polyanionic sodium compounds have been studied as cathode materials for SIBs. Advantages of sodium polyanions for SIBs include:[171]

1) diverse open-framework structures;

2) the presence of low-energy $Na^+$ migration pathways;

3) possibilities of tuning the operating voltage by modifying the local environments;

4) favorable structural energetics for a flat voltage response;

5) thermal and oxidative stability at high charging voltage due to their robust covalent frameworks.

Polyanionic framework compounds include phosphates, fluorophosphates, fluorosulfates, and sulfates. Advances in sodium polyanion compounds will be briefly introduced.

A typical sodium phosphate is $NaFePO_4$. However, it is inclined to exist in a maricite structure without free pathways for the diffusion of Na-ions.[172, 173] An olivine-type $NaFePO_4$ with electrochemical activity can be prepared by low-temperature Li/Na exchange from olivine-$LiFePO_4$.[174] Unfortunately, the olivine-type $NaFePO_4$ has sluggish electrochemical kinetics. The more-promising sodium phosphates are NASICON compounds, which feature large tunnels for the fast conduction of $Na^+$. NASICON is an acronym for sodium (Na) super ionic conductor. The NASICON structure is formulated as $Na_3M_2(XO_4)_3$, where X = $Si^{4+}$, $P^{5+}$, $S^{6+}$, $Mo^{6+}$, $As^{5+}$. $Na_3V_2(PO_4)_3$, which is well known for its high sodium ion conductivity, has been extensively studied.[175, 176] $Na_3V_2(PO_4)_3$ has a high voltage peak at around 3.37 V vs. $Na^+/Na$ and corresponds to the $V^{4+}/V^{3+}$ redox couple. A maximum capacity of 116 mA h $g^{-1}$ was reached at the 0.1 C rate. At the 10 C rate, 92.2% of the capacity was retained and as the rate increased to 20 C and 40 C, the retention was 80% and 54%, respectively.[175]

Sodium fluorophosphates have been explored as new cathode materials with high operating voltage for SIBs. The high operating voltage of sodium fluorophosphates is due to the presence of highly electronegative fluorine atoms in the covalent polyanionic framework, which can increase the voltage of the active redox couple. For example, $Na_3V_2(PO_4)_2F_3$,[177] $Na_2FePO_4F$,[178] and $Na_{1.5}VPO_{4.8}F_{0.7}$[179] have been reported. $Na_3V_2(PO_4)_2F_3$ was shown to have a high average voltage of 3.9 V and it is theoretically predicted to follow a single-phase behavior with negligible volume changes (2%).[177] Nazar and co-workers reported a $Na_2FePO_4F$ cathodes with a layer-like two-dimensional framework of $Fe_2O_7F_2$ bioctahedra connected by $PO_4$ tetrahedra, which host two $Na^+$ ions in the interlayer space. Both the charge

and discharge profiles exhibit two two-phase plateaus, centered at 2.90 V and 3.05 V versus $Na^+/Na$, and 80% of the 120 mA h $g^{-1}$ theoretical capacity can be maintained after 10 cycles.[178] However, the electrochemical kinetics of $Na_2FePO_4F$ are not as favorable as in $Na_{1.5}VPO_{4.8}F_{0.7}$. $Na_{1.5}VPO_{4.8}F_{0.7}$ exhibited a capacity retention of 95% and 84% after 100 and 500 cycles, respectively, at a rate of 1 C. The promising electrochemical performance can be attributed to the small volume change, fast Na-ion diffusion and lack of ordered compositions within the redox window.

$NaFeSO_4F$, a sodium fluorosulfate, has a tunnel type structure. The ionic conductivity is 7.14 $\times 10^{-7}$ $S^3$ $cm^{-1}$. It has a $Fe^{2+}/Fe^{3+}$ signature plateau centered at around 3.6 V. However, only ~0.07 Na can be extracted from this structure electrochemically and hence only ~6% of its theoretical capacity can be achieved.[180] On the contrary, its sulfate cousins, such as $Na_2Fe(SO4)_2 \cdot 2H_2O$ and $Na_2Fe_2(SO_4)_3$, are more electrochemically active. It was found that kröhnkite-type $Na_2Fe(SO_4)_2 \cdot 2H_2O$ displays a $Fe^{2+}/Fe^{3+}$ redox couple at about 3.25 V with good structural reversibility.[181] Interestingly, $Na_2Fe_2(SO_4)_3$ has the highest ever reported $Fe^{3+}/Fe^{2+}$ redox potential at 3.8 V versus $Na^+/Na$ along with fast kinetics. In a half cell, it displayed a sloping voltage profile and 85% of the theoretical capacity (102mA h $g^{-1}$) can be obtained.[182]

#### 1.2.1.3 Prussian blue cathodes

SIBs prefer cathode materials with open host frameworks containing a suitable transition-metal ion to host $Na^+$ with large size. Prussian blue analogues (PBAs) has a cubic structure consisting of $Fe^{2+}$ and $Fe^{3+}$ sitting on alternate corners of corner-shared iron octahedra bridged by cyano $(C\equiv N)^-$ ligands (**Figure 1.11**).[183] The open-framework contains channels (3.2 Å) and interstitial sites (4.6 Å), allowing rapid solid-state diffusion of $Na^+$.[171]

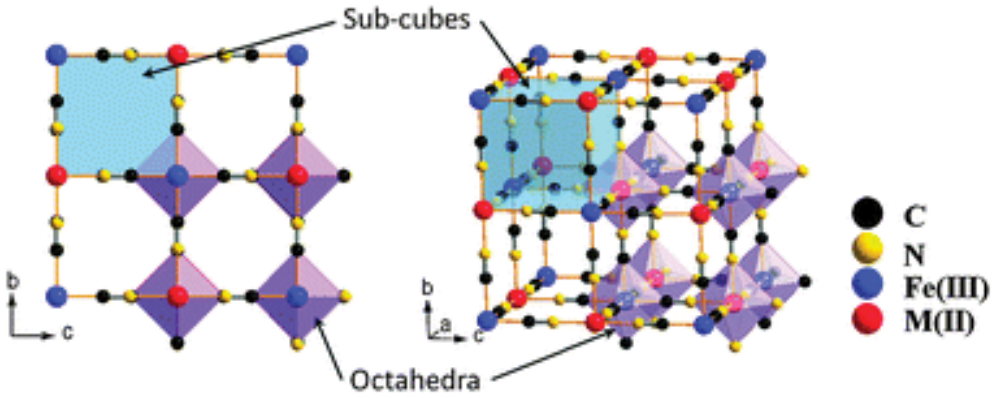


**Figure 1.11** Framework of Prussian blue analogues.[183]

Among PBAs, hexacyanoferrates are the most widely investigated because of the low cost and facile synthesis. The pioneering work by Goodenough and co-workers showed that insertion of Na into $KFe_2(CN)_6$ in a carbonate electrolyte exhibited a reversible capacity near 100 mA h $g^{-1}$ with no capacity fade in 30 cycles. $KFe_2(CN)_6$ cathode showed peaks at 2.97/2.92 V corresponding to oxidation–reduction of the high-spin $Fe^{3+}$-$Fe^{2+}$ couple bonding to N and peaks at 3.69/3.58 V corresponding to the low-spin $Fe^{3+}$-$Fe^{2+}$ couple bonding to C. However, the $KFe_2(CN)_6$ electrode showed a low coulombic efficiency in the initial cycling, which could be ascribed to crystal water in this PBA compound.[183]

### 1.2.2 Anode materials for SIBs

In contrast to the extensively investigated cathodes, reported anode materials that are able to react with sodium are limited. The reported anode materials can be categorized into carbon materials, intercalation-based materials, conversion reaction compounds and alloy anodes. **Figure 1.12** summarizes the specific capacities as well as the operation voltages of various anode materials. This section will discuss the development of anode materials for SIBs.

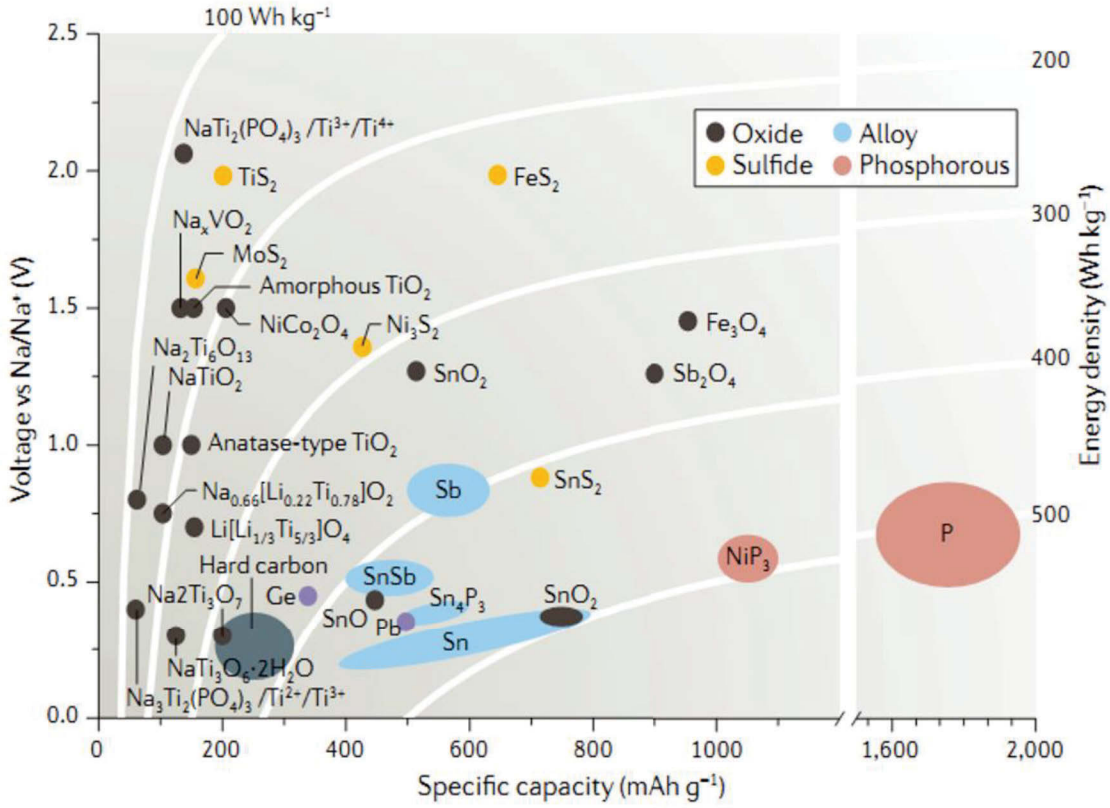


**Figure 1.12** Operation voltages vs. specific capacities of various anode materials for SIBs.[158]

### 1.2.2.1 Carbon materials

It was experimentally shown in earlier publications that graphite delivered limited reversible capacities of only around 12 mA h $g^{-1}$, which suggests that the formation of a stage 1 graphite intercalation compound is unfavorable.[184, 185] Computational investigations showed that the formation of either $NaC_6$ or $NaC_8$ has a negative intercalation potential, which means it is thermodynamically unfavorable. The development of compatible electrolyte affords Na intercalation in graphite galleries.[186-188] It is reported that in a diglyme-based electrolyte, the co-intercalation phenomenon results in a stage-I ternary intercalation compound with an estimated stoichiometry of $Na(diglyme)_2C_{20}$. This leads to high energy efficiency, small

irreversible loss during the first cycle, and a superior cycle life with capacities close to 100 mA h $g^{-1}$ for 1000 cycles and coulombic efficiencies >99.87 %.[186]

In contrast, the storage of Na in non-graphitic carbon materials (i.e. hard carbon, soft carbon and amorphous carbon) has been reported as thermodynamically feasible. The extent of Na intercalation depends critically on: i) the microstructure of carbon materials ($NaC_{70}$, $NaC_{30}$, and $NaC_{15}$ were formed for graphite, petroleum coke, and Shawinigan black, respectively); and ii) the particle size of the carbon used.[189] Among them, hard carbon has been widely studied as a promising anode. The storage mechanism of $Na^+$ in hard carbons is proposed as a "card-house" model: i) Na-ion intercalation between graphene sheets, corresponding to the sloping-voltage region and (ii) Na-ions filling in the pores between nano-graphitic domains, corresponding to the plateau region.[190] The number of defect sites in hard carbon is strongly related to the Na storage capacity in the slope-voltage region.[191] However, there is no consensus about the Na storage mechanism in the low-voltage plateau region. The debate focuses on whether Na metal nanoclusters are formed in this region.[192, 193, 194] To further improve the Na storage capacity of carbon materials, modifications by doping of heteroatoms, such as nitrogen[195] and sulfur,[196] have been investigated.

#### 1.2.2.2 Intercalation-based materials

Ti-based oxides have been the most widely investigated anode materials for Na intercalation because of their low cost and environmental benignity. The pioneering work conducted by Xiong et al. reported amorphous $TiO_2$ nanotubes as anodes in the voltage range between 0.9 and 2.5 V.[197] This work intrigued the investigations of Ti-based oxides with different polymorphs and nanostructures as host intercalation materials for Na-ion storage. The intercalation of $Na^+$ is normally accompanied by $Ti^{3+}/Ti^{4+}$ redox reactions.[198] Detailed

investigations have shown that Na insertion in $TiO_2$ follows: i) pseudo-capacitive reactions during the initial discharge process; ii) structural rearrangement, and finally iii) a disproportionation reaction and formation of $Ti^0$ and $O_2$ during further discharge. Then, iv) reversible Na de/insertion occurs in $Na_x(TiO_2)$ ($0.28 \leq x \leq 0.69$).[199]

$Li_4Ti_5O_{12}$ can also accommodate Na-ions and delivers a reversible capacity of about 150 mA h $g^{-1}$.[200] Since the Na-ion diffusion coefficient of $Li_4Ti_5O_{12}$ is 5 orders of magnitude smaller than Li-ion diffusion, the development of nanosized $Li_4Ti_5O_{12}$ is promising to improve the sodium-ion storage performance.[201] Sodium titanium oxides have also been investigated as anode materials for SIBs, including $Na_2Ti_3O_7$,[202] $Na_2Ti_2O_5$,[203] layered $NaTiO_2$,[204] $Na_2Ti_6O_{13}$,[205] and $Na_2Ti_7O_{15}$.[206]

**Table 1.2** Some of the MAX phases reported[207]

| 211 ($M_2AX$) | | | | | | 312 ($M_3AX_2$) | 413 ($M_4AX_3$) |
|---|---|---|---|---|---|---|---|
| $Ti_2AlC$ | $Ti_2CdC$ | $Ti_2GaC$ | $Ti_2InC$ | $Ti_2TlC$ | $Sc_2InC$ | $Ti_3AlC_2$ | $Ti_4AlN_3$ |
| $V_2AlC$ | $V_2GaC$ | $Cr_2GaC$ | $Ti_2AlN$ | $Ti_2GaN$ | $Ti_2InN$ | $V_3AlC_2$ | $V_4AlC_3$ |
| $V_2GaN$ | $Cr_2GaN$ | $Ti_2GeC$ | $Ti_2SnC$ | $Ti_2PbC$ | $V_2GeC$ | $Ti_3SiC_2$ | $Ti_4GaC_3$ |
| $Cr_2AlC$ | $Cr_2GeC$ | $V_2PC$ | $V_2AsC$ | $Ti_2SC$ | $Zr_2InC$ | $Ti_3GeC_2$ | $Ti_4SiC_3$ |
| $Zr_2TlC$ | $Nb_2AlC$ | $Nb_2GaC$ | $Nb_2InC$ | $Mo_2GaC$ | $Zr_2InN$ | $Ti_3SnC_2$ | $Ti_4GeC_3$ |
| $Zr_2TlN$ | $Zr_2SnC$ | $Zr_2PbC$ | $Nb_2SnC$ | $Nb_2PC$ | $Nb_2AsC$ | $Ta_3AlC_2$ | $Nb_4AlC_3$ |
| $Zr_2SC$ | $Nb_2SC$ | $Hf_2InC$ | $Hf_2TlC$ | $Ta_2AlC$ | $Ta_2GaC$ | | $Ta_4AlC_3$ |
| $Hf_2SnC$ | $Hf_2PbC$ | $Hf_2SnN$ | $Hf_2SC$ | | | | |

Two-dimensional (2D) metal carbides, carbonitrides and nitrides, denoted as MXenes, were first reported in 2011.[208] MXenes feature a 2D structure similar to graphene. They are formulated as $M_{n+1}X_nT_x$ (M-transition metal, X-carbon or nitrogen, T-surface terminations such as OH, O, and F) with n values varying from 1 to 3 for the existing MXenes. MXenes are prepared from their MAX phases (A is mainly a group IIIA or IVA element), which are layered hexagonal with A slaps sandwiched between M and X layers. The known MAX phases are listed in **Table 1.2**. In MAX, the M–A bonds are weaker than the M–X bonds, which makes the selective etching of A layers possible. Some MXenes have been successfully prepared from the corresponding MAX phases, such as $Ti_2C$, $Nb_2C$, $V_2C$, $Mo_2C$, $Ti_3C_2$, $Ti_3CN$, $Mo_2TiC_2$, $Mo_2Ti_2C_3$, and $Ti_4N_3$.[209-212] The first report about preparation of $Ti_3C_2$ MXene used hydrofluoric acid aqueous solution as the etchant at room temperature.[208] Because M atoms on MXene surfaces are unstable in air and should be satisfied by suitable ligands, MXenes surfaces are terminated by surface functionalization $T_x$ (T = OH, F, O, H, etc.). Further investigations have shown that by the combination of common, inexpensive hydrochloric acid (HCl) and fluoride salts, such as LiF, it is possible to dissolve aluminum from $Ti_3AlC_2$ and extract two-dimensional carbide layers $Ti_3C_2$.[213] It was shown that a variety of cations can be intercalated into the interlayer between MXene.[214] The HCl+LiF method thus achieves etching and intercalation in a single step. Followed by simple sonication in water, colloidal solutions of $Ti_3C_2T_x$ single- or few-layer can be obtained. In addition, a variety of organic molecules, such as urea, hydrazine, dimethyl sulfoxide, and tertiary amines can also intercalate in between MXene layers.[215, 216] Specifically, when dimethyl sulfoxide or tertiary amines are intercalated, multilayered MXenes can be delaminated into single- or few-layer flakes by sonication in water.

It is theoretically investigated that up to one monolayer (1 ML) of Na can be absorbed at the fcc hollow site on each side of MXene, corresponding to the chemical stoichiometry of $M_2CO_2Na_2$. This was evidenced by scanning transmission electron microscopy (STEM) by Wang et al. and two layers of Na ions occupying the interlayers were found.[217] The intercalated Na-ions prefer to stay on top of the C atoms in the $Ti_3C_2T_X$ layer and are about 0.23 nm apart from each other, in accordance with computational predictions.[218] On the other hand, theoretical investigations demonstrate low diffusion barriers for $Na^+$ on MXene. For $Ti_3C_2T_x$, a possible spatial hopping pathway with high structural symmetry between two nearest neighboring Na adsorption sites is that the Na-ions first move to the top of the nearest neighboring Ti(s) atoms, and then to the top of the C atoms (top C → top Ti(s) → top C). The diffusion barriers for these two paths are about 0.1087 and 0.4257 eV, respectively, suggesting that it is easier to diffuse from the top C to the top Ti(s) than from the reverse direction. Moreover, the calculated activation barriers for Na ion migration on oxygen terminated $Ti_2CO_2$, $V_2CO_2$, $Cr_2CO_2$, $Mn_2CO_2$, and $Mo_2CO_2$ were 0.18, 0.15, 0.09, 0.15, and 0.14 eV, respectively.[219] Considering the high electronic conductivity as well as fast ionic diffusion, MXenes are promising for sodium-ion storage, especially for high-rate applications. When applied as an anode material for sodium-ion storage, multilayered $Ti_2CT_x$ MXene delivered a reversible capacity of 175 mA h $g^{-1}$ at a current density of 20 mA $g^{-1}$. The multilayered $Ti_2CT_x$ electrode showed good rate capability. Even at a current density of 5000 mA $g^{-1}$, a capacity of 63 mA h $g^{-1}$ can be achieved. Multilayered $Ti_3C_2T_x$ has also been tested as a negative electrode for Na-ion storage and exhibited a capacity around 100 mA h $g^{-1}$.[217, 218] The Na-ion insertion potentials of MXenes can be tuned by changing the transition metal and surface functional groups.[219, 220] Another MXene, $V_2CT_x$, was successfully used for

positive electrodes, paired with hard carbon to assemble full cells delivering a maximum cell voltage of 3.5 V and a cell capacity of 50 mA h $g^{-1}$.[221]

#### 1.2.2.3 Conversion reaction compounds

Compared to LIBs, few metal oxides/sulfides can be used as anode materials for SIBs by conversion reactions. Among this type of anode materials, the reported metal oxides include iron oxides, cobalt oxides, and copper oxides. Hariharan et al. demonstrated that $Na^+$ electrochemically reacted with $Fe_3O_4$ to form Fe metal and $Na_2O$, providing a high specific capacity of around 400 mA h $g^{-1}$.[222] This value is much lower than the theoretical capacity (926 mA h $g^{-1}$), which can be ascribed to: i) sluggish kinetics of the Na-ion transfer in conversion reactions because of the larger ion size; and ii) different nature of the SEI layer formed in Na cells.[223-229] Jiang et al. fabricated a series of transition metal oxides including $Fe_2O_3$, $Mn_3O_4$, $Co_3O_4$, and NiO, and characterized their electrochemical properties as anodes for SIBs. The sodium uptake/extraction was confirmed by way of reversible conversion reactions.[230] The first experimental results by Klein et al. on different copper compounds showed that the conversion of copper-based compounds, such as CuO and CuS, with sodium proceeds over intermediate phases, as evidenced by XRD and electrochemical measurements.[231] The Na-ion storage properties of CuO were directly observed by *in situ* TEM. The sodiation process of CuO was shown to consist of three steps. $Cu_2O$ and $Na_2O$ were predominantly formed during the first step, then, on further reaction, the intermediate NaCuO phase nucleated. The final sodiation products were $Na_6Cu_2O_6$, $Na_2O$, and Cu.[232]

Metal sulfides, especially layered transition metal sulfides, attracted tremendous attentions as anode materials for SIBs because the unique layered structure is favorable for initial ion

intercalation/de-intercalation, and the following conversion chemistry enables high theoretical capacity. Molybdenum disulfide ($MoS_2$) has a lamellar structure with each layer stacking via Van der Waals interactions. In a single-layered $MoS_2$, there are numerous S-Mo-S units where molybdenum atoms are sandwiched in the center by sulfur atoms with strong covalent bonding. The Na-ion intercalation leads to a series of two-phase structural transitions from 2H-$MoS_2$ to 1T-$MoS_2$, which is confirmed at the atomic scale by aberration-corrected scanning transmission electron microscopy.[233] The intercalation process is partially staged. Depending on the depth of intercalation, the structure of $MoS_2$ can be partially recovered (to 1T-$MoS_2$) if less than 1.5 Na-ions per formula of $MoS_2$ are intercalated. However, its structure cannot be restored once it is decomposed to $Na_xS$ and metallic Mo. Dispersing $MoS_2$ in a carbon matrix with different dimensions showed enhanced electrochemical performance for sodium-ion storage.[234-240] However, the large irreversible capacity in the first cycle and the lack of understanding of interactions between $MoS_2$ and carbon are still the bottleneck for further applications of $MoS_2$ as anode material for SIBs.

$SnS_2$-based anode materials have been reported as one of the highest capacity anode materials because of the combination of conversion reaction and alloying reaction.[241] $SnS_2$ can be integrated with reduced graphene by either *in situ* growth[242] or post methods.[243] Meng and co-workers investigated the sodiation/desodiation processes of $SnS_2$/reduced graphene oxide composites.[244] It is determined that $Na_2S_2$ forms instead of $Na_2S$ at the fully discharged state. The as-formed $Na_2S_2$ works as a matrix to relieve the strain from the extensive volume expansion of the Na-Sn alloy reaction. Highly amorphous $SnS_2$ forms after one full cycle. A simple solid-state reaction method was applied to prepare carbon-coated $SnS_2$ ($SnS_2$/C) anode materials for SIBs by annealing metallic Sn, sulfur powder, and polyacrylonitrile in a

sealed vacuum glass tube. It should be noted that this method is less time-consuming and can be scaled up for mass production. In addition, efforts have been devoted to develop freestanding $SnS_2$ based electrode material. Wang and co-workers reported $SnS_2$@graphene nanosheet arrays grown on carbon cloth, which demonstrated promising electrochemical performance for SIBs.[245]

#### 1.2.2.4 Alloy anodes

Alloy anodes accommodate Na-ions by forming sodium-based alloys, giving a high theoretical specific capacity, as summarized in **Table 1.3**. The reported alloy anodes are mainly Group IVA and VA elements. Alloy anodes have low operation voltage versus sodium, which is desirable to develop high voltage devices. Among them, tin is inexpensive (around 20 USD/kg), relatively safe to work with as a powder (not extremely pyrophoric), nontoxic, and highly abundant. Tin is a promising anode material exhibiting high charge storage capacity both by weight and by volume. In addition, Sn forms a variety of compounds, such as SnO, $SnO_2$, SnS, $SnS_2$, and $Sn_4P_3$, which offer great opportunities to tune the electrochemical performances by chemical manipulation. These Sn-based compounds offers high specific capacities for sodium-ion storage by conversion reactions followed by Sn-Na alloying.[246]

**Table 1.3** Summary of properties of typical metal or metalloid materials for Na-ion batteries.[246]

| | Reduction product | Theoretical capacity (mA h $g^{-1}$) | Volumetric expansion ($Na_xX/X$) (%) | Average voltage (vs. $Na^+/Na$) (V) |
|---|---|---|---|---|

| | | | | |
|---|---|---|---|---|
| Sn | $Na_{3.75}Sn$ | 847 | 520 | 0.2 |
| Sb | $Na_3Sb$ | 660 | 393 | 0.6 |
| P | $Na_3P$ | 2596 | 408 (red)<br>500 (black) | 0.4 |
| Si | NaSi | 954 | 243 | 0.5 |
| Ge | NaGe | 369 | 305 | 0.3 |

The main challenge of Sn-based anode materials is their large volume change (up to 300%) during sodium insertion and extraction, which leads to pulverization of the active alloy particles and poor cycle stability. In order to overcome this problem, efforts have been devoted to compositionally manipulate and construct Sn-based nanostructures. In this context, carbon materials show potential applications, which can not only provide electronic conductive networks but also preserve the agglomeration of Sn nanoparticles. A Sn thin film was deposited on a soft and mesoporous wood fiber substrate, which showed a stable cycling performance of 400 cycles with an initial capacity of 339 mA h $g^{-1}$.[247] Tin-coated viral nanoforests have also been developed as binder-free composite electrodes. When applied as anode materials for SIBs, an initial capacity of 722 mA h (g Sn)$^{-1}$ along with 405 mA h (g Sn)$^{-1}$ retained after 150 deep cycles was achieved.[248] In addition, a mesoporous carbon (C) matrix has been applied to accommodate Sn nanoparticles.[249]

Sn-based compounds have also been integrated into carbon materials and 2D graphene/reduced graphene oxide are among the most popular ones. This is because the preparation is simple yet effective to improve the cycling performance of Sn-based anodes. For example, ultrafine $SnO_2$ nanoparticles (around 5 nm) were loaded on a reduced graphene

oxide framework with a weight ratio of 76.4% by a hydrothermal method. The electrode delivers a reversible Na-storage capacity of 330 mA h $g^{-1}$ with an outstanding capacity retention of 81.3% over 150 cycles.[250] Zhang and co-workers developed a facile and up-scalable wet-mechanochemical process to prepare $SnO_2$/graphene nanocomposites from $SnCl_2$ and graphene oxide (GO), which are ball-milled in aqueous media for sodium-ion storage.[251] An ice-templated preparation and sodium storage of ultrasmall $SnO_2$ nanoparticles (3–4 nm) embedded in three-dimensional (3D) graphene ($SnO_2$@3DG) has also been reported. The as-prepared $SnO_2$@3DG delivered a discharge capacity of 210 mA h $g^{-1}$ at a high rate of 800 mA $g^{-1}$.[252]

The insertion type anode materials for SIBs typically offers efficient pathways for sodium-ion insertion/extraction while have relatively low capacities. While the conversion type as well as alloy type anode materials can afford high specific capacities for sodium-ion storage but normally suffer from poor cycling performance due to the volume change during cycling. In this doctoral thesis, the focus was low cost Sn-based anode materials which experience alloying and/or conversion reactions and layered $MoS_2$ materials which show promising performances for sodium-ion storage in terms of capacity and rate capability. The emerging MXenes were also the attracting candidate due to the high ionic and electronic conductivity, which is desired for high-rate applications of SIBs.

## Chapter 2 Experimental

### 2.1 Overview

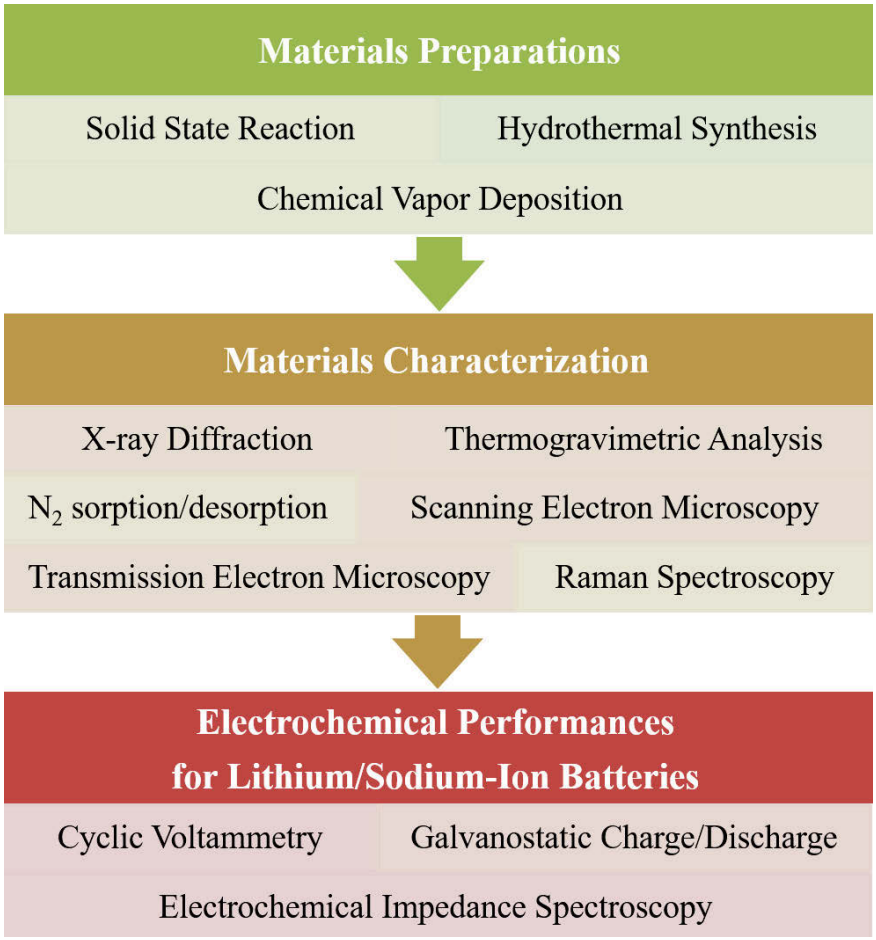


**Figure 2.1** Framework of the experiments.

**Figure 2.1** summarizes the methodologies and techniques used in this research work, which include:

1) Design and preparation of electrode materials by methods, such as solid state reactions, hydrothermal methods, and chemical vapor deposition (CVD), all chemicals used are listed in **Table 2.1**;

2) Characterizations of physical properties of the as-produced materials by different techniques, such as X-ray diffraction (XRD), thermogravimetric analysis (TGA), Raman spectroscopy, scanning electron microscopy (SEM), transmission electron microscopy (TEM), and high-resolution TEM (HRTEM);

3) Electrochemical measurements of the as-produced materials for lithium/sodium-ion batteries. To elucidate the mechanisms of electrode materials for sodium/lithium-ion storage, *ex situ* XRD, *in situ* Raman spectroscopy, and *ex situ* SEM were also applied to investigate some electrodes after/during electrochemical tests.

**Table 2.1** Chemicals used in the research project

| Chemicals | Formula | Purity | Supplier |
|---|---|---|---|
| Carbon black | C | 100 % | Sigma-Aldrich |
| Poly(vinylidene difluoride) (PVdF) | $(CH_2CF_2)_n$ | - | Sigma-Aldrich |
| Carboxymethyl cellulose sodium salt | $C_8H_{15}NaO_8$ | | Sigma-Aldrich |
| Ethanol | $CH_3CH_2OH$ | 95 % | Chem Supply |
| Ethylene carbonate | $(CH_2)_2CO_3$ | 99 % | Sigma-Aldrich |
| Graphite (natural flakes) | C | 75 % | Sigma-Aldrich |
| Hydrochloric Acid | HCl | 37 % | Sigma-Aldrich |
| Hydrogen peroxide solution | $H_2O_2$ | 50 % | Sigma-Aldrich |
| Manganese nitrate tetrahydrate | $Mn(NO_3)_2{\cdot}4H_2O$ | 97 % | Sigma-Aldrich |
| N-methyl pyrrolidinone (NMP, anhydrous) | $C_5H_9NO$ | 99.5 % | Sigma-Aldrich |
| Nitric acid | $HNO_3$ | 68 % | Sigma-Aldrich |
| Potassium permanganate | $KMnO_4$ | 99 % | Sigma-Aldrich |

| | | | |
|---|---|---|---|
| Lithium foil | Li | 99.999 % | Hohsen Corporation Japan |
| Propylene carbonate (PC, anhydrous) | $C_4H_6O_3$ | 99.7 % | Sigma-Aldrich |
| Polypropylene separator | $(C_3H_6)_n$ | 100 % | Celgard |
| Sodium nitrate | $NaNO_3$ | 99 % | Sigma-Aldrich |
| Urea | $H_2NCONH_2$ | 98 % | Sigma-Aldrich |
| Tin (IV) chloride | $SnCl_4 \cdot 5H_2O$ | 98 % | Sigma-Aldrich |

## 2.2 Materials preparation

### 2.2.1 Solid-state reaction

Solid-state reaction is the direct reaction of a mixture of solid starting materials, which is widely used for the preparation of a whole range of solid products. From the thermodynamic and kinetic considerations, it requires heat treatment at 500 to 1500 °C to allow the reactions to occur at an appreciable rate. The nucleation of products is difficult because of (a) the considerable differences in structure between reactants and products and (b) the large amount of structural reorganization that is involved in forming the products. The subsequent growth of the product layer may be even difficult because counter diffusion of precursors must occur right through the existing product layer to the new reaction interfaces. In this context, a key step is to mix the precise amounts reactants sufficiently to maximize area of contact between reacting solids. A typical procedure is outlined as follows:

*Reagents.* The reactants must be dried thoroughly and weighed according to the expected nature of the product. Fine grained materials should be used if possible in order to maximize surface area and hence reaction rates.

*Mixing.* After acquisition of precise quantities of the solid starting materials, the reactants are mixed. For manual mixing of small quantities, usually an agate mortar and pestle are employed. Sufficient amount of some volatile organic liquid, such as acetone or ethanol, is added to the mixture to aid homogenization.

*Heat treatment.* After mixing, the reactants are put in suitable containers chemically inert to the reactants under the heating conditions used and then heated. The heating program to be used depends strongly on the form and reactivity of the reactants. According to the demands of the final products, an appropriate protection gas (argon, helium, nitrogen, hydrogen, etc.) will be selected to avoid oxidization.

In this thesis, the solid-state reaction route was employed to prepare $LiMn_2O_4$ cathode materials for LIBs.

### 2.2.2 Hydrothermal method

The hydrothermal technique is becoming one of the most important tools for advanced materials processing, particularly owing to its advantages in the processing of nanostructured materials. The hydrothermal technique not only helps in processing monodisperse and highly homogeneous nanoparticles, but also acts as one of the most attractive techniques for processing nano-hybrid and nanocomposite materials. The term 'hydrothermal' is purely of geological origin. It was first used by the British geologist, Sir Roderick Murchison (1792-1871) to describe the action of water at elevated temperature and pressure, in bringing about changes in the earth's crust leading to the formation of various rocks and minerals. This technique is particularly suitable for the growth of large good-quality crystals while maintaining good control over their composition. The autoclaves used in this study are made

of stainless steel and the inside contains a polytetrafluoroethylene (PTFE) lining with 30 ml capacity, which is shown in **Figure 2.2**. In this doctoral study, the hydrothermal methods were employed to synthesize $SnO_2$/graphene aerogels, $MoS_2$@carbon paper, $SnS_2$/graphene composites, $MoS_2$/graphene heterostructures, and $SnO_2$/nitrogen-doped graphene composites.

## 2.3 Materials characterization

### 2.3.1 X-ray Diffraction (XRD)

The phase and crystallographic structure of as-prepared materials were characterized by X-ray diffraction in this doctoral study. The interaction of the incident X-rays with the sample produces constructive interference (and diffracted rays) when conditions satisfy Bragg's Law:

$$n\lambda=2d\sin\theta$$

where $d$ is the interplanar spacing, $\theta$ is the Bragg angle, $n$ is the order of reflection and $\lambda$ is the wavelength of the X-rays irradiation. By comparing the obtained XRD pattern to the known standard diffraction lines in the Joint Committee on Powder Diffraction Standards (JCPDS) database, the crystal phase can be identified.

### 2.3.2 Raman Spectroscopy

Raman spectroscopy is a molecular spectroscopy based on inelastic scattering of monochromatic light. It is a powerful tool for quantitative applications. In this thesis, it was used to detect defect information of carbon materials and identify the structure of compounds.

The specific vibrational information obtained in Raman spectroscopy arises from molecular bonds and symmetry. As a result, *in situ* Raman spectroscopy provides a powerful tool to

probe electrode and electrolyte during cycling in sodium/lithium-ion cells. The *in situ* Raman cell design is shown in **Figure 2.2**. A 2 mm hole was drilled through the back of a 2032 coin cell and a glass window was attached over the hole by epoxy adhesive. In this doctoral study, we used *in situ* Raman to investigate the sodiation/de-sodiation processes of $MoS_2$@carbon paper electrodes for sodium-ion batteries (**Chapter 6**).

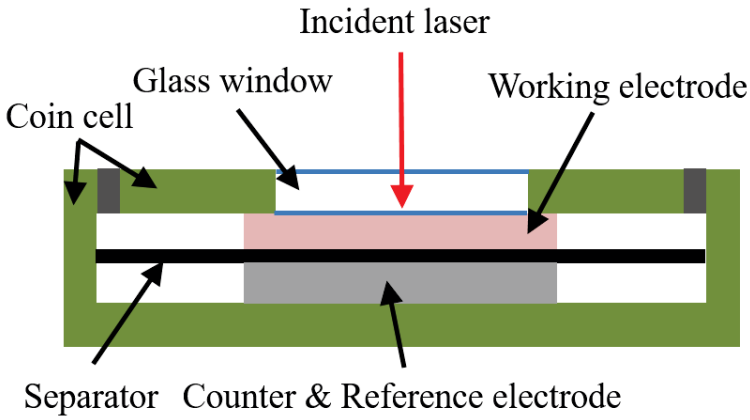


**Figure 2.2** Modified coin cell design for *in situ* Raman spectroscopy.

### 2.3.3 X-ray photoelectron spectroscopy (XPS)

X-ray photoelectron spectroscopy (XPS) is a surface-sensitive quantitative spectroscopic technique that measures the elemental composition at the surface (top 0 to 10 nm of the material being analyzed). XPS spectra are obtained by irradiating a material with a beam of X-rays while simultaneously measuring the kinetic energy and number of electrons. By analyzing the binding energies, the chemical state information, i.e., the local bonding environment of a species can be produced. XPS is also useful for quantitative analysis of surfaces, which gives relative quantification of different elements. In this doctoral study, XPS

was used to investigate the chemical states as well as the atomic percent of nitrogen species in nitrogen-doped graphene.

### 2.3.4 $N_2$ sorption/desorption measurement

To measure surface area, pore size and pore volume of the desired materials, $N_2$ sorption/desorption measurements were conducted by using a Micromeritics 3Flex analyzer at 77 K. The Brunauer-Emmett-Teller (BET) method was used to calculate surface areas of the as-produced samples in this work using the experimental points at a relative pressure of $P/P_0$ = 0.05-0.25. The pore size distribution was calculated by the Barret-Joyner-Halenda (BJH) method.

### 2.3.5 Thermogravimetric Analysis (TGA)

Thermogravimetric analysis (TGA) is a popular method of thermal analysis in which changes in physical and chemical properties of materials are monitored as a function of increasing temperature. For different applications, TGA can be conducted in air or inert atmosphere (*e.g.* $N_2$). For example, the carbonization temperature of biomass can be determined by TGA in $N_2$ atmosphere. To measure the weight ratio of carbon materials in carbon-based composites, normal air atmosphere is commonly used. The temperature can increase up to 1000 °C with a speed of 5-10 °C $min^{-1}$.

### 2.3.6 Scanning Electron Microscopy (SEM)

Field emission scanning electron microscopes (FESEM) provide a powerful tool to investigate the morphology of nanomaterials. In this study, high resolution FESEM (Zeiss Supra 55VP) was used, which was operated with an acceleration voltage of 20 kV. Sample

preparation for SEM includes either spreading sample powder directly onto a carbon tape or dropping a sample in isopropanol solution onto silicon substrates followed by drying in air. The Supra 55VP is also equipped with Oxford energy dispersive spectroscopy (EDS), which enables component and element percentages analysis.

### 2.3.7 Transmission Electron Microscopy (TEM)

To examine fine details of the as-produced electrode materials, TEM, which is capable of imaging at a significantly higher resolution, was used. By using high resolution TEM (HRTEM), lattice images are possible. Moreover, the phase features for crystalline samples can be captured by selected area electron diffraction (SAED). For a single crystal, the SAED pattern is characterized of a pattern of dots, while for a polycrystalline or amorphous solid material, it shows a series of rings.

## 2.4 Electrode preparation and battery assembly

### 2.4.1 Electrode preparation

For powder electrode materials, the electrodes were prepared by mixing the as-prepared material (70 wt. %), carbon black (20 wt. %) and poly (vinylidene fluoride) binder (PVDF, 10 wt. %) in N-methyl-2-pyrrolidone (NMP) to form a slurry. The resultant slurry was spread onto either Al foil (for cathode materials) or Cu foil (for anode materials) using a doctor blade and dried in a vacuum oven for 12 h, followed by pressing at 200 kg $cm^{-2}$. To ensure the reliability of the electrochemical results, the active material loading was about 1.1 mg $cm^{-2}$.

For the freestanding electrode materials, such as Sn@CNT-carbon paper and $MoS_2$@carbon paper, the as-prepared products were used directly without the aforementioned electrode preparation procedure.

### 2.4.2 Cell assembly

Electrochemical measurements were carried out using two-electrode coin cells. For LIBs, lithium foil was used as counter and reference electrode, and a Celgard 2400 as the separator. While for SIBs, sodium foil was used as counter and reference electrode, and glass fiber as the separator. The CR2032-type coin cells were assembled in an argon-filled glove box (UniLab, Mbraun, Germany), in which both the moisture and oxygen contents are controlled to be less than 0.1 ppm. The electrolyte used for LIBs was 1 M $LiPF_6$ in a 1:1 (volume ratio) mixture of ethylene carbonate and diethyl carbonate purchased from Zhangjiagang Guotai-Huarong New Chemical Materials Co., Ltd.. Home-made electrolyte (1 M $NaClO_4$ dissolved in a mixture of ethylene carbonate (EC) and propylene carbonate (PC) with a volume ratio of 1:1, in which 5 vol.% fluoroethylene carbonate (FEC) was added as electrolyte additive) was used for SIBs.

## 2.5 Electrochemical measurements

In this doctoral study, the electrochemical properties were tested by the following techniques, including galvanostatic charge-discharge, cyclic voltammetry, and electrochemical impedance spectroscopy. The details of these electrochemical measurements are discussed as follows.

### 2.5.1 Galvanostatic charge-discharge

Galvanostatic charge-discharge is conducted at a constant charge/discharge current within a certain voltage range. The specific charge/discharge capacities (Q) of electrode materials can be calculated by the following formula:

$$Q = I * t \qquad (2\text{-}1)$$

where I is the current density and t is the charge/discharge time. Rate performances of the as-produced electrode materials can be obtained by stepwise galvanostatic charge-discharge measurements at different current densities. Moreover, by repeating galvanostatic charge-discharge tests, the cycling performances can be obtained, which is another important parameter of electrode materials.

### 2.5.2 Cyclic voltammetry

Cyclic voltammetry (CV) is a type of potentiodynamic electrochemical measurement conducted at a constant ramping of voltage (scan rate, $V\ s^{-1}$). It applies a potential between a reference electrode and a working electrode and monitors the current between a working electrode and a counter electrode. When there are reduction or oxidation reactions on the working electrode at a certain potential, current peaks will appear. As a result, CV provides information about the redox potential and the electrochemical reaction rates of the electrode materials. In this doctoral study, the instrument used for CV is an electrochemical workstation produced by CH instruments.

### 2.5.3 Electrochemical Impedance Spectroscopy

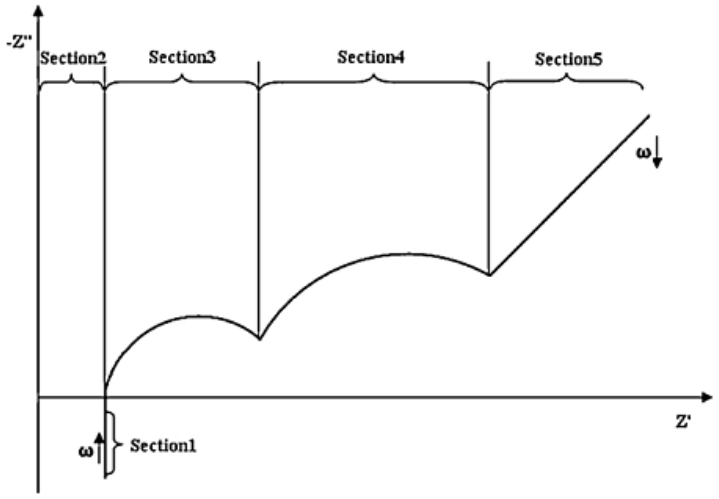


**Figure 2.3** Schematic impedance spectrum in a Nyquist plot for lithium/sodium-ion cells.

Electrochemical impedance spectroscopy (EIS) is a widely used experimental method to gain a deeper insight into electro-chemical systems.[253] Impedance spectra of lithium/sodium-ion cells show a characteristic behavior in a Nyquist plot. The sub-component sections and the associated assumed kinetic response processes are explained in more detail:

*Section 1*. At very high frequencies, the spectrum shows inductive behaviour caused by inductive reactance of metallic elements in the cell and wires;

*Section 2*. Ohmic resistance $R_{\Omega}$ of the cell at the intersection with the real axis, sum of the resistances of current collectors, active material, electrolyte, and separator;

*Section 3*. First semi-circle associated typically with the solid electrolyte interface (SEI) and is formed during cycling on the surface of the anode;

*Section 4*. Second semi-circle representing the double layer capacity and charge transfer resistance at the electrodes;

*Section 5*. Diffusion processes in the active material of the electrodes at very low frequencies.

In this doctoral study, Nyquist plots of different electrodes were prepared to investigate the kinetics of different electrode materials, which can be correlated with the electrochemical performances, such as specific capacity and rate capability.

## Chapter 3 Synthesis of Single Crystalline Spinel $LiMn_2O_4$ Nanorods for Li-ion Batteries with High Rate Capability and Long Cycle Life

### 3.1 Introduction

Rechargeable lithium-ion batteries (LIBs) have been successfully commercialized with a wide range of applications in our modern society.[133, 254-258] As a promising alternative to $LiCoO_2$ cathode materials in LIBs, spinel lithium manganese oxide ($LiMn_2O_4$) with an open three-dimensional framework structure allows for the facile insertion and extraction of lithium ions. It has attracted great technological and research interest because of the abundance of Mn (12th most abundant element in earth's crust), environmental friendliness and high safety.[56, 133, 134, 259, 260] However, the unstable rechargeability is a key problem, which prohibits its application.[58, 261, 262]

Considerable efforts have been devoted to mitigating the inferior cyclability of $LiMn_2O_4$, including doping and coating.[263] It has been widely acknowledged that high crystallinity can improve the stability of the crystallographic structure and charge-discharge cycling ability of $LiMn_2O_4$ by hindering Mn dissolution from the spinel structure into the electrolyte.[264, 265] Unfortunately, large single crystalline $LiMn_2O_4$ has been reported as having a $Li^+$ diffusion coefficient of $10^{-11}$ S $cm^{-2}$, an order of magnitude lower than that of polycrystalline $LiMn_2O_4$, which results in sluggish ionic kinetics.[266-268] This problem can be solved by preparing $LiMn_2O_4$ nanoarchitectures to decrease lithium ion diffusion length.[269] Among all the nanostructures, one-dimensional (1D) nanoarchitecture is particularly attractive owing to high length to diameter ratio and anisotropies. It has been reported that $Li^+$ and $e^-$ may be inserted into 1D nanoarchitectures synchronously, rendering them ionically and

electronically conductive simultaneously.[53, 270] Moreover, 1D nanomaterials have a large surface-to-volume ratio, which provide efficient active mass-electrolyte contact areas, giving rise to a high rate capability.[88] The small diameter enables better accommodation of the large volume changes without the initiation of fracture that commonly occur in bulk or micron-sized materials. These advantages endow promising performances to 1D electrode materials for LIBs.[271] However, the cubic crystals cannot grow in a one-dimensional direction, especially in the high-temperature sintering process, which is normally necessary for high-performance cathode materials.[86] Zhou et al. prepared high-quality single crystalline cubic spinel $LiMn_2O_4$ nanowires based on a novel reaction method using $Na_{0.44}MnO_2$ nanowires as a self-template.[86] Cui et al. reported the synthesis of ultrathin single crystalline $LiMn_2O_4$ nanowires with cubic spinel structure, which were synthesized by using a solvothermal reaction to produce α-$MnO_2$ nanowires followed by solid-state lithiation.[87] Cui et al. reported the hydrothermal synthesis of single-crystalline β-$MnO_2$ nanorods and their chemical conversion into free-standing single-crystalline $LiMn_2O_4$ nanorods using a simple solid-state reaction.[88] More than 85% of the initial charge storage capacity was maintained for over 100 cycles. Zhao and co-workers prepared single-crystalline nanotubes of spinel $LiMn_2O_4$ via a template-engaged reaction using β-$MnO_2$ nanotubes as a self-sacrificing template. About 70% of the initial capacity can be retained after 1500 cycles at a 5C rate.[265] As summarized in **Table 3.1**, it is still a big challenge to achieve above 85% retention of the initial charge storage capacity over 1000 cycles.

**Table 3.1** Summary of $LiMn_2O_4$ nanorods as cathode materials for lithium-ion batteries

| Mn-precursor | Cycling performance | Rate capability | Reference |
|---|---|---|---|
| β-$MnO_2$ nanorods | 85% capacity retention after 100 cycles at 1C | 100 mA h $g^{-1}$ at 1C | 88 |
| Manganese acetate | 60% capacity retention after 10 cycles at 1C | - | 272 |
| α-$MnO_2$ nanorods | 90% capacity retention after 100 cycles at 1C | 85% of the reversible capacity at 0.1C rate can be discharged at 5C rate | 264 |
| porous $Mn_2O_3$ nanorods | 90% capacity retention after 500 cycles at 2 C | 80 mA h $g^{-1}$ at 30 C | 53 |
| MnOOH nanorods | 89% capacity retention after 50 cycles at 1C | 100 mA h $g^{-1}$ at 5 C | 273 |
| $MnO_2$ nanorods | 98.9% capacity retention after 30 cycles at 1.0 mA $cm^{-2}$ | - | 274 |
| β-$MnO_2$ nanorods | 73% capacity retention after 500 cycles at 3C | 78 mA h $g^{-1}$ at 5 C | 275 |

Herein, we report the synthesis of single crystalline $LiMn_2O_4$ nanorods as the cathode materials for ultrahigh stable LIBs. Porous $Mn_3O_4$ nanorods were used to synthesize single crystalline $LiMn_2O_4$ nanorods. We developed a vacuum-assisted impregnation (VAI) method in order to mix $Mn_3O_4$ with LiOH homogeneously on a molecular level, which can facilitate the transfer of dissolved LiOH into the nanopores. Followed by solid-state reaction, single

crystalline $LiMn_2O_4$ with well-defined rod-like morphology were obtained. When applied as cathode materials for LIBs, the as-prepared $LiMn_2O_4$ nanorods showed an initial reversible capacity of 114 mA h $g^{-1}$ at 0.5C, excellent cyclability (95.6% capacity retention at a rate of 3C after 1000 cycles) and good high rate capability. Post-mortem nanostructural analyses confirmed the preservation of the 1D morphology after long-term cycling. 1D spinel $LiMn_2O_4$ nanorods could be a promising cathode material for LIBs with long cycle life.

## 3.2 Experimental

### 3.2.1 Synthesis of $MnO_2$ nanorods

1 mmol $MnSO_4 \cdot H_2O$ was dissolved into 20 mL distilled water to form a transparent solution, to which 1 mmol $(NH_4)_2S_2O_8$ was added consequentially. After mechanical stirring at room temperature for 1 h, the mixture was loaded into an autoclave with a capacity of 25 mL and then subjected to hydrothermal treatment at 140 $^oC$ for 12 h. Products were collected after the autoclave cooled to room temperature. For purification, the obtained products were washed with copious distilled water and then dried at 60 $^oC$ overnight.[276]

### 3.2.2 Synthesis of porous $Mn_3O_4$ nanorods

In a typical synthesis process, $MnO_2$ nanorods were heated to 280 $^oC$ under a flowing gas mixture of $H_2$ in Ar ($H_2$: 5%, Ar: 95%) at a flow rate of 100 sccm in a horizontal tube furnace. The ramp was set as 3 $^oC$ $min^{-1}$. After holding at 280 $^oC$ for 3 h, the furnace cooled to room temperature naturally. The specimen was changed from black $MnO_2$ to yellow $Mn_3O_4$ after $H_2$ treatment.

### 3.2.3 Synthesis of $LiMn_2O_4$ nanorods

$LiMn_2O_4$ nanorods were prepared by a facile impregnation-calcination method. LiOH was mixed with $Mn_3O_4$ by a vacuum-assisted impregnation process. Specifically, $LiOH{\cdot}H_2O$ was dissolved in ethanol, and then the as-synthesized $Mn_3O_4$ nanorods were mixed with the above LiOH solution. The solvent was slowly removed by evaporation in a vacuum oven at room temperature. The dried $LiOH/Mn_3O_4$ mixture was then subjected to high temperature calcination in a muffle furnace. After cooling to room temperature naturally, $LiMn_2O_4$ nanorods were obtained.

### 3.2.4 Characterization

The crystal structure and phases of as-prepared materials were characterized by X-ray diffraction (XRD, Siemens D5000) using Cu Kα radiation with a scanning step of 0.02° $sec^{-1}$. Morphologies were analyzed by field emission scanning electron microscopy (FESEM, Zeiss Supra 55VP). The details of morphology were further characterized by transmission electron microscopy (TEM) and high-resolution TEM (HRTEM, JEOL JEM-2011). The $N_2$ adsorption/desorption isotherms of materials were measured by a Micromeritics 3Flex Surface Characterisation Analyser at 77 K. The Brunauer–Emmett–Teller (BET) method was used to calculate to specific surface area. The pore size distribution was calculated by the Barrett–Joyner–Halenda (BJH) method. The total pore volume was calculated from the amount adsorbed at a maximum relative pressure.

### 3.2.5 Cell assembly and electrochemical testing

The electrodes were prepared by dispersing the as-prepared material (70 wt. %), carbon black (20 wt. %) and poly (vinylidene fluoride) binder (PVDF, 10 wt. %) in N-methyl-2-pyrrolidone (NMP) to form a slurry. The resultant slurry was spread onto Al foil using a

doctor blade and dried in a vacuum oven for 12 h, followed by pressing at 200 kg $cm^{-2}$. The active material loading was about 1.1 mg $cm^{-2}$. Electrochemical measurements were carried out using two-electrode coin cells with lithium foil as counter and reference electrode, and celgard 2400 as the separator. The CR2032-type coin cells were assembled in an argon-filled glove box (UniLab, Mbraun, Germany). The electrolyte (Zhangjiagang Guotai-Huarong New Chemical Materials Co., Ltd.) was 1 M $LiPF_6$ in a 1:1 (volume ratio) mixture of ethylene carbonate and diethyl carbonate. The charge-discharge measurements were performed at different current densities in the voltage range from 3.0 to 4.3 V *vs.* $Li^+/Li$ using a computer-controlled Neware Battery Testing system.

### 3.3 Results and Discussion

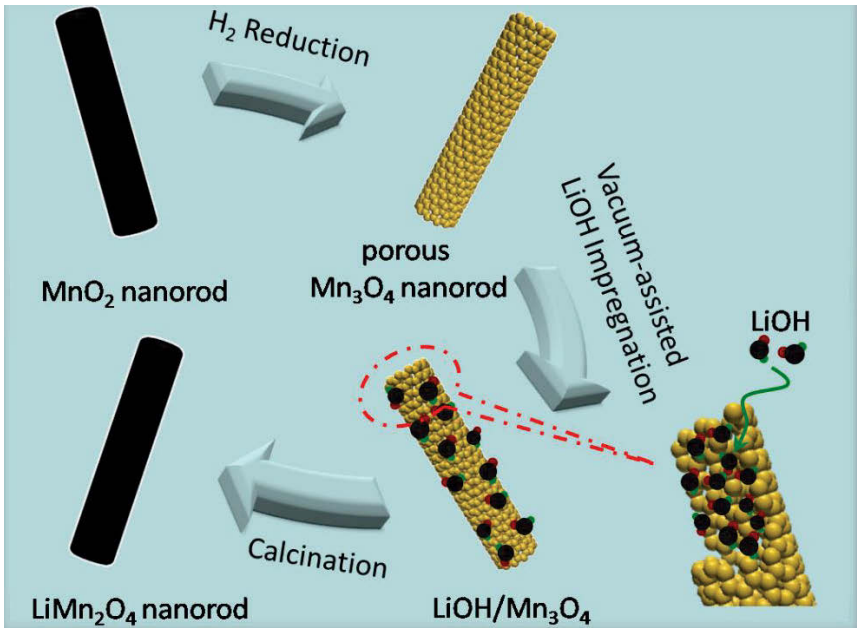


**Figure 3.1** A schematic illustration of the procedure for preparing the porous $Mn_3O_4$ nanorods and spinel $LiMn_2O_4$ nanorods.

It has been reported that $LiMn_2O_4$ nanorods can be prepared by lithiation of concrete β-$MnO_2$ nanorods.[88] However, the lithiation processes from $MnO_2$ surface to bulk may lead to the uneven distribution of $Li^+$ in the final $LiMn_2O_4$ products, resulting in the formation of some $Li^+$-poor spinel $LiMn_2O_4$. A lower Li/Mn ratio is accompanied by a higher degree of oxygen deficiency, which is responsible for a faster fading of the capacity during cycling.[277] To achieve the homogeneous reaction between Mn-precursor and Li-precursor, we elaborately designed the synthesis of $LiMn_2O_4$ nanorods by using porous $Mn_3O_4$ nanorods and LiOH as Mn- and Li-precursor, respectively. **Figure 3.1** schematically illustrates the synthesis process. In the first step, porous $Mn_3O_4$ nanorods were prepared by $H_2$ reduction of $MnO_2$, which is reported for the first time. The porous $Mn_3O_4$ nanorods are very promising precursors for preparing $LiMn_2O_4$ nanorods due to the porous structure which can provide voids to accommodate other molecules, for example, LiOH. As a result, the reaction of $Mn_3O_4$ with LiOH on molecular level can be realized. In the second step, LiOH was impregnated at room temperature into the nanopores of the $Mn_3O_4$ precursor by a vacuum-assisted impregnation method. Under vacuum condition, the residue of gases in the nanopores was forced outwards to balance pressure difference. Subsequently, the capillary force efficiently promoted the infiltration of the lithium precursor solution (LiOH dissolved in ethanol) into the pores of $Mn_3O_4$. After the evaporation of ethanol, homogeneous LiOH/$Mn_3O_4$ mixture was obtained. In the final step, the LiOH/$Mn_3O_4$ mixture was calcined in air at high temperature. Since the melting point of LiOH is 462 ºC, the liquefied LiOH will diffuse into the nanopores of $Mn_3O_4$ at elevated temperature, which further enhanced the homogeneous mixing of LiOH with $Mn_3O_4$. After calcination in air, the furnace cooled to room temperature naturally, and $LiMn_2O_4$ nanorods were obtained.

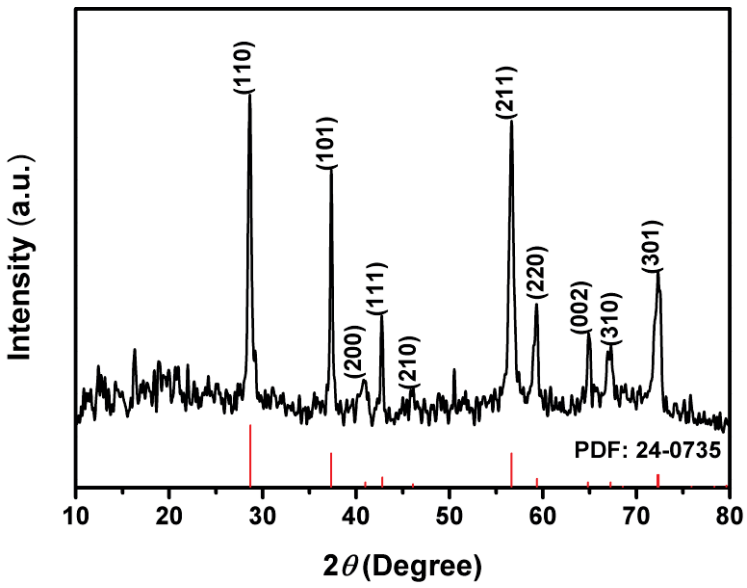


**Figure 3.2** XRD pattern of $MnO_2$.

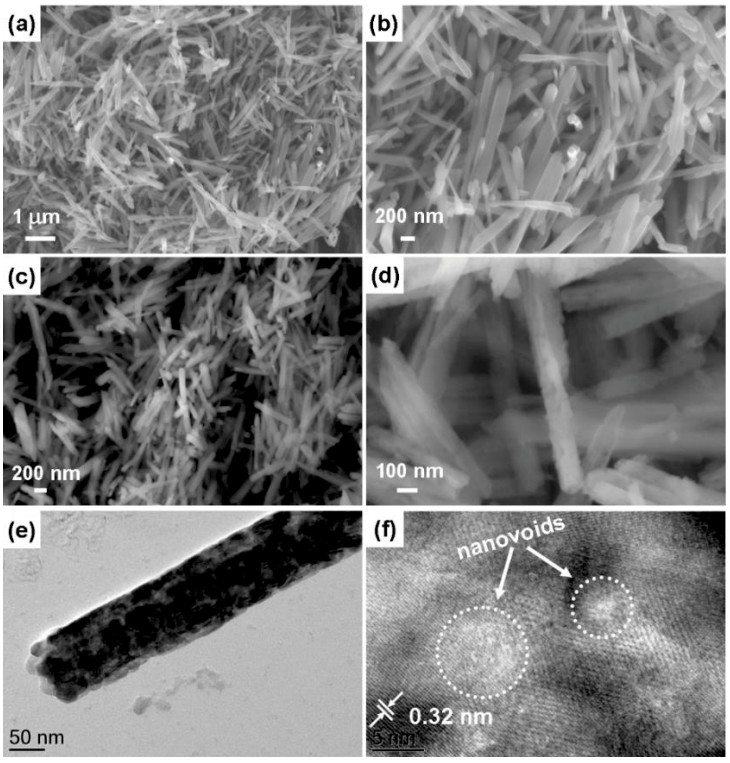


**Figure 3.3** Low-magnification and high-magnification SEM images of $MnO_2$ (a and b), $Mn_3O_4$ (c and d), illustrating the nanostructure of the as-synthesized products. TEM images of $Mn_3O_4$ (e and f).

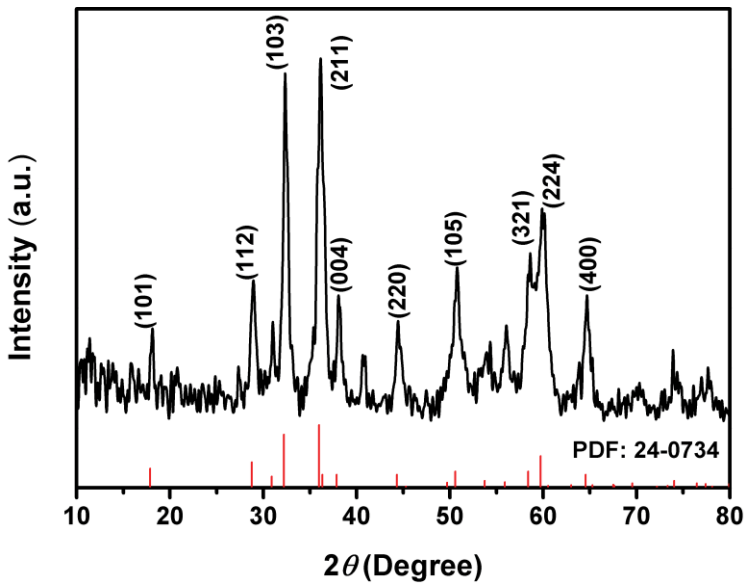


**Figure 3.4** XRD pattern of $Mn_3O_4$.

X-ray diffraction, scanning electron microscopy (SEM), transmission electron microscopy (TEM) and $N_2$ adsorption-desorption were employed to investigate the physical properties of the products in each step. As evidenced by **Figure 3.2**, $MnO_2$ were successfully prepared by the hydrothermal method. It can be seen in **Figure 3.3a** and **b** that the $MnO_2$ nanorods with a smooth surface have grown to a few micrometers in length and about 100 nm in diameter. Porous $Mn_3O_4$ was successfully obtained by $H_2$ reduction, as evidenced by the XRD pattern shown in **Figure 3.4**. **Figure 3.3c** and **d** present the SEM image of as-prepared porous $Mn_3O_4$ nanorods. After the reduction of $MnO_2$ to $Mn_3O_4$ in $H_2$ atmosphere, the 1D nanorod morphology was maintained, without any collapse of 1D nanostructure. Meanwhile, the smooth surface became rough and pores formed on the nanorods due to the partial elimination of oxygen (from 66.7 at.% to 57.1 at.%) and recrystallization. The TEM images shown in **Figure 3.3e** and **f** further demonstrate the porous nature of the $Mn_3O_4$ nanorods, in which nanopores can be clearly observed. The HRTEM image of a single nanorod (**Figure 3.3f**)

indicates that the nanorod is well crystallined, and the lattice spacing of 0.32 nm is indexed to the (112) crystal plane of $Mn_3O_4$.

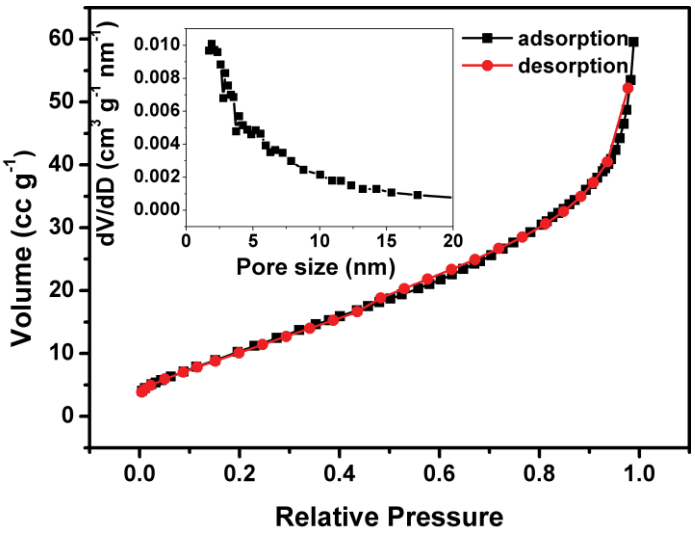


**Figure 3.5** $N_2$ adsorption-desorption analysis results for the as-synthesized porous $Mn_3O_4$ nanorods, the inset gives the pore size distribution of the $Mn_3O_4$ sample.

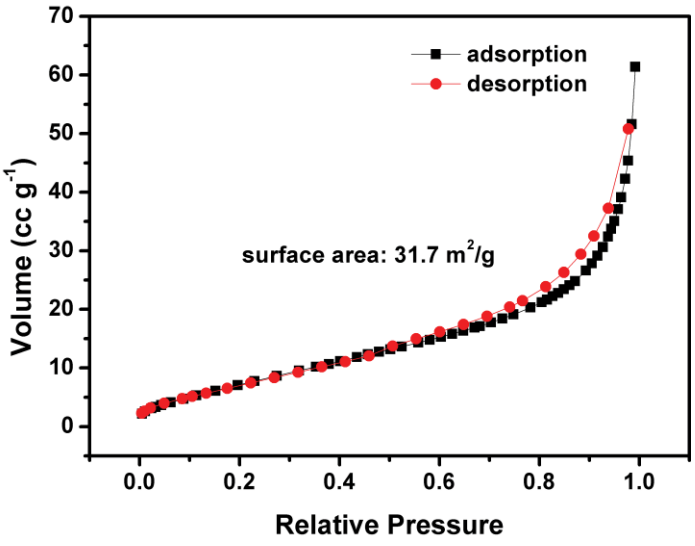


**Figure 3.6** $N_2$ adsorption-desorption analysis results of $LiOH/Mn_3O_4$ mixture prepared by vacuum-assisted impregnation method.

We used nitrogen adsorption-desorption measurement to determine the specific surface area and porous nature of the synthesized $Mn_3O_4$ nanorods, as presented in **Figure 3.5**. The isotherm profile of $Mn_3O_4$ can be categorized as type IV with a capillary condensation step and hysteresis loops, which are characteristic of typical porous materials. The Brunauer-Emmett-Teller (BET) specific surface area of $Mn_3O_4$ was measured to be 45 $m^2 g^{-1}$. The high surface area of $Mn_3O_4$ can be ascribed to the formation of the porous structure, as evidenced by the corresponding Barrett-Joyner-Halenda (BJH) pore size distributions calculated from the adsorption branch of the isotherms in the inset in **Figure 3.5**. The pore size distributions reveal that the $Mn_3O_4$ sample has pore sizes in the range of 2–10 nm with an average pore size of 7.2 nm. The total pore volume is 0.09 $cm^3 g^{-1}$. After the impregnation of a stoichiometric amount of LiOH (Li:Mn = 1:2), the specific surface area was reduced to 32 $m^2 g^{-1}$ (see **Figure 3.6**), which suggests that LiOH was successfully impregnated. The $Mn_3O_4$/LiOH mixture was then transformed into spinel $LiMn_2O_4$ by a solid-state reaction method at different temperatures, 650 ºC, 700 ºC, and 750 ºC, which are denoted as LMO-650, LMO-700, and LMO-750, respectively.

The XRD patterns shown in **Figure 3.7** confirm that the products prepared by the solid-state reaction method crystallized with the cubic $LiMn_2O_4$ phase with Fd3m space group (JCPDS 35–0782) after the heat treatment at 650–750 ºC. No diffraction peak from impurity phases was detected. The intensity and width of the XRD peaks became stronger and sharper, with increasing calcination temperature, corresponding to better crystallinity and a larger crystallite size.

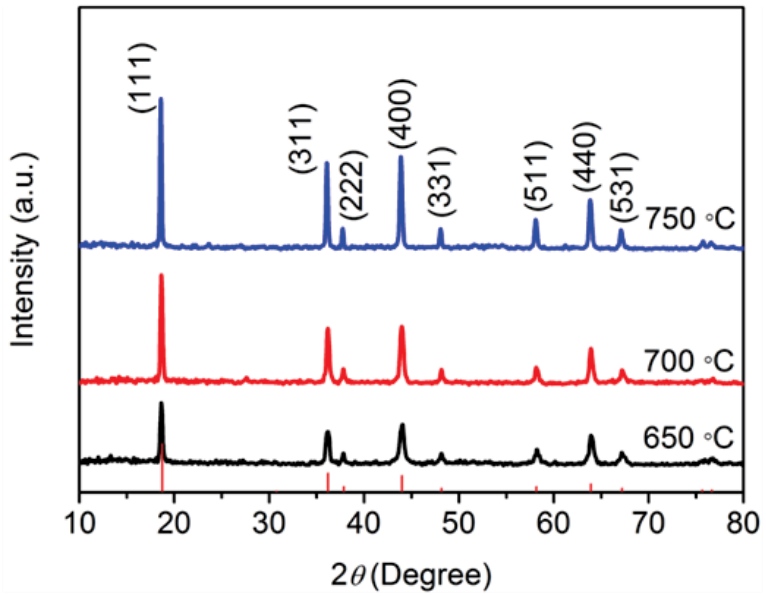


**Figure 3.7** XRD patterns of the product obtained at different calcination temperatures, all patterns agree well with the standard pattern of spinel $LiMn_2O_4$ (JCPDS 35-0782).

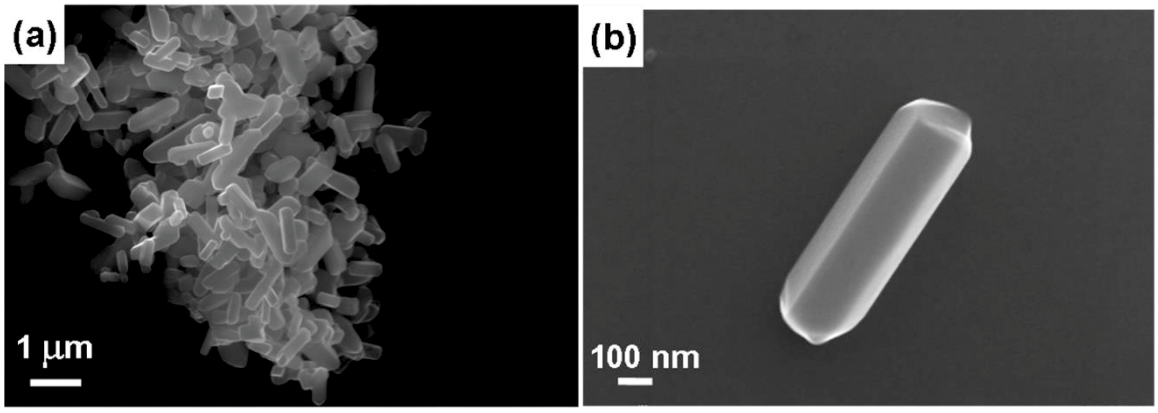


**Figure 3.8** (a) Medium- and (b) high-magnification FESEM images of $LiMn_2O_4$ nanorods.

The morphologies of the as-prepared $LiMn_2O_4$ materials were investigated by field-emission scanning electron microscopy (FESEM). As observed from the SEM images in **Figure 3.8a**, although $LiMn_2O_4$ was subjected to calcination at high temperature, the rod-like morphology was retained on conversion from $Mn_3O_4$ to $LiMn_2O_4$. The diameters of these $LiMn_2O_4$ nanorods are *ca.* 200 nm and their lengths are from 500 nm to 1 μm, which are determined

using high-magnification FESEM (**Figure 3.8b**). The lengths of $LiMn_2O_4$ nanorods are slightly shorter than those of $Mn_3O_4$ nanorods, which may be due to lattice shrinking during the oxidation of $Mn^{2+}$ to $Mn^{3+}/Mn^{4+}$.

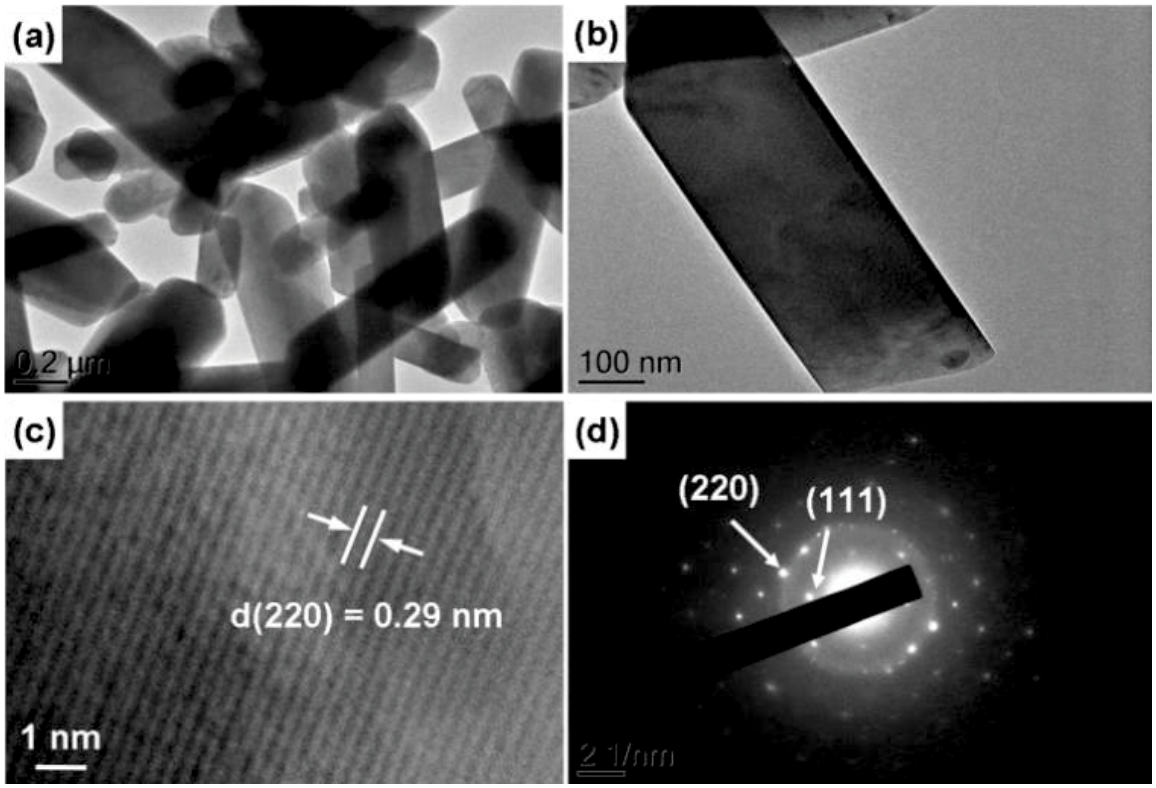


**Figure 3.9** (a) Low-magnification, (b) medium-magnification and (c) lattice-resolved high resolution TEM images of $LiMn_2O_4$ nanorods, (d) SAED pattern of a single crystalline $LiMn_2O_4$ nanorod.

This rod-like feature was also observed by TEM in **Figure 3.9a** and **b**. The measured neighbouring interplanar distances of 0.29 nm shown in **Figure 3.9c** are consistent with those of the $LiMn_2O_4$ (220) plane. The select area electron diffraction (SAED) pattern (**Figure 3.9d**) indicates that the nanorods are single crystalline.

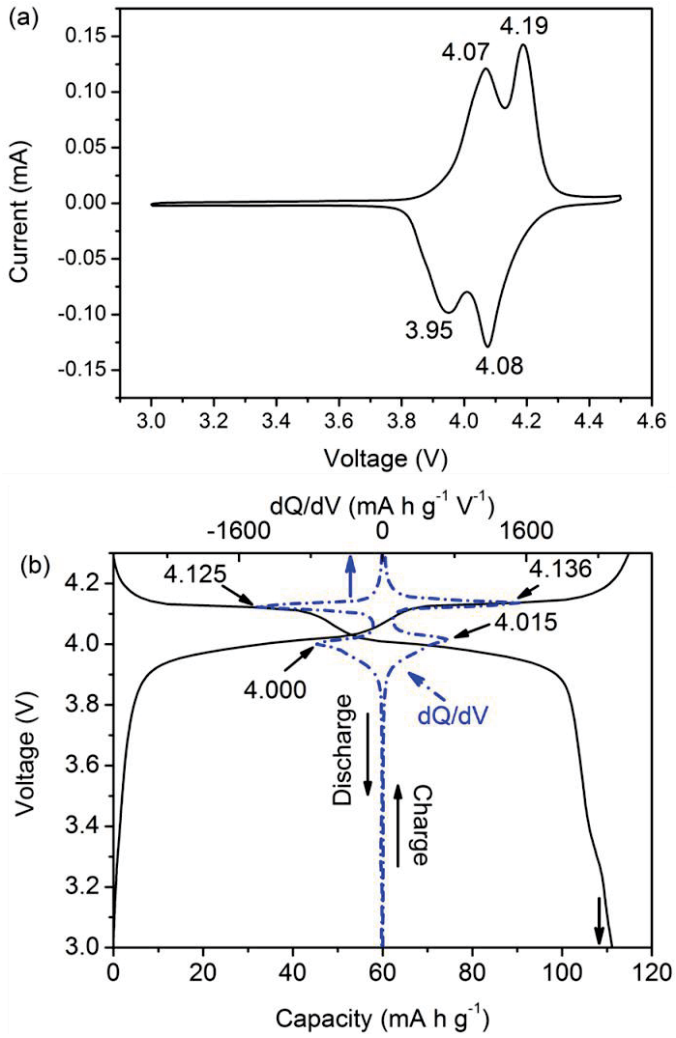


**Figure 3.10** Electrochemical characterization of $LiMn_2O_4$ nanorods. (a) Cyclic voltammetry curve between 3.0 and 4.5 V *vs.* $Li/Li^+$ at a scanning rate of 0.1 mV $s^{-1}$. (b) Galvanostatic charge/discharge curve and potentiostatic differential capacity *vs.* voltage (dQ/dV).

We applied cyclic voltammetry (CV) and galvanostatic charge/discharge cycling to examine the electrochemical properties of the $LiMn_2O_4$ nanorods treated at different temperatures. **Figure 3.10a** shows typical CV curve of a nanorod $LiMn_2O_4$ electrode sintered at 750 °C (LMO-750) at a scan rate of 0.1 mV $s^{-1}$ within a potential window of 3.0–4.5 V, which depicts the well-known electrochemical behaviors of the $LiMn_2O_4$ cathode. Two anodic peaks at 4.19 V and 4.07 V (*vs.* $Li^+/Li$) indicate the extraction of $Li^+$ from half of the tetrahedral sites

with Li-Li interaction, and then from the other half of the tetrahedral in which lithium ions do not have any nearest neighbor Li-Li interactions. It is found that the two peaks are not so clearly separated, indicating the simultaneous occurrence of the two-step process for the removal of $Li^+$.[55] Two cathodic peaks appear at 3.95 V and 4.08 V, respectively, corresponding to the two insertion processes.[278] Typical charge/discharge profiles are shown in **Figure 3.10b** within a voltage window of 3.0–4.3 V at a rate of 0.2C (1C = 148 mA $g^{-1}$). The charge–discharge curves present two obvious discharge plateaus associated with the two-stage mechanism of the electrochemical lithium intercalation and extraction at 3.9–4.1 V (low plateau) and 4.1–4.2 V (high plateau), which is in good agreement with the CV data.

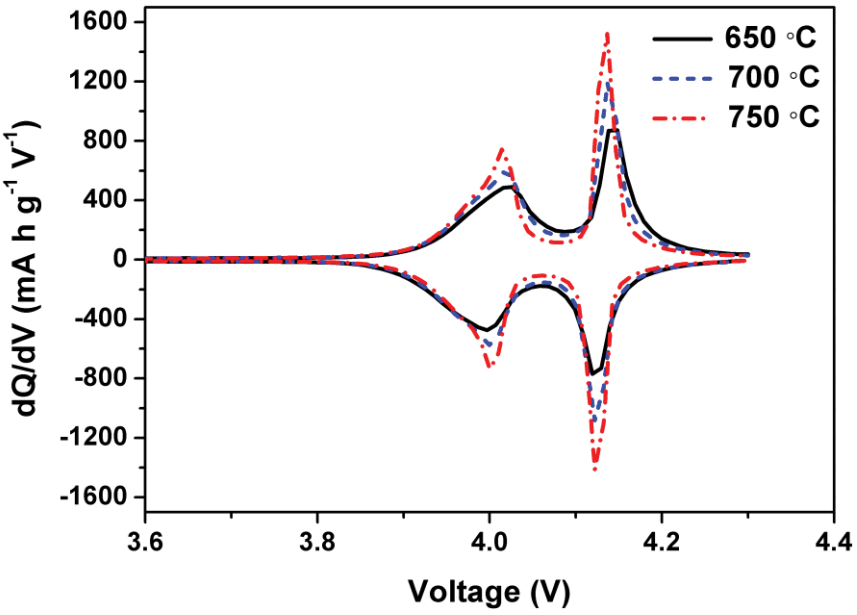


**Figure 3.11** Potentiostatic differential capacity *vs.* voltage (dQ/dV) of $LiMn_2O_4$ obtained at different calcination temperature at 0.2 C.

**Table 3.2** Electrochemical data derived from potentiostatic differential capacity curves of $LiMn_2O_4$ samples prepared at different temperatures.

| Temperature (ºC) | Cathodic peak position (V) | | Anodic peak position (V) | | Δ V (mV) |
|---|---|---|---|---|---|
| 650 | 4.021 | 4.144 | 3.997 | 4.124 | 24/20 |
| 700 | 4.018 | 4.139 | 4.000 | 4.125 | 18/14 |
| 750 | 4.015 | 4.136 | 4.000 | 4.125 | 15/11 |

The charge-discharge data have been converted into differential chronopotentiometric curves (DCC) in order to clearly distinguish the voltage plateaus difference in the charge and discharge curves (**Figure 3.11**), and the oxidation/reduction peak positions of $LiMn_2O_4$ prepared at different calcination temperatures are summarized in **Table 3.2**. The chronopotentiometric curves of all samples show two cathodic peaks located at around 4.02 and 4.14 V and two anodic peaks located at about 4.00 and 4.13 V, respectively. By comparing the DCCs of $LiMn_2O_4$ nanorods obtained at different sintering temperatures, we found that the oxidation and reduction peaks became sharper and more separated with the increase of the calcination temperature, corresponding to a flatter charge-discharge curve at each plateau. This indicates the improved homogeneity of Li-ion environment due to the improved crystallinity. The increased crystallinity can also facilitate the $Li^+$ diffusion by lowering the energy barrier for $Li^+$ insertion, which is evidenced by the fact that the cathodic peaks shift continuously to lower potentials with the increase of the calcination temperature (as shown in **Table 3.2**). It should be noted that the potential drop between the charge and the discharge process (ΔV) also decreases with the calcination temperature. As can be seen

in **Figure 3.10b**, the potential drop is only 11 mV (high plateau) at the rate of 0.2C for LMO-750, indicating the fast kinetics of the material owing to the 1D morphology characteristics of the product.[88]

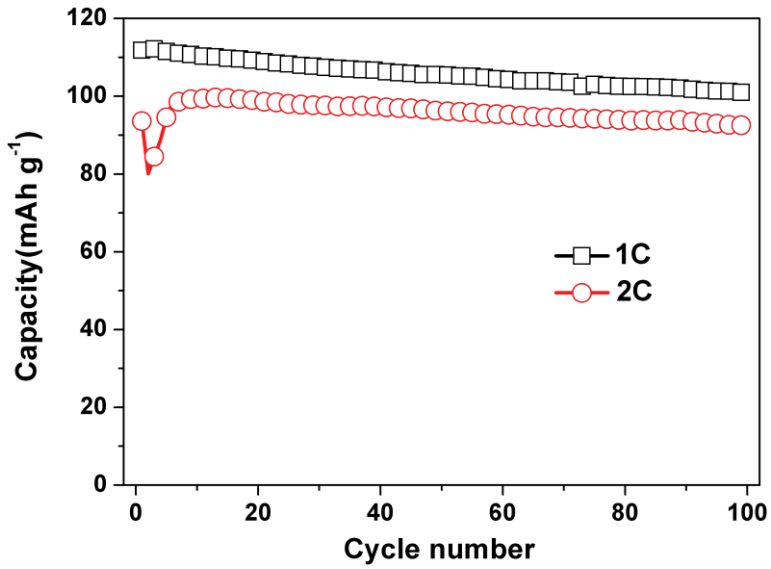


**Figure 3.12.** Cycling performance of LMO-650 at 1C and 2C. (1C = 148 mA $g^{-1}$)

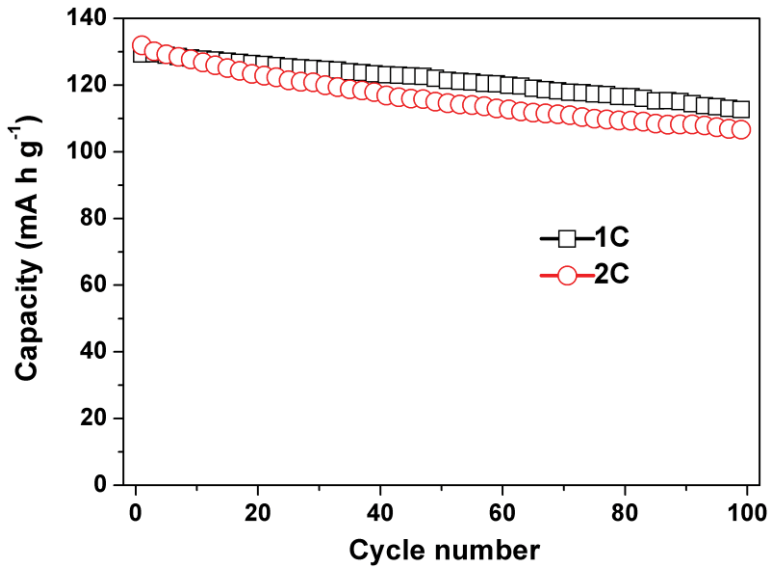


**Figure 3.13.** Cycling performance of LMO-700 at 1C and 2C.

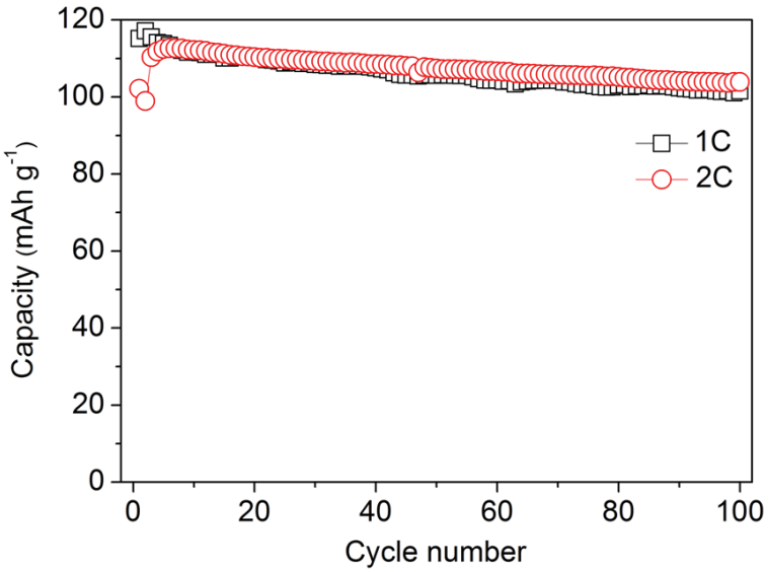


**Figure 3.14** Cycling performance of LMO-750 at 1C and 2C.

The electrochemical performance of $LiMn_2O_4$ nanorods was evaluated by galvanostatic charge/discharge cycling. As shown in **Figure 3.12**, the capacity of LMO-650 increased initially and reached a value of 113 mA h $g^{-1}$ at 1C. The initial increase of the capacity may be associated with initial inadequate wetting of the electrodes, which results in the insufficient utilization of the active material.[279] However, the cycling performance of LMO-650 was not satisfactory. After 100 cycles at 1C rate, it maintained 89.4% of the initial capacity, corresponding to a capacity loss of 0.106% per cycle. By increasing the calcination temperature, the electrochemical performance can be improved. LMO-700 delivered a capacity higher than that of LMO-650 (LMO-650 achieved 129 mA h $g^{-1}$ at 1C. However, the cycling performance of $LiMn_2O_4$ prepared at this temperature was still not improved, compared with LMO-650. After 100 cycles at 2C, LMO-700 only delivered a capacity of 106 mA h $g^{-1}$. The capacity loss was calculated to be 0.18% per cycle (**Figure 3.13**). When the calcination temperature was further increased to 750 $^{o}$C, the as-prepared $LiMn_2O_4$ achieved better cycling performance. As shown in **Figure 3.14**, after cycling at 2C for 100 cycles,

LMO-750 maintained a capacity of 97 mA h $g^{-1}$. The capacity loss was 0.07% per cycle. The improved cycling performance could be ascribed to the increased crystallinity, which is able to hinder Mn dissolution from the spinel structure into the electrolyte.[264, 265]

In order to compensate the loss of lithium during heat treatment, such as lithium sublimation, more LiOH than the stoichiometric amount is preferred during the synthesis process.[280] Furthermore, Xia and Yoshio demonstrated that the capacity loss for stoichiometric spinel $LiMn_2O_4$ at room temperature was due to the cubic (a = 8.145 Å) to cubic (a = 8.07 Å) phase transition on the 4.2 V plateau. This phase transition, and the capacity fading, can be suppressed by preparing a lithium-rich sample.[277] To this end, we deliberately increased the molar ratio of LiOH and $Mn_3O_4$ (denoted as Li:Mn ratio including 1.05:2, 1.1:2, 1.15:2 and 1.2:2) by increasing the feeding stock of LiOH. The calcination temperature was fixed at 750 $^oC$. As depicted in **Figure 3.15**, for $LiMn_2O_4$ prepared at a Li:Mn ratio of 1.05:2, the capacity was 126 mA h $g^{-1}$ at a rate of 1C, which is 85.1% of the theoretical capacity (148 mA h $g^{-1}$). After 500 cycles, the capacity maintained 95 mA h $g^{-1}$ with a capacity loss of 24.6% (0.049% per cycle). The Li:Mn molar ratio was further increased to 1.10:2. Obviously, as can be found in **Figure 3.16**, the obtained sample exhibited an improved cycling performance compared with $LiMn_2O_4$ obtained at a ratio of 1.05:2. At 1C, the initial capacity is 115 mA h $g^{-1}$. After 500 cycles, the capacity still maintained 107 mA h $g^{-1}$, and the capacity loss was 6.9% (0.014% per cycle). At 2C, the obtained $LiMn_2O_4$ showed a good cyclability within 500 cycles, the capacity loss per cycle was 0.0094%. At a higher rate, 3C for example, the capacity loss was higher (0.024% per cycle within 500 cycles). When the ratio was increased to 1.15:2, the high rate cyclability was improved, as shown in **Figure 3.17**. The capacity was 116 mA h $g^{-1}$ and 106 mA h $g^{-1}$ at a rate of 2C and 3C, respectively. Within 500 cycles, the capacity loss

was 0.016% per cycle at a rate of 3C, approximating the value at a rate of 2C (0.011% per cycle). When the Li:Mn ratio was increased to 1.2:2, it resulted in slightly lower initial capacity, which is in coincident with previous reports.[277] The actual Li:Mn molar ratio in the final product was determined to be 1.18:2 by an inductively coupled plasma mass spectrometer (ICP-MS).

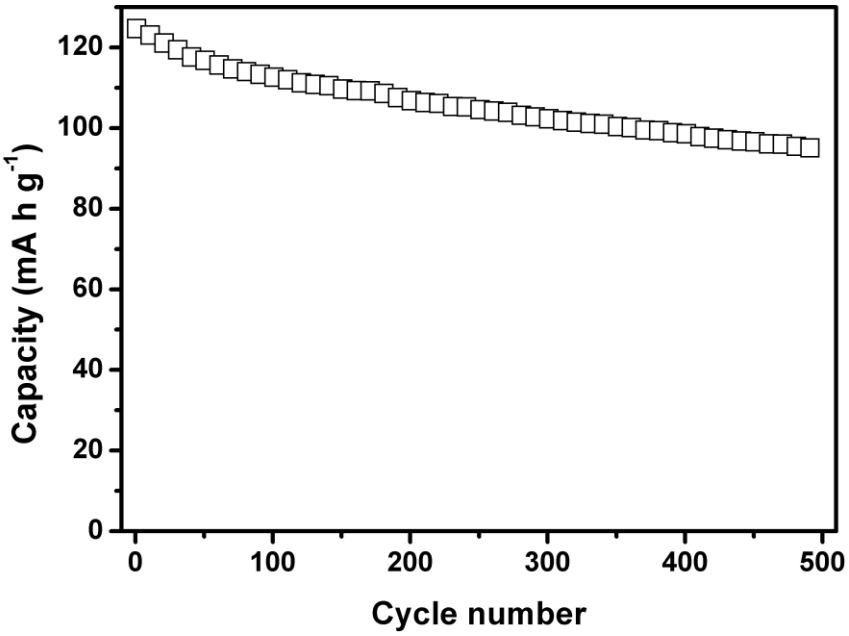


**Figure 3.15** Cycling performance of $LiMn_2O_4$ obtained from a precursor ratio (Li:Mn) of 1.05:2 at a rate of 1C.

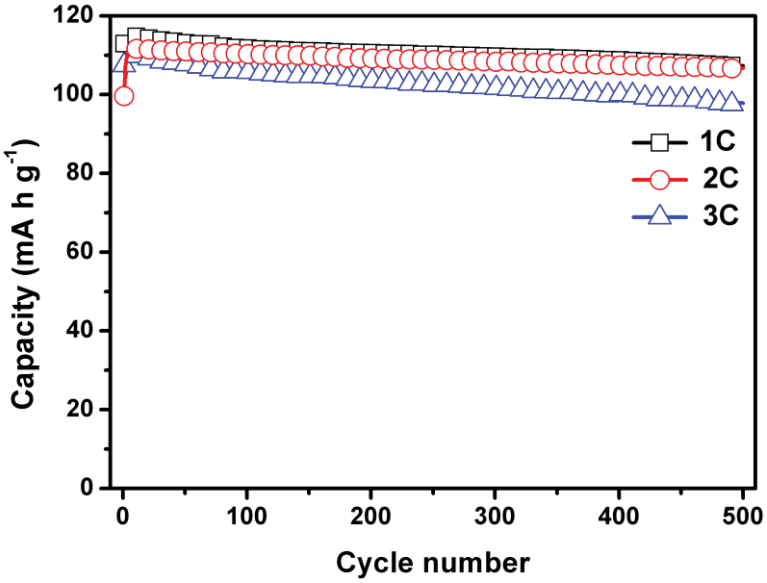


**Figure 3.16** Cycling performance of $LiMn_2O_4$ obtained from a precursor ratio (Li:Mn) of 1.10:2 at different rates.

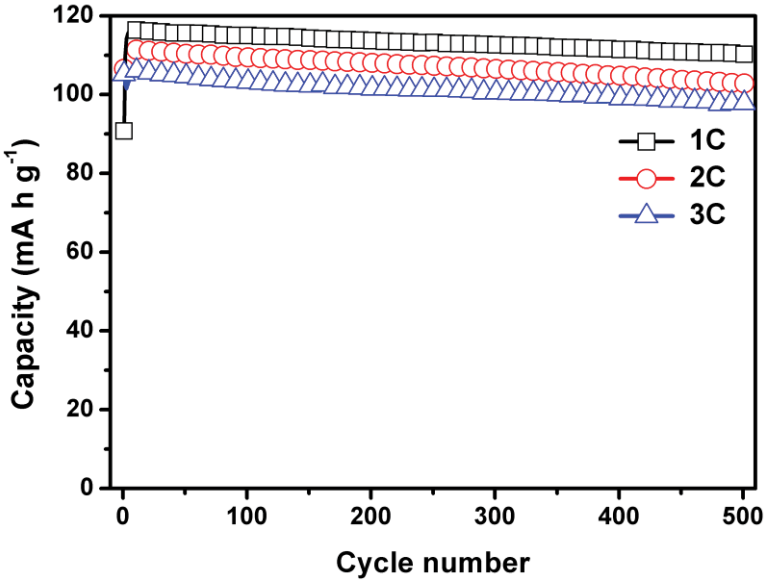


**Figure 3.17** Cycling performance of $LiMn_2O_4$ obtained from a precursor ratio (Li:Mn) of 1.15:2 at different rates.

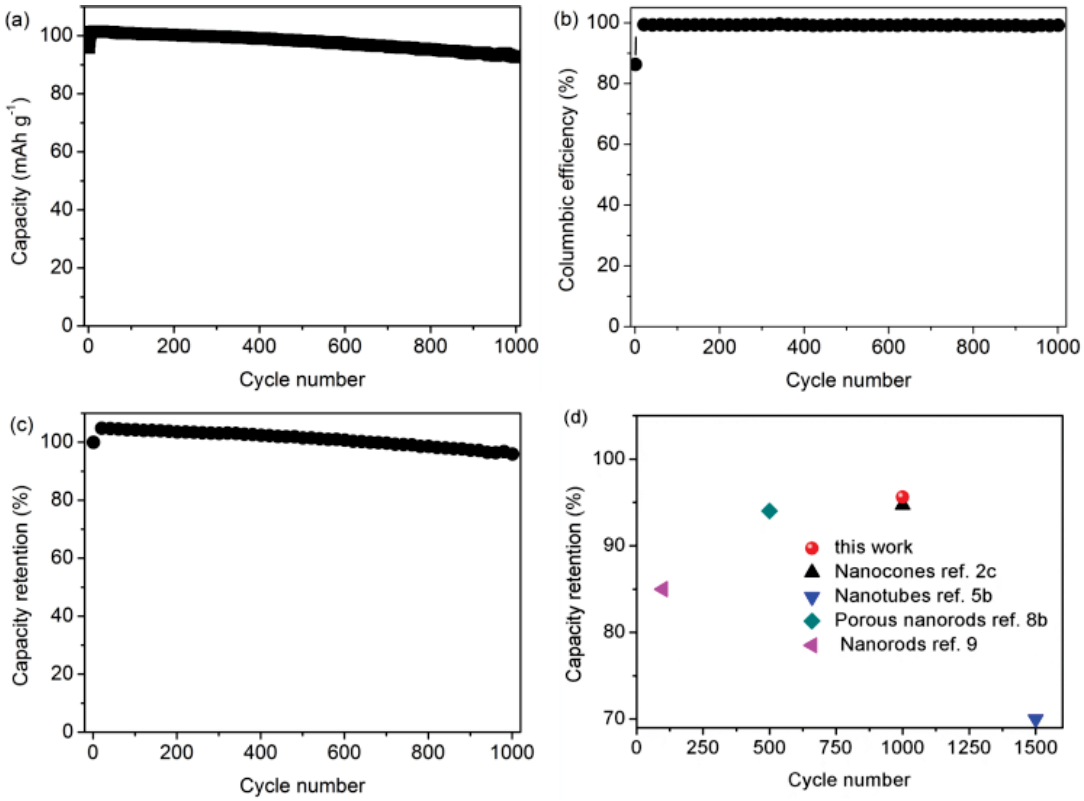


**Figure 3.18** (a) Cycling performance of $LiMn_2O_4$ nanorods obtained from a precursor ratio (Li:Mn) of 1.2:2 at the 3C rate. (b) The Coulombic efficiency as a function of cycle number. (c) Discharge capacity retention as a function of cycle number at 3C rate. (d) Capacity retention comparison with other $LiMn_2O_4$ nanoarchitectures reported recently.

**Figure 3.18a** shows the discharge capacity as a function of cycle number at the 3C rate. It delivered an initial discharge capacity of 101 mA h $g^{-1}$ with a coulombic efficiency of 86.3%. Surprisingly, excellent long-term stability on cycling has been obtained. After 1000 cycles, the cell retained 95.6% of its initial capacity at the 3C rate, as shown in **Figure 3.18c**. **Figure 3.18d** summarizes the cycling performance different $LiMn_2O_4$ nanoarchitectures as LIBs cathode reported so far. To the best of our knowledge, we achieved the best high rate long-term cycling performance for spinel $LiMn_2O_4$ cathode material. This result could pave the way for developing $LiMn_2O_4$–based LIBs with long cycle life. The cell also maintained high

coulombic efficiency, with an average value of 99.3% over 1000 cycles (as shown in **Figure 3.18b**). At this precursor ratio, $LiMn_2O_4$ sample lost the morphology characteristics of 1D nanorods when the calcination temperature was increased to 800 $^oC$, resulting in a lower specific capacity (**Figure 3.19**).

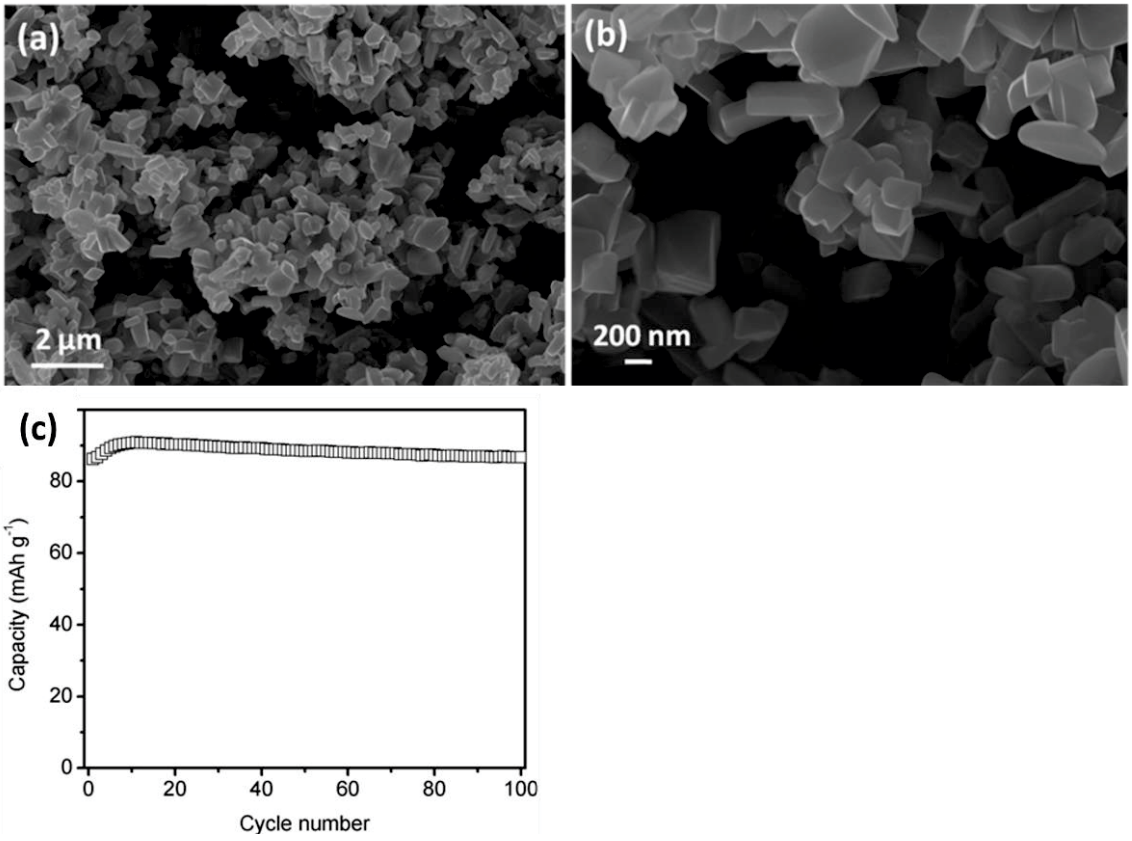


**Figure 3.19.** SEM images of $LiMn_2O_4$ obtained at a calcination temperature of 800 $^oC$ (a and b) at a Li:Mn ratio of 1.20:2 and the corresponding cycling performance at 3C at room temperature.

**Figure 3.20a** shows the charge-discharge profiles of $LiMn_2O_4$ nanorods at different C rates and the rate capability. The as-prepared $LiMn_2O_4$ nanorods exhibited good rate capability. The reversible capacity slightly decreases as the current density increases. The capacity was 114 mA h $g^{-1}$, 114 mA h $g^{-1}$, 111 mA h $g^{-1}$, 108 mA h $g^{-1}$, 103 mA h $g^{-1}$, 101 mA h $g^{-1}$ and

91 mA h $g^{-1}$ at a rate of 0.5C, 1C, 3C, 5C, 8C, 10C and 20C, respectively, suggesting excellent rate capability of the as-obtained single crystalline nanorods. The excellent rate performance of the $LiMn_2O_4$ nanorods results from the merits of 1D $LiMn_2O_4$, which allows fast $Li^+/e^-$ transportation. From **Figure 3.20b**, it should be noticed that when the current density reversed back to 0.5C after the high rate cycling measurement, the $LiMn_2O_4$ nanorods can preserve the original capacity. This confirms that the $LiMn_2O_4$ nanorods are able to tolerate high rate cycling, which is desirable for high power applications.

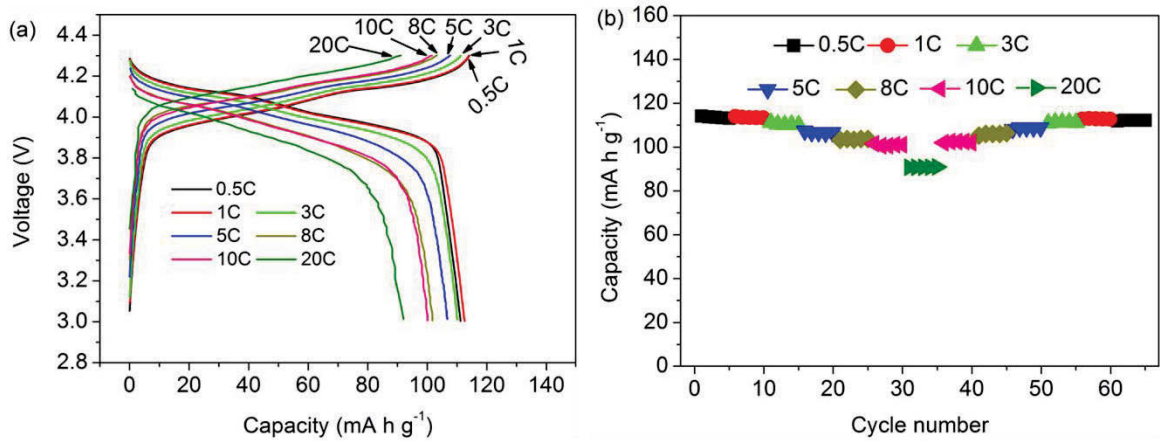


**Figure 3.20** (a) Charge-discharge profiles of $LiMn_2O_4$ nanorods at different C rates between 3.0 and 4.3 V in coin-type half cells (1C = 148 mA $g^{-1}$). (b) Rate capability of $LiMn_2O_4$ electrode at varied C rates.

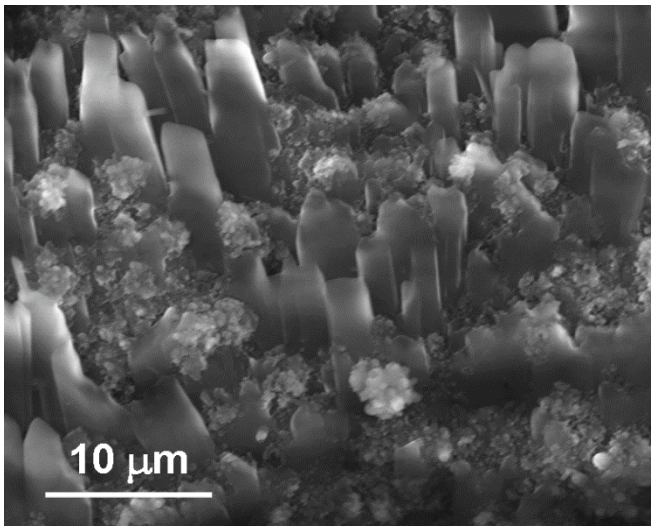


**Figure 3.21** SEM image of $LiMn_2O_4$ electrode after 1000 cycles.

The superior electrochemical performance of $LiMn_2O_4$ nanorods could be ascribed to the ultrahigh structural stability of the single crystalline and unique 1D nanoarchitecture with high length/radius aspect ratio, which allows for efficient electrode-electrolyte contact, and provides 1D electron transport pathways.[88] In order to examine the integrity of the rod-like morphology of $LiMn_2O_4$ after long-term cycling, we carried out post-mortem SEM analysis on the cycled electrodes. **Figure 3.21** shows the FESEM image of the $LiMn_2O_4$ electrode after 1000 cycles. The 1D rod-like architecture has been well preserved even after long-term charge/discharge cycling, suggesting that $LiMn_2O_4$ nanorods can tolerate the stress from volume expansion during repeated lithiation/de-lithiation processes, which endow long-term cycling stability to the as-synthesized $LiMn_2O_4$ nanorods.

### 3.4 Conclusions

Single-crystalline spinel $LiMn_2O_4$ nanorods have been successfully synthesized by a novel template-engaged reaction method using porous $Mn_3O_4$ nanorods as self-sacrificial

templates. By optimizing the synthesis parameters, including the sintering temperature and the precursor ratio, we found that $LiMn_2O_4$ nanorods prepared from LiOH and $Mn_3O_4$ with a molar ratio of 1.2:2 (Li:Mn) at 750 ºC showed excellent electrochemical performance as cathode materials for LIBs. This includes a capacity of 114 mA h $g^{-1}$ at 0.5C, excellent cyclability (95.6% capacity retention after 1000 cycles at a rate of 3C), and a good rate capability. The post-mortem FESEM analysis demonstrates that the single-crystalline $LiMn_2O_4$ nanorods exhibited ultrahigh structural stability. Even after 1000 cycles at 3C, the rod-like morphology has been well preserved. The superior electrochemical performance could be attributed to the anisotropies of the 1D morphology and the structural stability of the single-crystallinity. This work shows that single crystalline spinel $LiMn_2O_4$ nanorods could be promising cathode materials for LIBs with long cycle life.

# Chapter 4 A Comparative Investigation on the Effects of Nitrogen-doping into Graphene on Enhancing the Electrochemical Performance of $SnO_2$/graphene for Sodium-ion Batteries

## 4.1 Introduction

The global distribution of lithium and the future capital investment in lithium usage would make lithium-ion batteries (LIBs) costly for the large-scale applications. The rich sodium source makes sodium-ion batteries (SIBs) a sustainable and economically attractive electrochemical energy conversion and storage technique in the long term, which can be used as a near-term substitution for LIBs.[178, 200, 247, 248, 281-283] To support the practical applications of SIBs, one critical issue is to develop electrode materials with the capability for fast and stable sodium ion storage.[163, 284]

Carbon materials have been applied as scaffolds to support Na-ion host materials, such as phosphorous,[257, 258, 285] Sn-based compounds,[248, 286] and Sb-based materials,[287, 288] in order to increase the electronic conductivity and buffer the volume change of electrode materials during charge/discharge processes. Graphene has been widely used as effective building blocks for these purposes, owing to its high electronic conductivity, two-dimensional structure with high surface area, and flexibility.[241, 289-297] In order to meet the demand of high energy storage, numerous efforts have been devoted to enhancing the electrochemical performance of the graphene-based composite materials based on rational material manipulations. Chemical substitution of graphene by heteroatoms, such as B, N, and S, could bring new physicochemical functionalities.[298-301] It is rife that the doping of graphene matrix by nitrogen heteroatoms can improve the electrochemical performance for $Na^+$ storage.[195,

[302, 303] For example, Kang and co-workers have reported the enhanced electrochemical performance for SIBs in $TiO_2$/nitrogen-doped graphene nanocomposites with open pore channel compared to $TiO_2$/graphene counterparts.[302] Qin *et al.* found nitrogen-dopants in graphene can restrict further structural growth and result in smaller size of $TiO_2$, which contributes to the improved capacity and rate capability of $TiO_2$/nitrogen-doped graphene compared to $TiO_2$/graphene for SIBs.[303] However, to manifest the inherent nitrogen-doping effects for enhancing the sodium-ion storage performance, a logical comparison between nitrogen-doped graphene based nanocomposites and the nitrogen-free ones should be in a reasonable framework excluding: (1) the difference of the loading ratio of supported materials in the compared composites, (2) the possible morphology effects, such as the crystallinity and particle size of supported materials, the surface area of the composites determining the electrode/electrolyte contact. In this aspect, a rational and systematic comparison between nitrogen-doped graphene based nanocomposites and the nitrogen-free ones for $Na^+$ storage has still been unavailable. On the other hand, the previous reports available in this area often attribute the enhanced electro-activity of the nitrogen-doped graphene (NG) based nanocomposites to the increased electro-active sites within graphene networks and the improvement of electron transfer efficiency of the overall electrode due to nitrogen-doping.[302, 304] Nevertheless, the contribution ratio of each effect to the overall capacity enhancement is still ambiguous.

Herein, we choose $SnO_2$ as a typical example to investigate the intrinsic nitrogen-doping effects for improving the sodium-ion storage in the graphene-based nanocomposites. An *in situ* hydrothermal route was used to prepare $SnO_2$/nitrogen-doped graphene ($SnO_2$/NG) nanohybrids as anode materials for SIBs. For comparison, $SnO_2$/graphene ($SnO_2$/G)

nanohybrids with the same $SnO_2$ weight ratio were prepared by a similar procedure without nitrogen-doping agents. The results indicate that the particular characteristics in these two series of composites including the crystallinity, the particle size, and the morphology of $SnO_2$ are identical. Based on such a desirable system, a comparison between $SnO_2$/NG and $SnO_2$/G featuring analogous morphology as anode materials for SIBs has been conducted. The as-prepared $SnO_2$/NG electrode exhibits a higher sodium-ion storage capacity than the $SnO_2$/G counterpart. In particular, by controlled experiments using bare NG and graphene as anode materials for SIBs, we find that the improved electron transfer efficiency due to nitrogen-doping has an important contribution to the observed enhanced electrochemical performance; whereas the increased electro-active sites within graphene networks benefiting from nitrogen-doping has limited contribution to the overall electrochemical performance enhancement. This work could provide more specific information for understanding the effects of nitrogen-doping into graphene for improving the electrochemical performance of graphene based composites.

## 4.2 Experimental

### 4.2.1 Materials

Graphene oxide (GO) nanosheets were synthesized from natural graphite powders by a modified Hummer's method.[305] $SnO_2$/G and $SnO_2$/NG composites were produced by a hydrothermal method. Typically, $SnCl_4 \cdot 5H_2O$ (40 mg, Sigma-Aldrich, ≥ 98%) was mixed with GO aqueous suspension (40 mL, 1 mg $mL^{-1}$) by ultrasonication using a Branson Digital Sonifier (S450D, 40% amplitude). After ultrasonication for 1 h, the mixture was divided into two parts (20 mL each). To prepare $SnO_2$/NG nanohybrids, urea (5 g) was added to one part

and stirred for 30 min. Both solutions were then heated to 180 °C in a Teflon-lined autoclave (25 mL in capacity) and maintained at that temperature for 24 h. The precipitates were cooled to room temperature naturally, and then collected and washed with distilled water and ethanol several times. After drying at 60 °C in a vacuum oven overnight, the final products were obtained.

### 4.2.2 Structural and physical characterization

The crystal structure and phases of as-prepared materials were characterized by X-ray diffraction (XRD, Siemens D5000) using a Cu Kα radiation at a scanning step of 0.02° $sec^{-1}$. The morphology was analyzed by field emission scanning electron microscope (FESEM, Zeiss Supra 55VP). The crystal structure details were further characterized by transmission electron microscopy (TEM) and high-resolution transmission electron microscopy (HRTEM, JEOL JEM-2011). Simultaneous thermal-gravimetric analysis and differential thermal analysis (TGA/DTA) were performed with a 2960 SDT system to analyze the weight ratio of $SnO_2$ at a heating rate of 10 °C $min^{-1}$ in air from room temperature to 800 ºC. The XPS spectra were carried out on an ESCALAB 250Xi XPS System with a mono-chromated Al Ka X-ray source (13 kV 150 W 500 μm with pass energy of 100 eV for survey scans, or 20 eV for region scans). All of the binding energies were calibrated by C 1s as the reference energy (C 1s = 284.6 eV). Raman spectra were collected using a Renishaw inVia Raman spectrometer system (Gloucestershire, UK) equipped with a Leica DMLB microscope (Wetzlar, Germany) and a Renishaw He–Ne laser source that produced 17 mW at λ = 633 nm. The $N_2$-sorption measurement was carried out at 77 K with a Micromeritics 3Flex Surface Characterization Analyser.

### 4.2.3 Cell assembly and electrochemical testing

The electrodes were prepared by dispersing the as-prepared material (80 wt %) and poly (Vinylidene fluoride) binder (PVDF, 20 wt %) in N-methyl-2-pyrrolidone (NMP) to form a slurry. The resultant slurry was pasted onto copper foil using a doctor blade and dried in a vacuum oven for 12 h, followed by pressing at 200 kg $cm^{-2}$. The loading weight of the electro-active material is around 1.1 mg $cm^{-2}$. Electrochemical measurements were carried out using two electrode coin cells with Na metal as counter and reference electrodes and the glass microfiber (Whatman) as the separator. The CR2032-type coin cells were assembled in an argon-filled glove box (UniLab, Mbraun, Germany). The electrolyte solution was 1 M $NaClO_4$ dissolved in a mixture of ethylene carbonate (EC) and propylene carbonate (PC) with a volume ratio of 1:1 with a 5 vol.% addition of fluoroethylene carbonate (FEC). All the capacities were calculated based on the mass of the composites. Cyclic voltammetry (CV) was conducted on a CHI 660C instrument between 0.01 and 3 V *vs.* $Na/Na^+$ at room temperature. For the electrochemical impedance spectroscopy (EIS) measurement, the excitation amplitude applied to the cells was 5 mV. The charge-discharge measurements were performed at ambient temperature at different current densities in the voltage range from 0.01 to 3 V *vs.* $Na/Na^+$.

## 4.3 Results and Discussion

In the present study, a facile hydrothermal method has been developed to prepare $SnO_2$/NG nanohybrids using urea as the nitrogen precursor (**Figure 4.1**). $SnCl_4$ was mixed with GO aqueous suspension first. Because of the electrostatic interaction between $Sn^{4+}$ anions and negatively charged GO, $Sn^{4+}$/GO hybrids can be readily obtained in this step. The $Sn^{4+}$/GO

hybrids, together with urea, were then subjected to hydrothermal treatment. During hydrothermal treatment, $NH_3$ can be released slowly from urea, which can be used as nitrogen-doping agent in the confined space.[306] The low-temperature incorporation of nitrogen heteroatoms into graphene networks was achieved by the reason that the hydrothermal condition, *i.e.*, 180 °C and autogenous pressure, promoted the reaction between basic $NH_3$ and oxygen functionalities (such as carboxylic acid and hydroxyl species) and finally enabled the *in situ* doping of nitrogen.[306] The oxygen-containing groups on GO, such as carboxyl, hydroxyl and epoxy groups, act as the nucleation and growth sites, and homogeneously dispersed $SnO_2$ nanocrystals formed consequently. The nitrogen dopants can also interact with the $Sn^{4+}$, providing additional active sites for $SnO_2$ formation, which results in a strong coupling between metal species and N-doped graphene.[307, 308] Our synthesis protocol avoids high-temperature nitridation of graphene. For comparison, we prepared $SnO_2$/G using the same procedure without the addition of urea as a benchmark to investigate the nitrogen-doping effects of $SnO_2$/NG nanocomposites as anode materials for SIBs.

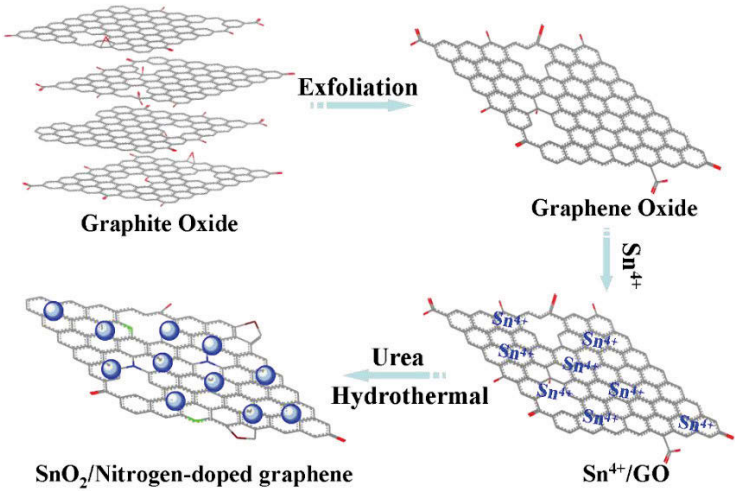


**Figure 4.1** Schematic illustration for the preparation of $SnO_2$/NG nanohybrids.

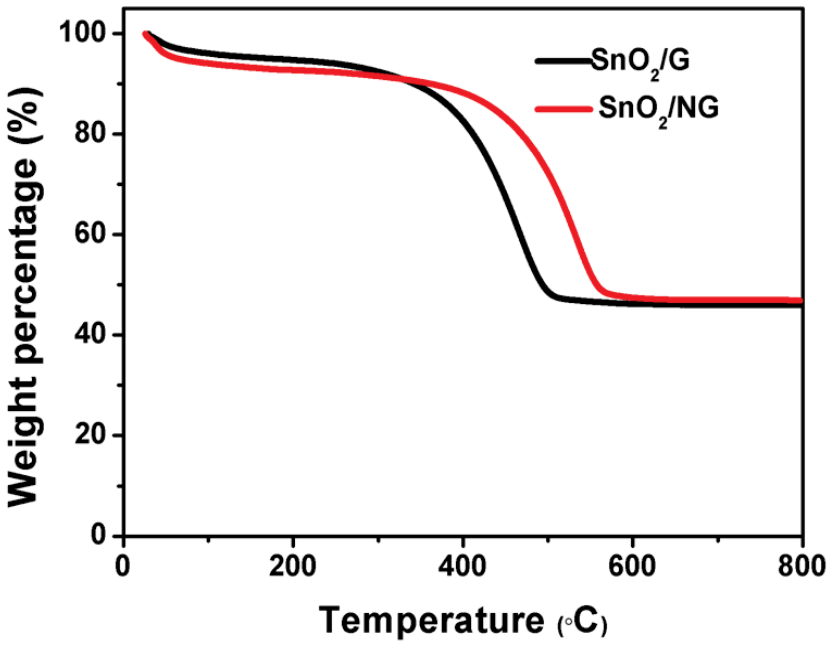


**Figure 4.2** TGA curves of the $SnO_2$/G and $SnO_2$/NG.

TGA curves in **Figure 4.2** suggest that $SnO_2$/G has the same $SnO_2$ weight ratio as $SnO_2$/NG (47.0%).

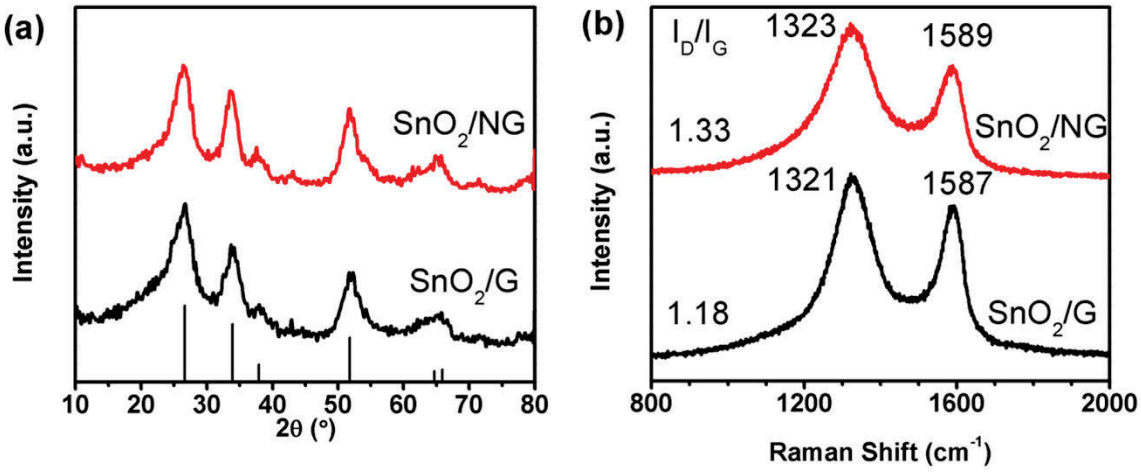


**Figure 4.3** (a) XRD patterns of $SnO_2$/NG and $SnO_2$/G composites. (b) Raman spectra of $SnO_2$/NG and $SnO_2$/G composites in the range of 800-2000 $cm^{-1}$.

The crystal structure of $SnO_2$/NG and $SnO_2$/G nanocomposites has been characterized by X-ray diffraction (XRD), as shown in **Figure 4.3a**. The XRD patterns show diffraction peaks at 26.6°, 33.7°, 37.9°, 51.8° and 65.3°, which can be well indexed to the pure tetragonal rutile phase of $SnO_2$ crystals with the space group of P42/mnm (JCPDS card No. 41-1445). Because of the balance between the depletion of oxygen-containing groups and the introduction of nitrogen heteroatoms,[306] there should be no big difference of the total sites for the growth of $SnO_2$ nuclei between NG and graphene, which is reflected by the XRD results. As calculated by Scherrer equation, the crystallite size of $SnO_2$ in $SnO_2$/NG (1.6 nm) is similar to that in $SnO_2$/G (1.4 nm). The microstructure of NG has been investigated by Raman spectroscopy, as presented by **Figure 4.3b**. Two characteristic peaks at 1323 and 1589 $cm^{-1}$ can be observed in the range of 800-2000 $cm^{-1}$, corresponding to the D band and G band of NG, respectively. Compared to the $SnO_2$/G counterpart, the as-synthesized $SnO_2$/NG nanohybrids exhibit an upshift of the D band and G band (from 1321 $cm^{-1}$ to 1323 $cm^{-1}$ for D band and from 1587 $cm^{-1}$ to 1589 $cm^{-1}$ for G band). This may originate from structural distortion of graphene caused by the different bond distances of C-C and C-N.[300] Moreover, $SnO_2$/NG shows a higher $I_D/I_G$ (intensity ratio between D band and G band) value (1.33) than that of $SnO_2$/G composites (1.18), which suggests a more disordered structure for NG than graphene owing to the introduction of N heteroatoms in graphene networks. Both the shift of band positions and the larger $I_D/I_G$ value indicate that nitrogen heteroatoms have been successfully inserted into graphene by the hydrothermal method.

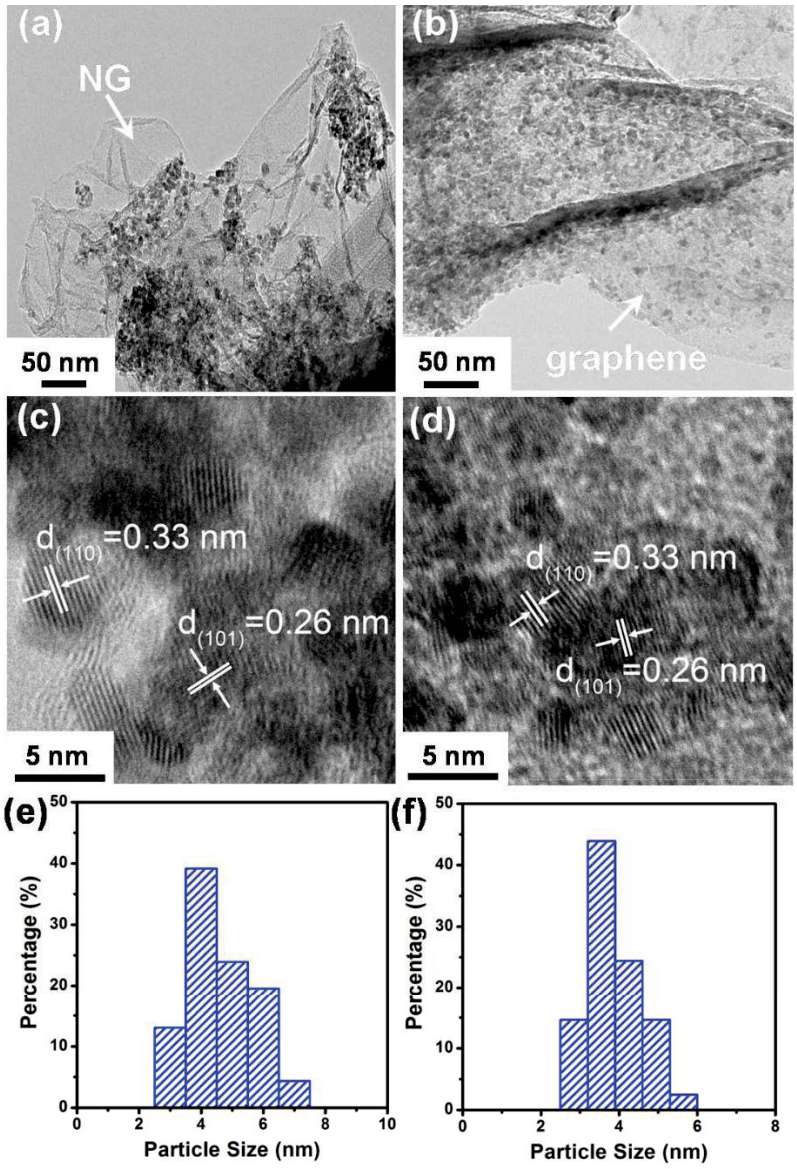


**Figure 4.4** Medium-magnification TEM image, high-resolution TEM image, $SnO_2$ particle size distribution of $SnO_2$/NG nanohybrids (a, c, and e) and $SnO_2$/G composites (b, d, and f).

TEM has been used to investigate the microstructures of the as-obtained $SnO_2$/NG and $SnO_2$/G, as depicted in **Figure 4.4**. The crumpling of NG layers, as observed in **Figure 4.4a**, is attributed to defect structures formed during the oxidation-reduction procedure for the synthesis of NG, which is in agreement with the Raman result. On the other hand, it can be clearly seen that ultrafine $SnO_2$ nanocrystals have been successfully loaded onto the surface

of NG after hydrothermal treatment. A high-resolution TEM image of $SnO_2$/NG nanohybrids is shown in **Figure 4.4c**, from which it can be observed that the crystal plane distance is 0.33 and 0.26 nm, corresponding to the (110) and (101) face of tetragonal $SnO_2$, respectively. The particle size distribution of $SnO_2$ in the as-prepared $SnO_2$/NG nanohybrids is shown in **Figure 4.4e**. And the average particle size of $SnO_2$ is calculated to be 4.7 nm. The morphology of $SnO_2$/G composites (**Figure 4.4b, d, and f**) is similar to that of $SnO_2$/NG, and the average particle size of $SnO_2$ in $SnO_2$/G composites is 4.0 nm.

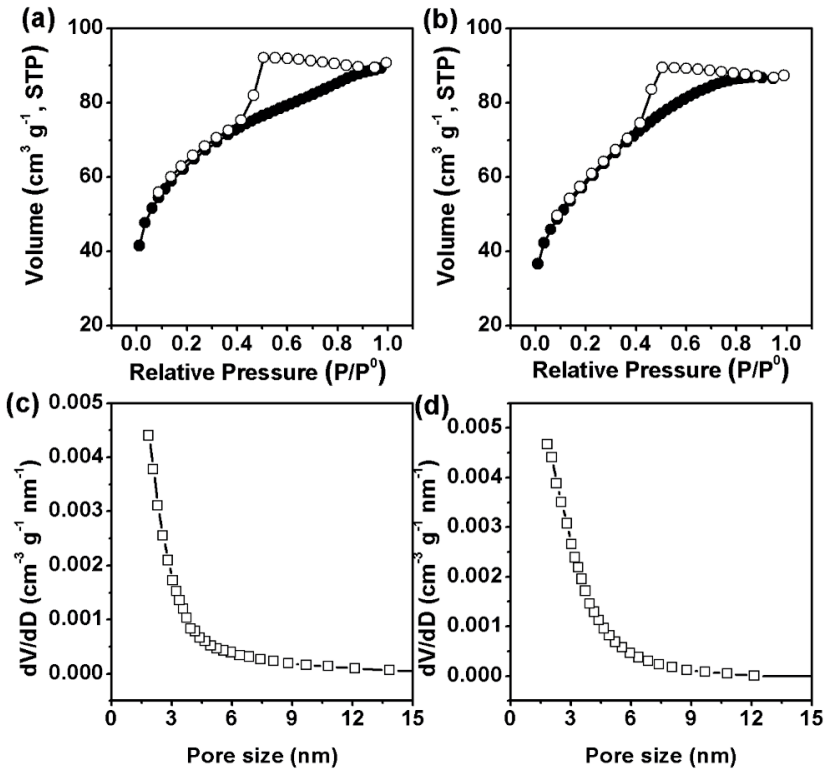


**Figure 4.5** $N_2$ sorption isotherms of the $SnO_2$/G (a) and $SnO_2$/NG composites (b). Pore size distribution of the $SnO_2$/G (c) and $SnO_2$/NG composites (d).

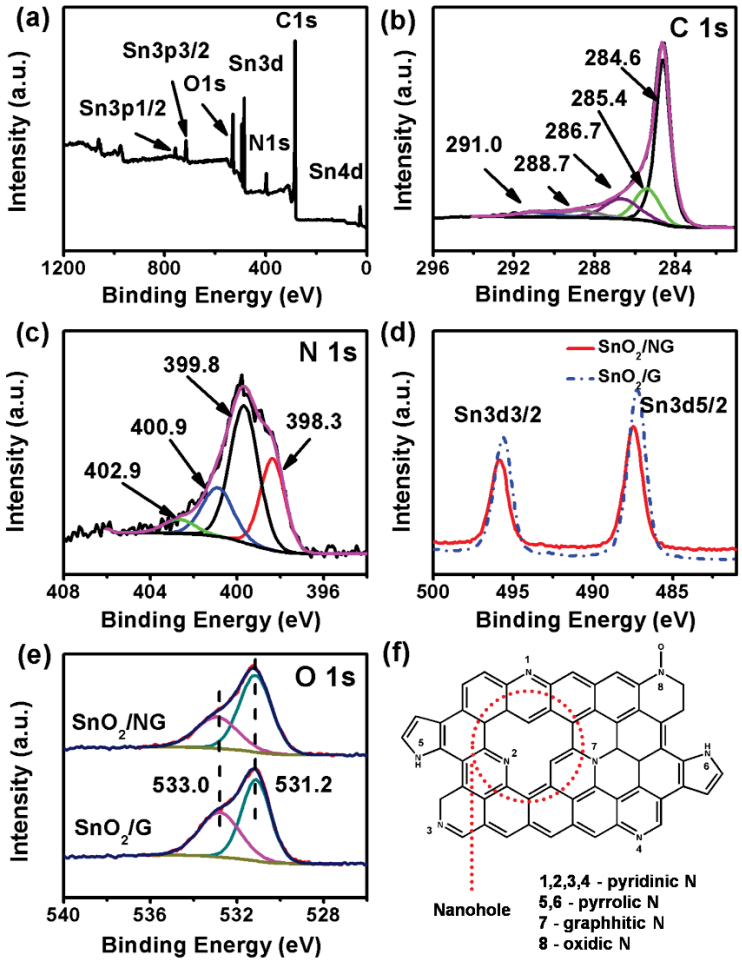


**Figure 4.6** XPS analysis of $SnO_2$/NG and $SnO_2$/G composites: (a) the survey spectrum, (b) high-resolution spectrum of C 1s, (c) N 1s spectrum, (d) XPS Sn 3d spectra, and (e) O 1s spectra. (f) Schematic illustration of different nitrogen species in NG.

**Figure 4.5** shows the nitrogen sorption isotherms of $SnO_2$/NG and $SnO_2$/G composites at 77 K. Both the adsorption-desorption curves can be classified as typical type-IV isotherm with an $H_1$-type loop hysteresis.[309] It is calculated that the BET surface area of $SnO_2$/G and $SnO_2$/NG material is very close, being 215 and 206 $m^2$ $g^{-1}$, respectively. It is calculated that the average pore diameter of $SnO_2$/NG nanocomposites is 3.0 nm, approximating to that of $SnO_2$/G nanocomposites (3.3 nm).

The X-ray photoelectron spectroscopy (XPS) experiments provide further evidences of the chemical configuration of nitrogen species and the interaction between $SnO_2$ nanocrystals and the NG matrix. From the survey XPS scan in **Figure 4.6a**, it can be indentified that the as-obtained $SnO_2$/NG composites are composed of C, N, O and Sn elements. No other signals can be found, which implies the purity of the as-synthesized samples. The high resolution C 1s spectrum is shown in **Figure 4.6b**, which can be fitted into five peaks at 284.6 eV (graphitic carbon), 285.4 eV ($N–C_{sp2}$), 286.7 eV ($N–C_{sp3}$), 288.7 eV (C=O) and 291.0 eV (shake-up satellite peak due to $\pi–\pi^*$ transitions in aromatic systems).[310] The overwhelming percentage of graphitic carbon suggests the graphitized nature of the NG in $SnO_2$/NG composites. The nitrogen bonding configuration can be obtained from the high resolution N 1s spectrum, as shown in **Figure 4.6c**. The result from the curve fitting indicates the presence of four different types of nitrogen species bonded to carbon in the composite: pyridinic N (398.3 eV), pyrrolic N (399.8 eV), graphitic N (400.9 eV) and oxidic N of pyridinic-N (402.9 eV).[311-315] Notably, the pyridinic and pyrrolic N species are dominant in the composite, indicating that nitrogen heteroatoms are mainly resident at the edges and/or the nanoholes of the two-dimensional graphene (**Figure 4.6f**). It is calculated that the total amount of nitrogen doped in NG is *ca.* 6.2 at.%. As shown in **Figure 4.6d**, the binding energy of Sn $3d_{3/2}$ and Sn $3d_{5/2}$ in $SnO_2$/G composite is 495.8 eV and 487.5 eV, respectively. In comparison, the location of the Sn XPS peaks in the $SnO_2$/NG composite shifts toward larger binding energy. **Figure 4.6e** shows the O 1s XPS spectrum of the $SnO_2$/NG composites, which can be deconvoluted into two peaks. The peak at 531.2 eV is assigned to C=O groups or shoulder peak of O 1s in $SnO_2$, and the peak at 533.0 eV is ascribed to C-OH and/or C-O-C groups (hydroxyl and/or epoxy).[316-318] The O/C ratio in NG is 0.073, which is much lower than that in graphene (0.126) due to the replacement of N. The same O 1s binding energy of $SnO_2$/NG composites as that

of $SnO_2$/G suggests that the different binding energy of Sn 3d in the as-prepared $SnO_2$/NG compared to that in $SnO_2$/G does not originate from size effects or charge correction issues. The XPS results indicate that $SnO_2$ nanocrystals are effectively coupled with the NG scaffold due to the nitrogen-doping, which facilitates the electron transfer at the interface between $SnO_2$ and NG during repeated sodiation/de-sodiation processes as discussed in the following part.

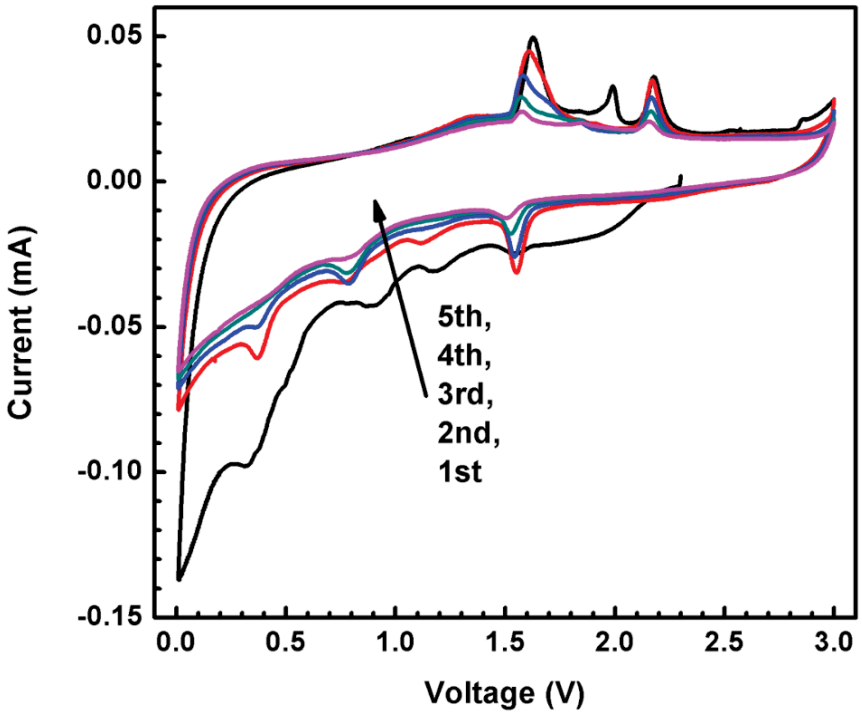


**Figure 4.7** CV profiles of the $SnO_2$/NG composites at a scan rate of 0.1 mV $s^{-1}$ between 0.01 and 3.0 V.

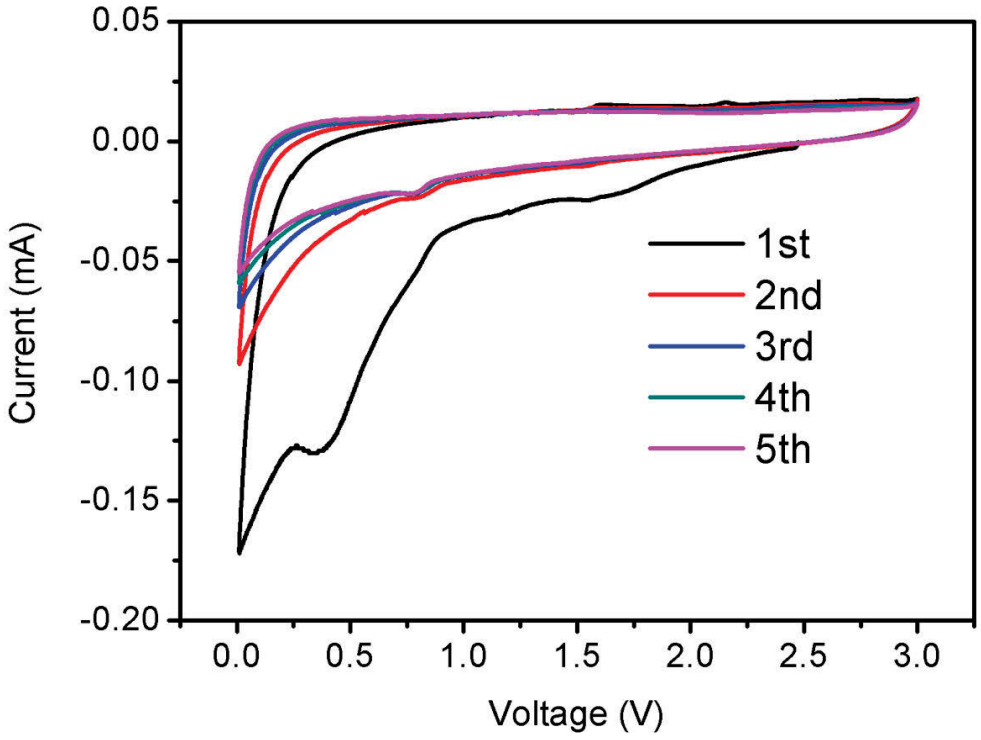


**Figure 4.8** CV profiles of NG at a scan rate of 0.1 mV $s^{-1}$ between 0.01 and 3.0 V.

The electrochemical reactions between $SnO_2$/NG and $Na^+$ have been investigated by cyclic voltammetry (CV), as shown in **Figure 4.7**. It has been revealed by TEM studies that upon sodium-ion insertion into $SnO_2$, a displacement reaction occurs to form the amorphous $Na_xSn$ nanoparticles dispersed in $Na_2O$ matrix,[319] and $SnO_2$ nanocrystals can be reversed back to the original phase at the charge state[262]. In the first discharge process, the peaks in the region from 3.0 V to 1.0 V could be ascribed to the $Na^+$ insertion into $SnO_2$ crystals to form the $NaSnO_2$ intermediate phase.[262] A pair of cathodic and anodic peaks located at 0.9 V and 1.6 V can be clearly observed. Since these two peaks can also be observed for the bare NG electrode (**Figure 4.8**), they can be ascribed to the interaction between $Na^+$ and impure atoms in the graphene network, such as O in residual oxygen-containing functional groups and N heteroatoms.[320] Because propylene carbonate (PC) decomposes at 0.7 V *vs.* $Li/Li^+$ and

$E^{o}(Na/Na^{+})$ is 0.33 V higher than $E^{o}(Li/Li^{+})$,[321] it is plausible to assign the cathodic peak at 0.35 V to PC decomposition in the present $Na^{+}$ half-cell where the Na piece was used as reference electrode, forming a solid-electrolyte interphase (SEI) at the $SnO_2$/NG electrode.[322] Besides, the peaks from 0.7 V to 0.01 V are associated with the alloying reaction to form $Na_xSn$ alloys embedded in the $Na_2O$ matrix during the cathodic process in the first cycle. In addition, a pronounced sodium insertion peak can be observed at near 0.01 V in each cycle, which is analogous to lithium insertion in carbonaceous materials.[323]

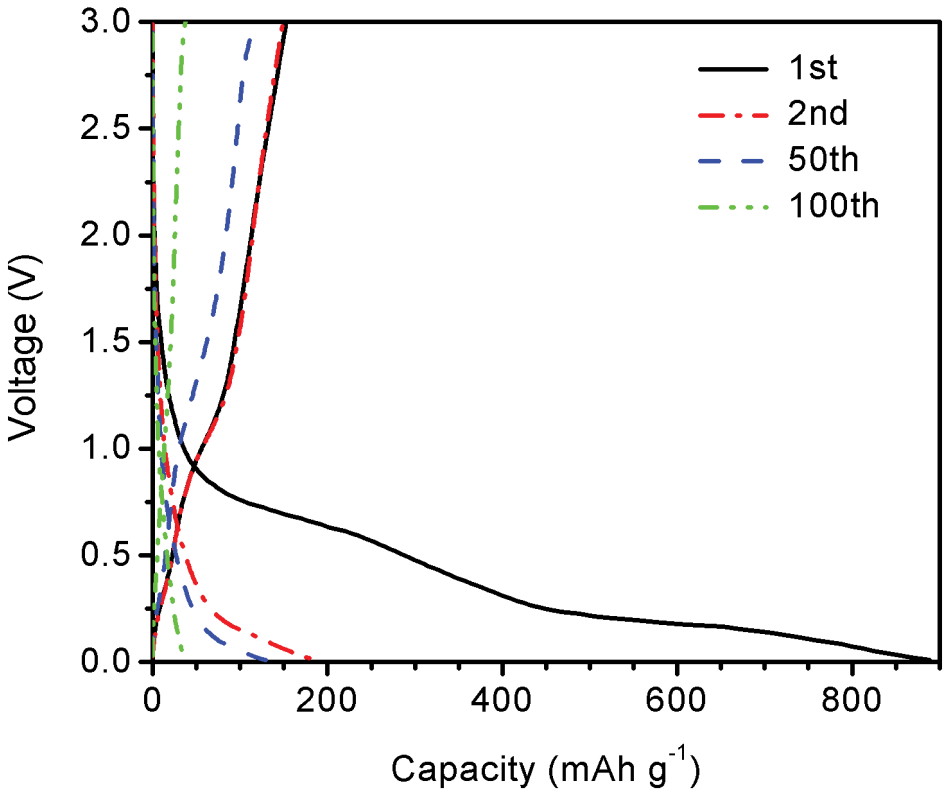


**Figure 4.9** Chare-discharge curves of bare $SnO_2$ at a current density of 20 mA $g^{-1}$.

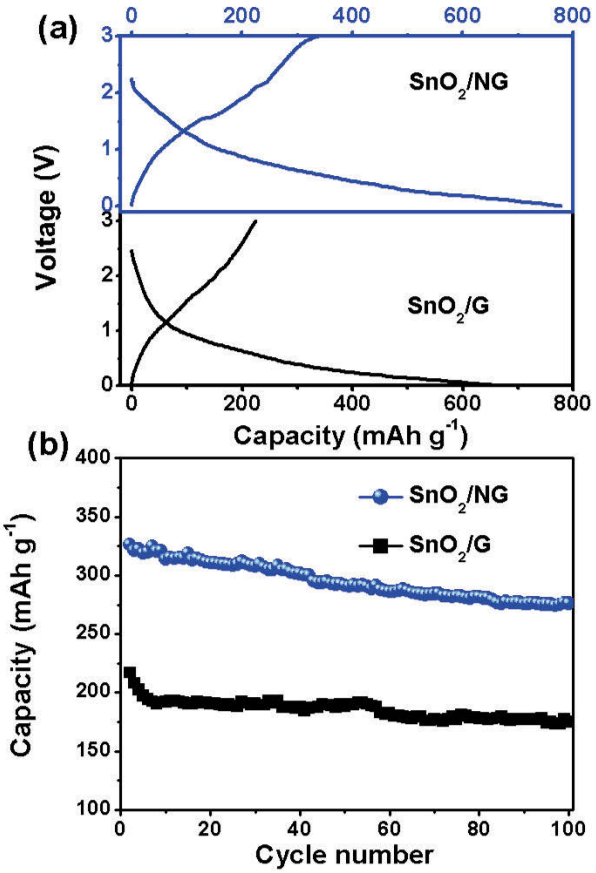


**Figure 4.10** (a) Galvanostatic charge-discharge profiles of the $SnO_2$/NG and $SnO_2$/G composites. (b) Cycling performance of $SnO_2$/NG and $SnO_2$/G composites at a current density of 20 mA $g^{-1}$ from the second cycle.

The advantages of the as-prepared $SnO_2$/NG over $SnO_2$/G as anode materials for SIBs have been investigated by galvanostatic discharge/charge measurements in the voltage range of 0.01-3.0 V. As can be seen in **Figure 4.9**, bare $SnO_2$ only delivers an initial reversible capacity of 153 mA h $g^{-1}$. The capacity dramatically drops to 38 mA h $g^{-1}$ after 100 cycles at a current density of 20 mA $g^{-1}$. Both $SnO_2$/G and $SnO_2$/NG show higher reversible capacities than bare $SnO_2$. Particularly, in the 1st cycle, the $SnO_2$/G electrode delivers a discharge and charge capacity of 652 mA h $g^{-1}$ and 225 mA h $g^{-1}$, respectively (**Figure 4.10a**). $SnO_2$/NG nanohybrids show much higher capacities as anode materials for SIBs. As shown in **Figure**

**4.10a**, the initial reversible capacity of the $SnO_2$/NG electrode is 339 mA h $g^{-1}$, which is 114 mA h $g^{-1}$ higher than that of $SnO_2$/G. The initial Coulombic efficiency of $SnO_2$/NG electrode is 43.6%. The 56.4% capacity loss of the $SnO_2$/NG electrode may be ascribed to the irreversible formation of the SEI layer on the electrode. According to previous investigations, the SEI is composed of inorganic and organic layers around the particles.[324, 325] The organic layers can form and dissolve reversibly, which contributes to the reversible capacity. On the contrary, the formation of an inorganic layer is an irreversible process. Interestingly, it is noted that $SnO_2$/NG nanocomposites have a higher initial Coulombic efficiency than that of $SnO_2$/G (34.5%), which indicates that nitrogen incorporation is beneficial for the reversibility of the $SnO_2$/NG electrode. The cycling performances of $SnO_2$/NG and $SnO_2$/G are shown in **Figure 4.10b**. $SnO_2$/NG exhibits a universally superior electrochemical performance, compared to $SnO_2$/G, within 100 cycles at a current density of 20 mA $g^{-1}$. $SnO_2$/NG electrodes delivered capacities of 305 and 283 mA h $g^{-1}$ in the $50^{th}$ and $100^{th}$ cycle, which are higher than those of $SnO_2$/G electrode (207 and 188 mA h $g^{-1}$), as shown in **Figure 4.11**.

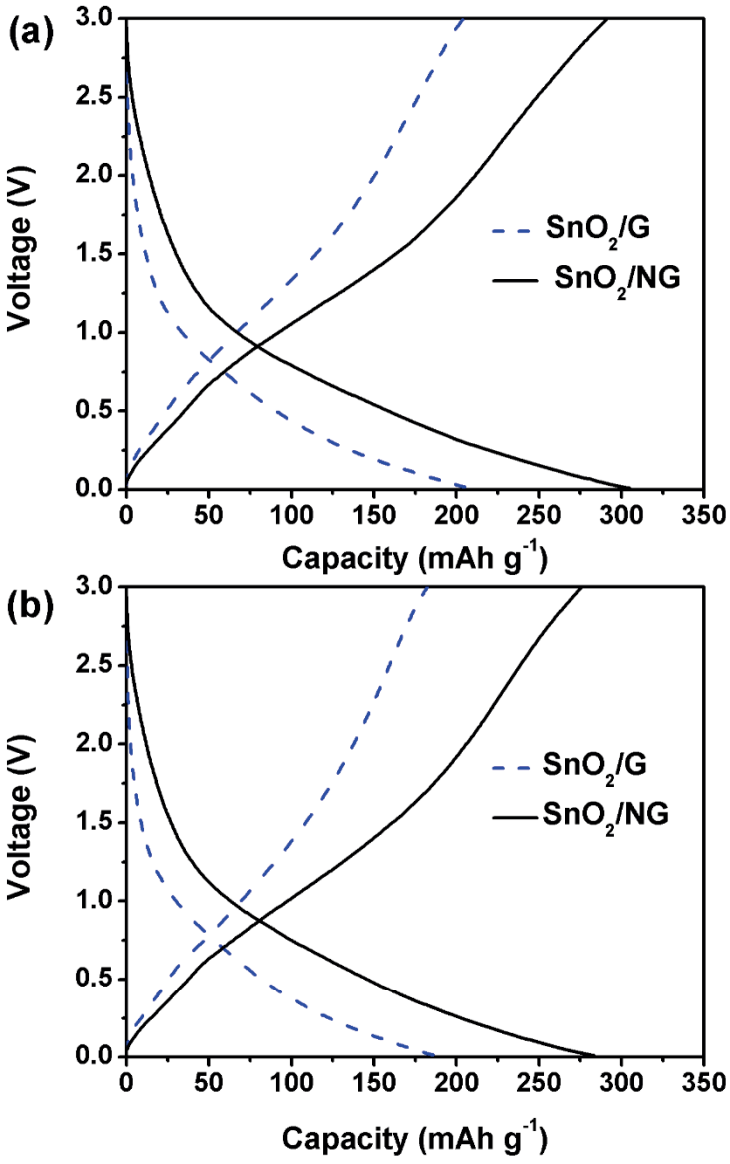


**Figure 4.11** Galvanostatic charge-discharge profiles of the $SnO_2$/NG and $SnO_2$/G composites of the 50$^{th}$ cycle (a) and 100$^{th}$ cycle (b) at 20 mA g$^{-1}$.

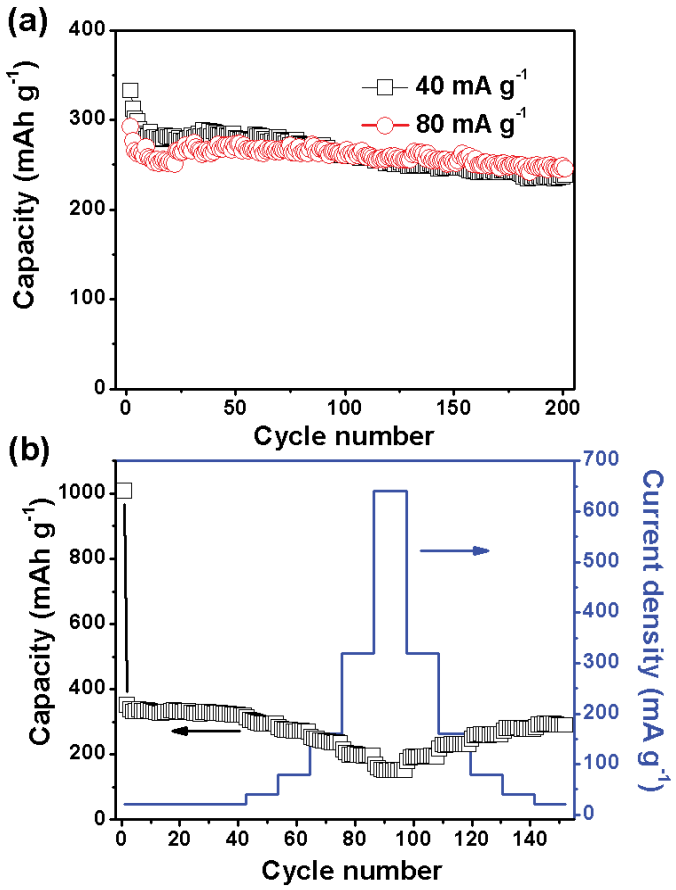


**Figure 4.12** (a) Cycling performance of $SnO_2$/NG composites at current densities of 40 and 80 mA $g^{-1}$ from the second cycle. (b) Rate performance of $SnO_2$/NG at different current densities.

**Figure 4.12a** shows the cycling performance of the $SnO_2$/NG nanohybrids at different current densities. The $SnO_2$/NG electrodes exhibit satisfying high rate performances. After 100 cycles, the $SnO_2$/NG anode still delivers high discharge capacities when cycled at different current densities: 238 mA h $g^{-1}$ at 40 mA $g^{-1}$, 246 mA h $g^{-1}$ at 80 mA $g^{-1}$, respectively. We also tested the multiple-step cycling characteristics of $SnO_2$/NG at 20, 40, 80, 160, 320, 640 mA $g^{-1}$ and 320, 160, 80, 40, 20 mA $g^{-1}$. As depicted in **Figure 4.12b**, the $SnO_2$/NG nanocomposite electrode shows an excellent high rate performance. At a current density of

640 mA $g^{-1}$, $SnO_2$/NG can still deliver a capacity of 170 mA h $g^{-1}$, which is preferable for high power density devices. When the current density reversed to the lower value (20 mA $g^{-1}$), the electrode recovered substantial capacities without obvious capacity decay.

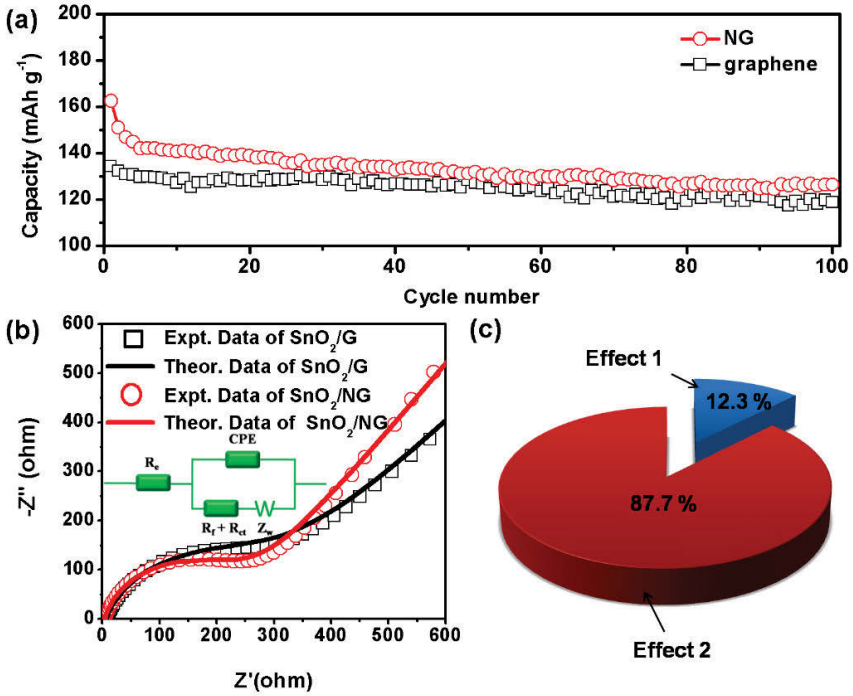


**Figure 4.13** (a) Cycling performance of graphene and NG at a current of 20 mA $g^{-1}$. (b) The Nyquist plots of the $SnO_2$/G and $SnO_2$/NG electrode, the inset shows the modeled equivalent circuit. (c) Contribution of different nitrogen-doping effects to the overall electrochemical performance enhancement of $SnO_2$/NG nanohybrids for SIBs compared to $SnO_2$/G, where Effect 1 is the increased electro-active sites within graphene matrix due to the nitrogen-doping and Effect 2 is the improved electron transfer efficiency within the $SnO_2$/NG electrode benefiting from nitrogen-dopants.

We experimentally observe that $SnO_2$/NG exhibits enhanced electrochemical performance for sodium-ion storage compared to the $SnO_2$/G counterpart. The TGA results, TEM analysis, and BET results clearly demonstrate that the electrochemical performance enhancement does not originate from either the loading ratio difference of $SnO_2$ or the morphology effect.

Consequently, it is reasonable to conclude that the nitrogen dopants in the graphene structure contribute to the improved capacity of $SnO_2$/NG compared to the $SnO_2$/G counterpart for $Na^+$ storage. Firstly, it is theoretically and experimentally well known that N substitution can enhance Li-ion storage in pristine graphene by inducing surface defects and introducing heteroatomic N into the graphene structure, which can provide additional sites for $Li^+$ adsorption.[298, 326-329] Similarly, NG matrix in $SnO_2$/NG nanocomposites could be more active for $Na^+$ storage than the graphene matrices in $SnO_2$/G nanohybrids. As evidenced by **Figure 4.13a**, bare NG exhibits an enhanced capacity compared to graphene. In the first cycle, NG delivers a reversible capacity of 163 mA h $g^{-1}$, this value is 29 mA h $g^{-1}$ higher than that of graphene. On the other hand, nitrogen-doping can enhance the electron transport properties of the $SnO_2$/NG electrode, as demonstrated by the Nyquist plots in **Figure 4.13b**. Both Nyquist plots are composed of a depressed semicircle in the moderate frequency region and a straight line in the low frequency region. Normally, the depressed semicircle is attributed to the charge transfer process. Apparently, the semicircle of $SnO_2$/NG is smaller than that of the $SnO_2$/G material, indicating that $SnO_2$/NG composites possess higher electron transfer efficiency. On the other hand, the low-frequency slope angle is 49° for $SnO_2$/NG negative electrode, whereas $SnO_2$/G has a slope angle of 38°. The much steeper straight line in the low frequency region suggests better Na-ion kinetics in $SnO_2$/NG electrodes than in $SnO_2$/G electrodes.[318] The improved Na-ion kinetics could be due to the higher electronegativity of NG than that of graphene.[330] The ac impedance spectra can be modeled by the modified Randles equivalent circuit presented in the inset in **Figure 4.13b**. $R_e$ is the electrolyte resistance, CPE represents constant phase element, $R_f$ is the resistance of the passivation film formed on the surface of the electrode, $R_{ct}$ is the charge-transfer resistance, and $Z_w$ is the Warburg impedance related to the diffusion of $Na^+$ into the bulk of the electrodes. The kinetic

parameters of $SnO_2$/G and $SnO_2$/NG electrodes are shown in **Table 4.1**. The values of $R_e$ and the combined surface film and charge transfer resistance $R_f + R_{ct}$ for the $SnO_2$/NG electrode are 4.6 and 254.8 Ω, which are lower than those for $SnO_2$/G electrodes (6.6 and 301.4 Ω). This indicates that nitrogen-doping of graphene is beneficial for high conductivity to promote electron and charge transfer with low electrolyte resistance.

**Table 4.1** Kinetic parameters of $SnO_2$/G and $SnO_2$/NG electrodes

| Electrode | $R_e$ (Ω) | $R_f + R_{ct}$ (Ω) |
|---|---|---|
| $SnO_2$/G | 6.6 | 301.4 |
| $SnO_2$/NG | 4.6 | 254.8 |

As illustrated by **Figure 4.14**, the improved electron transfer efficiency within the $SnO_2$/NG electrode can be ascribed to the following nitrogen-doping effects: 1) graphitic N can provide a strong n-doping effect, which contributes to the conductivity enhancement.[283, 299, 304, 331] 2) As revealed by the XPS analysis, $SnO_2$ nanocrystals are effectively bonded to NG scaffold. As a result, the electron transfer efficiency at the interface between $SnO_2$ and matrix is improved because a good adhesion and electrical contact between $SnO_2$ and NG is achieved. Both the increased electro-active sites within graphene matrix and the improved electron transfer efficiency due to nitrogen-doping make $SnO_2$/NG favorable for electrochemical $Na^+$ storage compared to $SnO_2$/G. However, taking account of the NG weight ratio in the as-prepared $SnO_2$/NG nanohybrids, the increased electro-active sites within graphene matrix due to nitrogen-doping only have a contribution of 14 mA h $g^{-1}$ (29 mA h $g^{-1}$ * $W_{NG}$ = 14 mA h $g^{-1}$, where $W_{NG}$ is the weight ratio of NG in the composite), which accounts for 12.3 % of

the overall capacity enhancement of the $SnO_2$/NG electrode compared to the $SnO_2$/G counterpart (114 mA h $g^{-1}$), as depicted in **Figure 4.13c**. Consequently, the important role of nitrogen-doping should lie in improving the electron transfer efficiency within the $SnO_2$/NG electrode during sodiation/de-sodiation processes.

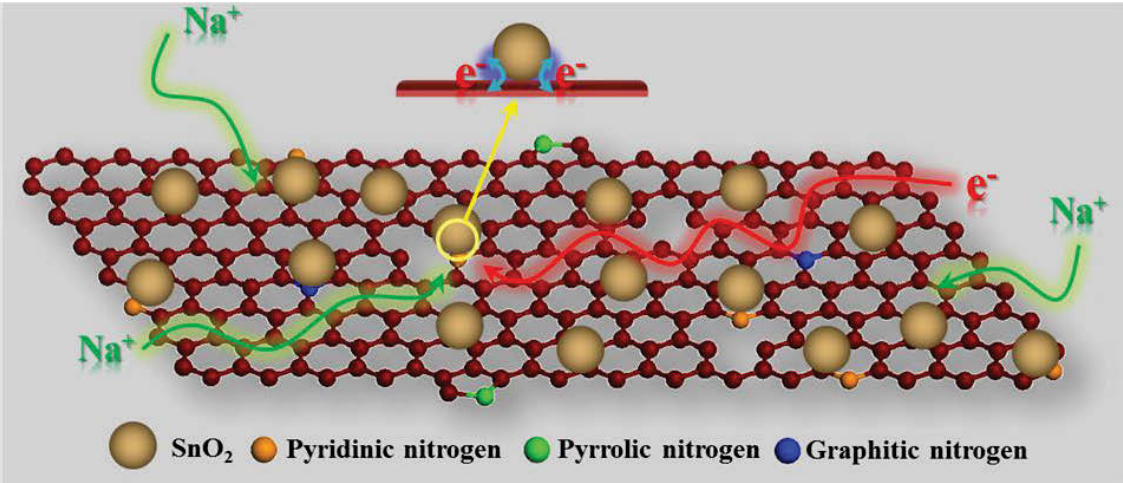


**Figure 4.14** $SnO_2$/NG nanohybrids as anode materials for SIBs.

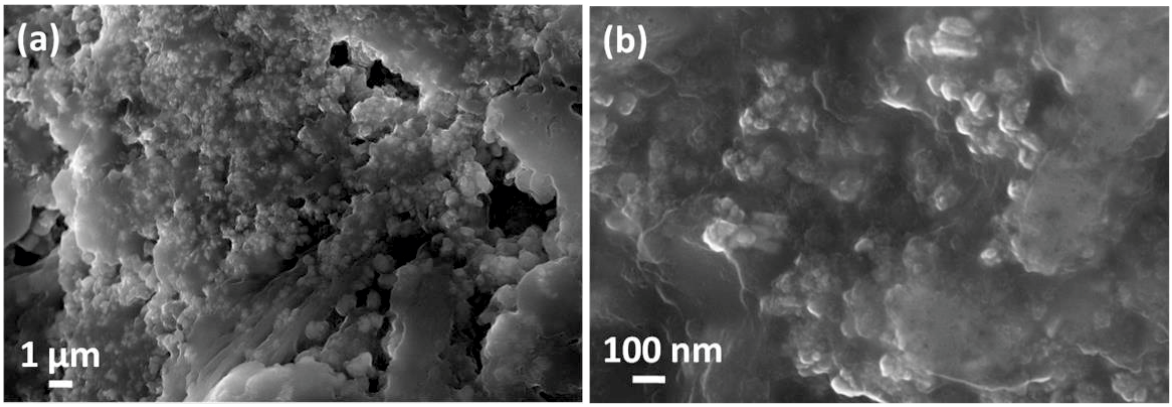


**Figure 4.15** SEM images of $SnO_2$/NG electrode after 100 cycles.

We carried out post-mortem SEM analysis on a $SnO_2$/NG electrode to check the integrity of the electrode. **Figure 4.15** shows the SEM images of the $SnO_2$/NG composite electrode after 100 cycles. Neither pulverization nor peeling off of $SnO_2$ can be observed due to the small

size of $SnO_2$ nanoparticles and the mechanical resilience of NG nanosheets, which can effectively buffer the big volume expansion during repeated charge/discharge processes. As a result, $SnO_2$/NG composites show good cycling stability as anode materials for SIBs.

### 4.4 Conclusions

In summary, $SnO_2$/NG nanohybrids have been successfully prepared by a facile hydrothermal method using urea as nitrogen-doping agents. The as-synthesized $SnO_2$/NG material contains ultrafine $SnO_2$ nanocrystals with an average particle size of 4.7 nm. When applied as anode material for sodium-ion batteries, the as-prepared $SnO_2$/NG nanohybrids exhibit an enhanced electrochemical performance for SIBs compared to the $SnO_2$/G counterpart. A comparison between $SnO_2$/NG nanohybrids and the $SnO_2$/G counterpart has been conducted in a reasonable framework to manifest the inherent nitrogen-doping effects for the enhancement of sodium-ion storage performance. It is found that although nitrogen-doping can improve the $Na^+$ storage capacity within the graphene networks by increasing electro-active sites, its contribution to the overall electrochemical performance enhancement of the $SnO_2$/NG compared to the $SnO_2$/G counterpart is limited. The the improvement of the electron transfer efficiency within the electrode due to nitrogen-doping plays the major role for the enhancement of the electro-activity of $SnO_2$/NG. This work highlights that nitrogen-dopants in graphene networks can effectively mediate the electron transfer between $SnO_2$ and NG, thereby offering fundamental concepts to rationally design graphene-based electrode materials with higher performance for SIBs.

# Chapter 5 $MoS_2$/Graphene Composite Anodes with Enhanced Performance for Sodium Ion Batteries: the Role of the Two-dimensional Heterointerface

## 5.1 Introduction

Two-dimensional (2D) layered metal sulfides (LMSs) with analogous structures to graphite, such as $MoS_2$,[237, 332, 333] $WS_2$,[334] SnS,[290, 335] and $SnS_2$,[241, 289] have been reported as potential electrode materials for SIBs. The open framework of these type of materials allows $Na^+$ to insert reversibly with acceptable mobilities. However, the further application of 2D LMSs is impeded by their inherent limitations. Firstly, these semiconductor metal sulfides have inherently low electronic conductivity, which affects their electrochemical performances for $Na^+$ storage. Secondly, owing to the high surface energy and interlayer van der Waals attractions,[336, 337] these thermally unstable 2D nanomaterials have a tendency to re-stack to minimize the surface energy. Furthermore, the significant volume change and mechanical stress concomitant with sodium ion insertion and extraction can induce the failure of the electrode and the loss of contact between active materials and the current collector, resulting in poor cycling stability.

Graphene has established itself as a promising candidate to circumvent these challenges. For example, $WS_2$/graphene,[334] SnS/graphene,[290] and $SnS_2$/graphene[241, 289] nanocomposites have already been successfully applied as anode materials for SIBs, showing a synergistic effect for sodium-ion storage, including improved capacity, rate capability, and cycling stability. In these reports, it is generally recognized that the enhanced electrochemical performances are attributed to the good electronic conductivity and mechanical resilience of graphene as 2D conformal building blocks for these layered sulfides. However, a fundamental understanding of the exact interaction mechanism between LMSs and graphene for improving the

electrochemical $Na^+$ storage performance is still unavailable. The heterointerface between LMSs and graphene has proven to be able to contribute to novel properties and new functionalities that cannot be achieved by individual constituting materials.[338-346] Therefore, investigations of the role of the heterointerface played in the sodium-ion storage in LMSs/graphene composites could enhance the in-depth understanding of the synergistic effects between LMSs and graphene. In comparison to other interfacial contact manners in the LMSs/graphene composites, such as point contact in particles/graphene nanocomposites[137] and line contact in nanotubes/graphene nanocomposites[347], 2D face contact constructed by assembling 2D LMS nanosheets on the surface of graphene nanosheets has received considerable attention recently.[348-350] Since this sheet-on-sheet structure can provide larger interfacial areas, it is more beneficial for studying the role of heterointerfaces for sodium-ion storage in LMSs/graphene composites.

In this chapter, by taking $MoS_2$ as a typical example, we established the correlations between the 2D heterointerface and the sodium-ion storage performance of LMSs/graphene composites. $MoS_2$/reduced graphene oxide (RGO) nanocomposites were prepared by a facile hydrothermal method using phosphomolybdic acid, L-cysteine and GO as precursors, by which the sheet-on-sheet $MoS_2$/RGO nanocomposites can be formed and the agglomeration of $MoS_2$ and RGO was suppressed simultaneously. Besides, the $MoS_2$/RGO nanocomposites with different $MoS_2$/RGO heterointerfacial areas were obtained by changing the ratio of $MoS_2$ to RGO and applied as anode materials electrode materials to investigate the role of the 2D $MoS_2$/graphene heterointerface for $Na^+$ storage. It is found that the synergistic effect contributing to the enhanced reversible capacity of $MoS_2$/RGO nanocomposites is closely related to the heterointerfacial area. First-principles calculations were performed to

investigate Na atoms adsorption and diffusion on $MoS_2$ and the $MoS_2$/graphene heterointerface, respectively. The corresponding band structure of $MoS_2$ and the $MoS_2$/graphene heterointerface and electron transfer between Na atoms and $MoS_2$ or the $MoS_2$/graphene heterointerface were also considered. The computational results demonstrate that Na prefers to be adsorbed on $MoS_2$ in the $MoS_2$/graphene heterostructure (Na/$MoS_2$/graphene) rather than intercalate into the $MoS_2$/graphene heterointerface ($MoS_2$/Na/graphene). Moreover, the 2D $MoS_2$/graphene heterointerface can significantly increase the conductivity of $MoS_2$, and capture more Na atoms, while maintaining high diffusion mobility of Na atoms on the $MoS_2$ surface and high electron transfer efficiency from Na to $MoS_2$. This work could not only enrich the functionalities of the $MoS_2$/graphene heterostructure, but also clarify the synergistic effect between $MoS_2$ and graphene for the enhancement of electrochemical Na-ion storage in $MoS_2$/RGO composites. The outcomes can facilitate the rational design of other 2D TMSs/graphene nanoassemblies as high performance electrode materials for Na-ion batteries.

## 5.2 Experimental Section

### 5.2.1 Sample preparation

Graphene oxide (GO) nanosheets were synthesized from natural graphite powders by a modified Hummers' method.[305] The $MoS_2$/RGO nanocomposite was then produced by a hydrothermal method. In a typical synthesis process, PMA was mixed with 20 mL GO aqueous suspension (1 mg $mL^{-1}$) by ultrasonication using a Brandson Digital Sonifer (S450D, 40% amplitude). After ultrasonication for 0.5 h, L-cysteine was added and mechanically stirred for another 0.5 h. For the preparation of MG-1, MG-2, and MG-3, the concentrations

of PMA were 0.81 mg $mL^{-1}$, 1.15 mg $mL^{-1}$, and 1.62 mg $mL^{-1}$, respectively, where the concentration of L-cysteine was fixed to 50 mg $mL^{-1}$. Then, the mixed precursor solution was heated to 200 °C in a Teflon-lined autoclave (25 mL in capacity) and maintained at 200 °C for 24 h. The precipitates were collected, and washed with distilled water and ethanol several times. The products were collected after drying at 60 °C in a vacuum oven overnight and then annealed at 800 °C for 2h in Argon atmosphere.

### 5.2.2 Structural and physical characterization

The crystal structure and phases of the as-prepared materials were characterized by X-ray diffraction (XRD, Siemens D5000) using Cu Kα radiation with a scanning step of 0.02° $sec^{-1}$. The morphology was analyzed by field emission scanning electron microscopy (FESEM, Zeiss Supra 55VP). The details of the morphology were further characterized by transmission electron microscopy (TEM) and high-resolution TEM (HRTEM, JEOL JEM-2011). The elemental analysis was conducted on Zeiss EVO MA 15 SEM equipped with an energy-dispersive X-ray spectrometer (EDX). The $MoS_2$ loading mass was measured using a TGA/differential thermal analysis (DTA) analyzer (TA Instruments, SDT 2960 module, New Castle, DE, USA) at a heating rate of 10 °C $min^{-1}$ in air from room temperature to 600 ºC. Raman spectra were collected with a Renishaw inVia Raman spectrometer system (Gloucestershire, UK) equipped with a Leica DMLB microscope (Wetzlar, Germany) and a Renishaw He-Ne laser source producing 17 mW at 633 nm.

### 5.2.3 Cell assembly and electrochemical testing

The electrodes were prepared by dispersing the as-prepared material (70 wt %), carbon black (20 wt %), and poly (vinylidene fluoride) binder (PVDF, 10 wt %) in N-methyl-2-pyrrolidone

(NMP) to form a slurry. The resultant slurry was pasted onto copper foil using a doctor blade and dried in a vacuum oven for 12 h, followed by pressing at 200 kg $cm^{-2}$. The mass of each electrode was around 1.0 mg $cm^{-2}$. Electrochemical measurements were carried out using two-electrode coin cells with Na metal as counter and reference electrode and glass microfiber (Whatman) as the separator. The CR2032-type coin cells were assembled in an argon-filled glove box (UniLab, Mbraun, Germany). The electrolyte solution was 1 M $NaClO_4$ dissolved in a mixture of ethylene carbonate (EC) and propylene carbonate (PC) with a volume ratio of 1:1. The charge-discharge measurements were performed at different current densities in the voltage range from 0.01 to 3 V *vs.* $Na^+/Na$ using a computer-controlled Neware Battery Testing system. For the $MoS_2$/graphene electrode, the obtained specific capacities are based on the total mass of $MoS_2$/graphene nanocomposite. Cyclic voltammetry (CV) was conducted by using a CHI 660C electrochemical workstation between 0.01 and 3 V *vs.* $Na^+/Na$ with a scan rate of 0.1 mV $s^{-1}$. For the electrochemical impedance spectroscopy (EIS), the excitation amplitude applied to the cells was 5 mV.

### 5.2.4 DFT calculations

The spin–unrestricted DFT calculations were carried out by using a $Dmol^3$ package.[351] Exchange–correlation functions are taken as generalized gradient approximation (GGA) with Perdew–Burke–Ernzerhof (PBE).[352] DFT semicorepseudopotentials (DSPPs) core treatment was implemented for relativistic effects, which replaced core electrons by a single effective potential. Double numerical plus polarization (DNP) was employed as the basis set. The convergence tolerance of energy of $10^{-5}$ Hartree was taken (1Hartree = 27.21 eV), and the maximal allowed force and displacement were 0.002 Hartree/Å and 0.005 Å, respectively.

In the simulation, three-dimensional periodic boundary conditions were taken. The simulation cell consisted of a 4 × 4 $MoS_2$ supercell. The *k*–point was set to 5 × 5 × 1, and all atoms were allowed to relax according to previous reports. After structure relaxations, the density of states (DOS) and band structure were calculated with a finer *k*–point grid of 15 × 15 × 1. The DFT+D method within the Grimme scheme was used in all calculations to consider the van der Waals forces,[353] and 18 Å vacuum over the $MoS_2$ layer or $MoS_2$/graphene was taken to minimize the interlayer interactions. For the diffusion of Na atoms on monolayer $MoS_2$, double layer $MoS_2$ and $MoS_2$/graphene, LST/QST and NEB tools in the DMOL$^3$ code were employed.

The adsorption energy ($E_{ad}$) of the Na atom on $MoS_2$ can be defined as follows:

$$E_{ad} = E_{MoS2+Na} - (E_{MoS2} + E_{Na}) \qquad (5\text{-}1)$$

where $E_{MoS2+Na}$, $E_{MoS2}$ and $E_{Na}$ are the total energies of monolayer $MoS_2$ with one Na atom adsorbed, monolayer $MoS_2$ and one Na atom in the same slab, respectively.

The interaction energy $E_{int}$ between $MoS_2$ and graphene layers can be determined by the equation:

$$E_{int} = E_{MoS2+graphene} - (E_{MoS2} + E_{graphene}) \qquad (5\text{-}2)$$

where $E_{MoS2+graphene}$, $E_{MoS2}$ and $E_{graphene}$ are the total energies of $MoS_2$/graphene bilayer structure, monolayer $MoS_2$and monolayer graphene in the same slab, respectively.

The adsorption energy $E_{ad}$ of the Na atom on $MoS_2$/graphene bilayer structure can be calculated by the equation:

$$E_{ad} = E_{MoS2/graphene+Na} - (E_{MoS2/graphene} + E_{Na}) \quad (5\text{-}3)$$

where $E_{MoS2/graphene+Na}$ is the total energies of the $MoS_2$/graphene structure with one Na atom adsorbed.

### 5.3 Results and Discussions

$MoS_2$/RGO nanocomposites have been synthesized as anode materials for Na-ion batteries by incorporating RGO with pre-synthesized $MoS_2$.[234, 292] However, in order to realize the functionalities of the 2D $MoS_2$/graphene heterointerface, it is required to prepare high-quality electrical contact between $MoS_2$ and RGO. Sheet-on-sheet structured $MoS_2$/RGO composites with controllable heterointerfaces were synthesized by a hydrothermal method, followed by a calcination process (as shown in Figure 5.1). GO is highly dispersible in water due to the existence of hydrophilic groups (hydroxyl, carboxyl and epoxy groups), which makes it a favorable precursor for the aqueous synthesis of RGO-based nanoarchitectures. Phosphomolybdic acid ($H_3PMo_{12}O_{40}$•$xH_2O$, PMA) is used as molybdenum precursor. In the first step, GO aqueous suspension was mixed with PMA and L-cysteine by mechanical stirring at room temperature. The PMA molecule is abundant in oxygen-containing functional groups and double bonds (see the molecular structure model of PMA in Figure 5.2), which can be attracted to graphene oxide through the noncovalent hydrogen bonds and the π-π interaction between the double bond in PMA and the conjugated RGO basal planes (Figure 5.1b). The PMA/L-cysteine/GO mixture was then transferred to an autoclave and subjected to hydrothermal treatment at 200 °C for 24 h. The oxygenated functional groups on the GO surface can act as nucleation sites for $MoS_2$, leading to the formation of $MoS_2$

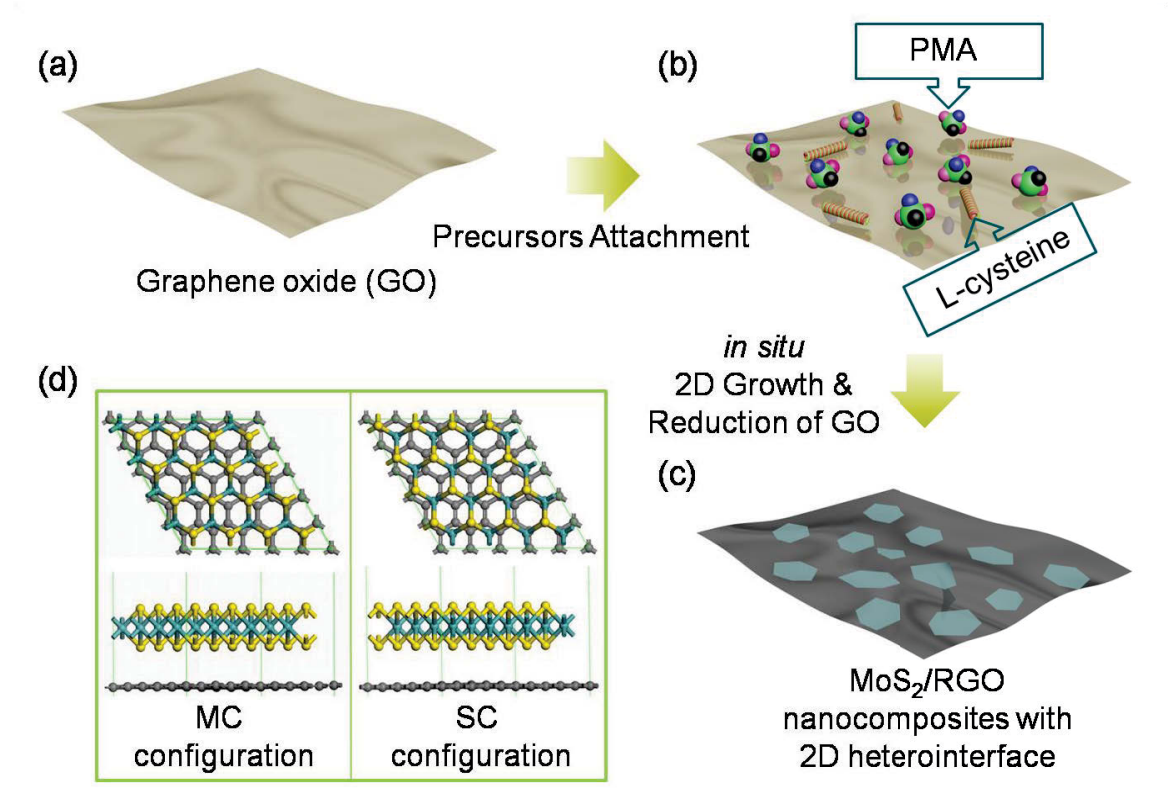


**Figure 5.1** Schematic illustration for the preparation of $MoS_2$/RGO heterostructures. As shown in (d), there are two possible stacking configurations: MC (Mo on top of C atoms) and SC (S on top of C atoms) configurations. The yellow, green and grey atoms represent S, Mo and C atoms, respectively.

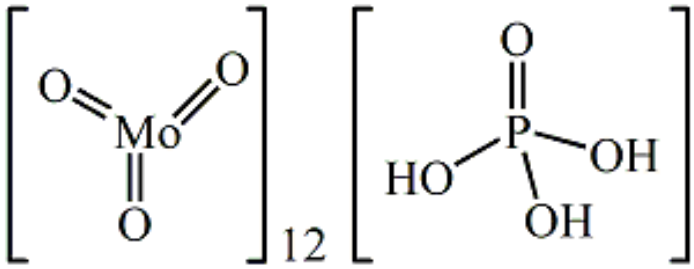


**Figure 5.2** Molecular structure of phosphomolybdic acid (PMA).

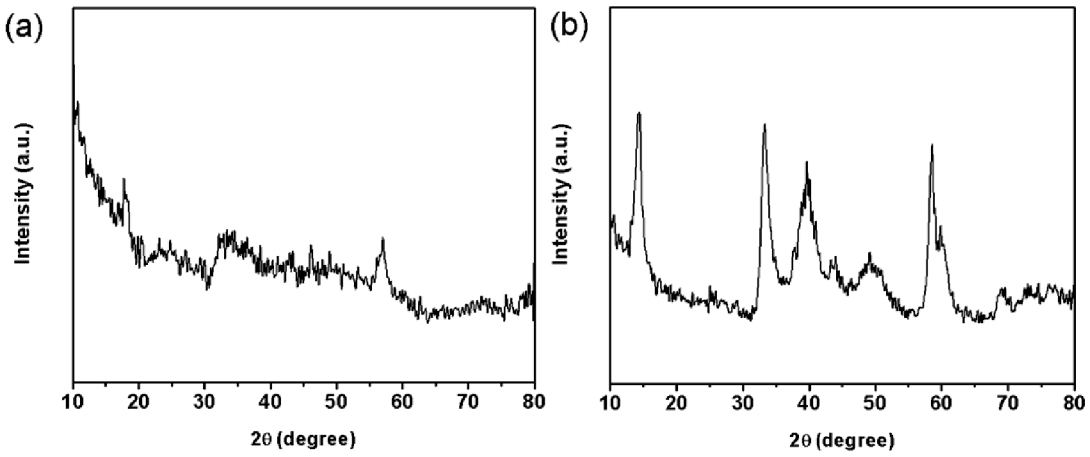


**Figure 5.3** XRD patterns of MG-3 composites before and after post-treatment.

crystal nucleus on the RGO surface.[354] Under hydrothermal conditions, PMA is transformed in situ to the $MoS_2$ nucleus in the presence of L-cysteine. Simultaneously, GO is reduced to RGO by $H_2S$ released from L-cysteine. L-cysteine could form a polymeric network structure under the solution-phase reaction, which facilitated the formation of a two-dimensional structure for the $MoS_2$.[355] The following crystal growth leads to the formation of 2D $MoS_2$ nanosheets covering the RGO basal plane, creating $MoS_2$/graphene heterointerfaces (Figures 5.1c). $MoS_2$/RGO composites were then subjected to high temperature calcination at 800 $^oC$ under Ar atmosphere, which further enhances the interfacial interaction between $MoS_2$ and RGO by increasing the crystallinity of $MoS_2$ (Figure 5.3) and reducing the residual oxygen moieties (Table 5.1). By increasing the stock of PMA, the weight ratio of $MoS_2$ and RGO can be tuned. In this way, three $MoS_2$/RGO composites with different $MoS_2$ to RGO ratios were prepared (denoted as MG-x, x = 1, 2, 3). As shown in Figure 5.1d, there are two possible $MoS_2$/graphene heterostructures: MC (Mo on the top of C atoms) and SC (S on the top of C atoms) structures. The total energy of the MC structure is only 11.8 meV $C^{-1}$, which is lower than that of SC, suggesting that both of the two structures are possible. The distances between

$MoS_2$ and graphene layers in MC and SC bilayers are 3.35 and 3.36 Å, respectively. The theoretical interaction energy between $MoS_2$ and graphene layers ($E_{int}$) is calculated to be -0.02 and -0.01 eV $C^{-1}$ for MC and SC bilayers, respectively, indicating the weak van der Waals interaction between $MoS_2$ and graphene.

**Table 5.1** Elemental composition obtained by EDX analysis of the MG-3 composites before and after post-treatment.

| Sample | Element | Weight percentage (%) | Atomic percentage (%) |
|---|---|---|---|
| Before calcination | C | 37.39 | 66.87 |
| | O | 6.10 | 8.19 |
| | Mo | 28.98 | 6.49 |
| | S | 27.54 | 18.45 |
| After calcination | C | 42.71 | 73.99 |
| | O | 4.25 | 5.53 |
| | Mo | 32.27 | 7.00 |
| | S | 20.77 | 13.48 |

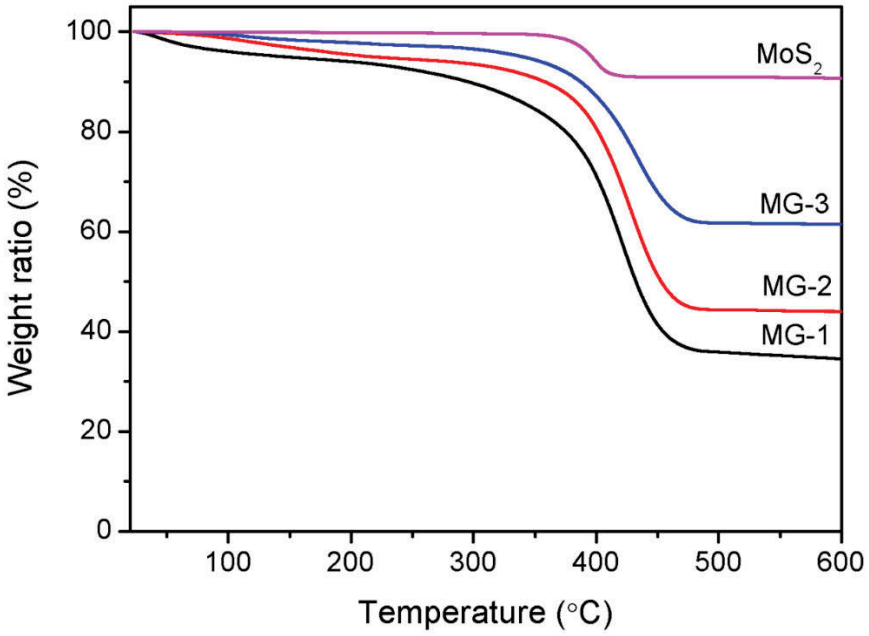


**Figure 5.4** TGA curves of $MoS_2$, MG-1, MG-2, and MG-3.

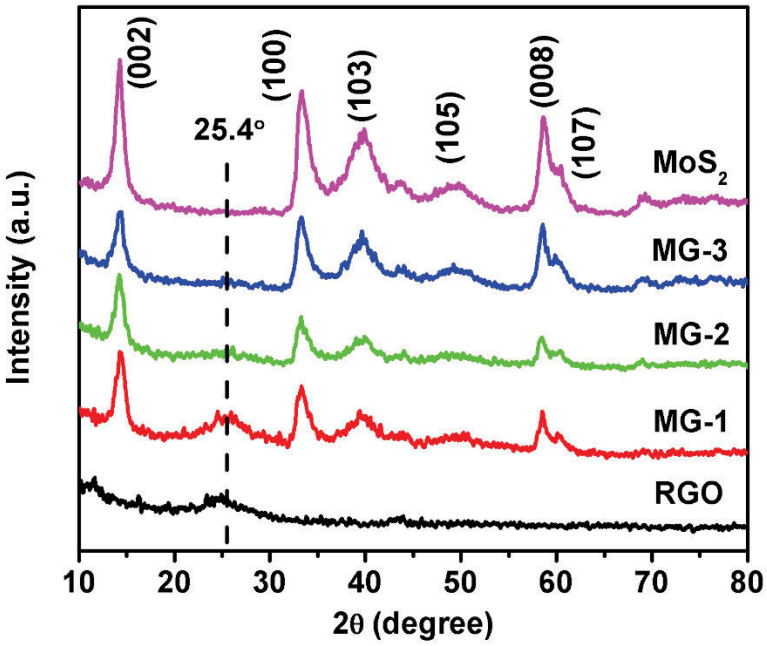


**Figure 5.5** XRD patterns of RGO, MG-1, MG-2, MG-3, and $MoS_2$.

By thermogravimetric analysis (TGA), the $MoS_2$ weight ratios in MG-x composites were determined to be 44.2% (MG-1), 49% (MG-2), and 68.7% (MG-3), respectively (as shown in **Figure 5.4**). **Figure 5.5** shows the X-ray diffraction (XRD) patterns of bare RGO, $MoS_2$

and the as-prepared MG-x samples. For bare RGO, a broad peak at 25.4° is discernable, which is the characteristic peak due to the random re-stacking of graphene layers during hydrothermal synthesis. However, for $MoS_2$/RGO composites, the intensity of the RGO diffraction peak decreased and disappeared with the increase of the $MoS_2$ ratio, suggesting that the percentage of $MoS_2$ in the MG-x samples is crucial for preventing the aggregation of RGO layers. It is clearly indicated that 2H-$MoS_2$ phases have formed in all of these samples as evidenced by peaks at 14.4°, 32.8°, 39.5°, 49.8°, 58.3° and 60.1°. The diffraction peaks correspond to the (002), (100), (103), (105), (110) and (008) planes of 2H-$MoS_2$ (JCPDS card number 37-1492). 2H-$MoS_2$ is structural analog of graphene, the basal (002) crystal planes of which are held together by van der Waals forces along *c*-axis. It should be noted that the intensity ratio of (002) and (100) peak of $MoS_2$ nanosheets ($I_{(002)}/I_{(100)}$) varies according to $MoS_2$ ratio, which decreases in the order MG-1 (2.67) > MG-2 (2.16) > MG-3 (1.30). Therefore, the (002) plane growth of $MoS_2$ crystals is restrained due to the incorporation of RGO in MG-x nanocomposites. The disappearance of the RGO (002) peak and the decrease of the $MoS_2$ (002) peak indicate the evolution of the $MoS_2$/RGO heterointerface with the increase of the $MoS_2$ ratio.

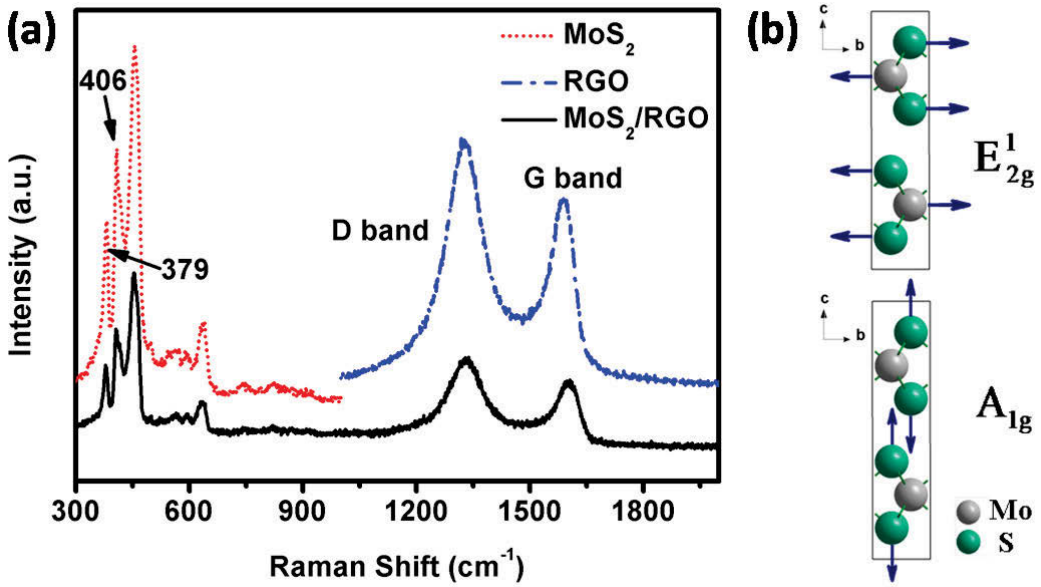


**Figure 5.6** (a) Raman spectra of $MoS_2$, RGO and MG-3, showing a set of $MoS_2$ Raman peaks together with D band and G band of RGO. (b) Schematic illustration of $E^1_{2g}$ and $A_{1g}$ vibration models.

Raman spectroscopy measurement was employed for further analysis of the as-obtained products, as shown in **Figure 5.6**. Bare RGO exhibits two typical peaks at 1326 $cm^{-1}$ and 1594 $cm^{-1}$, which are known as the D band and G band, respectively. With regard to MG-3 nanocomposites, a set of Raman peaks in the range of 300-1000 $cm^{-1}$ can be observed along with the RGO peaks, which originate from different Raman shift modes of the $MoS_2$ component. Specifically, the MG-3 displays Raman features at 379 $cm^{-1}$ and 406 $cm^{-1}$, which can be attributed to $E^1_{2g}$ and $A_{1g}$ vibration of $MoS_2$ nanosheets. The $E^1_{2g}$ Raman peak is associated with planar vibration and $A_{1g}$ is ascribed to the vibration of sulfides in the out-of-plane direction as illustrated in **Figure 5.6b**.

**Table 5.2** Elemental composition obtained by EDX analysis of the MG-x composites

| Sample | Element | Weight percentage (%) | Atomic percentage (%) |
|---|---|---|---|
| MG-1 | C | 58.75 | 79.41 |
| | O | 12.02 | 12.19 |
| | Mo | 18.98 | 3.21 |
| | S | 10.25 | 5.19 |
| MG-2 | C | 54.47 | 79.89 |
| | O | 7.24 | 7.98 |
| | Mo | 24.32 | 4.46 |
| | S | 13.97 | 7.67 |
| MG-3 | C | 42.71 | 73.99 |
| | O | 4.25 | 5.53 |
| | Mo | 32.27 | 7.00 |
| | S | 20.77 | 13.48 |

By using energy-dispersive X-ray (EDX) spectroscopy, the O/C atomic ratio in MG-1, MG-2, and MG-3 is 0.15, 0.10, and 0.07, respectively (**Table 5.2**).

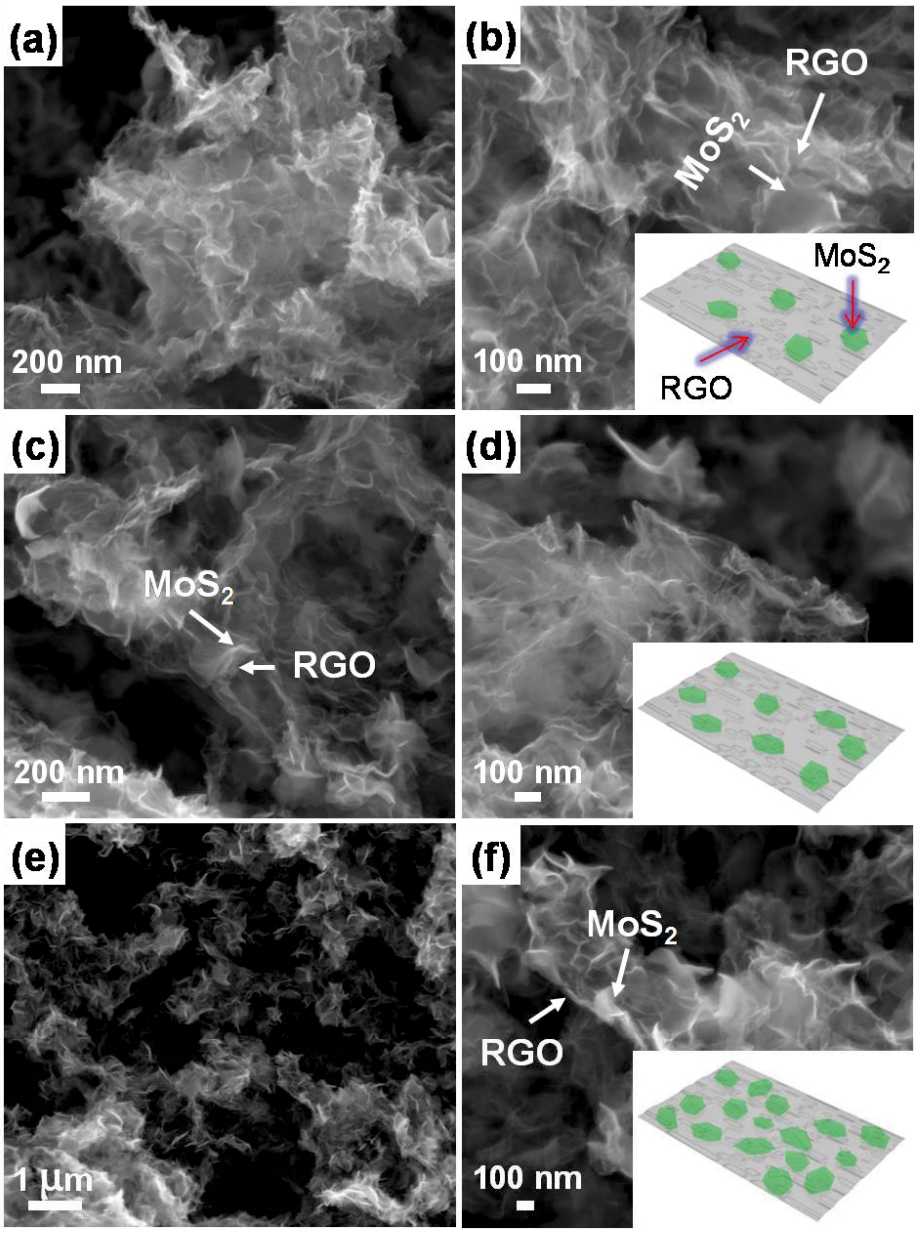


**Figure 5.7** SEM images of MG-1 (a and b), MG-2 (c and d), and MG-3 (e and f), showing the microstructural features of the nanocomposites, the inserts show the corresponding schematic illustrations of the composites.

The microstructure of MG-x heterostructures were analyzed by scanning electron microscopy (SEM) and transmission electron microscopy (TEM). **Figure 5.7** shows the SEM images of MG-x, providing a general view of the morphology over a large scale. Bare $MoS_2$ obtained from the same experimental procedure without RGO tends to aggregate due to the

high surface energy and interlayer van der Waals attraction,[336, 356] leading to the formation of three-dimensional flower-like agglomerations assembled by $MoS_2$ nanosheets (**Figure 5.8**). With the presence of RGO in the mixture, the MG-x composites show a curved thin flaky morphology as shown in **Figure 5.7**, which is composed of $MoS_2$ nanosheets grown parallel to RGO. The morphology is different from the previously reported $MoS_2$/RGO nanoarchitectures prepared from either $Na_2MoO_4$ or $(NH_4)_2MoS_4$ as Mo-source, where $MoS_2$ nanoparticles formed.[137, 354, 357] No $MoS_2$ agglomerations were formed in the MG-x composites, which suggests that RGO can stabilize $MoS_2$ nanosheets. The formation of separated $MoS_2$ nanosheets is favorable for the accessibility of reaction sites for $Na^+$. Moreover, as shown in **Figure 5.7b, c, and f**, $MoS_2$ ingredient has an intimate contact with RGO and no isolated $MoS_2$ was observed in all the three MG-x nanocomposites. With the increase of the ratio of $MoS_2$, the coverage of $MoS_2$ nanosheets on the RGO matrix increases correspondingly, which is in agreement with the XRD results.

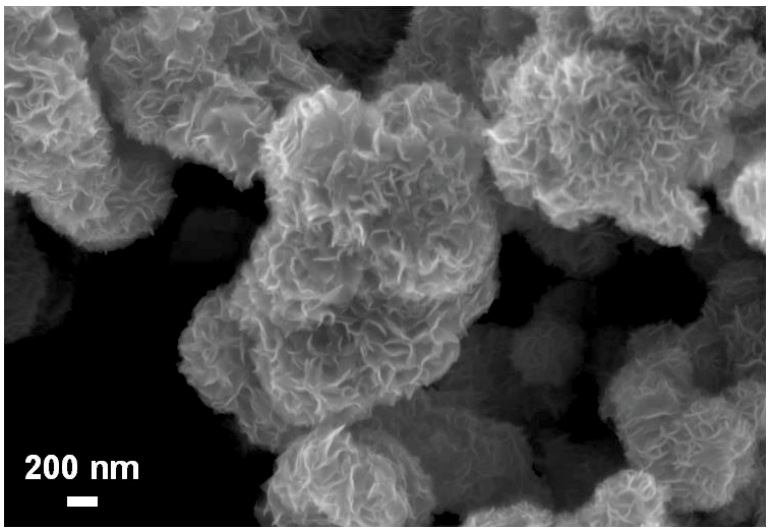


**Figure 5.8** SEM image of bare $MoS_2$.

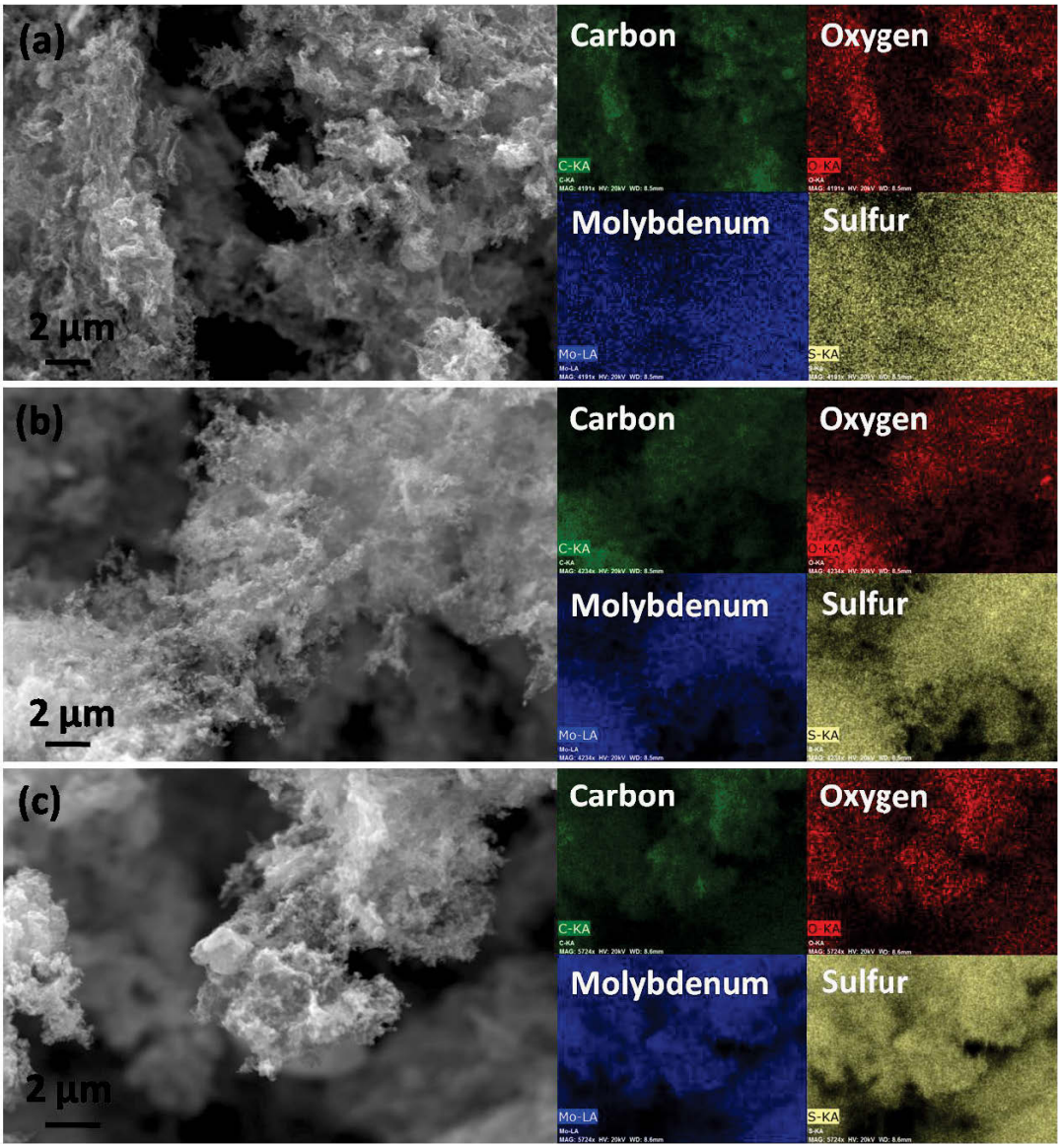


**Figure 5.9** SEM image and the corresponding EDX map of carbon, oxygen, molybdenum and of sulfur MG-1 (a), MG-2 (b), and MG-3 (c).

The elemental mapping images shown in **Figure 5.9** clearly illustrate that $MoS_2$ nanosheets are homogeneously mixed with RGO, no free $MoS_2$ can be found outside of RGO.

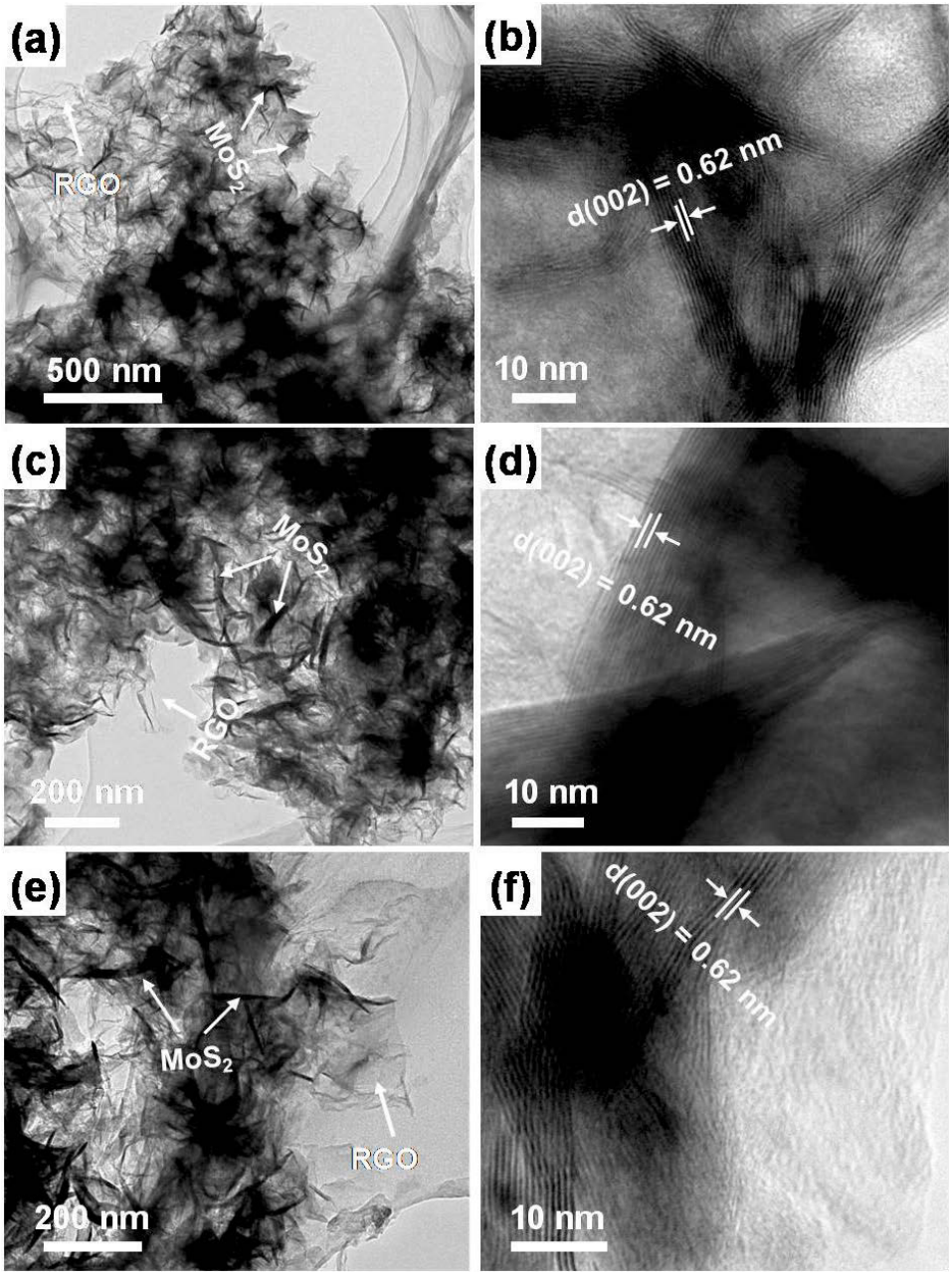


**Figure 5.10** TEM images of MG-x composites. (a, b) MG-1, (c, d) MG-2, and (e, f) MG-3.

The high-resolution TEM (HRTEM) images of the curled edge shown in **Figure 5.10b, d, and f** reveal lattice fringes with an interplanar spacing of 0.62 nm, which can be indexed as the (002) lattice planes of 2H-$MoS_2$. The van der Waals interfacial interaction between RGO and $MoS_2$ is strong enough to firmly bind $MoS_2$ with RGO. Even after long-term ultrasonic dispersion for TEM characterization, $MoS_2$ nanosheets are anchored onto the RGO substrate

and no free $MoS_2$ can be observed (as shown in **Figure 5.10a, c, and e**), indicating the relatively strong interfacial interaction between $MoS_2$ and RGO.

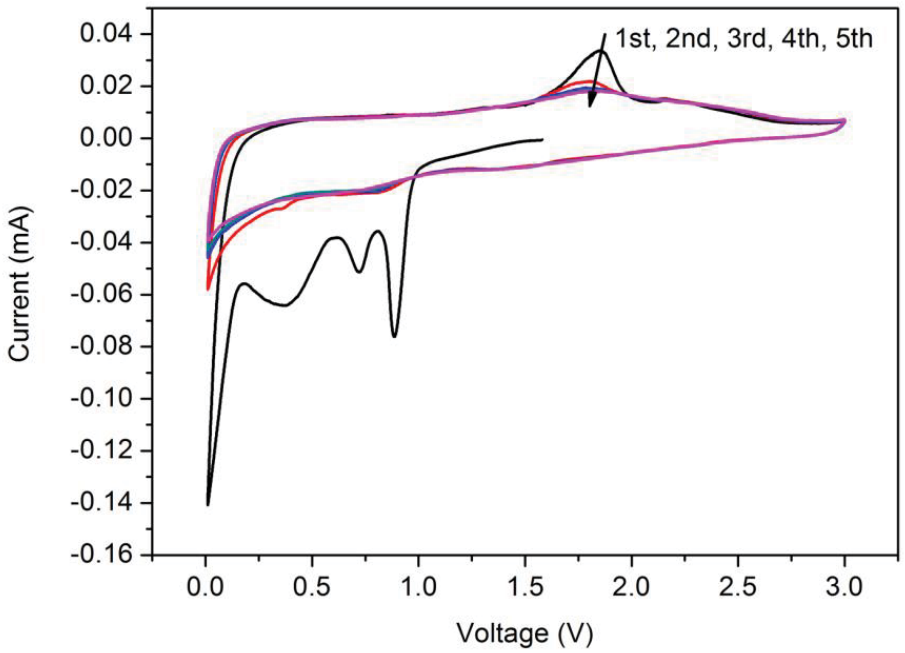


**Figure 5.11** CV curves of MG-3.

**Figure 5.11** depicts the cyclic voltammetry (CV) curves of MG-3 in the voltage range of 0.01-3.0 V. The cathodic peaks at 0.89 V and 0.71 V are ascribed to the two-step insertion of $Na^+$ into $MoS_2$.[233, 332] The broad peak located at 0.35 V could be associated with electrolyte decomposition to form solid electrolyte interphase (SEI) layer and the reversible conversion reaction: $MoS_2 + 4Na^+ + 4e^- \leftrightarrow Mo + 2Na_2S$.[234] According to previous investigations, the SEI is composed of inorganic and organic layers around the particles.[324, 325] The organic layers can form and dissolve reversibly, which contributes to the reversible capacity. On the

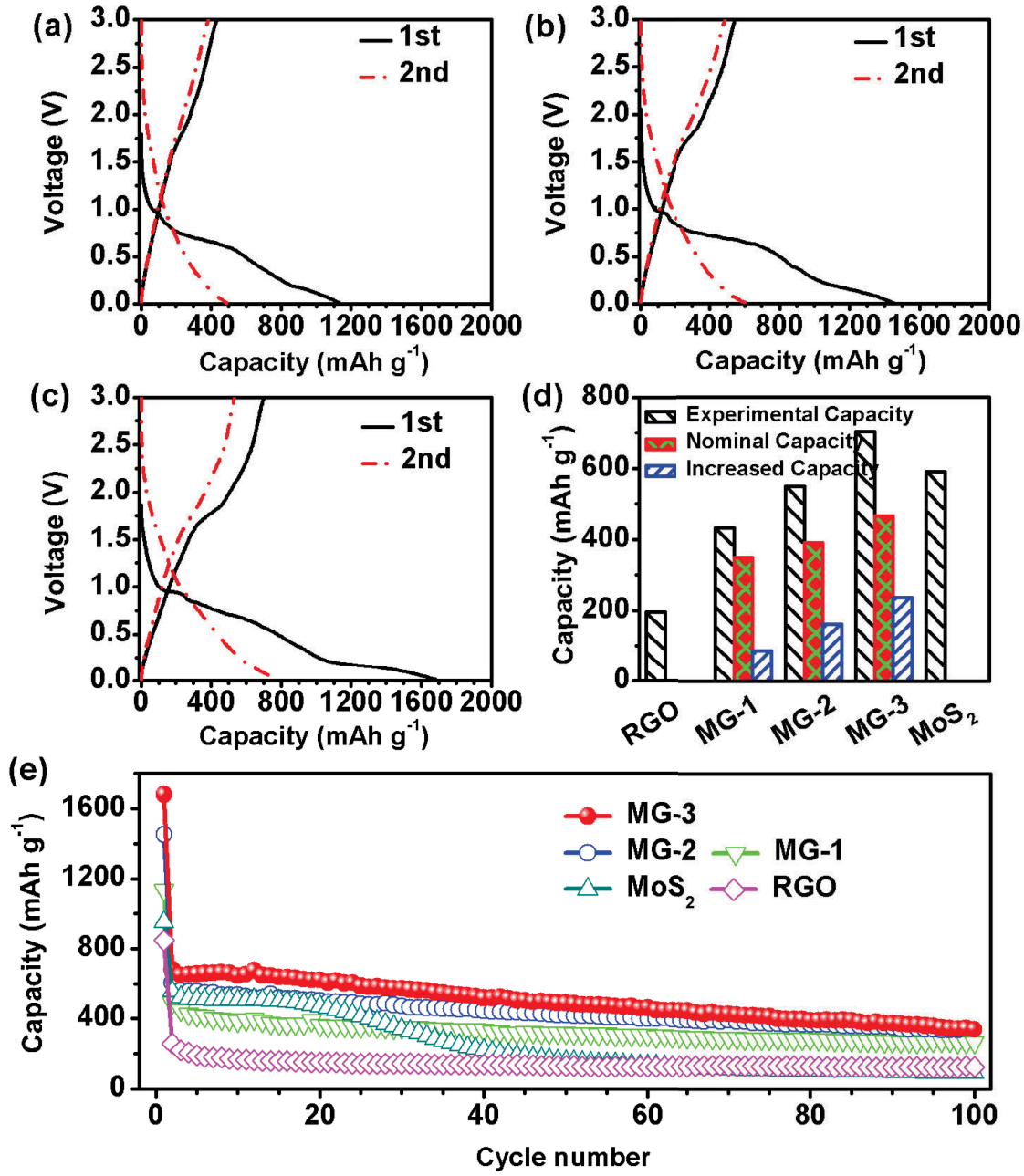


**Figure 5.12** Galvanostatic charge-discharge profiles of MG-1 (a), MG-2 (b), and MG-3 (c). (d) Initial reversible capacities of RGO, MG-x, and $MoS_2$ at a current density of 20 mA $g^{-1}$, and the nominal capacities based on experimental values. The blue bars indicate the increased capacities due to the intimate $MoS_2$/RGO heterointerface. (e) Cycling performance of MG-3, $MoS_2$, and graphene at a current density of 20 mA $g^{-1}$.

contrary, the formation of an inorganic layer is an irreversible process. In addition, a sharp peak at about 0.01 V is found, which can be assigned to the Na-ion insertion into RGO interlayers.[358, 359] From the second cycle, the CV curves overlap perfectly, indicating the high reversibility of the MG-3 electrode. Based on the reversible capacity of bare $MoS_2$ (590 mA h $g^{-1}$) and RGO (195 mA h $g^{-1}$), in combination with their weight ratios in MG-x composites, the nominal capacities of MG-x samples can be calculated as shown in **Figure 5.12d**. The galvanostatic charge-discharge curves of MG-1, MG-2, and MG-3 electrodes at a current density of 20 mA $g^{-1}$ are shown in **Figure 5.12a-c**. In the first discharge process, all of the MG-x samples show two plateaus in the range of 1.1-0.5 V, which are in good agreement with the CV curves, corresponding to the $Na^+$ intercalation processes in $MoS_2$ layers. It is noted that the MG-x electrodes deliver charge capacities lower than the corresponding discharge capacities, which could be ascribed to the irreversible formation of SEI layer. Interestingly, all MG-x samples exhibit reversible capacities exceeding the nominal values (**Figure 5.12d**). In particular, MG-3 having the maximum heterointerfacial areas can deliver a reversible capacity of 702 mAh $g^{-1}$, which is much higher than the nominal value of the total sum ($590 \times 0.687 + 195 \times 0.313 = 466$ mAh $g^{-1}$). This clearly indicates a synergistic effect for the enhancement of $Na^+$ storage capacity, which is beyond the simple principle of superposition between RGO and $MoS_2$. With increasing interfacial contact between RGO and $MoS_2$ (*e.g.* increasing the $MoS_2$ ratio), the enhanced capacity originating from the synergistic effect increases correspondingly. The increased capacities for MG-1, MG-2, and MG-3 electrodes are 84, 160, and 236 mA h $g^{-1}$, respectively. This result strongly suggests the correlation between the 2D heterointerface and the sodium-ion storage in $MoS_2$/RGO composites. This means that the composite with more heterointerfacial areas has higher $Na^+$ storage capacity. The favorable interfacial interaction also leads to a significantly improved

cycling performance of the MG-3 compared with bare $MoS_2$. As can be seen from **Figure 5.12e**, bare $MoS_2$ electrode suffers seriously from a quick decay of capacity. After 100 cycles, $MoS_2$ electrodes only delivered a capacity of 93 mA h $g^{-1}$. This could be due to the significant volume change and mechanical stress during sodium ion insertion/extraction processes, which can induce the failure of the electrode and the loss of contact between active materials and the current collector, resulting in poor cycling stability. For MG-x electrodes, MG-1 with the highest RGO ratio has the best cycling stability, which can maintain 61.3% of the capacity obtained in the second cycle after 100 cycles at a current density of 20 mA $g^{-1}$. The capacity retention of MG-2 nanocomposites with the moderate RGO ratio and MG-3 nanocomposites with the lowest RGO ratio are 61.2% and 49.0%, respectively. This could be ascribed to mechanical resilience of RGO that can effectively buffers the volume change of $MoS_2$ during repeated sodiation/de-sodiation processes.[290]

To gain an in-depth understanding of the role of the $MoS_2$/graphene heterointerfaces on the performance of electrochemical $Na^+$ storage, density functional theory (DFT) calculations using the Dmol$^3$ package[351] have been performed to calculate the adsorption and diffusion behaviors of Na on $MoS_2$ and $MoS_2$/graphene heterointerface. The adsorption behaviour of Na on both monolayer $MoS_2$ and $MoS_2$/graphene heterostructures are considered, with the results summarized in **Table 5.3**. There are three possible positions for Na adsorption on monolayer $MoS_2$, as numbered in **Figure 5.13a**. However, the structure with the Na atom adsorbed at the hollow site of a $MoS_2$ ring (**Figure 5.13b**) has the lowest energy, and it is set to be 0. The adsorption energy of the Na in **Figure 5.13b** is -1.49 eV, which is modest for Na storage and diffusion. Based on Mulliken atomic charge analysis, it is found that the Na atom transfers 0.709 *e* to $MoS_2$, which is promising because more than 2/3 of the valence

**Table 5.3** The total energy of $MoS_2$ and the $MoS_2$/graphene heterostructure with a Na atom adsorbed at representative positions, the corresponding adsorption energy of the Na atom and the charge transferred from Na atom to $MoS_2$ or $MoS_2$/graphene bilayer system are also provided

| | Na Position | Total energy (meV $C^{-1}$) | $E_{ad}$ (eV) | $Q$ (e) |
|---|---|---|---|---|
| $MoS_2$ monolayer | 1 | 0 | -1.49 | 0.709 |
| | 2 | 14.8 | -0.75 | 0.703 |
| | 3* | 0 | -1.49 | 0.709 |
| $MoS_2$/graphene MC | (a) | 0.54 | -2.56 | 0.706 |
| | (b) | 0 | -2.59 | 0.700 |
| | (c) | 0.016 | -2.59 | 0.699 |
| | (d) | 8.29 | -2.18 | 0.866 |
| | (e) | 6.66 | -2.26 | 0.896 |
| | (f) | 3.54 | -2.41 | 0.676 |
| $MoS_2$/graphene SC | (a) | 12.72 | -2.54 | 0.698 |
| | (b) | 12.17 | -2.57 | 0.692 |
| | (c) | 12.20 | -2.57 | 0.692 |
| | (d) | 24.77 | -1.94 | 0.809 |
| | (e) | 21.91 | -2.08 | 0.831 |
| | (f) | 17.55 | -2.30 | 0.698 |

* The Na atom would diffuse to position 1 automatically. 1-3 denote the possible adsorption position of Na atom as shown in Figure 6(a). (a)-(f) denote the corresponding adsorption positions as shown in Fig. 5.13(a)-(f).

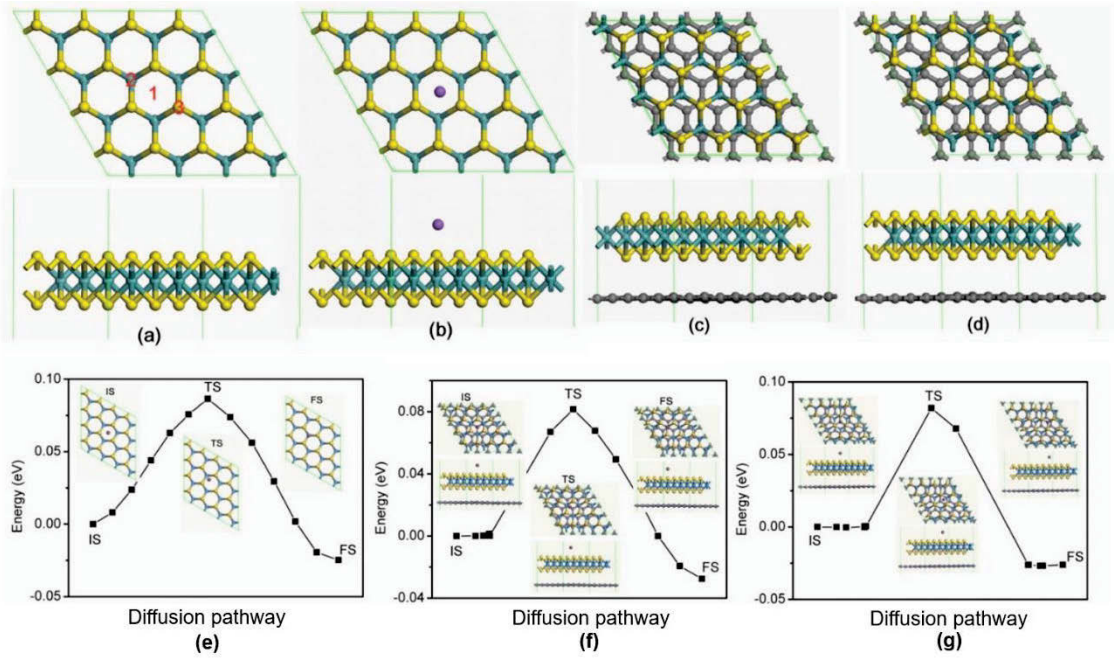


**Figure 5.13** (a) Atomic structure of monolayer $MoS_2$ supercell in the simulation, the numbers denote the possible adsorption position of Na atom. (b) The favorite structure of monolayer $MoS_2$ with a Na atom adsorbed. Configuration of MC bilayer (c) and SC bilayer (d). The energy minimum diffusion pathway of a Na atom on the monolayer $MoS_2$ (e), in MC bilayer (f), and in SC bilayer (g). The inserts in (e, f, and g) show the atomic structure of initial state (IS), transition state (TS) and final state (FS).

electrons can be transferred. The diffusion path of the Na atom on $MoS_2$ from the energy minimum adsorption site 1 to the second energy minimum adsorption site 2 is calculated through linear synchronous transition/quadratic synchronous transit (LST/QST) and nudged elastic band (NEB) methods. The result is shown in **Figure 5.13e**. The atomic structure of the initial state (IS), transition state (TS) and final state (FS) are also provided in this figure. At TS, the Na atom moves from the hollow site of the hexagon towards the top site of a Mo atom, and locates at the bridge site of two S atoms. The diffusion barrier is only ~86 meV, indicating the excellent mobility of Na atom on $MoS_2$.

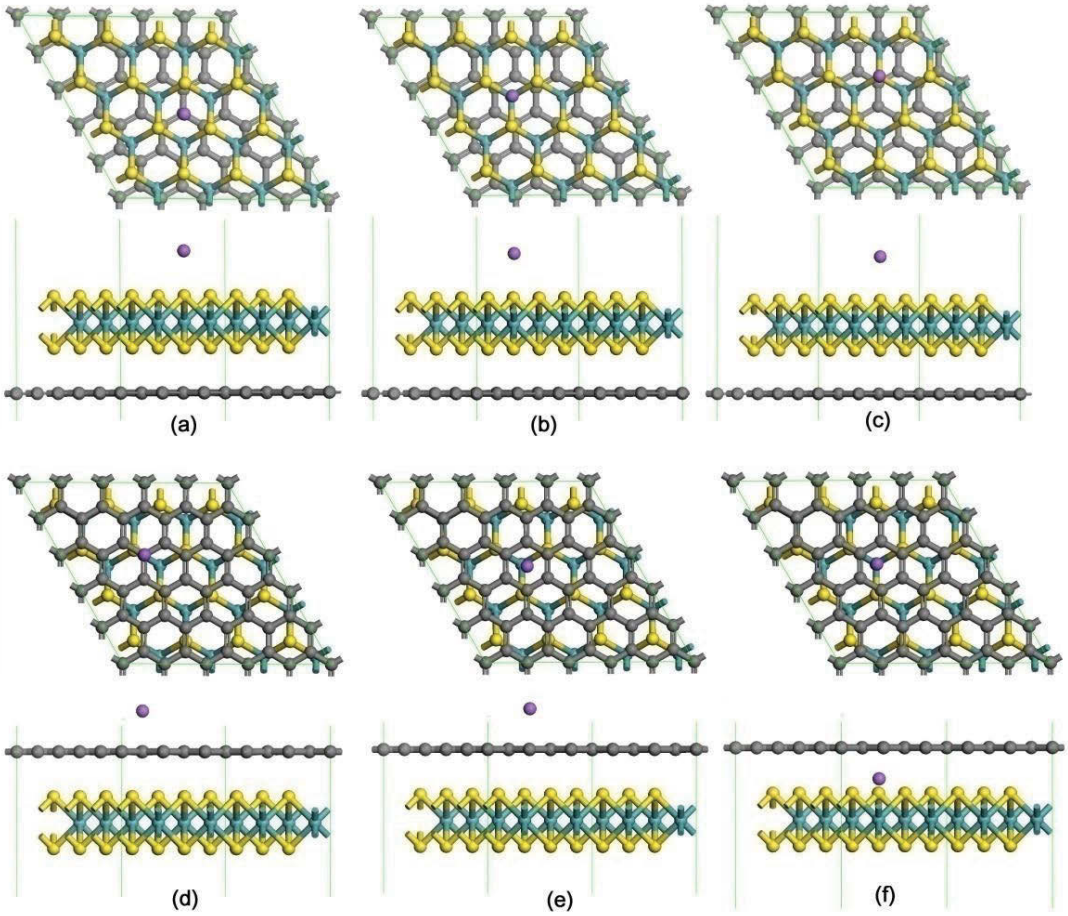


**Figure 5.14** Six representative configurations for a Na atom adsorbed on $MoS_2$/graphene bilayer structure. (a) Na adsorbed on the hollow site of a hexagonal ring over a $MoS_2$ layer, (b) Na adsorbed on the top of a Mo atom over $MoS_2$ layer, (c) Na adsorbed on the top of a S atom over $MoS_2$ layer, (d) Na adsorbed on the top of a C atom over graphene, (e) Na adsorbed on the top of the hollow site of a C ring over graphene, (f) Na adsorbed between graphene and $MoS_2$ layers.

For both MC and SC structured $MoS_2$/graphene heterointerfaces, there are six representative positions for Na adsorption (**Figure 5.14**). The energy of a Na atom adsorbed at the top of a Mo atom (**Figure 5.14b**) is the lowest and set to be 0. Previous investigations show that Li atoms prefer to accommodate themselves between $MoS_2$ and graphene layers.[360] However, it is found that both MC and SC structures with the Na atom adsorbed on the $MoS_2$ surface have the lowest energies, which indicates that the Na atom prefers to be adsorbed on the

$MoS_2$ in the $MoS_2$/graphene heterointerface. Moreover, the presence of graphene changes the adsorption behavior of the Na atom on $MoS_2$. As discussed, the Na atom adsorbed at the hollow site of a $MoS_2$ hexagon ring on the pristine $MoS_2$ monolayer has the lowest energy. On the contrary, our calculation results show that the energy differences for the three different adsorption sites on the $MoS_2$/graphene heterostructure are very small (< 0.5 meV $C^{-1}$), which suggests that all the three representative adsorption sites on the surface of $MoS_2$ in the $MoS_2$/graphene heterointerface are possible.

The interfacial interaction between $MoS_2$ and graphene can enhance the adsorption of the Na atom while maintaining the efficient diffusion of Na. As shown in **Table 5.3**, the adsorption energy ($E_{ad}$) of the Na atom is -2.59 and -2.57 eV for MC and SC structures, respectively, which are much higher than the adsorption energy -1.49 eV of a Na atom on a monolayer of $MoS_2$. In addition, ~0.7 *e* of the Na atom adsorbed into the $MoS_2$ surface in both MC and SC structures is transferred to the $MoS_2$ layer, which is very similar to the amount 0.709 *e* transferred in the case of monolayer $MoS_2$. The diffusion of Na on $MoS_2$ in the $MoS_2$/graphene heterostructure was also investigated. Because the structures of the Na atom adsorbed at three sites on the $MoS_2$ layer have very close energies, the diffusions among the three structures in both MC and SC structures should all be considered, as shown in **Figure 5.13f** and **g**. After LST/QST and NEB calculations, it is found that the diffusion barriers among the three adsorption configurations are similar to each other for both MC and SC structures. However, the diffusion from the hollow position of a $MoS_2$ ring to the top site of a S atom in a MC structure has the lowest diffusion barrier of 0.082 eV, while it is 0.085 eV for the diffusion from the hollow position of a $MoS_2$ ring to the top site of a S atom in a SC structure, which are also almost the same as that in a monolayer $MoS_2$ (0.086 eV). Therefore,

the diffusion can occur effectively at room temperature when the barrier is lower than 0.75 eV. Consequently, the diffusion of Na atoms on the $MoS_2$ surface is fast on both the $MoS_2$ surface and the $MoS_2$/graphene heterointerface. Based on above results, it is concluded that the presence of a graphene layer does not change the amount of electrons transferred from Na atoms to $MoS_2$ or the diffusion barrier, but increases the adsorption energy of Na atoms on the $MoS_2$ surface, which indicates more Na atoms can be trapped in the $MoS_2$/graphene heterointerface.

The band structures of $MoS_2$ before and after Na atom adsorption are shown in **Figure 5.15a** and **b**. Pristine monolayer $MoS_2$ has a ~1.8 eV direct band gap at the *K*-point, which is consistent with the reported values of 1.62 eV[361] and 1.8 eV[362]. After Na atom adsorption, the Fermi level shifts up ~1.5 eV compared with bare $MoS_2$, indicating the strong n-type doping of $MoS_2$, which is contributed by a large amount of electron transfer from the Na atom to the $MoS_2$ layer. However, the Na-$MoS_2$ system still has a wide band gap of 1.74 eV, which hinders the transport of electrons during charge-discharge. $MoS_2$/graphene heterointerface can improve electronic conductivity compared with bare $MoS_2$. The band structure of the bilayer $MoS_2$/graphene system in both MC and SC structures, with and without Na atom adsorption, is calculated and shown in **Figure 5.15c-f**. To clearly show the effect of graphene on the conductivity of the $MoS_2$/graphene heterointerface, the band structure of pristine graphene is also provided in **Figure 5.15c** and **e**, from which it is clearly shown that the bilayer system has a near zero band gap and similar conductive behavior to pristine graphene

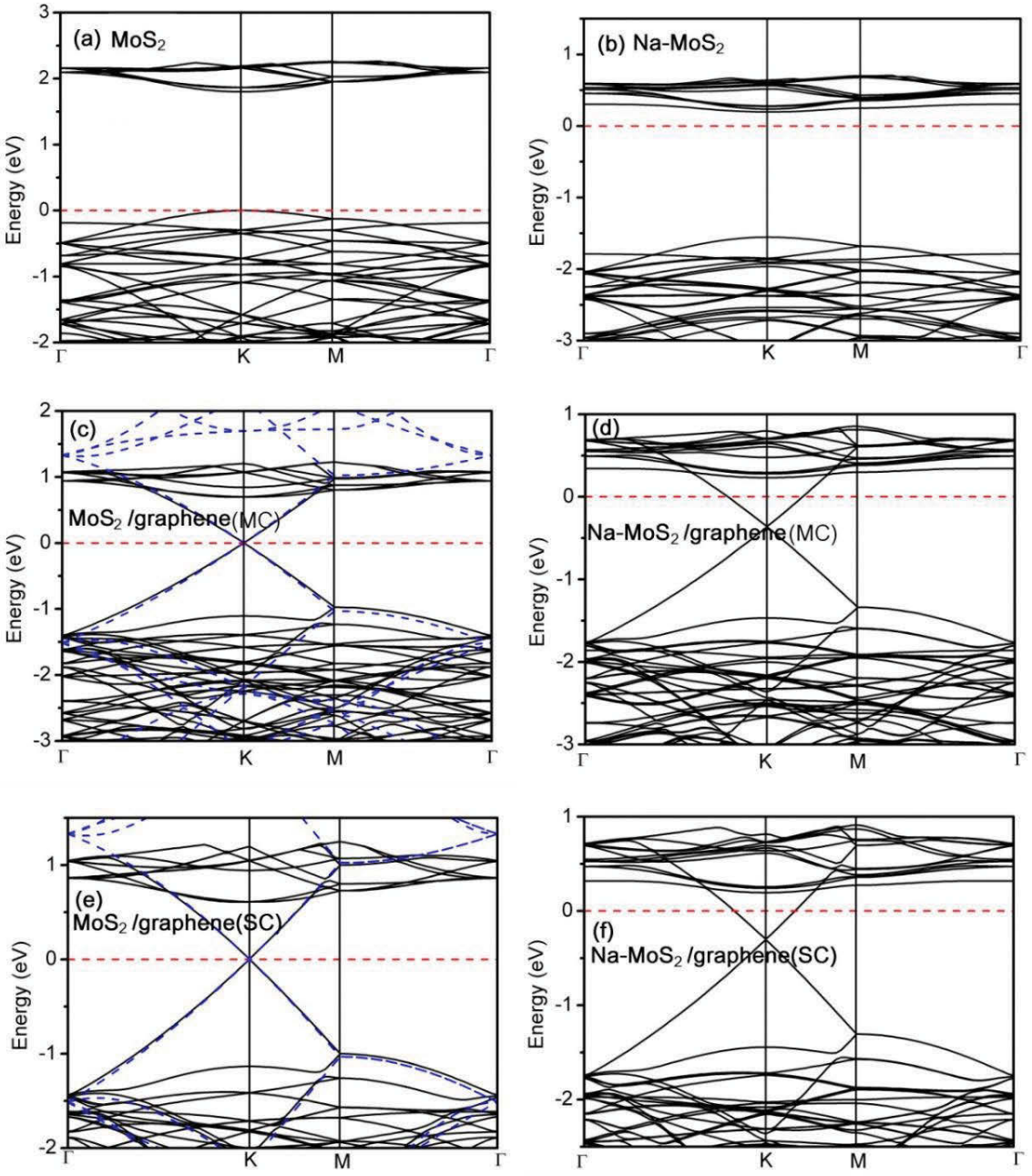


**Figure 5.15** The band structures of monolayer $MoS_2$ (a), $MoS_2$/graphene bilayer with MC structure (c), and $MoS_2$/graphene bilayer with SC structure (e). (b), (d), and (f) show the corresponding band structure after the adsorption of Na. The blue dashed lines are the band structure of pristine graphene and the red dashed line denotes the Fermi level.

at the Dirac *K*-point. On the other hand, the presence of the $MoS_2$ layer also changes the band structure of graphene, where the bands in the valence band away from the Dirac *K*-point shift

further away from the Dirac *K*-point in both MC and SC structures. However, the distances of such bands from the Dirac *K*-point in MC and SC structures are different owing to the different stacking configurations. After Na adsorption at its preferred position, the Fermi level shifts upward and n-type doping is present, which is similar to the case of monolayer $MoS_2$. In MC and SC, the Fermi level shifts ~0.36 and ~0.30 eV in MC and SC structures, respectively, while it shifts ~1.5 eV in monolayer $MoS_2$. This difference is induced by the presence of the graphene layer, which receives part of the transferred electrons of Na atoms from the $MoS_2$ layer. The computational calculations clarify the unique role of the $MoS_2$/graphene heterointerface for enhancing the Na storage performance, including the increase of the conductivity of the $MoS_2$/graphene bilayer system, the capture of more Na, and the maintenance of high diffusion mobility of Na atoms on the $MoS_2$ surface, and high electron transfer efficiency from Na to $MoS_2$. Due to the presence of the $MoS_2$/graphene heterointerface, more Na atoms can be adsorbed with large amounts of electrons transferred to the $MoS_2$ layer and a high diffusion mobility on the $MoS_2$ surface, while the graphene is the highly conductive conductor to transport the transferred electrons. This would result in high Na storage capacity and excellent rate capability.

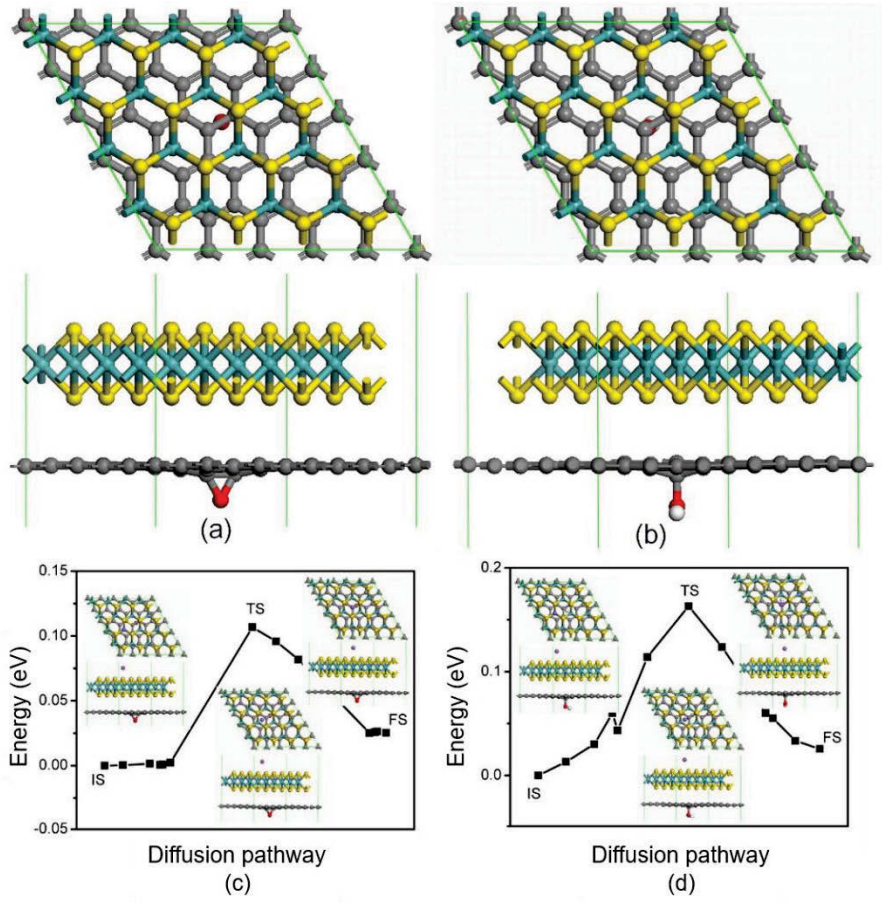


**Figure 5.16** Atomic structure of a Na atom adsorbed on $MoS_2$/RGO (MC configuration) with epoxy (a) and hydroxyl (b) groups in RGO, respectively. The corresponding energy minimum diffusion pathways of a Na atom on $MoS_2$/RGO with epoxy and hydroxyl groups in RGO are shown in (c) and (d) respectively.

Since there are residual oxygen-containing moieties (such as hydroxyl and epoxy groups) in RGO chemically derived from the reduction of graphene oxide in our MG-x samples, the effect of such residual oxygen-containing groups on the Na adsorption and diffusion on the $MoS_2$/graphene heterointerface is also considered. Due to the very similar energy and properties for both MC and SC configurations, the MC configuration is taken as the example to investigate the effects of hydroxyl and epoxy groups in graphene. After considering all the possible position of the hydroxyl and epoxy groups, it is found that the epoxy or hydroxyl

group prefers to locate below the graphene layer as shown in **Figure 5.16a** and **b**. The interaction between the graphene and $MoS_2$ is still a weak van der Waals interaction with an interaction action energy of ~0.03 eV $C^{-1}$ for both cases, which is a little bit stronger than that in $MoS_2$/graphene system without oxygen-containing groups. For the adsorption of Na atoms, similar to the case in **Figure 5.14**, after consider all the possible adsorption positions, it is found that the Na atom prefers to adsorb on top of a Mo atom for both cases, while the adsorption energies are -2.64 and -2.75 eV in $MoS_2$/graphene system with epoxy and hydroxyl group, respectively. The adsorption is a little bit stronger than that in $MoS_2$/graphene system without oxygen function groups. With the presence of the oxygen-containing groups, the Na atom transfers ~0.71 *e* to $MoS_2$, a little more than that in $MoS_2$/graphene system without oxygen. The corresponding diffusion behavior was also investigated and the energy minimum diffusion pathway is shown in **Figure 5.16c** and **d**. The diffusion barriers are 0.107 and 0.16 eV in the $MoS_2$/graphene system with epoxy and hydroxyl groups, respectively, which indicates that the high mobility of the Na atom in the $MoS_2$/graphene heterostructure is maintained in the presence of epoxy and hydroxyl groups. Consequently, even with residual oxygen-containing moieties in graphene, the $MoS_2$/graphene heterostucture is still superior for Na storage compared to the bare $MoS_2$ by storing more Na ions, while maintaining a high diffusion mobility of Na atoms on the $MoS_2$ surface and a high electron transfer efficiency from Na to $MoS_2$.

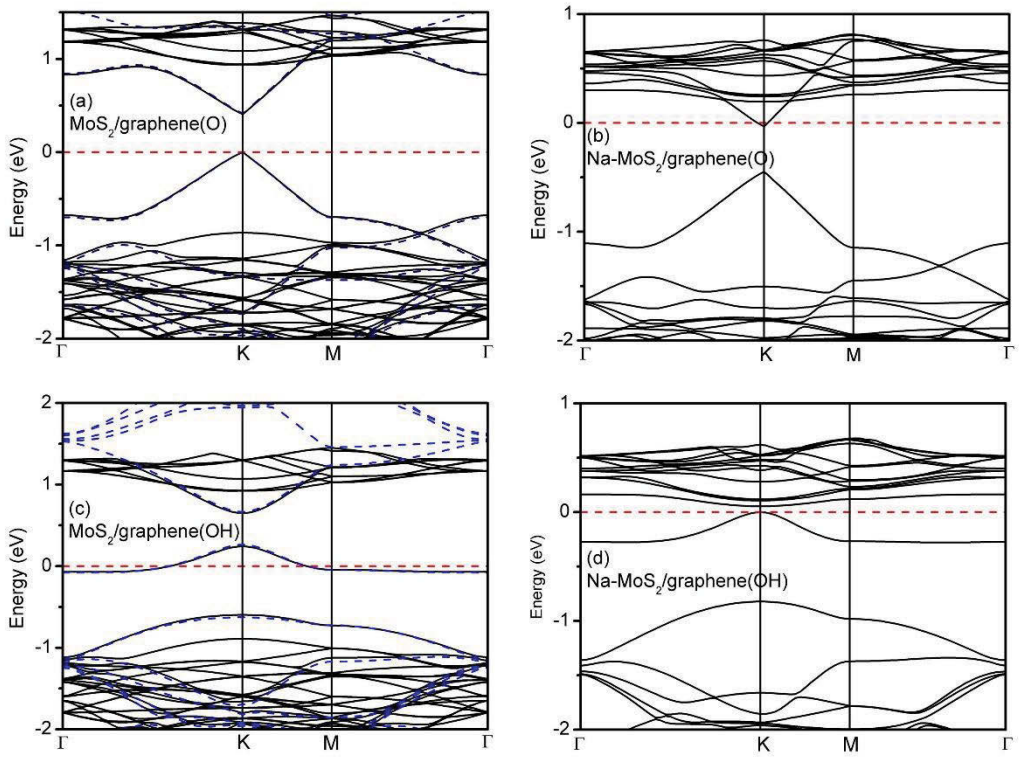


**Figure 5.17** The band structure of $MoS_2$/RGO (MC configuration) with epoxy (a) and hydroxyl (c) groups in RGO. After the Na atom adsorption, the corresponding band structures are shown in (b) and (d), respectively.

To understand the conductivity changes in the presence of oxygen-containing groups, the band structures of the $MoS_2$/graphene with epoxy and hydroxyl groups are shown in **Figure 5.17**. It is shown that the band gap of $MoS_2$ reduces from ~1.8 to 0.5 eV after combining with graphene with epoxy group, and no band gap is found in $MoS_2$/graphene with hydroxyl group. After the Na adsorption, the Fermi level shifts up ~0.5 and ~0.25 eV in $MoS_2$/graphene system with epoxy and hydroxyl groups, respectively. The corresponding band gap of $MoS_2$/graphene with epoxy group disappears, while it is ~0.05 eV for $MoS_2$/graphene with hydroxyl group. Therefore, the conductivity of $MoS_2$ is improved after coupling with graphene containing oxygen functional groups, *i.e.* the oxygen-containing groups in

graphene would not change the promising electrochemical properties for sodium ion batteries.

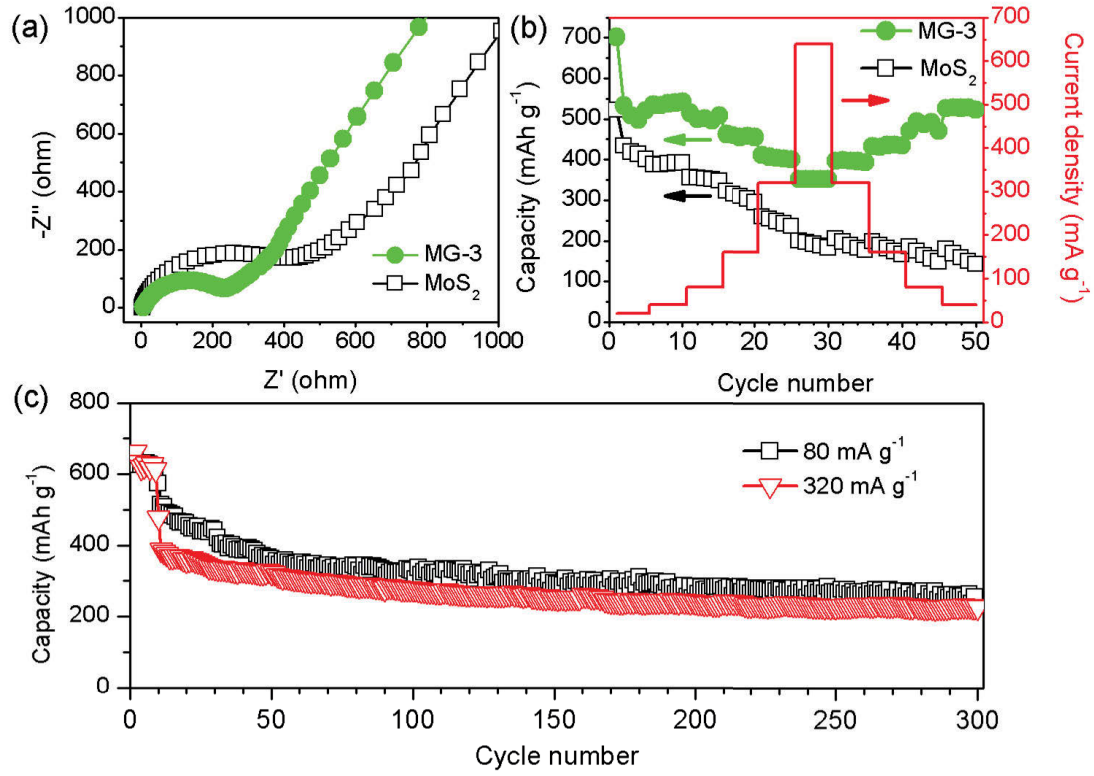


**Figure 5.18** (a) Nyquist plots of MG-3 and $MoS_2$ as anode materials in the charged state (3.0 V *vs.* $Na^+/Na$). (b) Rate performance of MG-3 and $MoS_2$ electrodes. (c) Discharge capacity as a function of cycle number of MG-3 electrode from the second cycle at high current densities of 80 mA $g^{-1}$ and 320 mA $g^{-1}$. The first 20 cycles were tested at a current density of 20 mA $g^{-1}$.

The *in-situ* hybridization of $MoS_2$ and RGO plays an important role in constructing $MoS_2$/RGO heterostructures with enhanced electrochemical performances for $Na^+$ storage. Firstly, RGO as macromolecular surfactants can effectively stabilize $MoS_2$ nanosheets with high surface energy, realizing high-dispersive $MoS_2$ supported on RGO. As a result, more reactive sites are available for the electrode/electrolyte interaction. Secondly, this soft integration method enables high-quality electrical contact between $MoS_2$ and RGO, which

ensures the functionality of the $MoS_2$/graphene heterointerface for Na-ion storage performance. The enhanced electrical conductivity of MG-3 due to the intimate interfacial interaction is confirmed by electrochemical impedance spectroscopy (EIS) measurements. **Figure 5.18a** shows the Nyquist plots of EIS for MG-3 and $MoS_2$. The Nyquist plots consist of a single depressed semicircle in the high-medium frequency region and an inclined line at low frequency. Obviously, MG-3 features a much smaller semicircle diameter than that of $MoS_2$, indicating a high electrical conductivity and a rapid charge-transfer reaction for $Na^+$ insertion and extraction. The faster charge-transfer ability leads to an excellent high-rate performance of the MG-3 electrode. Continuous cycling was carried out at the following current densities: 20 mA $g^{-1}$, 40 mA $g^{-1}$, 80 mA $g^{-1}$, 160 mA $g^{-1}$, 320 mA $g^{-1}$, and 640 mA $g^{-1}$. As shown in **Figure 5.18b**, the good rate capability of the MG-3 with intimate heterointerfaces becomes more evident with the increase of the charge/discharge current density. Even when the current density increases to 640 mA $g^{-1}$, MG-3 retains a capacity of 352 mA h $g^{-1}$, which is 50.2% of the capacity obtained at 20 mA $g^{-1}$. Furthermore, when the current density is reversed to 40 mA $g^{-1}$, the MG-3 electrode can recover its capacity after 45 cycles, suggesting its excellent rate performance and cycling stability. However, the bare $MoS_2$ electrode suffers from continuous capacity fading and it fails to recover the capacity when the current density reversed to the low value. From **Figure 5.18c** it can be seen that the MG-3 electrode also exhibits good cycling performance at high current densities. After 300 cycles, MG-3 retained $Na^+$ storage capacities of 254 mA h $g^{-1}$ and 227 mA h $g^{-1}$ at 80 mA $g^{-1}$ and 320 mA $g^{-1}$, respectively.

The promising electrochemical performance of $MoS_2$/RGO nanocomposites could be attributed to the 2D heterointerfaces between $MoS_2$ and RGO, which results in a synergistic

effect towards the $Na^+$ storage over $MoS_2$/RGO. In particular, the van der Waals interaction between RGO and $MoS_2$ leads to an intimate interfacial interaction, which helps ameliorate the re-stacking and aggregation of $MoS_2$ nanosheets. Consequently, more active sites are available for the electrode/electrolyte interaction. The intimate interfacial interaction also improves the interfacial electron transfer during sodiation/de-sodiation, which can maximize the conductivity of RGO. Moreover, without deteriorating the diffusion behaviors of Na and the electron transfer efficiency from Na to $MoS_2$, $MoS_2$/graphene heterointerfaces show the ability to enhance the adsorption of Na, which is also beneficial for the Na-ion storage in sodium-ion batteries.

## 5.4 Conclusions

In summary, a series of sheet-on-sheet structured $MoS_2$/RGO nanocomposites with different heterointerfacial areas have been successfully prepared by a facile bottom-up hydrothermal method followed by a calcination process. The synergistic effect contributes to the improved capacity for Na-ion storage through increasing the heterointerfacial area. In particular, MG-3 with maximum heterointerfacial areas can deliver a reversible capacity of 702 mAh $g^{-1}$ for sodium-ion batteries. The MG-3 electrode also demonstrated excellent rate capabilities. Even at a high current density of 640 mA $g^{-1}$, MG-3 can still deliver a capacity of 352 mA h $g^{-1}$. It is found that the 2D $MoS_2$/graphene heterointerface can increase the conductivity of $MoS_2$ and capture more Na atoms, while maintaining the high diffusion mobility of Na on the $MoS_2$ surface and high electron transfer efficiency from Na to $MoS_2$. Our findings could enhance the understanding of 2D graphene-based heterostructures, which is important for the rational design of high-performance electrode materials for sodium-ion batteries.

## Chapter 6 $SnS_2$ Nanoplatelet/Graphene Nanocomposites as High Capacity Anode Materials for Sodium Ion Batteries

### 6.1 Introduction

Recently, tin-based compounds have been investigated as anode materials due to the high theoretical capacity of tin (847 mA h $g^{-1}$).[248, 249, 286, 358, 363-368] For example, SnSb alloy achieved a capacity of 435 mA h $g^{-1}$ over 50 cycles.[358] Kumta and co-workers also reported a mechanically milled Sn/C composite, which exhibited a stable capacity of 410 mA h $g^{-1}$.[366] To buffer the volume change and aggregation of Sn during cycling, Wang *et al.* developed tin-coated viral nanoforests as SIB anode materials, which demonstrated an initial capacity of 722 mA h $(g\text{-}Sn)^{-1}$, with a good cyclability.[248]

$SnS_2$ has a layered hexagonal $CdI_2$-type crystal structure, consisting of tin cations sandwiched between two layers of close-packed sulfur anions.[369] These triple layers are stacked along the *c*-axis and held together by van der Waals interactions with an interlayer distance of 0.59 nm, which provides channels for $Na^+$ diffusion. Therefore, $SnS_2$ could be a promising anode candidate for SIBs. Based on the reaction of $4SnS_2 + 31Na^+ + 31e^- \rightarrow Na_{15}Sn_4 + 8Na_2S$, $SnS_2$ can deliver a theoretical sodium storage capacity of 1136 mA h $g^{-1}$. It is expected, however, that the volume change during alloying-dealloying could lead to pulverization of the electrode. As pointed by Guo *et al.*, this issue could be addressed by building continuous carbon networks.[370, 371] Herein, we report the use of $SnS_2$/graphene nanocomposites as anode materials for Na-ion batteries. The $SnS_2$/graphene nanocomposites were synthesized by a morphology-controlled hydrothermal method using L-cysteine as both sulfur precursor and morphology directing agent. The as-prepared composites feature a platelet-on-sheet

nanostructure. Remarkably, a reversible capacity of 725 mA h $g^{-1}$ was achieved. Moreover, the $SnS_2$/graphene nanocomposites also demonstrated an improved cyclability and enhanced high-rate capability.

## 6.2 Experimental Section

### 6.2.1 Sample preparation

Graphene oxide (GO) nanosheets were synthesized from natural graphite powders by a modified Hummers' method.[305] The $SnS_2$/graphene nanocomposite was then produced by a hydrothermal method. In a typical synthesis process, 65 mg $SnCl_4 \cdot 5H_2O$ (Sigma-Aldrich, ≥ 98%) was mixed with 20 mL GO aqueous suspension (1 mg/mL) by ultrasonication using a Brandson Digital Sonifer (S450D, 40% amplitude). After ultrasonication for 0.5 h, 89 mg L-cysteine was added and mechanically stirred for another 0.5 h. Then, the mixed precursor solution was heated to 180 °C in a Teflon-lined autoclave (25 mL in capacity) and maintained at 180 °C for 24 h. The precipitates were cooled down to room temperature, collected, and washed with distilled water and ethanol several times. After drying at 60 °C in a vacuum oven overnight, the final products were obtained.

### 6.2.2 Structural and physical characterization

The crystal structure and phases of the as-prepared materials were characterized by X-ray diffraction (XRD, Siemens D5000) using Cu Kα radiation with a scanning step of 0.02° $sec^{-1}$. The morphology was analyzed by field emission scanning electron microscopy (FESEM, Zeiss Supra 55VP). The details of the morphology were further characterized by transmission electron microscopy (TEM) and high-resolution TEM (HRTEM, JEOL JEM-2011). The $SnS_2$ loading mass was measured using a TGA/differential thermal analysis (DTA) analyzer

(TA Instruments, SDT 2960 module, New Castle, DE, USA) at a heating rate of 10 °C $min^{-1}$ in air from room temperature to 900 ºC. Raman spectra were collected with a Renishaw inVia Raman spectrometer system (Gloucestershire, UK) equipped with a Leica DMLB microscope (Wetzlar, Germany) and a Renishaw He-Ne laser source producing 17 mW at 633 nm.

### 6.2.3 Cell assembly and electrochemical testing

The electrodes were prepared by dispersing the as-prepared material (70 wt %), carbon black (20 wt %), and poly (vinylidene fluoride) binder (PVDF, 10 wt %) in N-methyl-2-pyrrolidone (NMP) to form a slurry. The resultant slurry was pasted onto copper foil using a doctor blade and dried in a vacuum oven for 12 h, followed by pressing at 200 $kg/cm^2$. The mass of each electrode is around 1.0 mg. Electrochemical measurements were carried out using two-electrode coin cells with Na metal as counter and reference electrode and glass microfiber (Whatman) as the separator. The CR2032-type coin cells were assembled in an argon-filled glove box (UniLab, Mbraun, Germany). The electrolyte solution was 1 M $NaClO_4$ dissolved in a mixture of ethylene carbonate (EC) and propylene carbonate (PC) with a volume ratio of 1:1. The charge-discharge measurements were performed at different current densities in the voltage range from 0.01 to 3 V *vs.* $Na^+/Na$ using a computer-controlled Neware Battery Testing system. For the $SnS_2$/graphene electrode, the obtained specific capacities are based on the total mass of $SnS_2$/graphene nanocomposite. Cyclic voltammetry (CV) was conducted by using a CHI 660C electrochemical workstation between 0.01 and 3 V *vs.* $Na^+/Na$ with a scan rate of 0.1 mV/s. For the electrochemical impedance spectroscopy (EIS), the excitation amplitude applied to the cells was 5 mV.

### 6.3 Results and Discussion

The phase and purity of the as-prepared $SnS_2$/graphene nanocomposites were characterized by X-ray diffraction (XRD), as shown in **Figure 6.1**. The diffraction peaks at 15.0°, 28.2°, 32.1°, 41.9°, 50.0°, 52.5°, 55.0°, and 60.6° can be well indexed to the (001), (100), (101), (102), (110), (111), (103), and (201) crystal planes, respectively, of layered hexagonal phase $SnS_2$ (JCPDS card no. 23-0677). The crystal parameters were calculated to be a = b = 3.649 Å and c = 5.899 Å. It should be noted that the intensity of the (001) peak is weak compared to the standard data, which indicates the limited growth of the (001) crystal plane and the formation of $SnS_2$ platelets. Furthermore, no diffraction peak corresponding to graphene was observed in the XRD pattern at 2θ = 26.6°, suggesting that the $SnS_2$ nanoplatelets could effectively prevent the restacking of graphene nanosheets.[372] No impurity phases were detected.

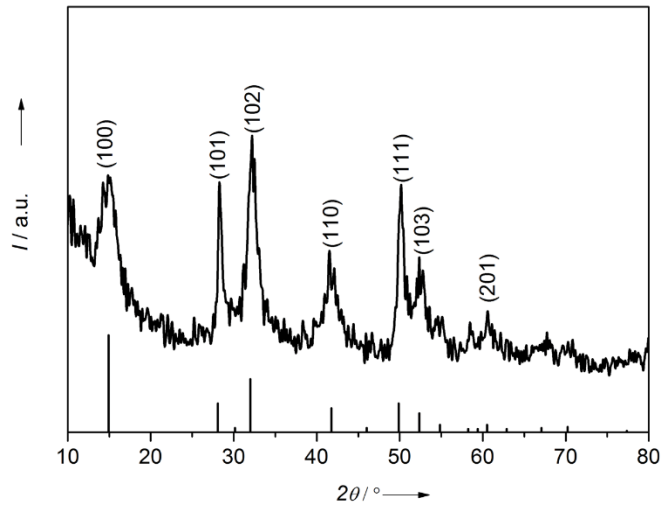


**Figure 6.1** XRD pattern of the as-prepared $SnS_2$/graphene composites. *I* = Intensity.

The morphology of the $SnS_2$/graphene nanocomposites was analyzed by scanning electron microscopy (SEM) and transmission electron microscopy (TEM). **Figure 6.2a** shows a low magnification SEM image of the $SnS_2$/graphene nanocomposites, which presents a sheet-like morphology. **Figure 6.2b** demonstrates that the individual $SnS_2$ nanoplatelets are surrounded by graphene nanosheets and have an edge-to-edge distance of about 80 nm. Bare $SnS_2$ nanoplatelets aggregate, however, and form large agglomerations (**Figure 6.3**). Therefore, the graphene nanosheets act as a "heterogeneous dispersing agent" to prevent the aggregation of $SnS_2$ nanoplatelets. The separation of $SnS_2$ nanoplatelets by graphene nanosheets will enhance the electrochemical performance for Na-ion storage because more exposed surfaces are available for the reaction between Na ions and $SnS_2$, compared to bare $SnS_2$ nanoplatelets.

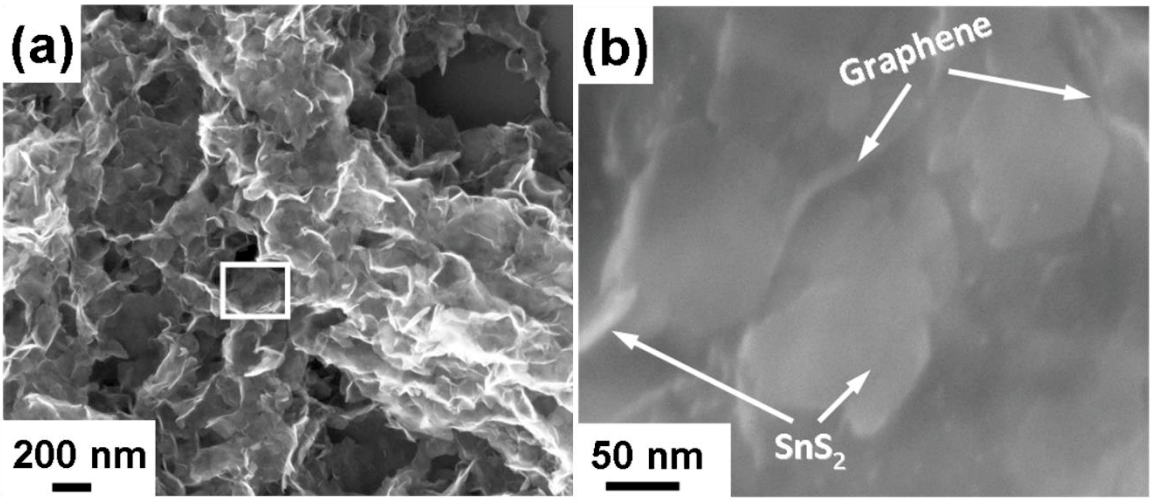


**Figure 6.2** (a) Low-magnification SEM image of $SnS_2$/graphene nanocomposites. (b) Enlarged view of the area marked by a white square in (a), showing the morphological features of graphene and $SnS_2$.

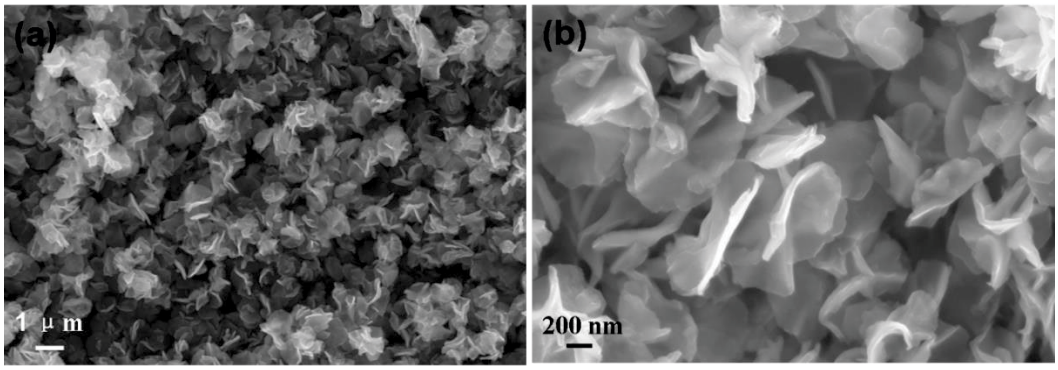


**Figure 6.3** SEM images of $SnS_2$ nanoplatelets.

The $SnS_2$/graphene nanocomposites were further characterized by TEM (**Figure 6.4a-d**). Ultrathin graphene nanosheets are clearly distinguishable in **Figure 6.4a**. Moreover, $SnS_2$ nanoplatelets projecting up from the edge can also be observed on the graphene matrix. The high-resolution TEM (HRTEM) image as shown in **Figure 6.4c** indicates that the $SnS_2$ nanoplatelets are formed from $SnS_2$ layers stacked along the [001] direction with an interlayer distance of 0.59 nm, which is consistent with the XRD results.

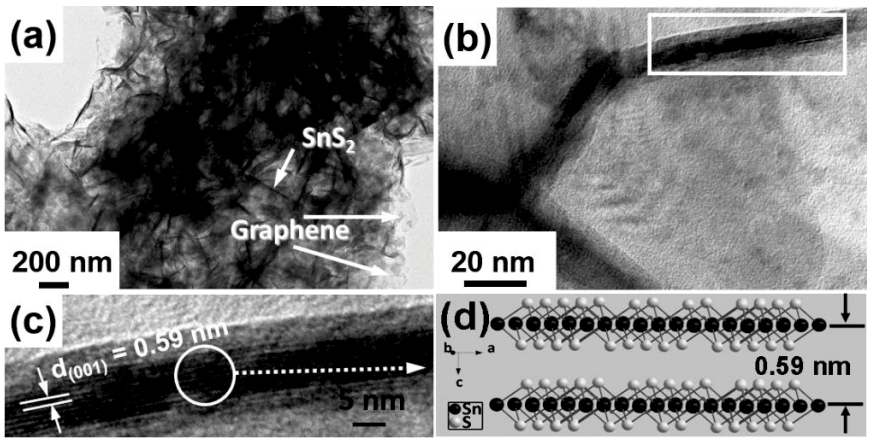


**Figure 6.4** (a) and (b) Low and high magnification TEM images of the $SnS_2$/graphene composites, respectively. (c) HRTEM image of an individual $SnS_2$ nanoplatelet oriented along the [001] direction, taken from the rectangular region in (b). (d) Structural simulation of layered $SnS_2$, with an interlayer distance of 0.59 nm.

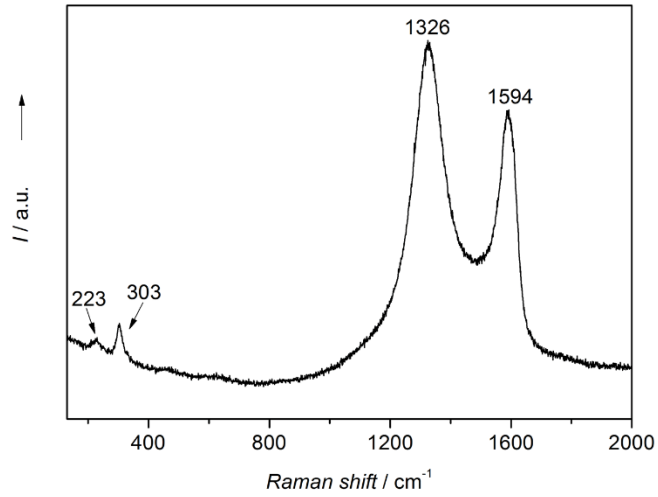


**Figure 6.5** Raman spectrum of $SnS_2$/graphene nanocomposites in the range of 130-2400 $cm^{-1}$. *I* = Intensity.

**Figure 6.5** shows the Raman spectrum of the $SnS_2$/graphene nanocomposites. The Raman peaks located at 223 $cm^{-1}$ and 303 $cm^{-1}$ can be ascribed to the $E_g$ and $A_{1g}$ modes of $SnS_2$.[373] The spectrum also exhibits two peaks at 1326 $cm^{-1}$ and 1594 $cm^{-1}$. The peak at 1326 $cm^{-1}$ is the D line, which originates from the breaking mode of six-atom rings of graphene. The peak at 1594 $cm^{-1}$ is known as the G peak, corresponding to the high-frequency $E_{2g}$ phonon of graphene at the Γ point.[374, 375] The intensity ratio of the D peak to the G peak ($I_D/I_G$) is calculated to be 1.34. The Raman spectrum confirmed the successful synthesis of $SnS_2$/graphene nanocomposites by the hydrothermal method.

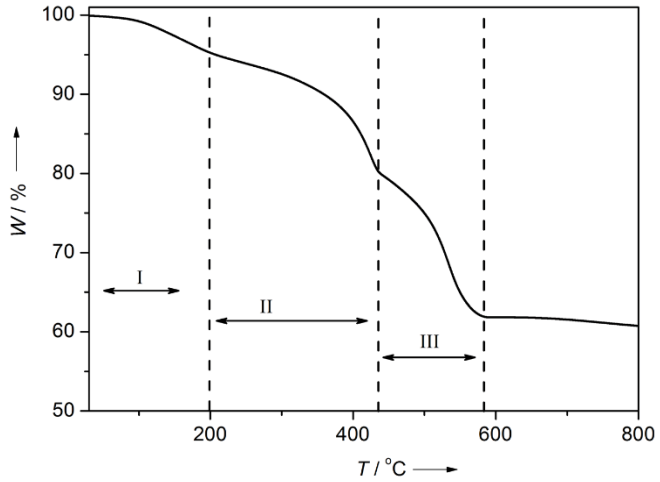


**Figure 6.6** TGA curve of $SnS_2$/graphene nanocomposites. *W* = Weight percentage, *T* = Temperature.

To determine the mass percentage of graphene in the as-prepared nanocomposites, thermogravimetric analysis (TGA) was conducted from 30 °C to 900 °C at a heating rate of 10 °C $min^{-1}$ in dry air. The results are shown in **Figure 6.6**, in which three major steps of weight loss could be observed. The first step from room temperature to about 200 °C could be ascribed to the evaporation of absorbed water and the removal of oxygen-containing functional groups (hydroxyl, epoxy, carbonyl, *etc.*) from the graphene. The second step, occurring between 200 °C and 425 °C, corresponds to oxidation of $SnS_2$ to $SnO_2$,[376] while the last step observed between 425 °C and 580 °C is due to the combustion of graphene nanosheets. From the TGA analysis, the weight percentage of $SnS_2$ in the nanocomposites is calculated to be 65.5%.

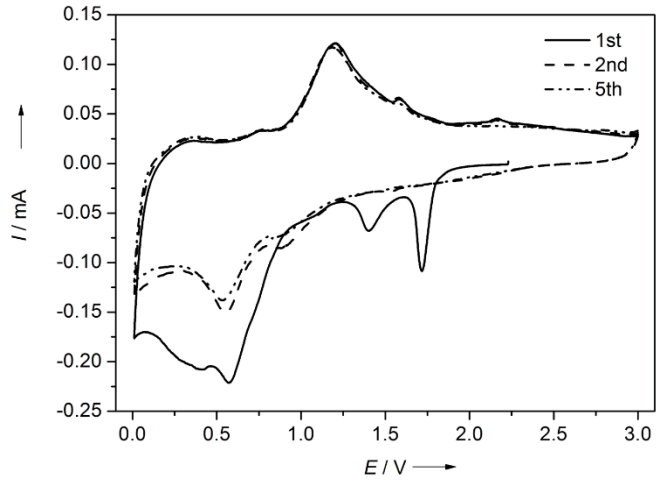


**Figure 6.7** CV curves for selected cycles of $SnS_2$/graphene composites at a scan rate of 0.1 mV $s^{-1}$ in the range of 0.01-3 V *vs.* $Na^+$/Na. *I* = Current, *E* = Potential.

The electrochemical reactivity of the $SnS_2$/graphene hybrid nanosheets was evaluated by cyclic voltammetry (CV) (**Figure 6.7**). In the first cathodic scan, cathodic peaks were observed at 1.73, 1.41, 0.58, and 0.01 V, respectively. The two cathodic peaks at higher voltage (1.73 V and 1.41 V) could be assigned to the formation of $NaSnS_2$, which is similar to our previous work on $SnO_2$/Na system[262]:

$$SnS_2 + Na^+ + e^- \rightarrow NaSnS_2 \quad (6\text{-}1)$$

The cathodic peak at 0.58 V corresponds to the reduction reaction (6-2), leading to the formation of metallic Sn and $Na_2S$:

$$NaSnS_2 + 3Na^+ + 3e^- \rightarrow Sn + 2Na_2S \quad (6\text{-}2)$$

The broad cathodic peaks ranging from 0.58 to 0.01 V are associated with Na-Sn alloying based on reaction (6-3).

$$Sn + xNa^+ + xe^- \rightarrow Na_xSn \quad (6\text{-}3)$$

Moreover, the reduction peak positioned at 0.01 V is assigned to the Na-ion storage on graphene.[358] In the anodic process, several oxidation peaks can be identified, corresponding

to the reversible de-alloying of $Na_xSn$. It should be noted that the CV curves for the 2nd and 5th cycles overlap well with each other, indicating excellent reversibility of the $SnS_2$/graphene electrode for sodium ion storage.

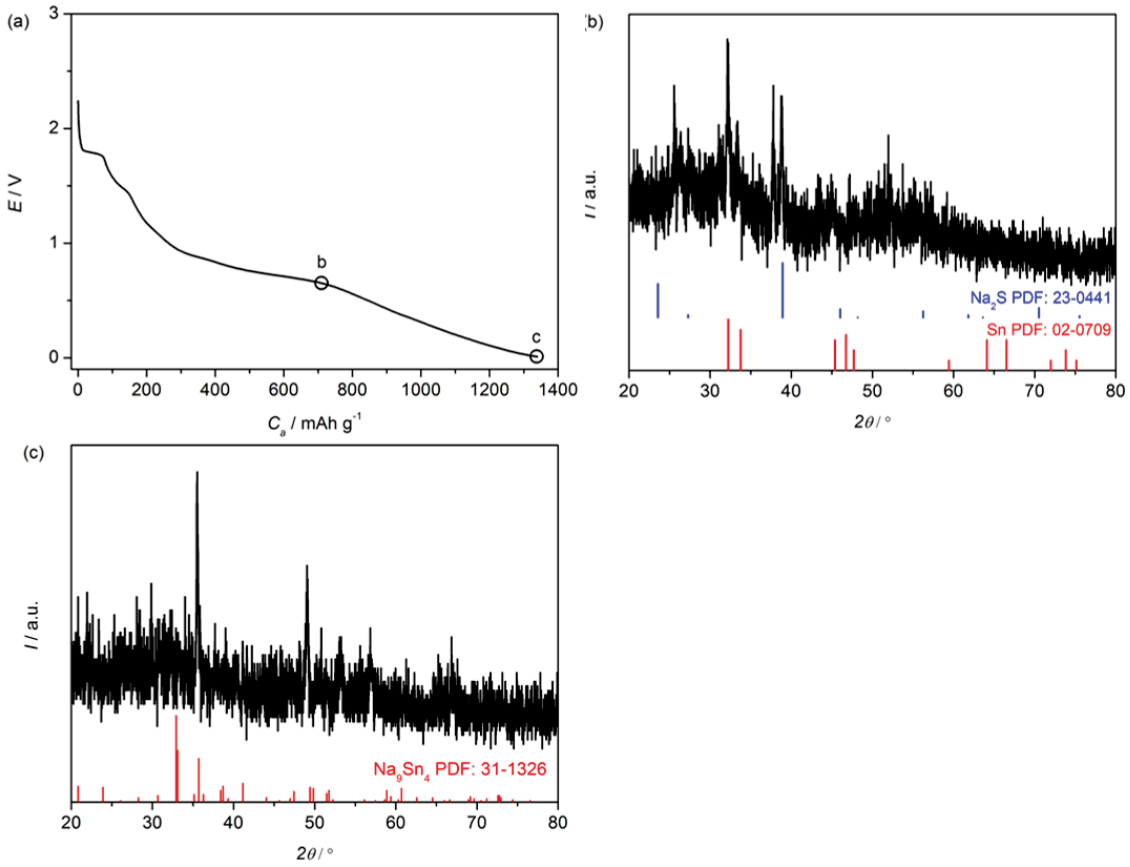


**Figure 6.8** (a) The initial discharge profile of $SnS_2$/graphene at a current density of 20 mA $g^{-1}$. (b), (c) Ex-situ XRD patterns of $SnS_2$/graphene electrode discharged to different state as marked in the profile, in which the standard diffraction peaks of different products are located at the bottom. $E$ = Potential, $C_a$ = Capacity, $I$ = Intensity.

The $Na^+$ storage mechanism was confirmed by the *ex-situ* XRD of the electrode material discharged to the required states. As shown in **Figure 6.8b**, when the electrode was discharged to 0.58 V, a mixture of Sn and $Na_2S$ can be found in the discharge product, which evidenced the reaction according to equation (6-2). Furthermore, after further discharging the

cell to 0.01 V (**Figure 6.8c**), the XRD pattern corresponds to Na-Sn alloy ($Na_9Sn_4$, PDF: 31-1326). It indicates the formation of Na-Sn alloy at a lower voltage as proposed by equation (6-3).

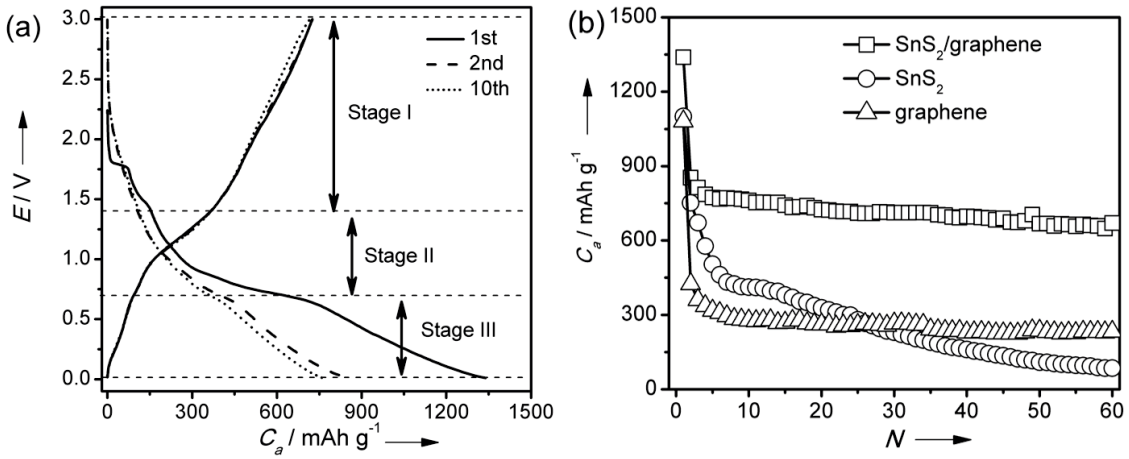


**Figure 6.9** (a) The 1st, 2nd, and 10th charge-discharge profiles of $SnS_2$/graphene at a rate of 20 mA $g^{-1}$. (b) Cycling performance of $SnS_2$/graphene, $SnS_2$, and graphene at a rate of 20 mA $g^{-1}$. $E$ = Potential, $C_a$ = Capacity, $N$ = Cycle number.

**Figure 6.9a** shows the charge-discharge profiles of the $SnS_2$/graphene nanocomposite electrode for the 1st, 2nd, and 10th cycles. The $SnS_2$/graphene anode delivered a total discharge capacity of 1339 mA h $g^{-1}$ in the first cycle, which is higher than that of the bare $SnS_2$ (1100 mA h $g^{-1}$, **Figure 6.10**). The initial reversible capacity of $SnS_2$/graphene is 725 mA h $g^{-1}$. The irreversible capacity is mainly caused by the formation of irreversible solid electrolyte interphase (SEI) on the electrode.[367] From the first discharge curve of the $SnS_2$/graphene anode, we can see that the discharge process consists of three stages, namely, Stage I (3.0-1.4 V), Stage II (1.4-0.7 V), and Stage III (0.6-0.01 V), which agree very well with the CV peaks in **Figure 6.7**. When the cell was discharged to 1.4 V, it delivered a capacity of 150 mA h $g^{-1}$. Subsequently, as the cell was further discharged to 0.7 V, a total capacity of 600

mA h $g^{-1}$ was achieved. **Figure 6.9b** shows the cycling performance of the $SnS_2$/graphene, bare $SnS_2$, and graphene at a current density of 20 mA $g^{-1}$. The discharge capacity of the $SnS_2$/graphene nanocomposite is higher than that of the bare $SnS_2$ and graphene. Moreover, the $SnS_2$/graphene demonstrated a much improved cycling performance compared to bare $SnS_2$ nanoplatelets, as the $SnS_2$/graphene maintained a total capacity of 670 mA h $g^{-1}$ after 60 cycles. On the other hand, the bare $SnS_2$ exhibited significant capacity fading and only delivered a capacity of 86 mA h $g^{-1}$ after 60 cycles.

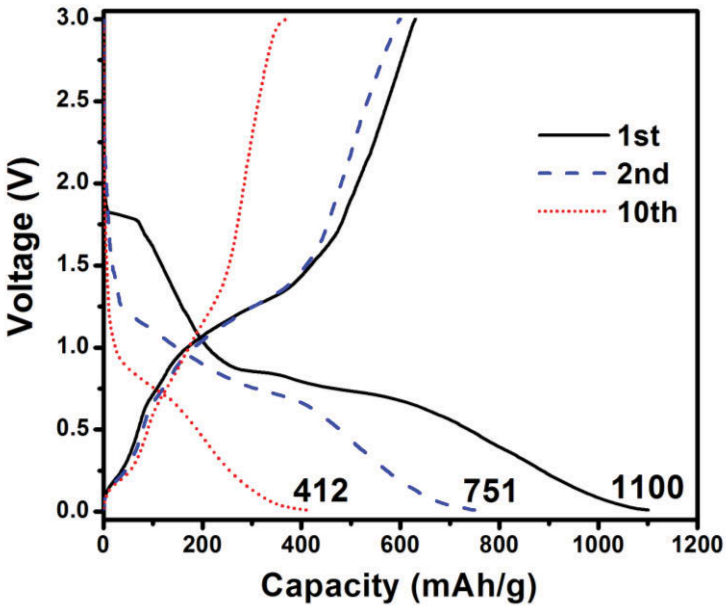


**Figure 6.10** The 1st, 2nd and 10th cycle charge-discharge profiles of $SnS_2$ at a rate of 20 mA $g^{-1}$.

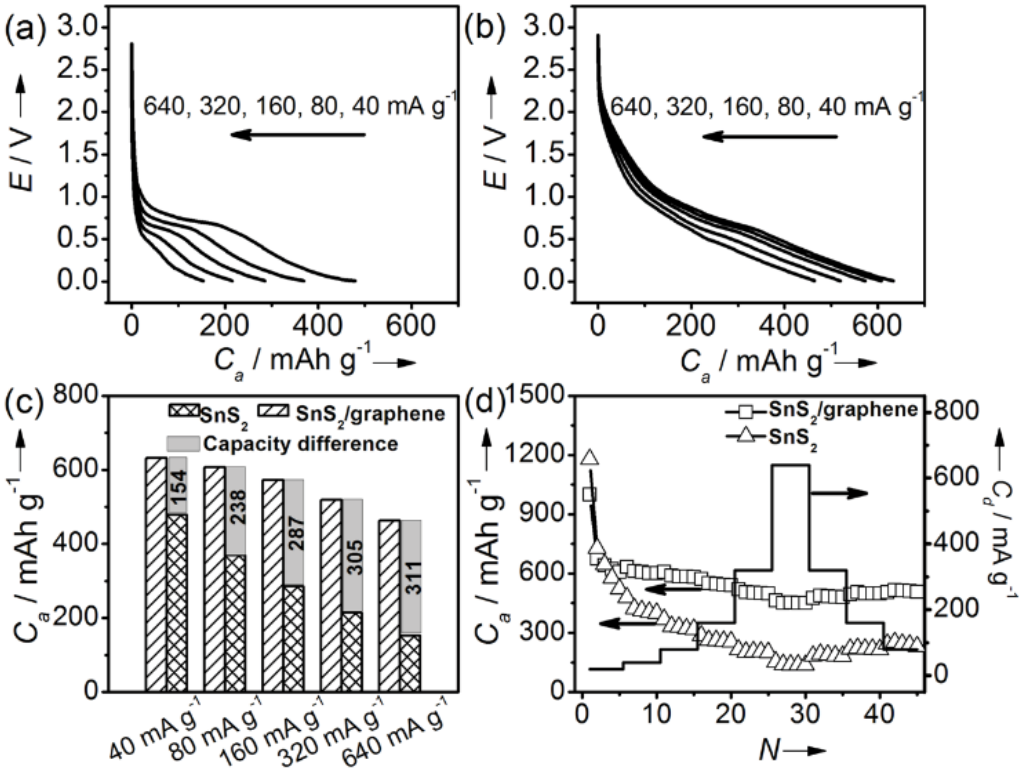


**Figure 6.11** Discharge curves of $SnS_2$ (a) and $SnS_2$/graphene nanocomposites (b) at current densities of 40, 80, 160, 320, and 640 mA $g^{-1}$, respectively. (c) Comparison of discharge capacities of $SnS_2$ and $SnS_2$/graphene nanocomposites at current densities of 40, 80, 160, 320, and 640 mA $g^{-1}$, respectively. (d) Rate performance of $SnS_2$ and $SnS_2$/graphene nanocomposites at currents of 20, 40, 80, 160, 320, 640, 320, 160, and 80 mA $g^{-1}$, respectively. $E$ = Potential, $C_a$ = Capacity, $N$ = Cycle number, $C_d$ = Current density.

The superior electrochemical performance of the $SnS_2$/graphene composite was further demonstrated by cycling tests under high current densities. Both the bare $SnS_2$ and the $SnS_2$/graphene nanocomposite electrodes were tested by multiple-step varied current densities: 40, 80, 160, 320, and 640 mA $g^{-1}$, respectively. The results are presented in **Figure 6.11**. The discharge profiles in the first cycle are shown in **Figure 6.11a** and **b**. The capacities of the bare $SnS_2$ at current densities of 40, 80, 160, 320, and 640 mA $g^{-1}$ are 478, 369, 285, 214, and 152 mA h $g^{-1}$, respectively. The discharge capacity of the bare $SnS_2$ electrode

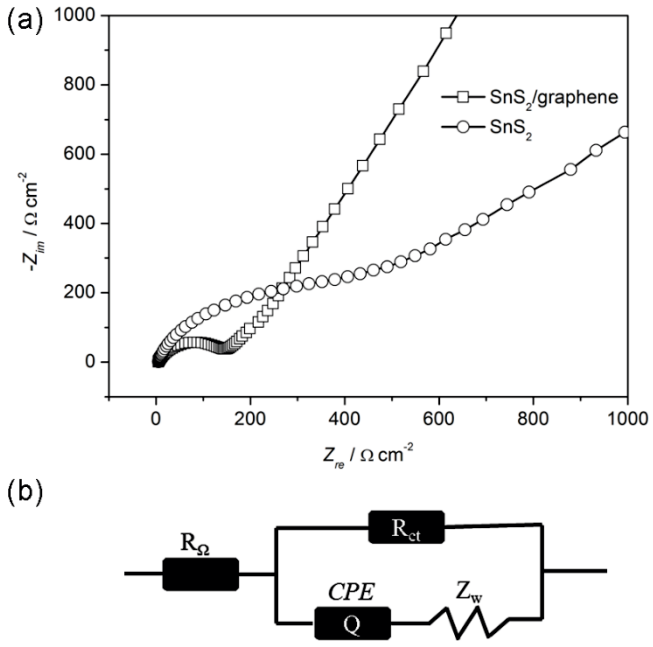


**Figure 6.12** (a) Nyquist plots of $SnS_2$ and $SnS_2$/graphene nanocomposites. (b) The corresponding equivalent circuit ($R_\Omega$: Ohm resistance; $R_{ct}$: Charge transfer resistance; $Z_w$: Warburg diffusion process; *CPE*: constant-phase element).

dramatically decreased with increasing current density. The $SnS_2$/graphene nanocomposite delivered discharge capacities of 632, 607, 572, 519, and 463 mA h $g^{-1}$, respectively, at the same current densities. The difference in the capacities of the $SnS_2$ and the $SnS_2$/graphene electrodes is shown in **Figure 6.11c**. With gradually increasing current density, the capacity difference increased from 154 mA h $g^{-1}$ to 238, 287, 305, and 311 mA h $g^{-1}$, respectively. Furthermore, the $SnS_2$/graphene nanocomposite exhibited a much better rate capability and longer cycle life than that of bare $SnS_2$ anode. When $SnS_2$ reacts with sodium ions, there is a dramatic volume increase, inducing cracking and pulverization. The graphene network is able to provide elastic buffer space to accommodate the volume expansion/contraction during $Na^+$ insertion/extraction processes, which is effective for preserving the integrity of the electrode under progressive cycling. In addition, graphene is well known for its excellent

electrical conductivity (~ 10000 $cm^2$ $V^{-1}$ $s^{-1}$)[377] which can be regarded as a "highway" for electron transport and is vital for a rapid charge-transfer process. Therefore, $SnS_2$/graphene electrode can deliver stable specific capacities at various current rates (as shown in **Figure 6.11d**).

Electrochemical impedance spectroscopy (EIS) measurements were conducted on cells with $SnS_2$ and $SnS_2$/graphene electrodes in order to investigate the reasons for the observed differences in the sodium storage performance at room temperature. The corresponding Nyquist plots are shown in **Figure 6.12**. Both the bare $SnS_2$ and the $SnS_2$/graphene electrodes exhibit typical Nyquist plots, consisting of a single depressed semicircle in the high-medium frequency region and an inclined line at low frequency. The numerical value of the diameter of the semicircle on the $Z_{re}$ axis gives an approximate indication of the charge transfer resistance ($R_{ct}$),[378, 379] while the straight line indicates Warburg-type behaviour. The kinetic differences of $SnS_2$/graphene and bare $SnS_2$ electrodes were further investigated by modeling AC impendence spectra based on the modified Randles equivalent circuit, and the corresponding equivalent circuit is shown in Fig 9(b). The value of the charge-transfer resistance $R_{ct}$ was 147 Ω $cm^{-2}$ for $SnS_2$/graphene, which is significantly lower than that of bare $SnS_2$ (429 Ω $cm^{-2}$). The reduced charge-transfer impedance will increase the electrode kinetics, and consequently, improve the electrochemical performance of the $SnS_2$/graphene electrode for sodium storage.

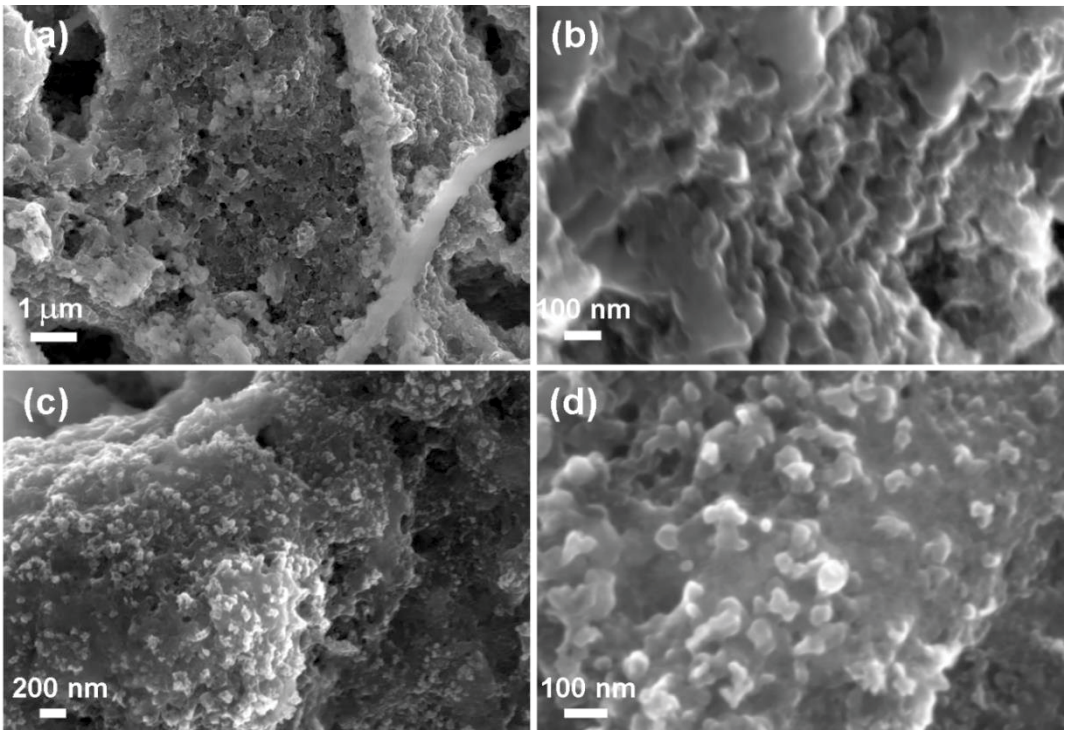


**Figure 6.13** SEM images of $SnS_2$ electrode (a and b) and $SnS_2$/graphene electrode (c and d) after cycling.

We examined the morphology of $SnS_2$ and $SnS_2$/graphene electrodes after cycling by *ex-situ* SEM (as shown in **Figure 6.13**). For $SnS_2$/graphene electrodes, $SnS_2$ nano-platelets lost the platelet-like morphology after reaction with $Na^+$ and transformed into nanoparticles, which uniformly distributed in the graphene matrix. On the contrary, we can see that agglomerates formed for $SnS_2$ electrodes (as shown in **Figure 6.13a** and **b**). The *ex-situ* SEM results further verified that graphene nanosheets act as a "heterogeneous dispersing agent" for $SnS_2$.

### 6.4 Conclusion

We successfully prepared $SnS_2$/graphene nanocomposites by a facile hydrothermal method. SEM and TEM analyses revealed the two-dimensional platelet-on-sheet morphology. When the $SnS_2$/graphene nanocomposites were applied as anode materials in Na-ion batteries, a

high specific sodium ion storage capacity of 725 mA h $g^{-1}$ in the first cycle was achieved. Moreover, the $SnS_2$/graphene electrode showed a good cyclability and enhanced high-rate capability. The improved electrochemical performance should be ascribed to the unique 2D nanoarchitecture, in which graphene nanosheets act as a "heterogeneous dispersing agent" to overcome the aggregation of the $SnS_2$ nanoplatelets and provide electrically conductive networks.

## Chapter 7 Three-dimensional Networked $SnO_2$/Graphene Aerogel with Hierarchically Porous Architecture for High-Rate Performance Sodium-Ion Batteries

### 7.1 Introduction

Graphene has been regarded as an effective nano-building block to support nanoparticles due to its high surface area and unique electrical and mechanical properties.[293, 295-297, 307] In this regard, 2D graphene nanosheets have been widely used to support $Na^+$ host materials (*e.g.*, $SnO_2$,[250, 367, 368, 380] SnS,[290] $SnS_2$[241, 289]) have demonstrated improved performances as anode materials for SIBs. It has been reported that layered $SnS_2$ loaded on graphene exhibited enhanced electrochemical performances compared to bare $SnS_2$ electrode, including improved capacity and cyclability.[241, 289] Moreover, SnS@graphene transformed from $SnS_2$@graphene demonstrated decent performance as anode materials for SIBs.[290] However, in most cases, the 2D graphene nanosheets tend to re-stack during the drying process due to the interlayer van der Waals interactions. This results in decreased accessible surface area and insufficient electron and ion transport, which is one of the major issues that limit the high-rate performance of the electrodes. For example, Wang *et al.* reported that $SnO_2$/graphene composites exhibited a capacity of 143 mA h $g^{-1}$ at a current density of 640 mA $g^{-1}$.[367] Zhang and co-workers reported a capacity of 193 mA h $g^{-1}$ at a current density of 600 mA $g^{-1}$ based on the total mass of the graphene composites.[380] To achieve higher power density to support large-scale applications of SIBs, the rate performance of current graphene-based anode materials needs to be further improved.

Herein, by taking $SnO_2$ as a typical example, we demonstrate the wide scope of improving the high-rate performance of graphene-based electrode materials by constructing 3D

architectures with hierarchically porous structure. A facile wet chemistry method was used to prepare 3D $SnO_2$/graphene composites, in which graphene nanosheets self-bridge to form continuous 3D networks with interconnected porous channels and $SnO_2$ nanoparticles are homogeneously distributed on graphene nanosheets. The graphene conducting networks provide an efficient and continuous electron pathway, which can minimize the interparticle electron transfer. Furthermore, the large interstitial areas with interconnected hierarchical pores enable efficient electrolyte penetration, which is beneficial for sufficient electrode/electrolyte interactions. The integration of $SnO_2$ nanoparticles with hierarchically porous graphene frameworks can lead to fast $Na^+$ diffusivity and high electronic conductivity. When applied as anode materials for SIBs, the as-prepared $SnO_2$/graphene aerogel exhibited a high reversible capacity of 451 mA h $g^{-1}$. After being cycled at 20 mA $g^{-1}$ for 100 cycles, the $SnO_2$/graphene electrode still maintained a capacity of 322 mA h $g^{-1}$, which is 8.5 times over the bare $SnO_2$ electrode. The 3D $SnO_2$/graphene composite also demonstrated a promising high-rate performance, *i.e.*, 220 mA h $g^{-1}$ at a current density of 640 mA $g^{-1}$, which is better than that of other $SnO_2$/C materials.

## 7.2 Experimental

### 7.2.1 Materials preparation

Graphene oxide (GO) nanosheets were synthesized from natural graphite powders by a modified Hummers' method.[305] In a typical synthesis process for the preparation of $SnO_2$/graphene aerogels, $SnCl_4 \cdot 5H_2O$ was mixed with 20 mL GO aqueous suspension (2 mg $mL^{-1}$, pH = 6) by mechanical stirring at room temperature for 0.5 h. Then, the mixed precursor solution was heated to 180 °C in a Teflon-lined autoclave (25 mL in capacity) and

maintained at 180 °C for 24 h. The precipitates were cooled down to room temperature, collected, and washed with distilled water and ethanol several times. The products were collected after being freeze-dried at -80 °C overnight. The mass of $SnCl_4 \cdot 5H_2O$ for the preparation of SGA-1, SGA-2, SGA-3, and SGA-4 were 19, 28, 112, and 168 mg, respectively.

### 7.2.2 Structural and physical characterization

The crystal structure and phases of the as-prepared materials were characterized by X-ray diffraction (XRD, Siemens D5000) using Cu Kα radiation with a scanning step of 0.02° $sec^{-1}$. The morphology was analyzed by field emission scanning electron microscopy (FESEM, Zeiss Supra 55VP). The details of the morphology were further characterized by transmission electron microscopy (TEM) and high-resolution TEM (HRTEM, JEOL JEM-2011). The $SnO_2$ loading ratio was measured using a TGA/differential thermal analysis (DTA) analyzer (TA Instruments, SDT 2960 module, New Castle, DE, USA) at a heating rate of 10 °C $min^{-1}$ in air from room temperature to 800 ºC. The TGA balance sensitivity is +/- 0.1 µg. About 2 mg of samples was used for each TGA measurement.

### 7.2.3 Cell assembly and electrochemical testing

The electrodes were prepared by dispersing the as-prepared material (70 wt%), carbon black (20 wt%), and poly (vinylidene fluoride) binder (PVDF, 10 wt%) in N-methyl-2-pyrrolidone (NMP) to form a slurry. The resultant slurry was pasted onto copper foil using a doctor blade and dried in a vacuum oven for 12 h, followed by pressing at 200 kg $cm^{-2}$. The mass of each electrode is around 1.0 mg. The area of each electrode is 1.0 × 0.9 $cm^2$. Electrochemical measurements were carried out using two-electrode coin cells with Na metal as counter and

reference electrode and glass microfiber (Whatman) as the separator. CR2032-type coin cells were assembled in an argon-filled glove box (UniLab, Mbraun, Germany). The electrolyte solution was 1 M $NaClO_4$ dissolved in a mixture of ethylene carbonate (EC) and propylene carbonate (PC) with a volume ratio of 1:1, in which 5 vol.% fluoroethylene carbonate (FEC) was added as electrolyte additive. The charge-discharge measurements were performed at different current densities in the voltage range from 0.01 to 3 V *vs.* $Na^+/Na$ using a computer-controlled Neware Battery Testing system. For the $SnO_2$/graphene electrode, the obtained specific capacities were based on the total mass of the $SnO_2$/graphene composite. Cyclic voltammetry (CV) was conducted by using a CHI 660C electrochemical workstation between 0.01 and 3 V *vs.* $Na^+/Na$ with a scan rate of 0.1 mV $s^{-1}$. For the electrochemical impedance spectroscopy (EIS), the excitation amplitude applied to the cells was 5 mV.

### 7.3 Results and Discussion

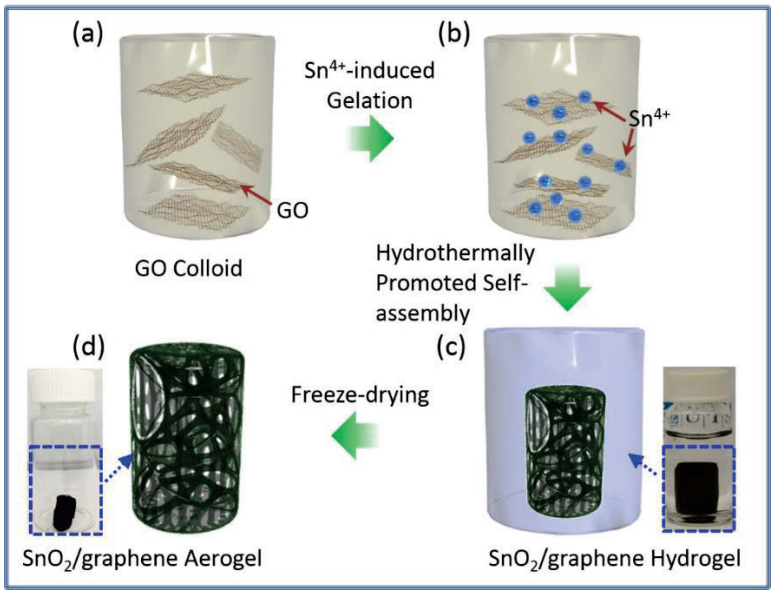


**Figure 7.1** Schematic illustration for the preparation of $SnO_2$/graphene aerogels.

The $SnO_2$/graphene aerogel was prepared by a self-assembly method. **Figure 7.1** shows the preparation process. Graphene oxide (GO), a well-known amphiphilic macromolecule with hydrophilic oxygen-containing groups (carboxylic groups and hydroxyl groups) and a more hydrophobic basal plane, was used as the precursor for the supramolecular assembly of graphene through a wet chemistry approach. In a typical process, GO powder was dispersed in water to form a concentration of 2 mg $mL^{-1}$. The amphiphilic property of GO leads to the formation of stable GO colloids in water (**Figure 7.1a**). As a result of the ionization of the carboxylic groups and hydroxyl groups on GO surface, GO nanosheets became negatively charged, which has been evidenced by zeta potential analysis.[381] Then, $SnCl_4 \cdot 5H_2O$ was added into the GO colloid. The positively charged $Sn^{4+}$ ions attached to the GO surfaces due to the electrostatic attraction. As a result, the electrostatic repulsion force was screened, resulting in the gelation of GO colloids. In this step, the binding interactions, such as the hydrogen bonding, π-π stacking and hydrophobic effect, drove the formation of $Sn^{4+}$/GO assemblies. Moreover, $Sn^{4+}$ ions with high coordination capability act as cross-linkers, which are beneficial for the construction of 3D architecture.[382] In the third step, the $Sn^{4+}$/GO gel was subjected to hydrothermal treatment at 180 $^oC$ for 24 h. The hydrolysis of $Sn^{4+}$ and crystallization resulted in the formation of $SnO_2$ nanoparticles. As shown in **Table 7.1**, GO has an O/C atomic ratio of 0.647. After hydrothermal reduction, the ratio was reduced to 0.147, suggesting the efficient reduction of GO by the hydrothermal treatment at 180 $^oC$.[383] The reduction can increase the binding interactions and decrease the repulsion force between adjacent graphene nanosheets, which promotes the self-assembly process to form $SnO_2$/graphene hydrogel (**Figure 7.1c**). The $SnO_2$/graphene hydrogel was then freeze-dried at -80 $^oC$ overnight and the resultant aerogel was obtained (**Figure 7.1d**).

**Table 7.1** Elemental analysis of GO and graphene obtained by hydrothermal reduction

| | Carbon (at.%) | Oxygen (at.%) | O/C ratio |
|---|---|---|---|
| GO | 60.7 | 39.3 | 0.647 |
| graphene | 87.2 | 12.8 | 0.147 |

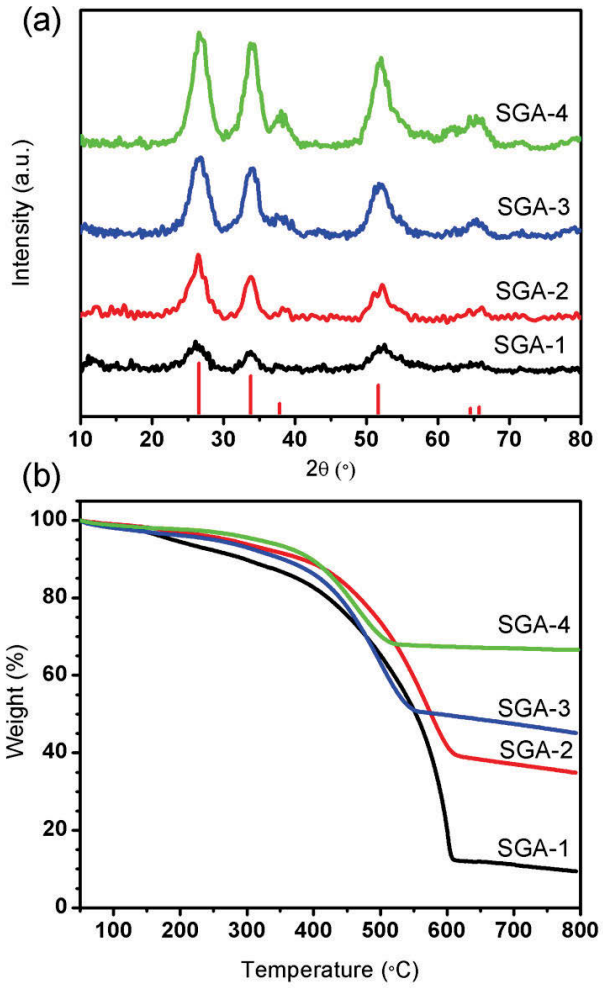


**Figure 7.2** XRD patterns (a) and TGA curves (b) of SGA-1, SGA-2, SGA-3, and SGA-4. The TGA measurement was conducted at a heating rate of 10 °C $min^{-1}$ in air from room temperature to 800 ºC.

By increasing the concentration of $Sn^{4+}$, a series of $SnO_2$/graphene aerogels with different $SnO_2$ ratio were obtained (denoted as SGA-x, x = 1, 2, 3, and 4). **Figure 7.2a** shows the XRD

patterns of the as-prepared SGA-x aerogels. All four aerogels display diffraction peaks at 26.6°, 33.9°, 37.9°, 51.8°, 64.7°, and 65.9°, which can be indexed to the (110), (101), (200), (211), (112), and (301) planes of rutile $SnO_2$ (JPCDS No. 41-1445), respectively. Thermogravimetric analysis (TGA) on the as-prepared aerogels was performed in air at a heating rate of 10 °C $min^{-1}$ to measure the weight ratio of $SnO_2$ in aerogels. As shown in **Figure 7.2b**, the $SnO_2$ weight contents in SGA-1, SGA-2, SGA-3, and SGA-4 were determined to be 12.1 wt%, 38.5 wt%, 48.4 wt%, and 67.3 wt%, respectively.

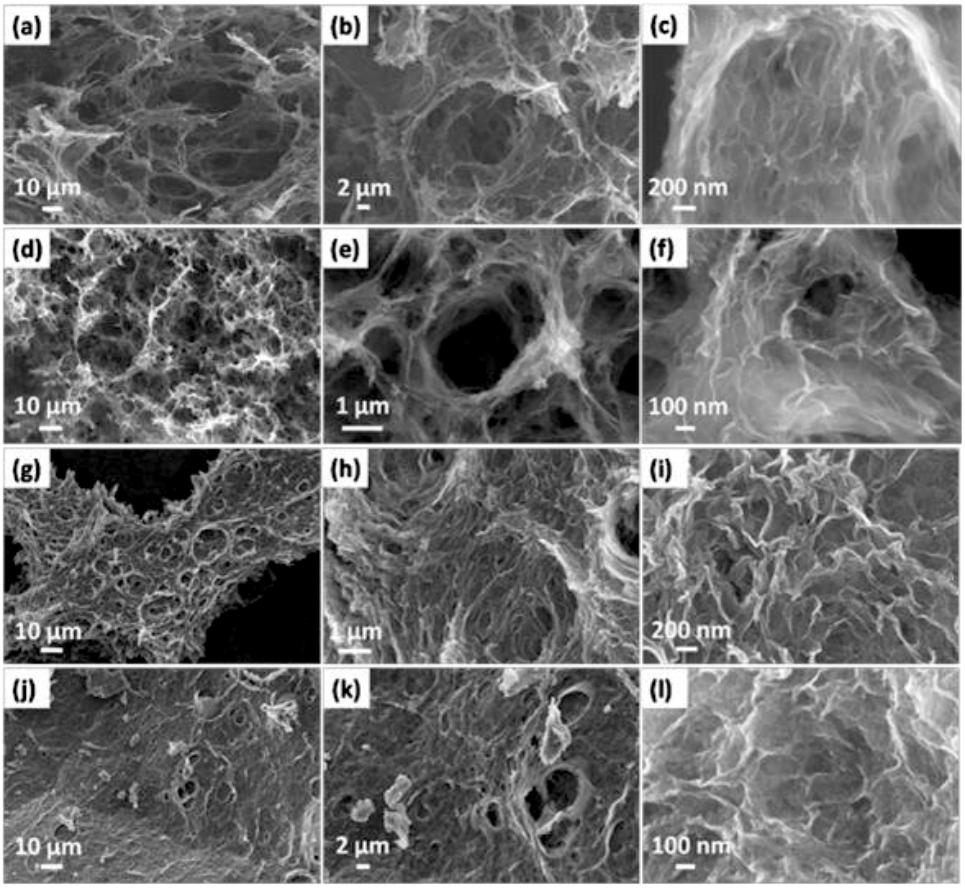


**Figure 7.3** Low, medium, and high magnification SEM images of SGA-1 (a, b, c), SGA-2 (d, e, f), SGA-3 (g, h, i), and SGA-4 (j, k, l). The scale bars in a, b, d, e, g, h, j, and k are 10, 2, 10, 1, 10, 1, 10, and 2 µm, respectively, and the scale bars in c, f, i, and l are 200, 100, 200, and 100 nm, respectively.

The morphology and microstructure of the as-prepared samples were characterized by scanning electron microscopy (SEM), as shown in **Figure 7.3**. The SGA-1 prepared at the lowest $Sn^{4+}$ concentration displays a well-defined, highly interconnected and 3D graphene skeleton with hierarchical pores ranging from several to tens of micrometers (**Figure 7.3a and b**). Such an open structure is favorable for the diffusion and transport of electrolyte during rapid charge/discharge processes. From the high-resolution SEM image of the SGA-1 (**Figure 7.3c**), the corrugated graphene nanosheets with pores can be clearly identified. Similar morphology of graphene nanosheets can also be observed in other aerogels (**Figure 7.3f, i, and l**). As can be seen from **Figure 7.3(d and e)**, when the concentration of $Sn^{4+}$ in the $Sn^{4+}$/GO precursor increases, the interconnected porous 3D graphene framework with continuous macropores still can be maintained in the resultant aerogel (SGA-2). However, the size of the macropores decreases obviously (**Figure 7.3d and e**). It should also be noted that the thickness of the graphene wall in SGA-2 increases, compared to SGA-1. This could originate from the energetically favorable layer-by-layer re-stacking of GO nanosheets due to the screening effect of $Sn^{4+}$ for the electrostatic repulsion force between adjacent GO nanosheets. The re-stacking of GO nanosheets is more serious at a high $Sn^{4+}$ concentration, which leads to the disappearance of interconnected macropores in the SGA-3 (**Figure 7.3g and h**) and SGA-4 (**Figure 7.3j and k**). From the SEM results, it can be concluded that the balance of the binding interactions and the electrostatic repulsion force can be effectively tuned by the concentration of $Sn^{4+}$ in the $Sn^{4+}$/GO precursor. It is the key factor to determine the morphology evolution and structure of supramolecularly self-assembled aerogels.

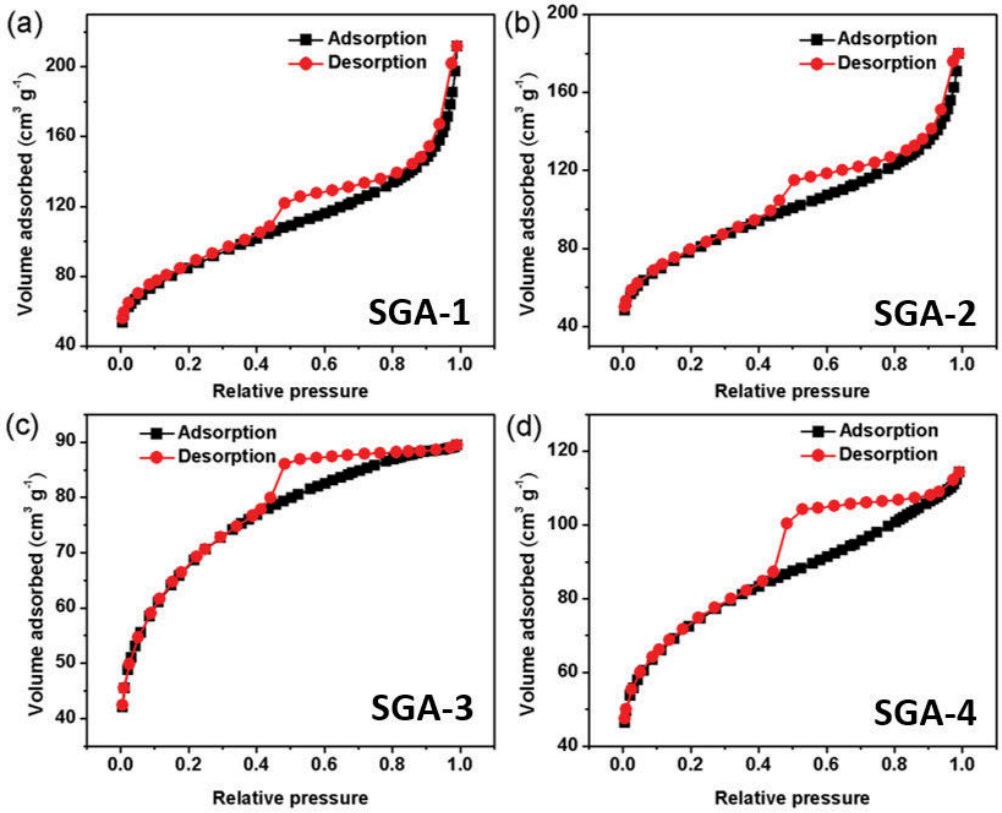


**Figure 7.4** $N_2$ isotherms of SGA-1 (a), SGA-2 (b), SGA-3(c), and SGA-4(d).

**Table 7.2** Survey of the BET surface area and pore volume of the as-prepared SGA-1, SGA-2, SGA-3, and SGA-4

| Sample | BET surface area ($m^2$ $g^{-1}$) | Pore volume ($cm^3$ $g^{-1}$) |
|---|---|---|
| SGA-1 | 292 | 0.27 |
| SGA-2 | 270 | 0.23 |
| SGA-3 | 246 | 0.12 |
| SGA-4 | 226 | 0.08 |

The nitrogen-sorption characterizations further highlight the important role of $Sn^{4+}$ concentration in constructing hierarchically porous architecture (**Figure 7.4**). As a result of

the increased concentration of $Sn^{4+}$ in the $Sn^{4+}$/GO precursor, the BET surface area of the as-prepared aerogels decreases in the order of SGA-1 (292 $m^2 g^{-1}$) > SGA-2 (270 $m^2 g^{-1}$) > SGA-3 (246 $m^2 g^{-1}$) > SGA-4 (226 $m^2 g^{-1}$). The pore volumes of SGA-1, SGA-2, SGA-3, and SGA-4 are 0.27, 0.23, 0.12, and 0.08 $cm^3 g^{-1}$, respectively (**Table 7.2**). Obviously, the pore volume decreases in the same order as the surface area, which is ascribed to the re-stacking of graphene nanosheets due to the screened electrostatic repulsive force at high $Sn^{4+}$ concentration.

Transmission electron microscopy (TEM) was employed to further investigate the microstructural characteristics of the as-prepared aerogels (**Figure 7.5**). For SGA-1 with a $SnO_2$ weight ratio of 12.1%, $SnO_2$ nanoparticles are loosely dispersed on graphene nanosheets (**Figure 7.5a**). The TEM images of SGA-2, SGA-3 and SGA-4 (**Figure 7.5b-d**) illustrate that $SnO_2$ nanoparticles are uniformly and densely packed on graphene nanosheets when the $SnO_2$ weight ratio is increased. It is worth noting that no big $SnO_2$ agglomerates could be found in any of the composites. On the contrary, bare $SnO_2$ tended to aggregate to form big agglomerates (**Figure 7.6**). These results suggest that there is a favorable interaction between $SnO_2$ nanoparticles and the graphene matrix, and graphene can effectively prevent the aggregation of $SnO_2$ nanoparticles. The lattice-resolved high-resolution TEM image of a single $SnO_2$ nanoparticle shows a neighboring interplanar distance of 0.33 nm, which can be indexed to the (110) plane of rutile $SnO_2$. The selected-area electron diffraction (SAED) pattern in **Figure 7.5f** exhibits distinct diffraction rings, corresponding to the (110), (101), (210), and (310) crystalline planes of $SnO_2$. This indicates that the $SnO_2$ nanoparticles are crystalline, which is in agreement with the XRD result.

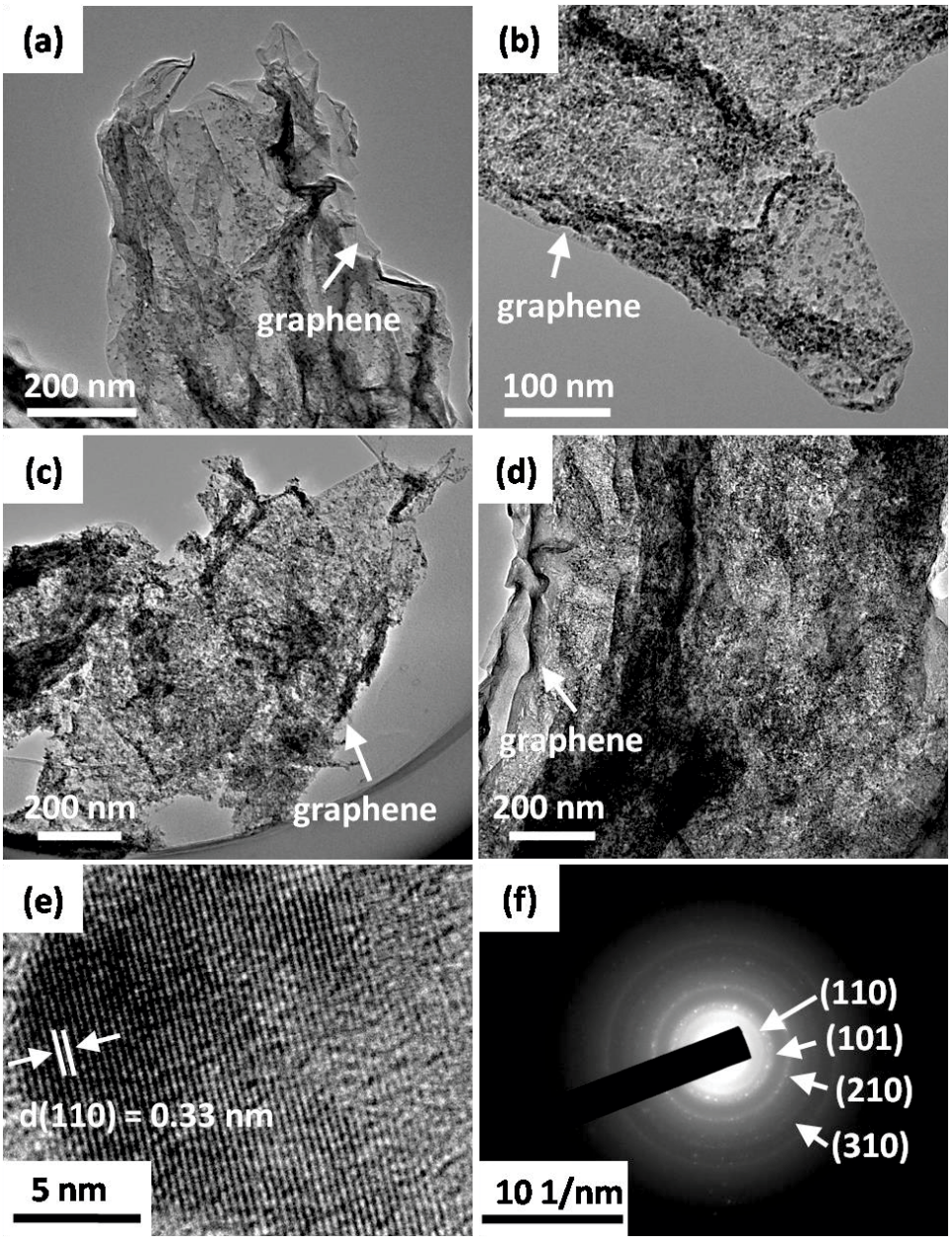


**Figure 7.5** TEM images of SGA-1 (a), SGA-2 (b), SGA-3 (c), and SGA-4 (d). Lattice-resolved high-resolution TEM image of a single $SnO_2$ nanoparticle (e), showing a neighboring interplanar distance of 0.33 nm, which can be indexed to the (110) plane of $SnO_2$. SAED pattern of $SnO_2$ (f).

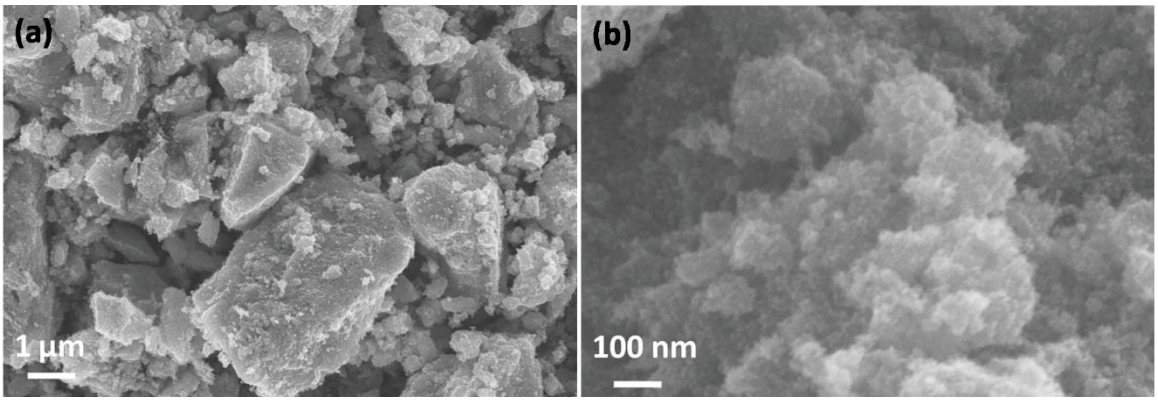


**Figure 7.6.** SEM images of bare $SnO_2$.

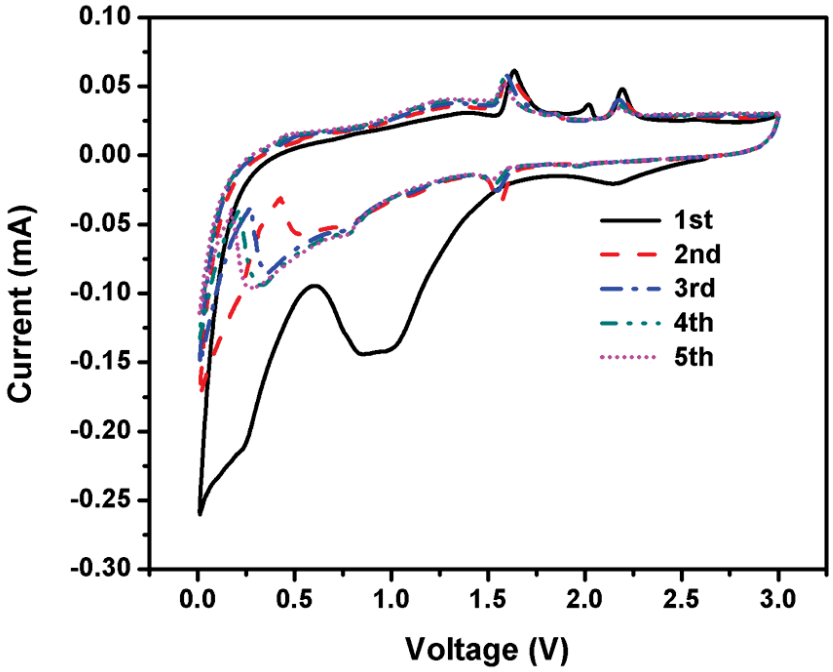


**Figure 7.7** CV curves of the as-prepared SGA-2.

The electrochemical performance of the as-prepared $SnO_2$/graphene aerogels was investigated by cyclic voltammetry (CV) in the voltage window of 0.01-3.0 V *vs.* $Na^+/Na$. As shown by the CV curves in **Figure 7.7**, the $SnO_2$/graphene electrode shows a broad cathodic peak from 1.6 V to 0.6 V, which is composed of two peaks at 1.0 V and 0.8 V,

respectively. The cathodic peak located at 1.0 V can be ascribed to the conversion reaction between $SnO_2$ and $Na^+$ to form metallic Sn embedded within amorphous $Na_2O$ matrix according to $SnO_2 + 4Na^+ + 4e^- \rightarrow Sn + 2Na_2O$, which has been confirmed by TEM observation.[262, 319] The other peak at 0.8 V originates from the decomposition of film-forming additive in the electrolyte (fluoroethylene carbonate, FEC), forming a passivation layer on the surface of the electrode, which is beneficial for the stable cycling during repeated charge-discharge processes.[384] In the following cathodic scan, the peaks in the region between 0.6 V and 0.01 V are related to the decomposition of propylene carbonate (PC), Na-Sn alloying reaction to form $Na_xSn$ compounds and the $Na^+$ storage within graphene nanosheets.[250] Based on the theoretical results by Ceder's group and assuming that the cell has an overpotential of 0.1 V,[385] the cathodic peaks at 0.2 and 0.01 V are assigned to the alloying reactions between Na and Sn to form NaSn and $Na_{15}Sn_4$.

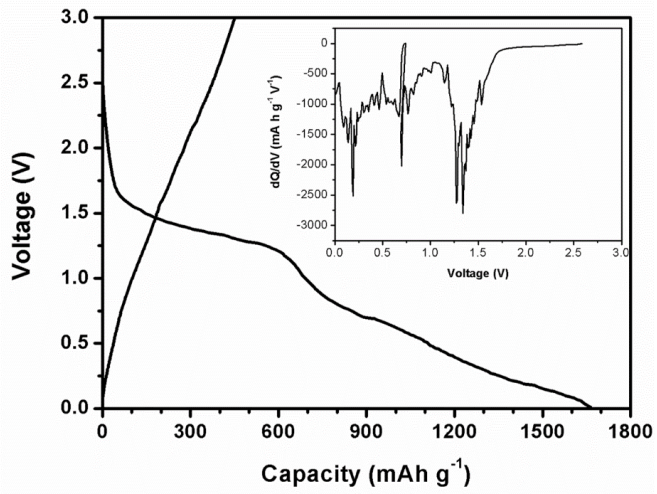


**Figure 7.8** Charge-discharge curves of SGA-2 at a current density of 20 mA $g^{-1}$. The insert shows the derivative curve (dQ/dV *vs.* V) of the 1st discharge process.

**Figure 7.8** shows the charge/discharge curves of the SGA-2 electrode and the insert is the derivative curves (dQ/dV *vs.* V). In the first discharge process, the cathodic peak between 1.5 V and 1.2 V is related to the conversion reaction from $SnO_2$ to metallic Sn. The cathodic peaks observed at 0.2 V and 0.01 V agree well with the CV results, corresponding to the alloying processes of Sn with Na to form NaSn and $Na_{15}Sn_4$. The SGA-2 electrode achieved an initial discharge capacity of 1665 mA h $g^{-1}$ with a reversible capacity of 451 mA h $g^{-1}$ at the current density of 20 mA $g^{-1}$. The initial irreversible capacity loss could be ascribed to the irreversible formation of the solid-electrolyte interface (SEI) layer on the electrode.

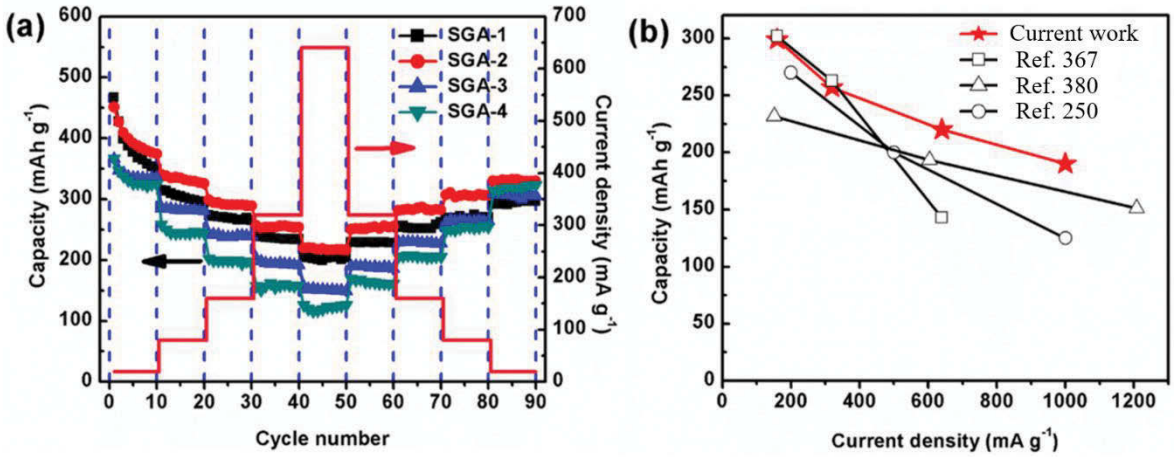


**Figure 7.9** (a) Rate performance of the as-prepared SGA-1, SGA-2, SGA-3, and SGA-4. (b) A comparison between the SGA-2 electrode and a variety of recently reported $SnO_2$/graphene anode materials for SIBs. The capacities were estimated based on the total mass of the composite.

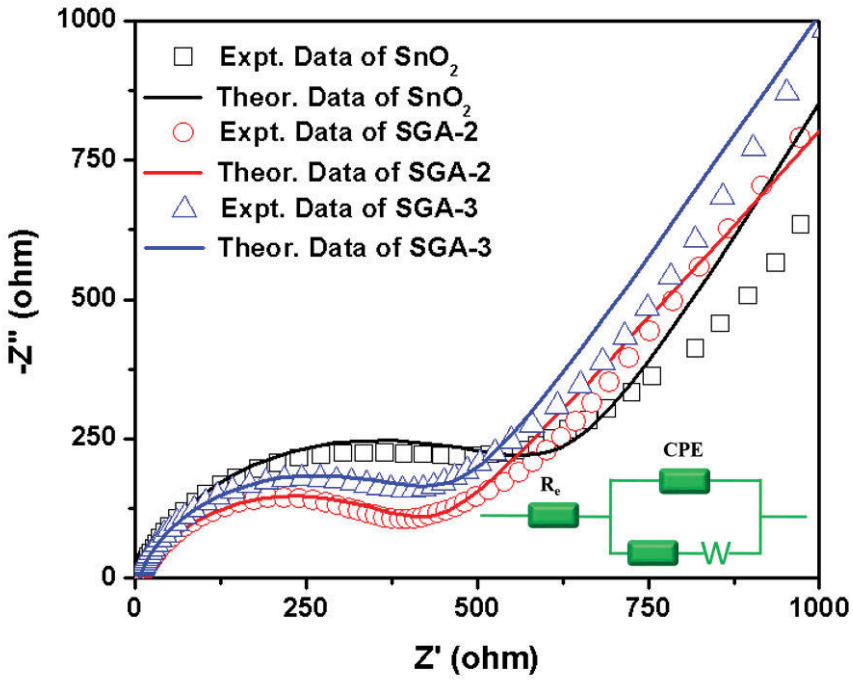


**Figure 7.10** The Nyquist plots of the $SnO_2$, SGA-2 and SGA-3 electrode, the inset shows the modeled equivalent circuit. $R_e$ is the electrolyte resistance, CPE represents constant phase element, $R_{ct}$ is the charge-transfer resistance, and $Z_w$ is the Warburg impedance.

**Table 7.3** Kinetic parameters of the $SnO_2$ and SGA-2 electrode

| Electrode | $R_e$ (Ω) | $R_{ct}$ (Ω) |
|---|---|---|
| $SnO_2$ | 7 | 631 |
| SGA-2 | 8 | 420 |
| SGA-3 | 6 | 464 |

**Figure 7.9a** shows the rate capabilities of the as-prepared aerogels. Since $SnO_2$ is the dominate host material for $Na^+$, the SGA-2 electrode delivers a higher capacity than that of SGA-1 electrode, owing to the higher loading ratio of $SnO_2$. The SGA-2 electrode exhibits

an initial reversible capacity as high as 451 mA h $g^{-1}$ at the current density of 20 mA $g^{-1}$. At the current density of 20 mA $g^{-1}$, SGA-3 and SGA-4 with high $SnO_2$ loading ratio only deliver initial reversible capacities of 366 and 367 mA h $g^{-1}$, which are lower than that of the SGA-2. This can be attributed to the stacking of $SnO_2$/graphene, inducing the insufficient electrode/electrolyte interaction, thereby resulting in incomplete electrode use. Moreover, the electronic conductivity decreases when increasing the content of semiconductive $SnO_2$. This is evidenced by the electrochemical impedance spectroscopies shown in **Figure 7.10** and **Table 7.3**, which suggest that SGA-3 exhibited a higher charge-transfer resistance (464 Ω) than that of SGA-2 (420 Ω). The excellent rate performance of the SGA-2 electrode becomes more evident as the current density increases because of faster $Na^+$ penetration within interconnected pores. As the current density increases step-by-step after 10 cycles at 40, 80, 160, 320, and 640 mA $g^{-1}$, the SGA-2 electrode delivered 340, 299, 257, and 220 mA h $g^{-1}$, respectively. The hierarchically porous conformation with uniform $SnO_2$ nanoparticles loaded on the 3D open conductive graphene network allowed fast reversible insertion/extraction of $Na^+$, which is favorable for high-rate charge and discharge. When the current density is reversed to 20 mA $g^{-1}$ after high current cycling, a reversible capacity of 349 mA h $g^{-1}$ was retained. We also compared the rate performance of the SGA-2 (38.5% $SnO_2$) in this work with other $SnO_2$/graphene electrodes reported in recent literature. These include $SnO_2$/graphene (60% $SnO_2$),[367] $SnO_2$/graphene (74% $SnO_2$),[250] and $SnO_2$/graphene (75.5% $SnO_2$)[380]. The results are shown in **Figure 7.9b**. The as-prepared SGA-2 with the lowest $SnO_2$ loading ratio exhibits highest capacity and rate performance among all previously reported $SnO_2$-based composites, which is desirable for high-power applications.

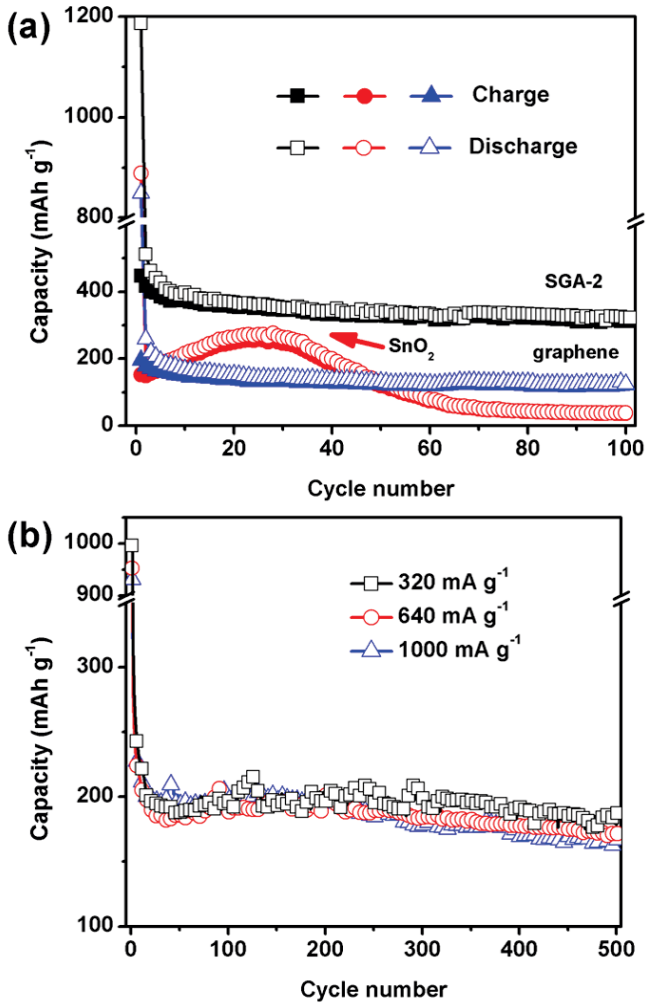


**Figure 7.11** (a) Cycling performance of SGA-2, $SnO_2$, and graphene electrode at a current density of 20 mA $g^{-1}$ (22.2 μA $cm^{-2}$). (b) Cycling performances of SGA-2 at current densities of 320, 640, and 1000 mA $g^{-1}$.

In order to evaluate long-term cycle stability, galvanostatical discharge/charge test were carried out at 20 mA $g^{-1}$ for 100 cycles (as shown in **Figure 7.11a**). The theoretical capacity of $SnO_2$ in the first discharge process is 1378 mA h $g^{-1}$ based on the reaction of $4SnO_2 + 31Na^+ + 31e^- \rightarrow Na_{15}Sn_4 + 8Na_2O$. For bare $SnO_2$ electrode, an increase of the capacity was observed in the first 25 cycles due to the activation process.[380] However, the capacity of the bare $SnO_2$ electrode droped to 38 mA h $g^{-1}$ after 100 cycles, which could be ascribed to the

large volume variation during repeated charge/discharge processes. As shown in **Figure 7.11a**, the SGA-2 electrode exhibited higher capacities than that of both graphene and bare $SnO_2$, which can be attributed to the dispersing and conducting effects of graphene for $SnO_2$ nanoparticles. Graphene has an initial reversible capacity of 195 mA h $g^{-1}$. Based on the weight ratio of graphene in SGA-2 (61.5%), graphene contributes a capacity of 120 mA h $g^{-1}$, which accounts for 26.6% of the overall capacity of SGA-2 (451 mA h $g^{-1}$). Hence, the contribution of $SnO_2$ to the overall capacity is 73.4%. The cycling stability of the SGA-2 electrode has been improved, compared to the bare $SnO_2$ electrode, owing to the small size of $SnO_2$ nanoparticles and the buffering effect of graphene nanosheets. This unique architecture can effectively tolerate large volume change during repeated charge/discharge processes. After 100 cycles, the SGA-2 electrode still maintained a capacity of 322 mA h $g^{-1}$, which is 8.5 times over the bare $SnO_2$ electrode. Furthermore, the as-prepared SGA-2 electrode shows promising cycling performance at high current density. After 500 cycles, the discharge capacities were maintained at high values when cycled at different current densities: 179 mA h $g^{-1}$ at 320 mA $g^{-1}$, 172 mA h $g^{-1}$ at 640 mA $g^{-1}$, and 168 mA h $g^{-1}$ at 1000 mA $g^{-1}$ (**Figure 7.11b**). The SGA-1, SGA-3, and SGA-4 electrodes also demonstrated stable cycling performances (as shown in **Figure 7.12-7.14**).

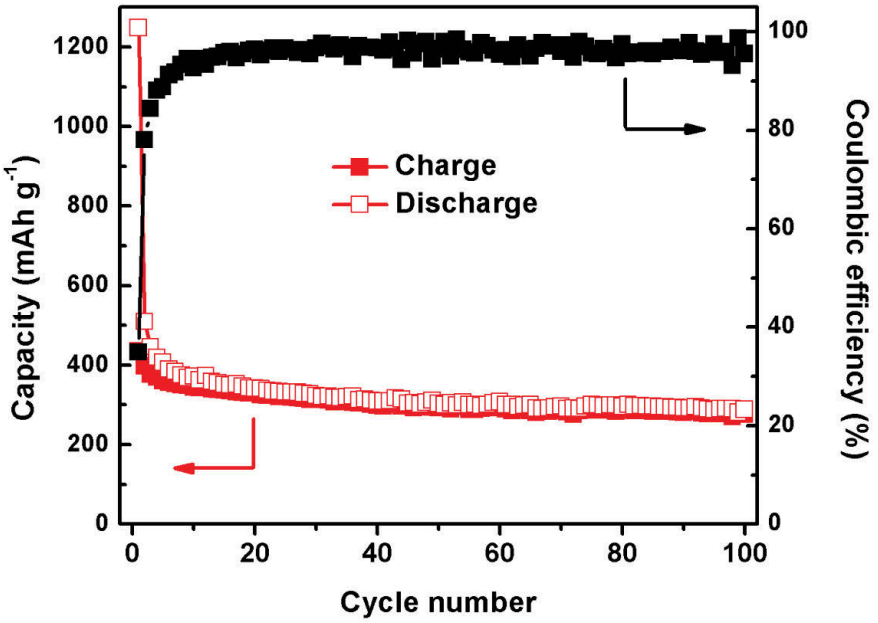


**Figure 7.12** Cycling performance and the Coulombic efficiency of the SGA-1 electrode at a current density of 20 mA $g^{-1}$.

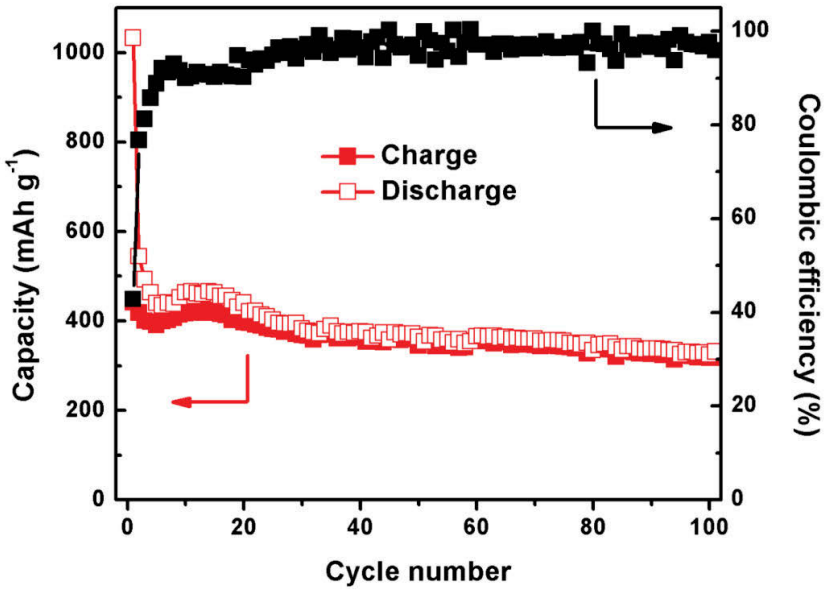


**Figure 7.13** Cycling performance the Coulombic efficiency of the SGA-3 electrode at a current density of 20 mA $g^{-1}$.

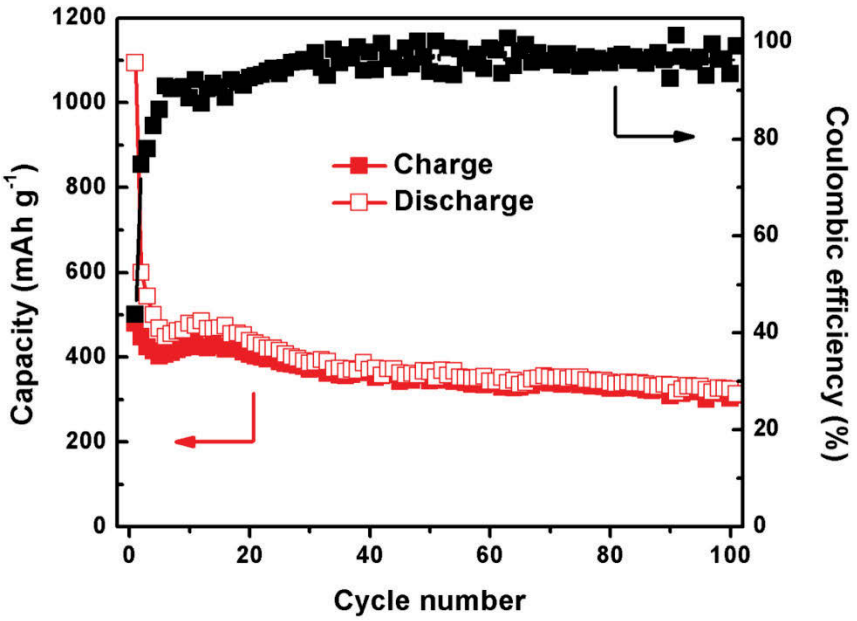


**Figure 7.14** Cycling performance the Coulombic efficiency of the SGA-4 electrode at a current density of 20 mA $g^{-1}$.

The comparison of the charge transfer behavior between 3D aerogel (SGA-2) and $SnO_2$ was conducted by electrochemical impedance spectroscopy (EIS) measurements. The results are shown in **Figure 7.10** and **Table 7.3**. The SGA-2 electrode shows a charge-transfer resistance ($R_{ct}$) of 420 Ω, which is lower than that of $SnO_2$ electrode (631 Ω). Therefore, the SGA-2 electrode possesses a higher exchange current density ($i_0 = RT/nFR_{ct}$) than that of $SnO_2$, indicating more preferable sodium-ion diffusion kinetics, which favors fast sodiation/de-sodiation processes.[386]

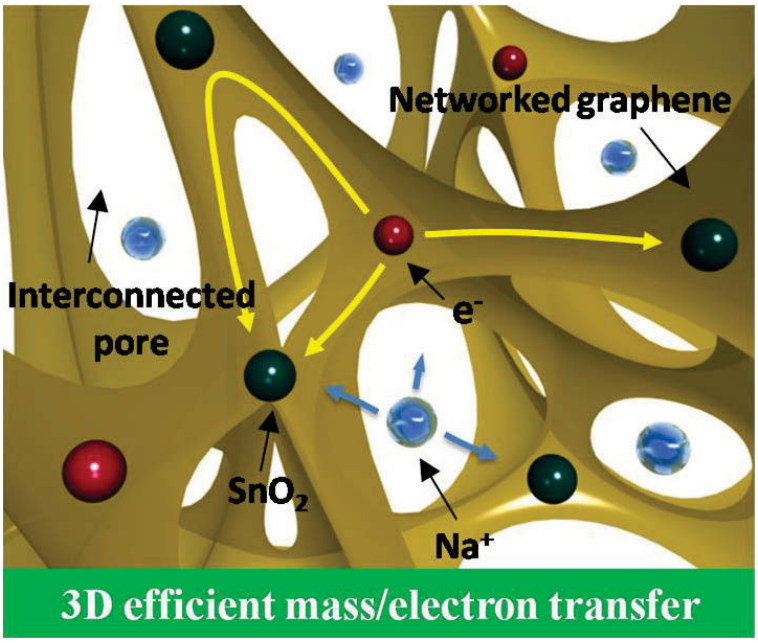


**Figure 7.15** Schematic illustration of the charge transfer within $SnO_2$/graphene aerogel electrodes, showing that the 3D hierarchically porous architecture favors both fast $Na^+$ diffusion and efficient electron transfer.

The promising electrochemical performance of $SnO_2$/graphene aerogel could be ascribed to the open 3D architecture, in which $SnO_2$ nanoparticles are homogeneously loaded on the conductive graphene framework with hierarchically porous structure (as schematically depicted in **Figure 7.15**). This unique architecture guarantees 3D efficient mass/electron transfer. Firstly, due to the presence of the interconnected channels, a high flux of Na-ions within the porous architecture is realized, which promises easy ion accessibility for the electro-active material ($SnO_2$). Secondly, the networked graphene skeleton consists of a fast and continuous electron pathway, which allows electrons to flow along the conductive network to reach $SnO_2$ nanoparticles. The optimized mass transport and electron transfer enables excellent high-rate performance of the as-prepared $SnO_2$/graphene aerogels. Thirdly, graphene acts as dispersing agent to circumvent the agglomeration of $SnO_2$ nanoparticles,

which is beneficial for the electrode/electrolyte interaction. Furthermore, the flexible graphene matrix provides good strain accommodation to mitigate the volume change of $SnO_2$ nanoparticles during repeated sodiation/de-sodiation processes, which helps improve the cycling stability.

### 7.4 Conclusions

In summary, $SnO_2$/graphene aerogels were successfully prepared by the $Sn^{4+}$-mediated gelation of GO colloids followed by hydrothermally promoted self-assembly. The as-prepared aerogels display a hierarchically porous structure with $SnO_2$ nanoparticles homogeneously loaded on the networked graphene scaffold. The unique architecture is favorable for the efficient $Na^+$ and electron transfer simultaneously, which endows $SnO_2$/graphene composite anodes with promising capacities and high-rate performance for sodium-ion storage. The $SnO_2$/graphene aerogels exhibited an initial reversible capacity of 451 mA h $g^{-1}$ with a stable cycling performance at the current density of 20 mA $g^{-1}$. Even at the high current density of 1000 mA $g^{-1}$, the electrode achieved a capacity of 168 mA h $g^{-1}$ after 500 cycles.

# Chapter 8 Sn@CNT Nanopillars Grown Perpendicularly on Carbon Paper: a Novel Free-standing Anode for Sodium Ion Batteries

## 8.1 Introduction

Some elementary substances that can form alloys with sodium provide substantial alternatives to host more Na-ions, such as Sn (847 mA h $g^{-1}$), Pb (485 mA h $g^{-1}$), Sb (600 mA h $g^{-1}$), and P (2560 mA h $g^{-1}$). Among them, Sn-based electrode materials have attracted extraordinary attention.[247, 248] This is owing to: (i) the cheap and abundant sources of tin;[387] (ii) the variety of Sn-based compounds with different physiochemical properties, such as SnO, [388] $SnO_2$,[250, 262, 367, 368] $SnS_2$,[241, 289] $Sn_{4+x}P_3$,[257, 258] and intermetallic compounds [358, 389, 390].

However, bare Sn-based materials suffer from low kinetics associated with the slow solid-state diffusion of $Na^+$ in electrodes ($Na^+$ is 55% larger than $Li^+$).[391] To circumvent the sluggish $Na^+$ diffusion kinetics, reducing the dimensions by using nanosized materials is more effective than increasing the ion diffusion co-efficient D, because the time constant t for diffusion is proportional to the square of the diffusion length L ($t \approx L^2/D$).[133] Therefore, it is desirable to prepare nanostructured Sn for SIBs. Unfortunately, the insertion of $Na^+$ induces huge volume expansion (420%), which leads to rapid capacity fading of the electrode. Some positive efforts have been made to increase the cyclability of Sn nanostructures by the introduction of electronically conductive ingredients such as carbon and conducting polymers. For example, in order to buffer the mechanical stress associated with the sodiation process, Hu *et al.* developed an anode consisting of a Sn thin film deposited onto a hierarchical wood fibre substrate.[247] To buffer the volume change and aggregation of Sn during cycling, Wang *et al.* developed tin-coated viral nanoforests as SIB anode materials.[248]

Kumta and co-workers reported a mechanically milled Sn/C composite as anode material for SIBs.[366] These studies suggest that it is effective to improve the electrochemical properties in SIBs by dispersing tin nanostructures in a carbon matrix. In these Sn-based electrodes, the electro-active material was mixed with polymeric binder and conductive agent, which was then coated as a film electrode onto the current collector (copper foil) by a dispersion technique. However, the metal current collector is relatively heavy in weight (10 mg $cm^{-2}$), which accounts for about 10 wt.% of the total weight of the cell.[392] Furthermore, the traditional electrode manufacturing technique falls short of preserving the benefits of electrochemistry at nanoscale: (i) the use of binder will significantly decrease the electrical conductivity of the electrode, hindering the potential applications in high-performance SIBs; (ii) the penetration of $Na^+$ in the film-like electrode is limited due to the stacking of the components (electro-active material, binder, and carbon black); (iii) there are some problems arising from the interfaces, *i.e.*, the current collector/active material interface and active material/active material interface.[391] To meet the requirements for high-performance SIBs, an ideal electrode configuration is a free-standing electrode having three-dimensional (3D) architecture, which consists of one-dimensional (1D) electro-active material grown periodically in a vertical fashion on an ultralight conductive substrate.[393, 394] This ideal electrode architecture is able to provide efficient 3D transport pathways for both $Na^+$ ions and electrons, enabling SIBs to achieve superior electrochemical performance, such as high capacity and excellent rate capability.

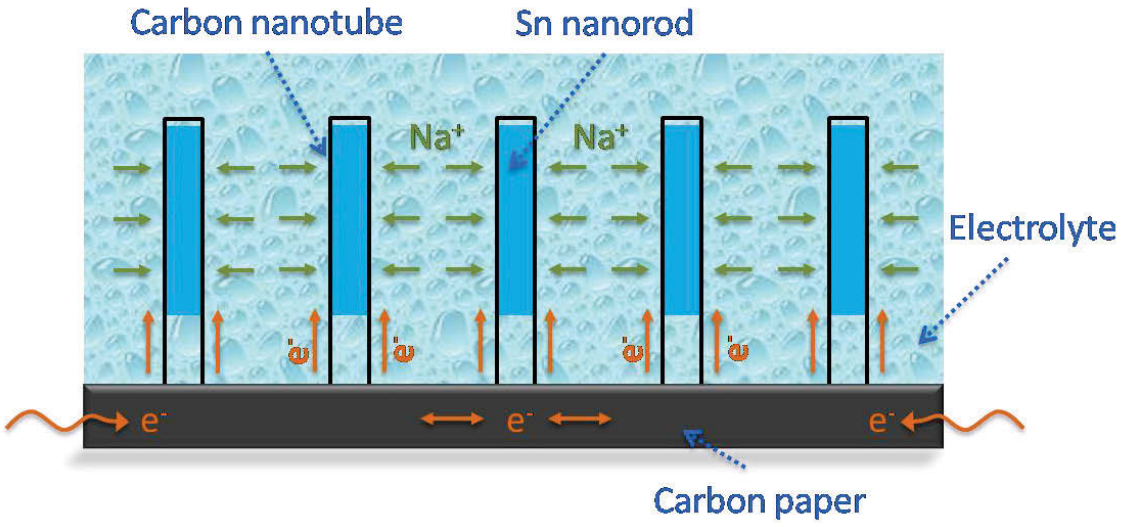


**Figure 8.1** The schematic illustration of the 3D free-standing electrode consisting of core-sheath structured Sn@CNT nanopillars grown vertically on carbon paper.

Herein, we report the preparation of core-sheath structured Sn@carbon nanotube (Sn@CNT) nanopillars grown vertically on carbon paper (defined as Sn@CNT-CP) through a novel and facile soaking-chemical vapour deposition (S-CVD) technique. The architecture of the free-standing Sn@CNT-CP electrode is shown in **Figure 8.1**. The conformation has the following characteristics: firstly, the integrated material can be directly applied as self-supported electrode without the use of binder and current collector, which significantly reduces the total mass of SIBs; secondly, the $Na^+$ diffusion kinetics can be improved, owing to the high length/radius ratio of 1D nanorods; thirdly, the Sn@CNT nanopillars grown in a vertically aligned manner provide an open architecture for sufficient electroactive material/electrolyte contact; fourthly, in the present electrode geometry, each Sn@CNT nanopillar is connected to the carbon paper, which offers direct 1D electronic pathways allowing a more efficient charge transport. Moreover, the carbon paper serves as a dispersive matrix for Sn, which is beneficial for the cyclability. These merits endow the 3D Sn@CNT-CP anode with promising

electrochemical performance for Na-ion storage. The as-prepared electrode exhibited a reversible capacity of 887 μA h $cm^{-2}$, an excellent high rate capability and an extended cycle life.

## 8.2 Experimental

### 8.2.1 Sample preparation

Commercial facial tissue (FT) was used as the source of carbon paper owing to its ultralight, thin and porous merits. FT was purified as follows. Firstly, FT with desired shape and size was soaked in 20 mL of distilled water and left still for 2 h. 4 mL concentrated hydrochloric acid was then added to the above mixture, which was left undisturbed for another 12 h. The solid was washed by vacuum filtration for several times with distilled water to remove the impurities. The wet tissue was added to a solution containing 0.7 g of $SnCl_4 \cdot 5H_2O$ dissolved in 5 mL $H_2O$ for 30 min to ensure thorough soaking of the FT. After removing from $SnCl_4$ aqueous solution, the tissue was subjected to freezing-drying overnight, and FT homogeneously loaded with $SnCl_4$ was obtained. Sn@CNT-CP was obtained by an ambient pressure chemical vapour deposition (APCVD) method using acetylene ($C_2H_2$) as the carbon source under elevated temperature. In detail, a piece of $SnCl_4$-loaded FT was put into an $Al_2O_3$ boat and placed in the middle of a horizontal tube furnace. The tube furnace was perfused with 80 sccm $H_2$/Ar mixed gas ($H_2$: 10%) until the temperature reached 300 °C at a ramp of 5 °C $min^{-1}$ and then the atmosphere was changed to a reactive gas mixture ($C_2H_2$/Ar gas, $C_2H_2$: 5%, 80 sccm). The temperature was further raised to 600 °C at a heating rate of 5 °C $min^{-1}$. After holding at 600 °C for 2 h, the tube furnace cooled to room temperature

under pure Ar flow naturally, and core-sheath structured Sn@CNT grown vertically on carbon paper was produced.

### 8.2.2 Structural and physical characterization

The crystal structure and phases of the as-prepared materials were characterized by X-ray diffraction (XRD, Siemens D5000) using Cu Kα radiation with a scanning step of 0.02° $sec^{-1}$. The morphology was analysed by field emission scanning electron microscopy (FESEM, Zeiss Supra 55VP). The details of the morphology were further characterized by transmission electron microscopy (TEM) (HRTEM, JEOL JEM-2011). The elemental mapping was conducted on Zeiss EVO MA 15 SEM equipped with EDX. The Sn loading mass was measured using a TGA/differential thermal analysis (DTA) analyser (TA Instruments, SDT 2960 module, New Castle, DE, USA) at a heating rate of 10 °C $min^{-1}$ in air from room temperature to 700 ºC. The pyrolysis of FT was investigated on the same TGA/DTA analyser at a heating rate of 5 °C $min^{-1}$ in $N_2$ flow from room temperature to 1000 ºC. Raman spectra were collected with a Renishaw inVia Raman spectrometer system (Gloucestershire, UK) equipped with a Leica DMLB microscope (Wetzlar, Germany) and a Renishaw He-Ne laser source producing 17 mW at 633 nm.

### 8.2.3 Electrochemical testing

CR2032-type coin cells were assembled in an argon-filled glove box (UniLab, Mbraun, Germany). The as-obtained Sn@CNT-CP was cut into 0.6 × 0.6 $cm^2$ and directly used as a self-supported electrode. For comparison, binder-enriched electrodes were prepared by dispersing Sn@CNT-CP composites (80 wt %), carbon black (10 wt %), and poly (vinylidene fluoride) binder (PVDF, 10 wt %) in N-methyl-2-pyrrolidone (NMP) to form a slurry. The

resultant slurry was pasted onto copper foil using a doctor blade and dried in a vacuum oven for 12 h, followed by pressing at 200 kg $cm^{-2}$. Na metal pieces were used as counter and reference electrode. The positive and negative electrodes were electronically separated by glass microfiber (Whatman) saturated with electrolyte. The electrolyte solution was 1 M $NaClO_4$ dissolved in a mixture of ethylene carbonate (EC) and propylene carbonate (PC) with a volume ratio of 1:1, in which 5 vol.% fluoroethylene carbonate (FEC) was added as electrolyte additive. The charge-discharge measurements were performed at different current densities in the voltage range from 0.01 to 2.6 V *vs.* $Na^+/Na$ using a computer-controlled Neware Battery Testing system. Cyclic voltammetry (CV) was conducted by using a CHI 660C electrochemical workstation between 0.01 and 2.6 V *vs.* $Na^+/Na$ with a scan rate of 0.1 mV $s^{-1}$. For the electrochemical impedance spectroscopy (EIS), the excitation amplitude applied to the cells was 5 mV.

### 8.2.4 Full Na-ion cell assembly

A coin cell (CR2032) was assembled for full cell testing. The cathode was $Na_{0.80}Li_{0.12}Ni_{0.22}Mn_{0.66}O_2$ mixed with carbon black and PVDF in the weight ratio of 85:10:5. Free-standing Sn@CNT-CP was used as anode directly. The cathode to anode weight ratio was 3:1. The electrolyte was the same as that used in the half-cell testing and Whatman glass microfiber was used as separator. Galvanostatic charge/discharge was conducted on a computer-controlled Neware Battery Testing system between 1.0–4.2 V.

## 8.3 Results and Discussions

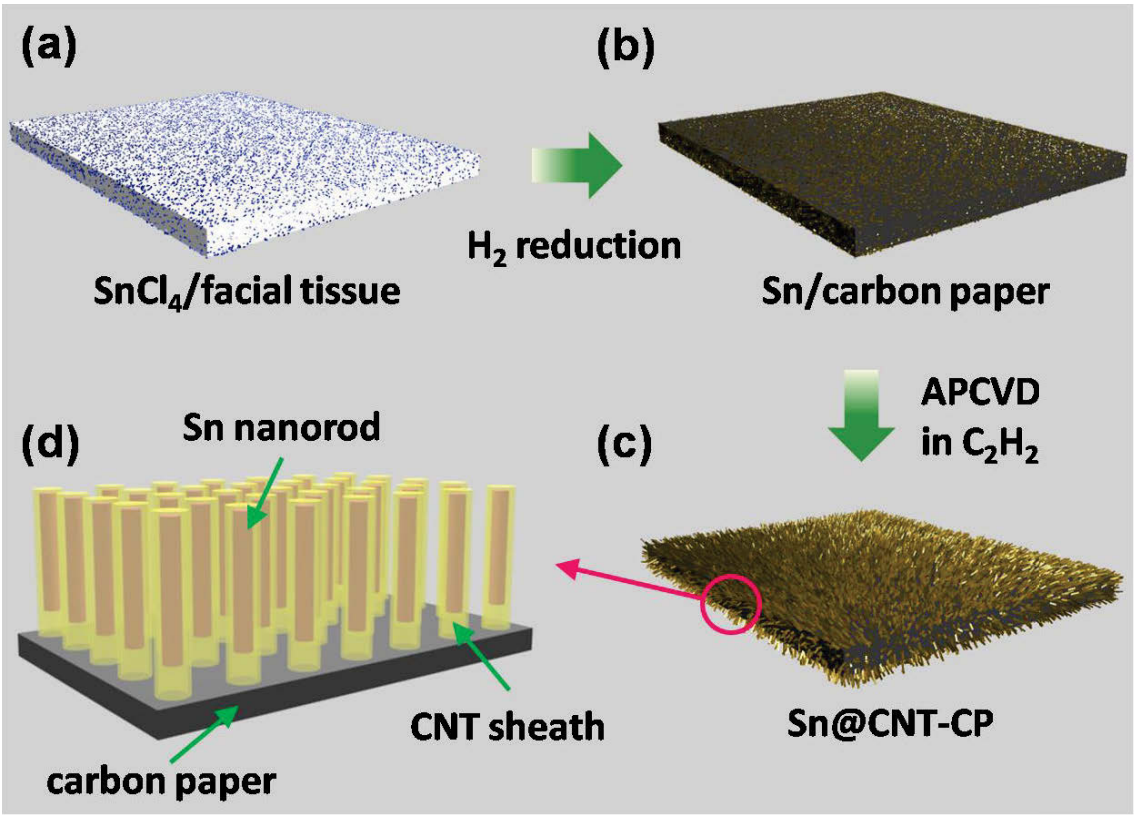


**Figure 8.2** A schematic illustration for the preparation procedure of 3D Sn@CNT-CP free-standing electrode. (a) $SnCl_4$/FT. (b) Sn/carbon paper. (c) Sn@CNT-CP electrode with 3D nanoarchitecture. (d) Structural details of the 3D Sn@CNT-CP.

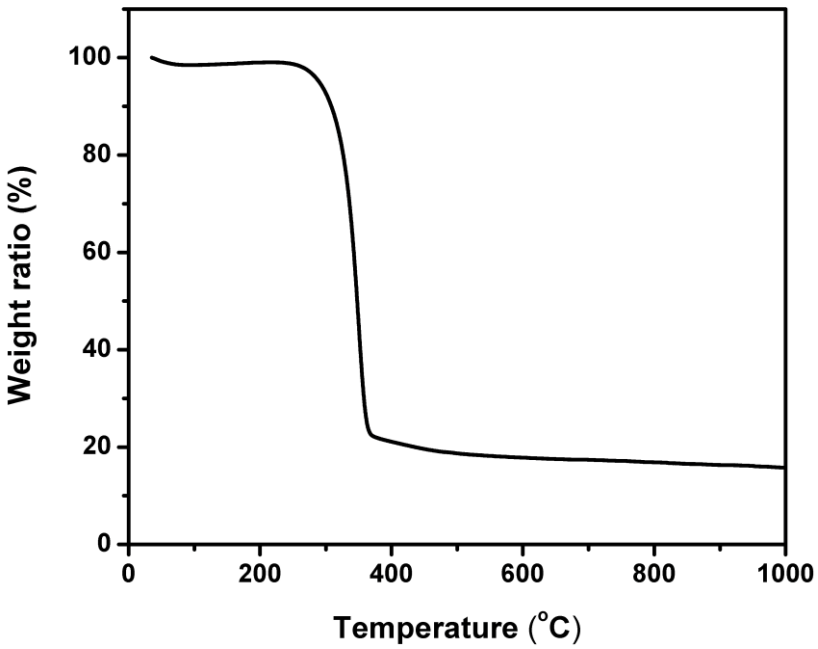


**Figure 8.3** TGA curves of FT in $N_2$ atmosphere.

**Figure 8.2** shows the schematic illustration of the material transformation during the synthesis process of 3D Sn@CNT-CP free-standing electrodes. $SnCl_4$ was homogeneously dispersed on FT by a soaking followed by a freeze-drying process (**Figure 8.2a**). The $SnCl_4$/FT was then transformed to tin-core/carbon nanotube sheath with a coaxial structure grown vertically on carbon paper by a chemical vapour deposition (CVD) approach in a horizontal tube furnace. Under $H_2$ atmosphere at 300 $^oC$, $SnCl_4$ was reduced to metallic Sn (**Figure 8.2b**). During this process, liquid Sn drops formed on the carbon paper because of its low melting point (232 $^oC$). A carbon layer was deposited around the liquid-state Sn due to the catalytic decomposition of $C_2H_2$. Continuous feeding of carbon source led to the longitude growth of carbon to form CNT due to its anisotropic properties [395]. Driven by capillary forces, the molten Sn embedded in the soft carbon matrix was absorbed into the interiors of CNT, forming the well-defined core-sheath Sn@CNT heterogeneous structure (**Figure 8.2c and d**). As identified by the thermogravimetric analysis (TGA) of FT (**Figure**

**8.3**), the de-hydrogenation and de-oxygenation processes of FT occur in a temperature range of 250–500 °C. After high temperature treatment, the FT was carbonized to carbon paper, which was interwoven by carbon fibres (**Figure 8.4**). Notably, carbon paper obtained from FT is ultralight (2.5 mg $cm^{-2}$) compared to copper foil (~10 mg $cm^{-2}$), which can significantly reduce the weight of the battery.

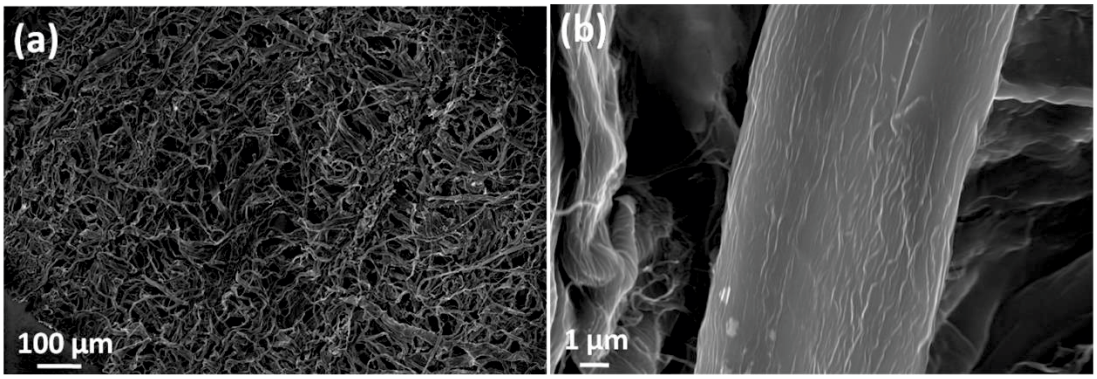


**Figure 8.4** SEM images of the carbon paper.

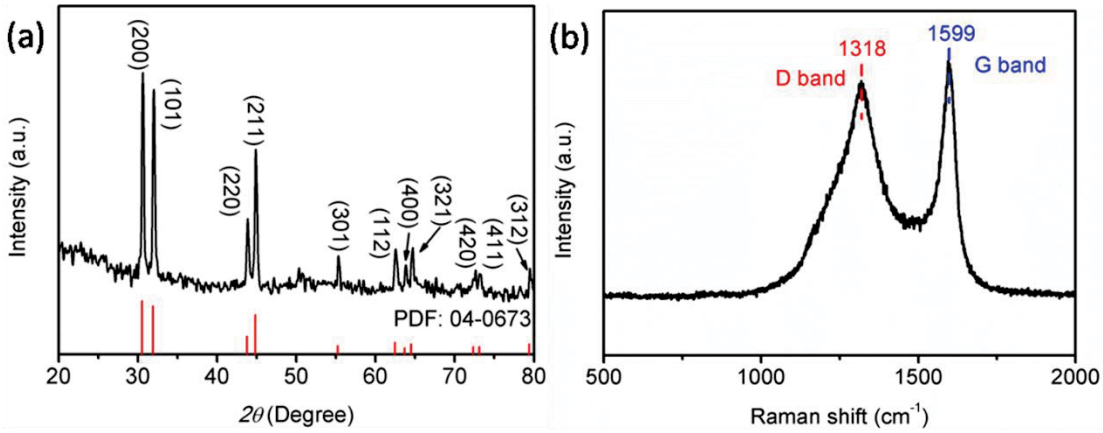


**Figure 8.5** (a) XRD pattern and (b) Raman spectrum of the Sn@CNT-CP electrode.

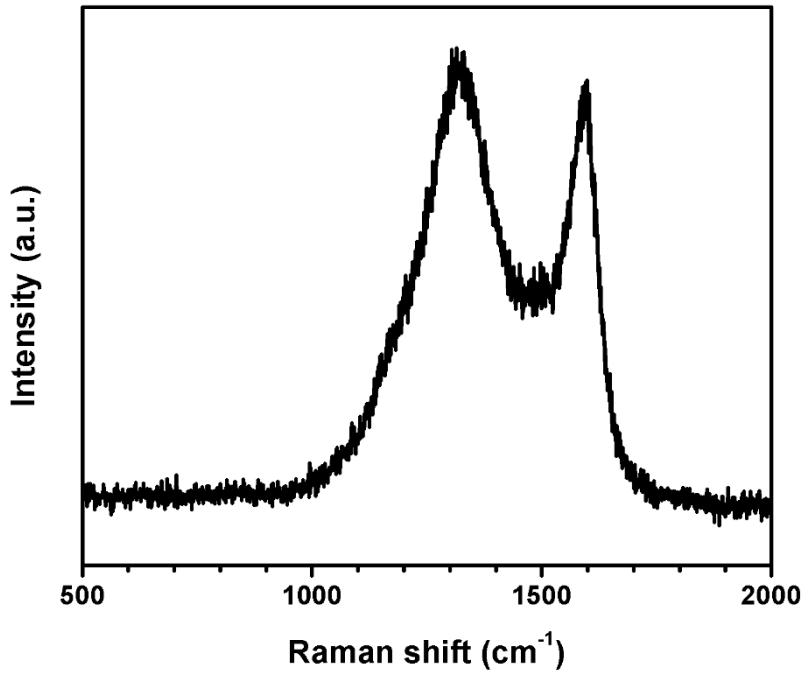


**Figure 8.6** Raman spectrum of the bare carbon paper (CP) obtained from the carbonization of facial tissue (FT).

X-ray diffraction (XRD) measurements were carried out in the range of 10–80° to determine the crystalline phase of the product. As shown in **Figure 8.5a**, all peaks in the XRD pattern can be well indexed to the β-Sn phase (JCPDS No. 04-0673). This indicates that $SnCl_4$ has been successfully reduced to metallic Sn. It should be noted that no characteristic diffraction peak of graphitic carbon can be observed, indicating the amorphous carbon formed in the final product. As shown in **Figure 8.5b**, Raman spectrum of the Sn@CNT-CP displays broad bands at 1318 and 1599 $cm^{-1}$, which are characteristic peaks of carbon materials. The peak at 1318 $cm^{-1}$ is assigned to D band, which originates from the defect-induced mode. The peak at 1599 $cm^{-1}$ is known as G band ($E_{2g}$ graphitic mode). The intensity ratio between D band and G band ($I_D/I_G$) is *ca.* 0.91. The Raman spectrum of bare CP (**Figure 8.6**) shows D band and G band at the same positions as that of the Sn@CNT-CP but with an $I_D/I_G$ value of 1.07.

These results suggest that FT has been transformed to carbon after the thermal treatment. To identify the loading content of Sn in the Sn@CNT-CP, TGA was performed in air at a heating rate of 5 $^{o}$C min$^{-1}$. **Figure 8.7** depicts the TGA curve of Sn@CNT-CP. According to the previous report, the oxidation of Sn to $SnO_2$ normally starts at around 300 $^{o}$C [396]. However, no signal corresponding to the transformation from Sn to $SnO_2$ can be observed from room temperature to 500 $^{o}$C for the Sn@CNT-CP sample. It suggests that the thermal stability of Sn confined in a CNT layer is much higher than bare Sn. Based on the TGA result, the Sn loading density was determined to be 1.2 mg cm$^{-2}$.

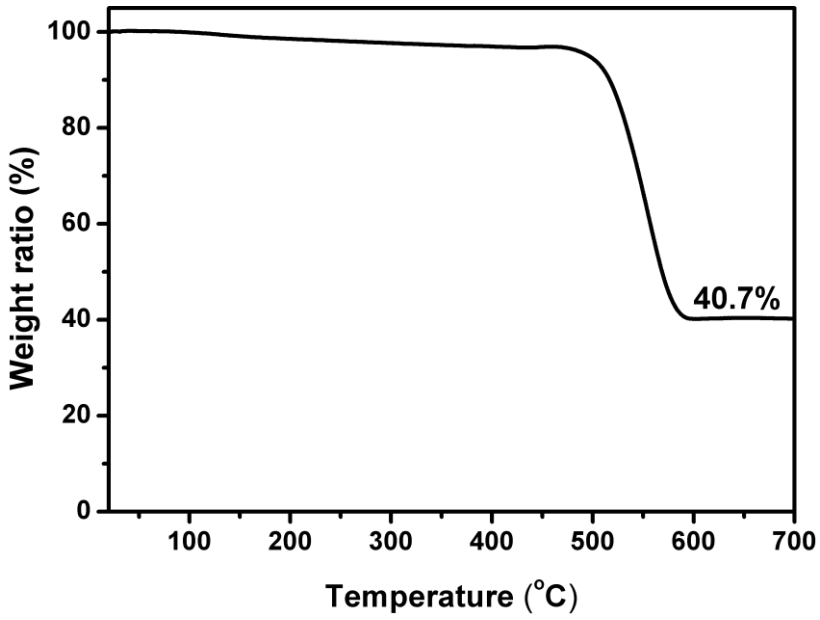


**Figure 8.7** TGA curves of Sn@CNT-CP (in air atmosphere).

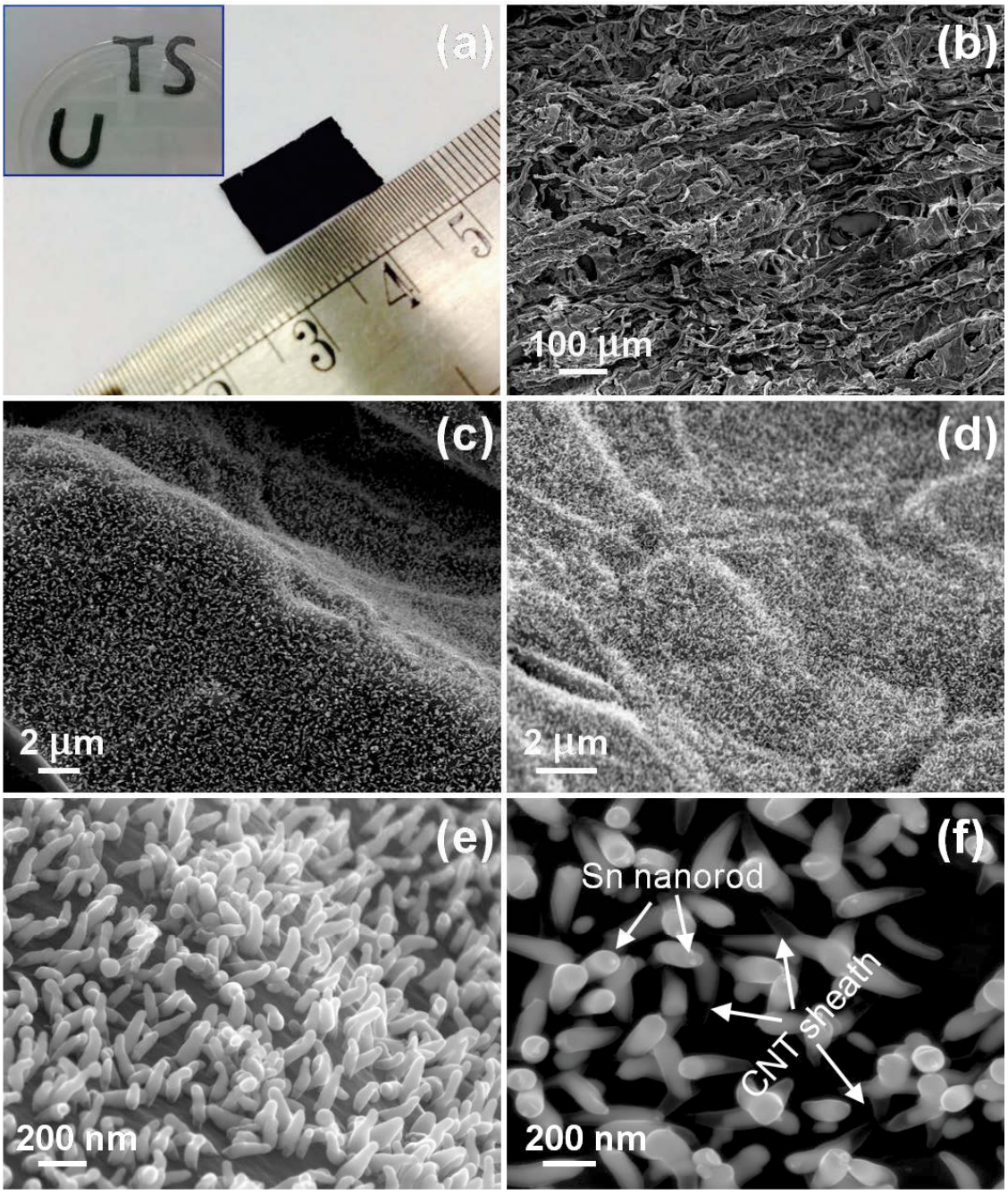


**Figure 8.8** (a) Digital photograph of a rectangular Sn@CNT-CP free-standing electrode, the insert shows "UTS" shaped Sn@CNT-CP. (b) Low- and (c, d) medium- magnification SEM images of Sn@CNT-CP. (e and f) High-magnification SEM images of Sn@CNT-CP with a hierarchical structure.

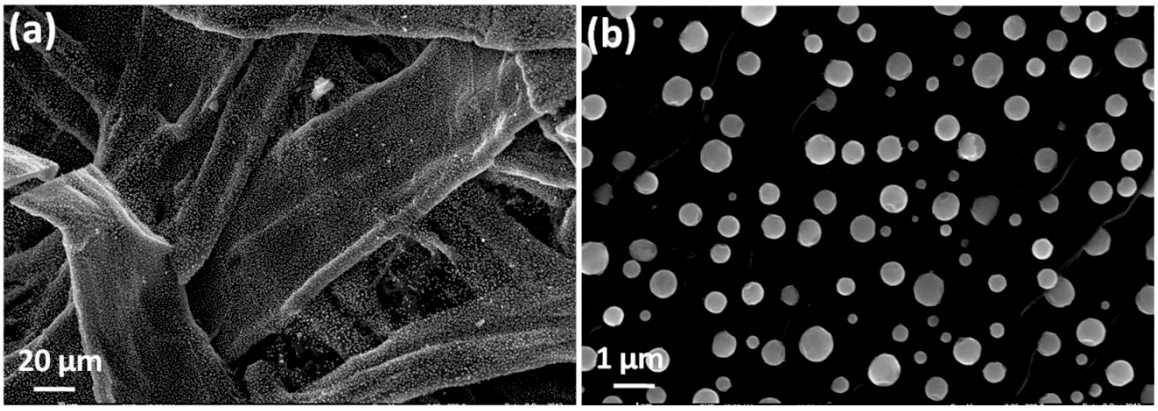


**Figure 8.9** SEM images of the products prepared by the same procedure without $C_2H_2$.

The flexibility of the $SnCl_4$/FT precursor enables the preparation of Sn@CNT-CP electrodes with different patterns (**Figure 8.8a**). **Figure 8.8b** shows the low-magnification SEM image of the as-prepared free-standing electrode. The large interstitial areas were formed between constituent carbon microbelts, which are beneficial for the absorption of electrolyte. As a result, Sn@CNT-CP has a high electrolyte uptake of 604%, corresponding to 4.4 mL $g^{-1}$. Moreover, the cross-linked carbon microbelts provide electrical conduction for the electrode. **Figure 8.8c and d** show the medium-magnification SEM images of Sn@CNT-CP, which demonstrate a hierarchical 3D architecture of Sn@CNT-CP. It can be seen that the entire carbon paper is densely and uniformly covered by Sn@CNT nanopillars. The detailed morphology analyses were performed by high magnification SEM images (**Figure 8.8e**). The as-deposited Sn@CNT nanopillars are nearly perpendicular to the carbon paper matrix. As shown in **Figure 8.8f**, the Sn@CNTs grew to about 200 nm in length and about 60 nm in diameter after 2 h growth at 600 $^oC$ in $C_2H_2$. The Sn@CNTs self-assemble and form a nano-

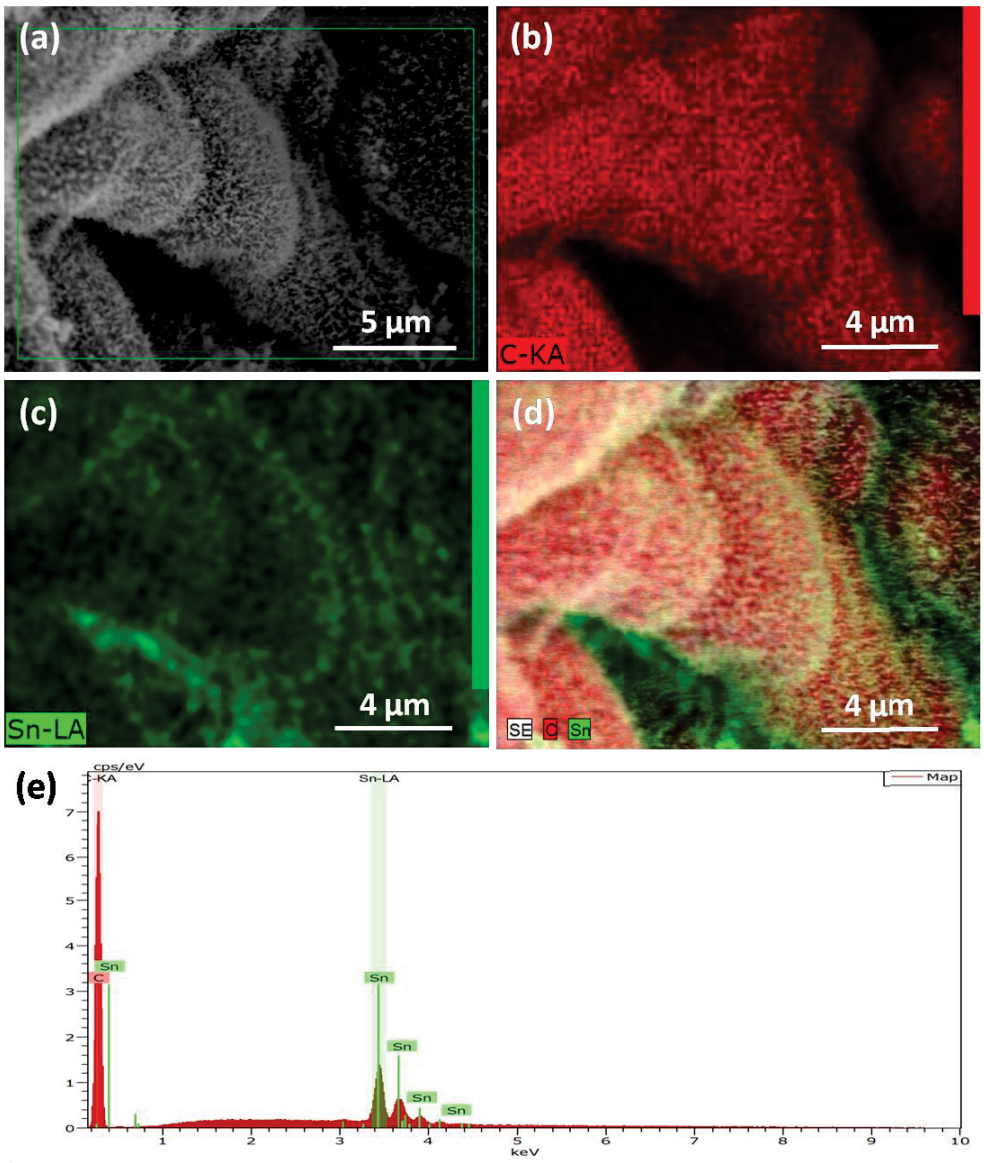


**Figure 8.10** SEM energy dispersive spectroscopic (EDS) characterization of Sn@CNT-CP (a-d). (a) SEM image, (b and c) C and Sn elemental mapping of the region shown in the marked area in (a), (d) an integrated C- and Sn-elemental mapping image. (e) EDX spectrum of the Sn@CNT-CP.

forest architecture, generating a loose porous nanostructure with abundant open voids. This unique structure is preferred for sodium-ion batteries, providing large area for electrode/electrolyte interaction. However, without the confinement effect of CNT, liquefied

Sn aggregates to minimize the surface energy, forming Sn spheres on carbon paper (**Figure 8.9**). Owing to the homogeneous distribution of Sn-source on carbon paper, tubular-structured Sn@CNT nanopillars are well dispersed on carbon fibre, as evidenced by SEM mappings shown in **Figure 8.10a-d**. **Figure 8.10e** shows the energy dispersion X-ray (EDX) spectrum of the as-prepared Sn@CNT-CP electrode, in which the peaks of C and Sn are obviously identified. No other peaks can be found, suggesting the purity of the product. The CNT layer functions as an efficient conductor in the longitudinal direction between carbon paper matrix and Sn nanorod, which is preferred for high rate charge-discharge processes. The SEM results confirmed that 3D Sn@CNT-CP free-standing electrodes were successfully synthesized by the novel S-CVD process.

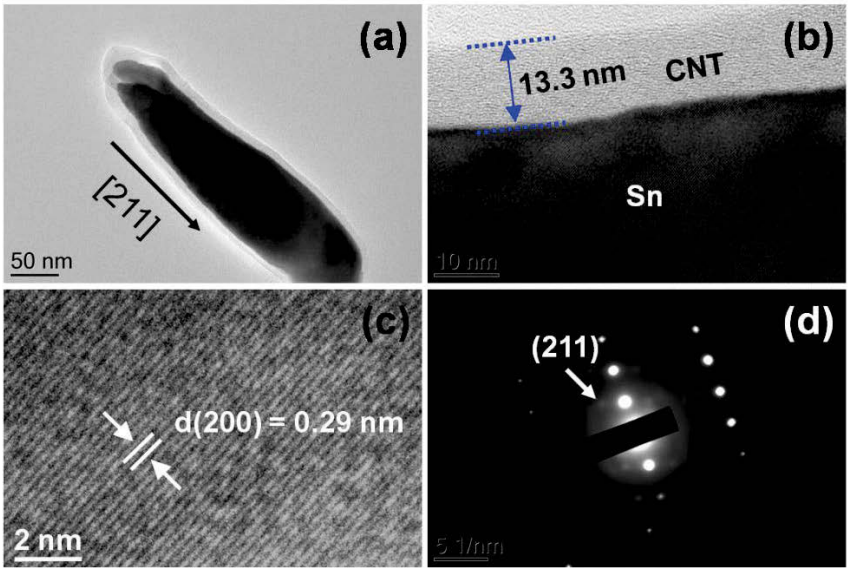


**Figure 8.11** (a) TEM image of a single Sn@CNT nanopillar. (b) HRTEM image, showing the thickness of the CNT layer. (c) Lattice-resolved high-resolution TEM image. (d) SAED pattern of (a), demonstrating the single crystalline nature of a Sn nanopillar.

**Figure 8.11a-c** show the transmission electron microscopy (TEM) images of an Sn@CNT nanopillar. The TEM image shown in **Figure 8.11a** further confirms that the rod-like

Sn@CNT has a core-sheath structure. The thickness of the CNT wall is determined to be ~ 13.3 nm by the HRTEM image in **Figure 8.11b**. A lattice-resolved high-magnification TEM image in **Figure 8.11c** shows that the lattice distance is 0.29 nm, corresponding to the (002) crystal plane of Sn. **Figure 8.11d** is the selected area electron diffraction (SAED) pattern taken from the **Figure 8.11a**. It indicates that the Sn-core is single crystalline, and the growth direction of the Sn nanopillar can be identified to be along the [211] direction as indexed in **Figure 8.11d**, in which the (211) crystal plane with a d-spacing of 2.02 Å can be observed.

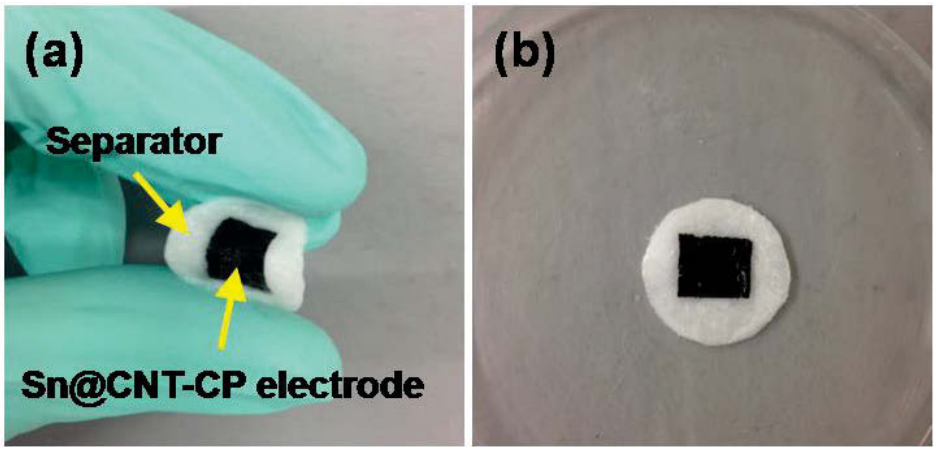


**Figure 8.12** The photograph of the separator-supported Sn@CNT-CP electrode being bent (a) and released (b).

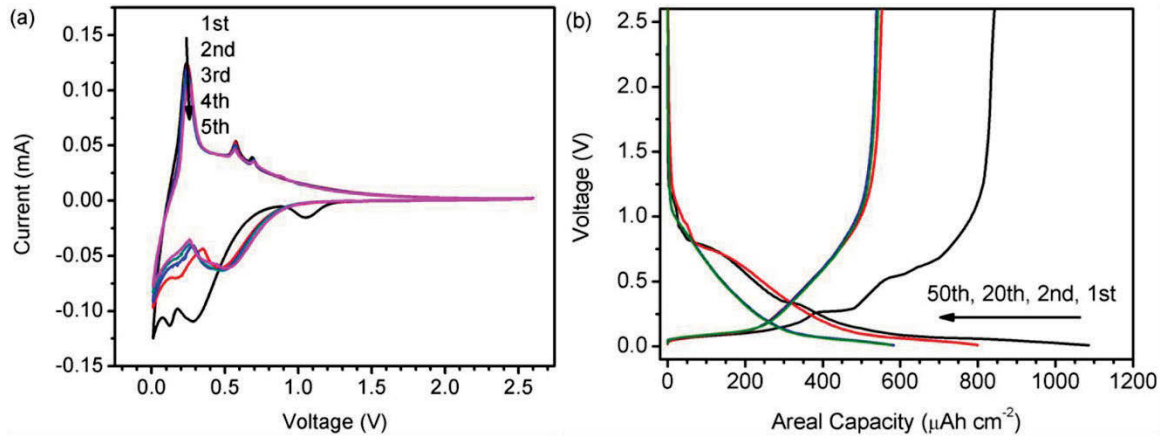


**Figure 8.13** (a) CV curves of Sn@CNT-CP composite at a scan rate of 0.1 mV $s^{-1}$ in the range of 0.01-2.6 V *vs.* $Na/Na^+$. (b) Charge-discharge curves of Sn@CNT-CP electrode at a current density of 50 μA $cm^{-2}$.

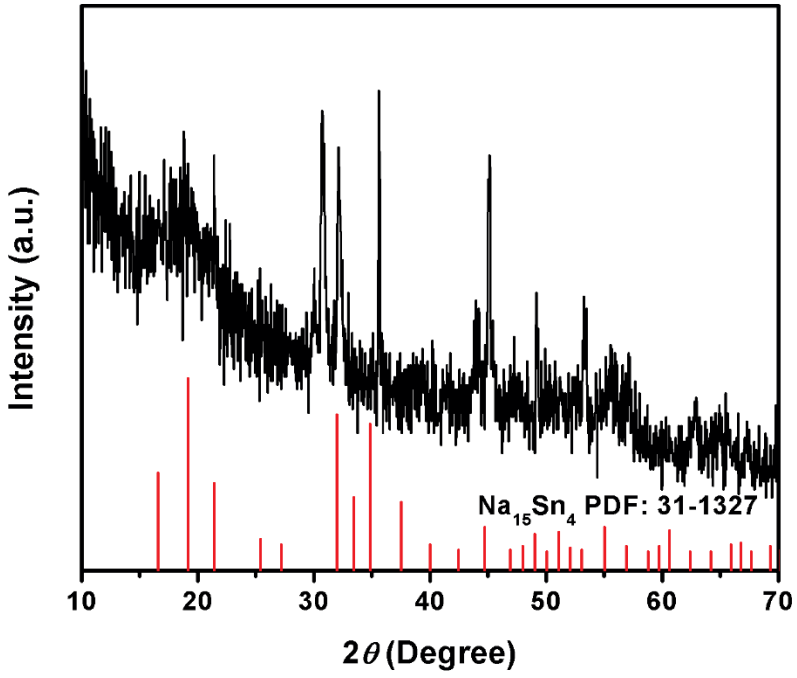


**Figure 8.14** XRD pattern of Sn@CNT-C electrode discharged to 0.01 V.

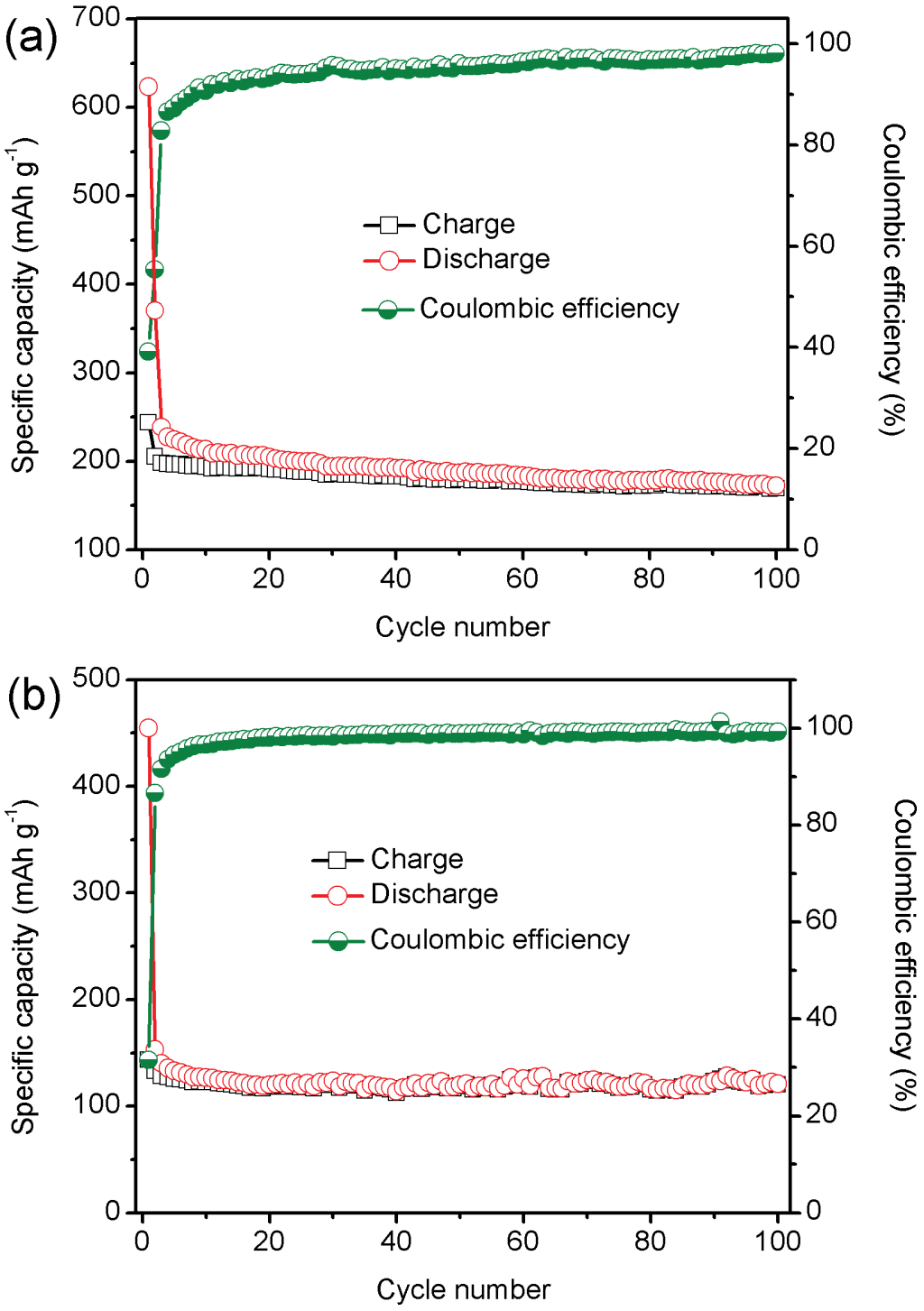


**Figure 8.15** Cycling performances of (a) Sn@CNT-CP electrode and (b) carbon electrode prepared by the traditional dispersion technique.

The as-prepared Sn@CNT-CP electrodes were directly used as free-standing anodes in Na-ion batteries without using current collectors or binders. We tested the flexibility of the as-prepared Sn@CNT-CP sample in practical conditions, *i.e.* with the impregnation of the electrolyte. Under this circumstance, the free-standing Sn@CNT-CP electrode supported on the separator (glass microfiber, Whatman) is bendable, which is shown in **Figure 8.12a**. When being released, no collapse of the electrode can be observed (**Figure 8.12b**). This indicates the bendable property of the as-prepared Sn@CNT-CP electrode. Cyclic voltammetry (CV) and galvanostatic charge/discharge cycling were performed to evaluate the electrochemical performance of the Sn@CNT-CP. As shown in **Figure 8.13a**, in the first cycle, a cathodic peak at 1.05 V can be observed, which is assigned to the interaction between $Na^+$ and the surface functional groups of carbon [331]. In the following cathodic scanning, a broad integrated peak starting at 0.75 V is distinguishable, which originates from the formation of a solid electrolyte interface (SEI), Na-Sn reaction to form $Na_xSn$ alloys and $Na^+$ insertion into carbon. The peak at 0.3 V, which disappears in the following cycles, could be ascribed to the decomposition of propylene carbonate (PC) [397]. During the CV scan, an overpotential of 0.1 V needs to be considered due to the sluggish $Na^+$ diffusivity [249]. In this regard, three dominant reduction peaks at 0.5, 0.2, and 0.01 V observed in the second cathodic scan can be attributed to the formation of $NaSn_5$, NaSn, and $Na_{15}Sn_4$ according to the theoretical research reported by Ceder's group [385]. The *ex situ* XRD experiment suggests the formation of $Na_{15}Sn_4$ crystalline when the Sn@CNT-CP electrode was discharged to 0.01 V (**Figure 8.14**). In the de-sodiation processes, three well-defined anodic peaks can be identified at 0.2, 0.5 and 0.7 V, corresponding to de-sodiation from $Na_{15}Sn_4$, NaSn and $NaSn_5$, respectively [248]. The shape and the position of the oxidation peaks do not change after the second cycle, indicating the excellent reversibility and stability of the Sn@CNT-CP electrode.

**Figure 8.13b** shows the charge-discharge curves of the Sn@CNT-CP electrode at a current density of 50 μA $cm^{-2}$ in the voltage range of 0.01–2.6 V. In the first cycle, the Sn@CNT-CP electrode achieved a discharge capacity of 1085 μA h $cm^{-2}$ with a charge capacity of 887 μA h $cm^{-2}$. It is calculated that the initial reversible specific capacity contributed from Sn is 644 mA h $g^{-1}$, which is 76% of the theoretical value (847 mA h $g^{-1}$ based on the formation of $Na_{15}Sn_4$). The initial Coulombic efficiency is calculated to be 81.7%. For comparison, Sn@CNT-CP composites were pasted onto Cu foil by the traditional dispersion technique using PVDF as polymeric binder. The initial Coulombic efficiency of the binder-free Sn@CNT-CP electrode is much higher than that of the binder-enriched electrode (34.3%, **Figure 8.15**). The increased initial Coulombic efficiency could be attributed to the unique 3D electrode configuration, which reduces side reactions by minimizing the additional supplementary interfaces, such as the current collector/active material interface and active material/active material interface.

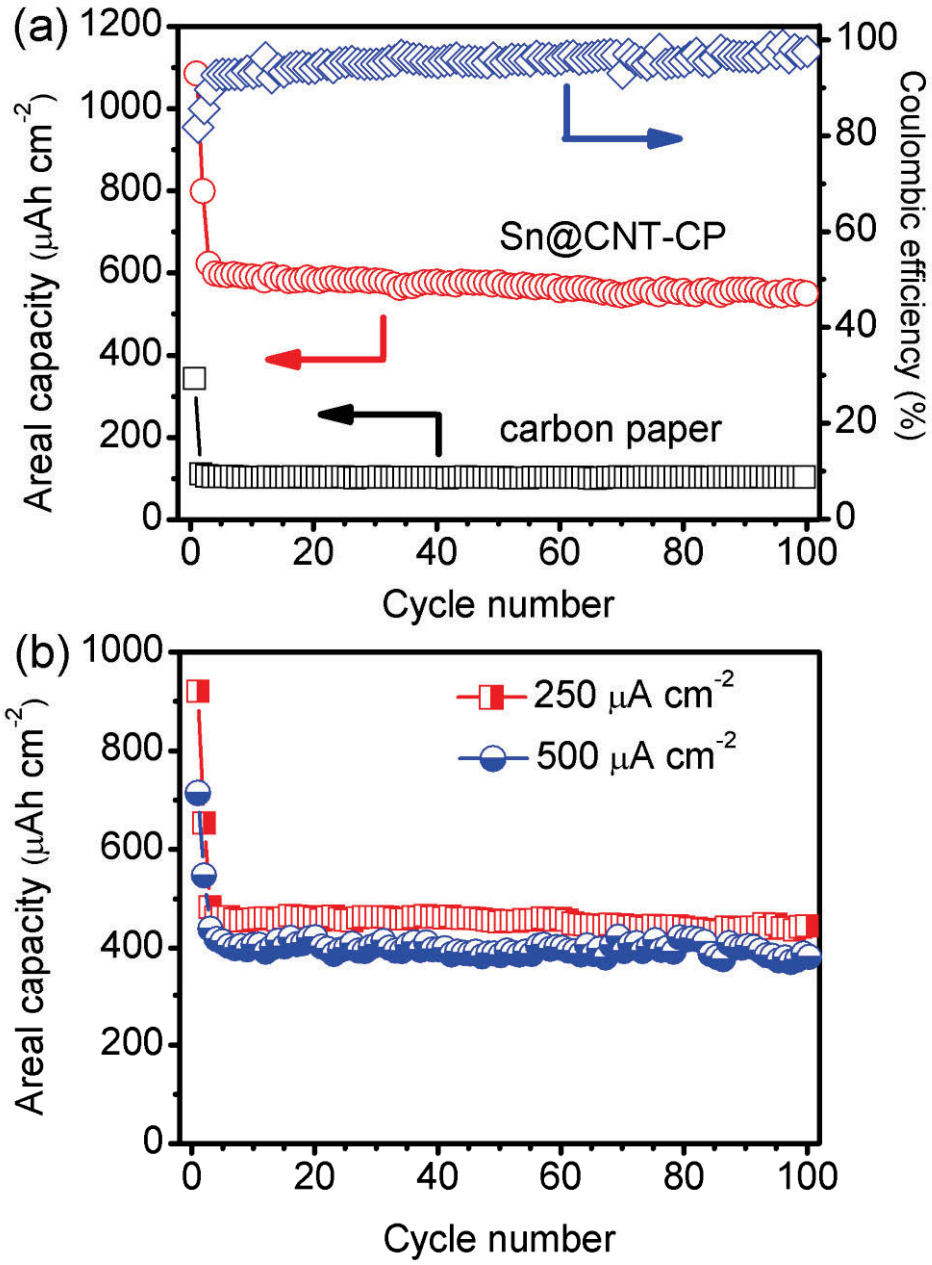


**Figure 8.16** (a) Cycling performance of the Sn@CNT-CP and the carbon paper electrode at a current density of 50 μA $cm^{-2}$, and the corresponding Coulombic efficiency of the free-standing Sn@CNT-CP electrode. (b) Cycling performance of Sn@CNT-CP at 250 μA $cm^{-2}$ and 500 μA $cm^{-2}$.

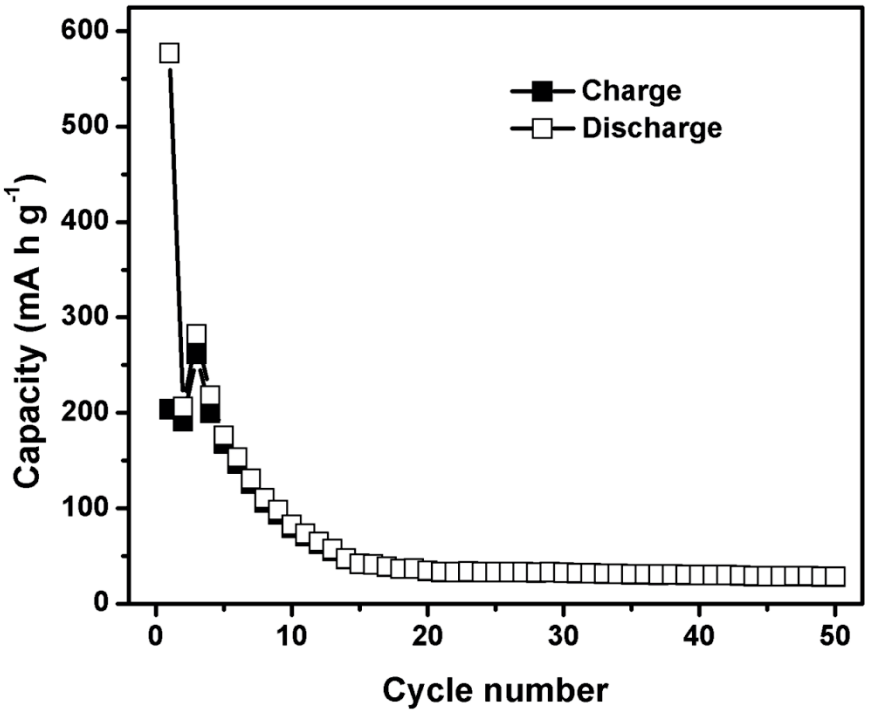


**Figure 8.17** Cycling performance of bare Sn electrode prepared by the traditional dispersion technique at a current density of 80 mA $g^{-1}$.

The galvanostatic discharge-charge cycling performances of Sn@CNT-CP and blank carbon paper electrodes at 50 μA $cm^{-2}$ are shown in **Figure 8.16a**. Bare carbon paper delivered a poor electrochemical activity. The initial discharge capacity of bare carbon paper was 341 μA h $cm^{-2}$. The discharge capacity decreased to 109 μA h $cm^{-2}$ in the second cycle. After 100 cycles, the blank carbon electrode maintained a capacity of 102 μA h $cm^{-2}$. The bare Sn electrode suffered from dramatic capacity fading upon cycling (**Figure 8.17**). After 50 cycles, only 13.8% of the initial reversible capacity was maintained. The rapid capacity decay of bare Sn electrode could be attributed to the pulverization of the electrode originating from the large volume changes of Sn (420%) during charge/discharge processes [248]. The Sn@CNT-CP electrode showed a high and stable capacity within 100 cycles. After cycling at 50 μA $cm^{-2}$ for 100 cycles, the Sn@CNT-CP electrodes still delivered a capacity of 550

μA h $cm^{-2}$. The good cycling performance of Sn@CNT-CP could be benefited from the dispersing effect of carbon paper[398] and the buffering capability of CNT sheaths for the $Na_xSn$ alloy formation[399]. A high Coulumbic efficiency has also been observed for the free-standing Sn@CNT-CP electrode, which gradually increases from 81.7% (in the first cycle) to a stable value of ~ 97% in the following cycles. We also tested the cyclability of the Sn@CNT-CP electrode at high current densities (as shown in **Figure 8.16b**). The free-standing Sn@CNT-CP electrode demonstrated promising performances on long-term cycling. The electrode delivered specific capacities of 445 μA h $cm^{-2}$ and 377 μA h $cm^{-2}$ at the current density of 250 μA $cm^{-2}$ and 500 μA $cm^{-2}$ after 100 cycles, respectively.

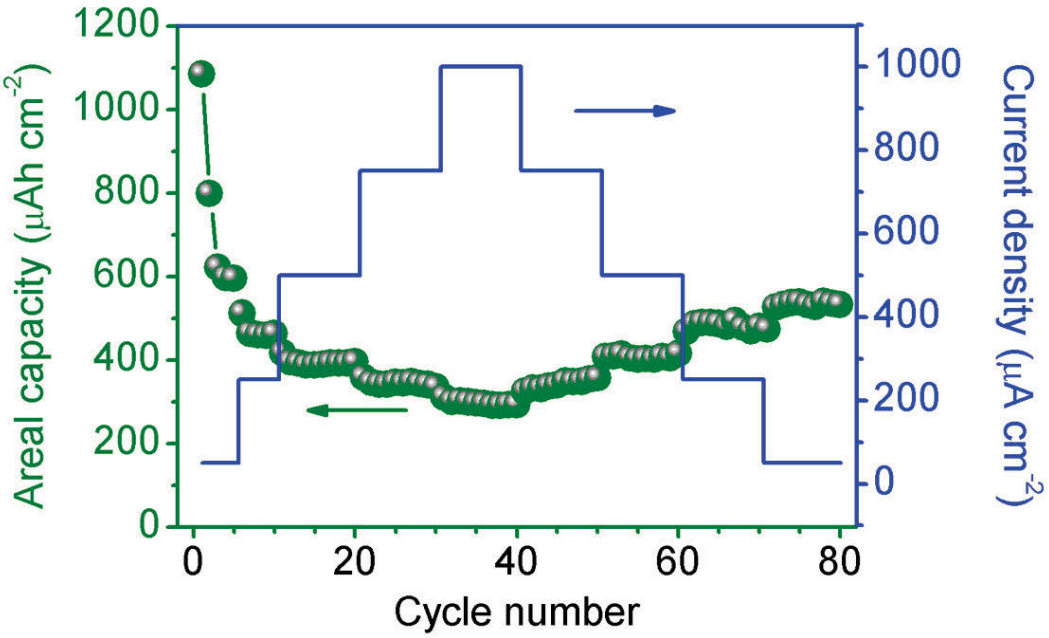


**Figure 8.18** Rate performance of the Sn@CNT-CP free-standing electrode.

**Figure 8.18** shows the rate performance of the Sn@CNT-CP electrode at varied current densities. Even at high current densities of 750 μA $cm^{-2}$ and 1000 μA $cm^{-2}$, the electrode still achieved a capacity of 341 μA h $cm^{-2}$ and 299 μA h $cm^{-2}$, respectively. After cycling at high

current densities, the cell capacity can almost recover to the original capacity when the current density reversed to low values. This confirms that the Sn@CNT-CP electrode tolerates high rate cycling. The superior electrochemical performances could be ascribed to the unique 3D architecture of the electrode, which boosts both ionic and electronic conductivity. Sn nanorods encapsulated in a CNT sheath with a high aspect ratio feature a high ionic conductivity, which can improve the sluggish $Na^+$ transfer kinetics. Meanwhile, Sn nanorods arranged in a highly ordered manner perpendicular to the carbon paper substrate offer the maximum active sites for electrode/electrolyte contact. Furthermore, carbon nanotube layers provide electronic conductivity for the Sn core. The as-prepared free-standing electrode with 3D hierarchical structure can be used directly without polymeric binder. Consequently, the electronic conductivity can be improved, which is required for high-rate charge/discharge processes.

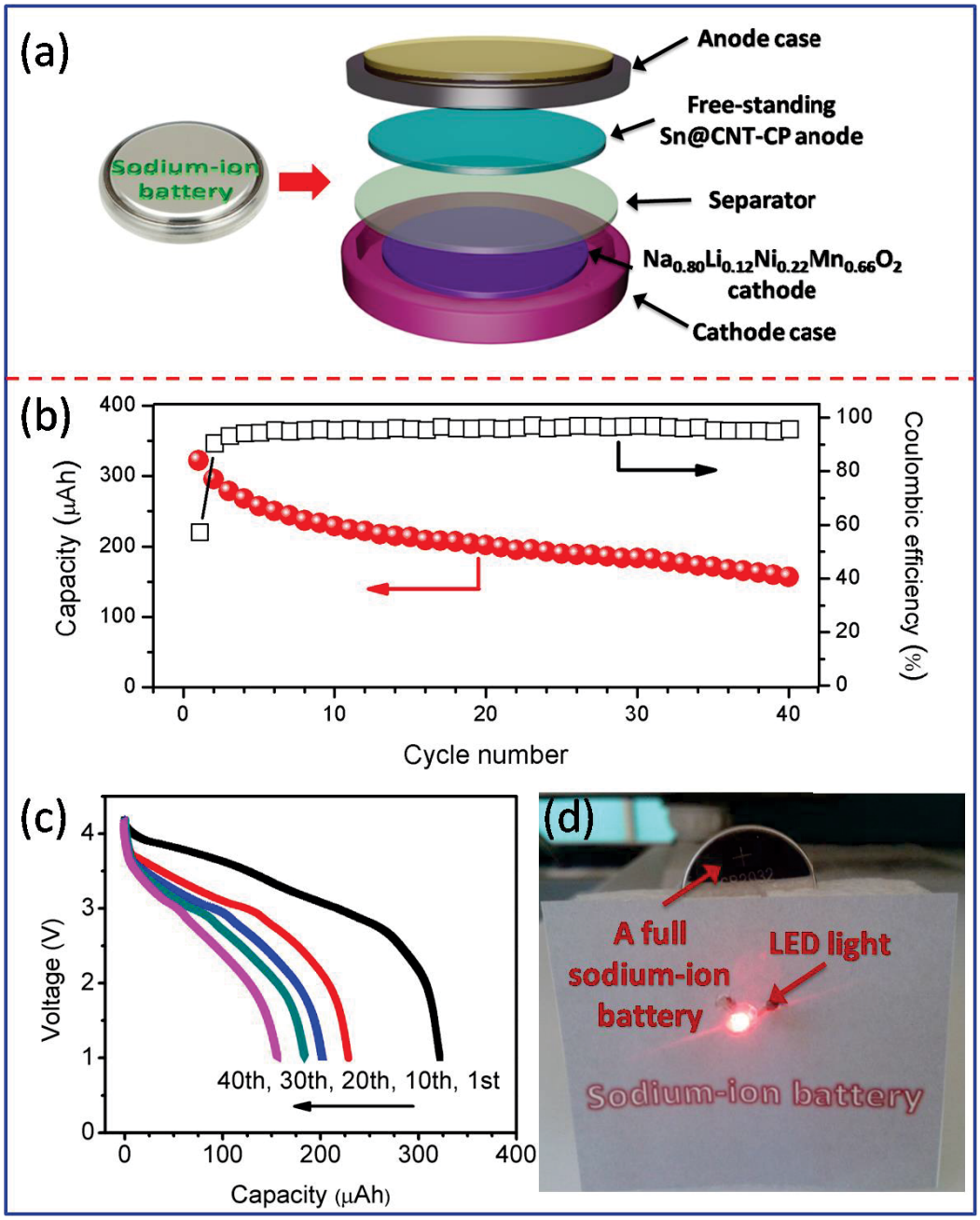


**Figure 8.19** (a) Schematic illustration of a full Na-ion battery with $Na_{0.80}Li_{0.12}Ni_{0.22}Mn_{0.66}O_2$ as cathode and free-standing Sn@CNT-CP as anode. (b) Cycling performance and Coulombic efficiency of the full Na-ion battery. (c) Discharge curves of the 1st, 10th, 20th, 30th, and 40th cycle. (d) A photograph shows that a full Na-ion battery can store the electrical energy to light up a LED.

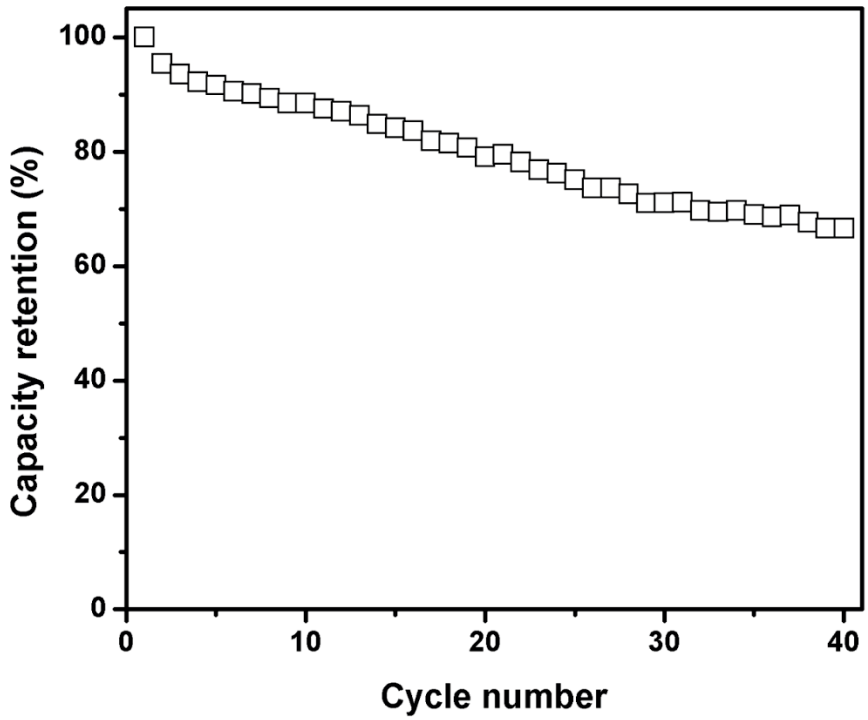


**Figure 8.20** Cycling performance of $Na_{0.80}Li_{0.12}Ni_{0.22}Mn_{0.66}O_2$ cathode in a half cell.

To elucidate the potential practical application of the as-prepared Sn@CNT-CP for Na-ion batteries, a full cell was assembled using free-standing Sn@CNT-CP as anode and lithium-substituted layered $Na_{0.80}Li_{0.12}Ni_{0.22}Mn_{0.66}O_2$ as cathode, which is schematically shown in **Figure 8.19a**. P2-$Na_{0.80}Li_{0.12}Ni_{0.22}Mn_{0.66}O_2$ has a theoretical capacity of 118 mAh $g^{-1}$ without significant phase transformation up to 4.4 V [166]. The mass loading ratio between cathode and anode is 3:1. The full cell was charged and discharged in a voltage window of 1.0–4.2 V. **Figure 8.19c** shows the discharge curves of the 1$^{st}$, 10$^{th}$, 20$^{th}$, 30$^{th}$ and 40$^{th}$ cycle of the full cell. The initial charge capacity was 563 μA h. A discharge capacity of 322 μA h was obtained at a current of 52 μA. The irreversible capacity in the first cycle could be mainly ascribed to the anode, due to the formation of an irreversible SEI layer. From **Figure 8.19b**, it can be observed that the full cell maintained a Coulombic efficiency of 95.5% in the

following cycles. The full Na-ion battery can deliver a reversible capacity of around 160 μA h over 40 cycles. In the pristine P2-$Na_{0.80}Li_{0.12}Ni_{0.22}Mn_{0.66}O_2$, 85 % of $Li^+$ ions reside in the $TMO_2$ (TM = transition metal) layer, while the remaining 15% of $Li^+$ ions can be found in $O_h/T_d$ sites in the Na layer. The migration of $Li^+$ and $Na^+$ of the P2-$Na_{0.80}Li_{0.12}Ni_{0.22}Mn_{0.66}O_2$ cathode during charge/discharge process has been investigated by *ex situ* NMR [166]. It is suggested that at full charged state, some Li ions migrate from the $TMO_2$ layer to the Na layer. When the cathode is discharged, a fraction of $Li^+$ in the $TMO_2$ layer is lost. The loss of $Li^+$ has negative effect on the cycling performance of the P2-$Na_{0.80}Li_{0.12}Ni_{0.22}Mn_{0.66}O_2$ cathode. We tested the cycling performance of the P2-$Na_{0.80}Li_{0.12}Ni_{0.22}Mn_{0.66}O_2$ cathode in a half cell (**Figure 8.20**), which exhibited a gradual capacity fading upon cycling. After 40 cycles, 70% of the initial capacity is obtained. Consequently, the capacity loss of the as-assembled full cell during repeated charge/discharge processes could mainly originate from the cathode side. The development of more suitable cathode material for SIBs is expected to improve the cycling performance of the free-standing Sn@CNT-CP based full Na-ion batteries. The as-assembled Na-ion battery was electrically connected with a red light-emitting-diode (LED). As shown in **Figure 8.19d**, the LED glowed brightly when powered by a Na-ion cell with $Na_{0.80}Li_{0.12}Ni_{0.22}Mn_{0.66}O_2$ as cathode and Sn@CNT-CP as anode.

## 8.4 Conclusions

In summary, we developed a facile strategy to synthesize a free-standing 3D Sn@CNT-CP electrode with promising performances for sodium-ion batteries. The synthesis process involves the pyrolysis of low-cost and ultralight facial tissue at high temperature to generate self-supported carbon paper. Simultaneously, CVD growth of vertically aligned Sn nanorods wrapped by CNT on the carbon paper is achieved by local catalytic decomposition of

acetylene around liquefied Sn. When directly applied as free-standing anodes for SIBs, the as-prepared Sn@CNT-CP electrode exhibited promising electrochemical performances, including high capacity (887 μA h $cm^{-2}$) and an extended cycle life. The Sn@CNT-CP electrode also demonstrated a high rate capability. We used the as-prepared free-standing Sn@CNT-CP as anode and lithium-substituted layered $Na_{0.80}Li_{0.12}Ni_{0.22}Mn_{0.66}O_2$ as cathode to assemble a full sodium-ion battery. The full Na-ion battery can be used to sufficiently power a LED light. It is expected that the strategy and concept reported in this work could inspire the development of high performance sodium-ion batteries.

## Chapter 9 $MoS_2$ Nanosheets Vertically Aligned on Carbon Paper: a Freestanding Electrode for Highly Reversible Sodium Ion Batteries

### 9.1 Introduction

$MoS_2$, a layered material with S-Mo-S motifs stacked together by van der Waals forces, received extraordinary attention in the last few years. Many inroads have been made recently in developing $MoS_2$ based electrode materials for SIBs. For example, $MoS_2$ nanoflowers with expanded interlayers have been prepared as intercalation-type electrode materials in the voltage window of 0.4-3.0 V.[333] When the voltage window is expanded to 0.01-3.0 V, $MoS_2$ follows an intercalation-conversion mechanism for $Na^+$ storage. Due to the low conductivity and the huge volume variations of $MoS_2$ during charge/discharge processes, bare $MoS_2$ electrodes exhibited poor rate capability and fast capacity decay upon cycling.[400] To overcome this limitation, dispersing $MoS_2$ in carbon matrices with high electronic conductivity has proved effective for improving the electrochemical properties in SIBs. Different $MoS_2$-carbon hybrid materials have been tested as anodes for SIBs, such as $MoS_2$ nanodots embedded in carbon nanowires,[237] $MoS_2$/graphene composites,[234, 238, 292, 400] $MoS_2$/CNT composites,[235] and $MoS_2$/carbon nanospheres[239]. Usually, current collectors, conductive agents and binders are needed to fabricate film electrodes, which inherently increases the total weight and cost of SIBs. Furthermore, they suffer from low initial Coulombic efficiency (ICE < 60%). The low ICE originates from: (i) the formation of solid electrolyte interfaces (SEI) caused by electrolyte decomposition; (ii) adverse side reactions between inactive components (conductive agent and binder) and sodium metal; (iii) electrical contact failure of the electrode; and (iv) an excessive interface between carbon and electrolyte, which leads to considerable side reactions.[236] This low ICE requires a larger mass of the

corresponding cathode material in full cells, thereby increasing the total weight and cost of SIBs. Rational geometrical design to give electrode materials a high ICE is a key research topic in SIBs. Moreover, anode materials must have high rate performance to achieve high power density and long cycle life for SIBs. Here, we report on deposition of $MoS_2$ nanosheets on carbon derived from paper towel ($MoS_2$@C) to prepare freestanding anode material for SIBs with a high ICE, promising rate capability and long cycle life. In this hierarchically-structured $MoS_2$@C composite electrode, dense $MoS_2$ nanosheets are vertically aligned on carbon fibers. This desirable integration of $MoS_2$ and carbon in a harmonious manner can ensure good electronic connection between $MoS_2$ and carbon and can retard the direct access of electrolyte to the carbon. On the other hand, freestanding $MoS_2$@C electrodes can be directly used without the additional conductive agents and binders, thereby overcoming the adverse side reactions between the inactive components and sodium. Consequently, $MoS_2$@C achieved a high ICE of 79.5%. Meanwhile, the exposure of hierarchical $MoS_2$ nanosheets to electrolyte ensures desirable material/electrolyte interactions and as a result, $MoS_2$@C electrode exhibited a high reversible capacity and a good rate capability. Moreover, the utilization of paper towel-derived carbon paper as the conducting scaffold to prepare the freestanding $MoS_2$@C electrode provides an easy and low-cost electrode manufacturing process and hence would reduce the cost of sodium-ion batteries. To investigate the sodiation/desodiation mechanism of $MoS_2$@C electrode, we conducted *in situ* Raman measurements, which reveal that a $MoS_2$ phase transition from 2H-$MoS_2$ to 1T-$MoS_2$ starts at 0.9 V during discharge. This transition reverses after full charge, which allows for retaining the designed architecture.

## 9.2 Experimental Section

### 9.2.1 Sample preparation

Commercial paper towel (PT, Scott) was used as the biomass source of carbon paper. For purification, PT was firstly soaked in HCl solution (2 mol $L^{-1}$, 20 mL) for 24 h and then washed by vacuum filtration several times with de-ionized water. The purified PT was dried in a vacuum oven at 80 $^{o}$C overnight before further use. To load $MoS_2$ nanosheets, 76.7 mg of ammonium molybdate tetrahydrate ($(NH_4)_6Mo_7O_{24}\cdot 4H_2O$, AMT) and thiourea (1 g) was dissolved in 20 mL deionized water to form a homogeneous solution in the first step. In the following step, purified PT (76.7 mg) was soaked in this solution, which was then hydrothermally treated at 180 $^{o}$C for 24 h. $MoS_2$-loaded PT was washed with deionized water followed by drying at 80 $^{o}$C overnight. $MoS_2$-PT was calcined at 800 $^{o}$C for 2 h under Ar atmosphere in a horizontal tube furnace to obtain freestanding $MoS_2$@C. For comparison, carbon paper was prepared in a similar way, besides applying a hydrothermal treatment. Carboxy methyl cellulose sodium salt (CMC) coated $MoS_2$@C ($MoS_2$@C-CMC) was prepared by dip-coating. Briefly, $MoS_2$@C was dipped into CMC dissolved in a mixture of ethanol and water (volumetric ratio 3:2) followed by overnight drying at 80 $^{o}$C in a vacuum oven. The CMC content was ~10% in the $MoS_2$@C-CMC electrode.

### 9.2.2 Structural and physical characterization

The crystal structure and phase composition of the as-prepared materials were characterized by X-ray diffraction (XRD, Siemens D5000) using Cu Kα radiation with a scanning step of 0.02° $sec^{-1}$. The morphology was analysed by field emission scanning electron microscopy (FESEM, Zeiss Supra 55VP). The details of the morphology were further characterized by

transmission electron microscopy (TEM) (HRTEM, JEOL JEM-2011). The elemental mapping was conducted on a Zeiss EVO MA 15 SEM equipped with EDX. The carbon content in $MoS_2$@C composites was measured using a TGA/differential thermal analysis (DTA) analyser (TA Instruments, SDT 2960 module, New Castle, DE, USA) at a heating rate of 10 °C $min^{-1}$ in air.

### 9.2.3 Electrochemical testing

CR2032-type coin cells were assembled in an argon-filled glove box (UniLab, Mbraun, Germany). The as-obtained $MoS_2$@C electrode was cut into 0.6 × 0.6 $cm^2$ and directly used as self-supported electrode. Na foil was used as the counter and reference electrode. The positive and negative electrodes were electronically separated by glass microfiber (Whatman) saturated with electrolyte. The electrolyte solution was 1 M $NaClO_4$ dissolved in a mixture of ethylene carbonate (EC) and propylene carbonate (PC) with a volume ratio of 1:1, in which 5 vol.% fluoroethylene carbonate (FEC) was added as electrolyte additive. The charge-discharge measurements were performed at different current densities in the voltage range from 0.01 to 3.0 V *vs.* $Na^+$/Na using a computer-controlled Neware Battery Testing system. Cyclic voltammetry (CV) was conducted by using a CHI 660C electrochemical workstation between 0.01 and 3.0 V *vs.* $Na^+$/Na with a scan rate of 0.1 mV $s^{-1}$. The electrochemical impedance spectroscopy (EIS) measurements were performed at charged state with a 10 mV amplitude.

### 9.2.4 *In situ* Raman measurements

Modified CR2032-type coin cells equipped with a random orientation quartz window were used for *in situ* Raman measurements. Confocal *in situ* Raman spectroscopy analysis of the

batteries was performed on a Renishaw inVia (Gloucestershire, UK) microspectrometer in the reflective mode by using a 632.8 nm He-Ne laser focused through a ×63 times magnification and 0.7 numerical aperture objective. The laser spot size in the focal plan was ~1 μm. The reflected light from the sample was directed to the CCD detector by a grating with 1200 lines/mm. The setup possesses a spectral resolution of ~2 $cm^{-1}$.

### 9.3 Results and Discussions

**Figure 9.1a** shows the procedure for preparing the freestanding $MoS_2$@C paper electrodes. Woven loosely by cellulose fibers, commercial paper towel (PT) was used as the growth substrate. Before the loading of $MoS_2$, PT was purified in 1 M HCl for 24 h and washed

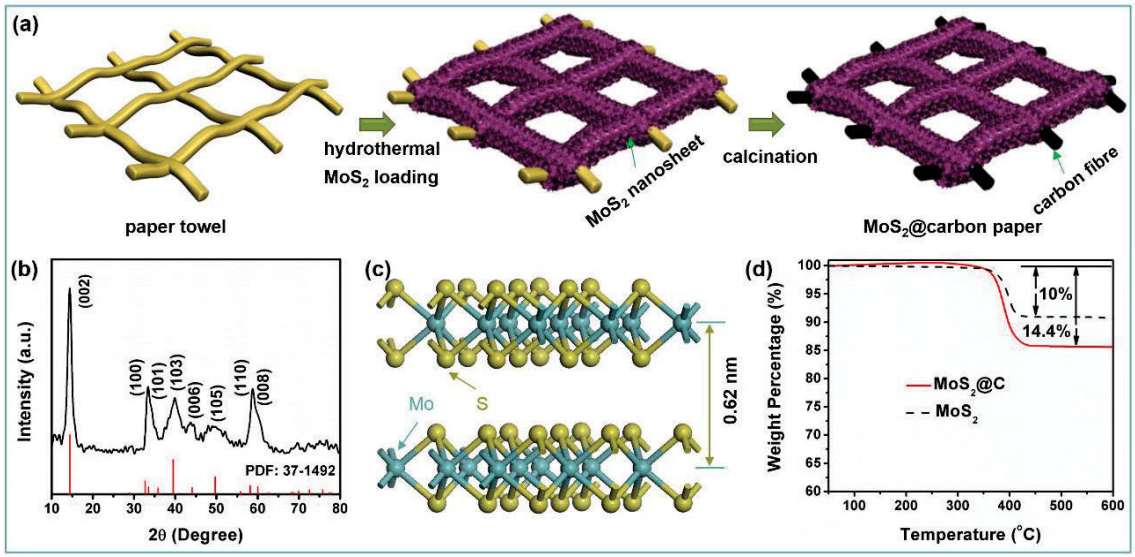


**Figure 9.1** (a) Schematic illustration for the preparation of $MoS_2$ vertically aligned on carbon paper, which includes $MoS_2$-loading by hydrothermal deposition followed by annealing under Ar. (b) XRD patterns of the as-prepared $MoS_2$@C, indicating the 2H phase of $MoS_2$. (c) The simulated structure of 2H-$MoS_2$. (d) TGA curves of bare $MoS_2$ and $MoS_2$@C in air.

sequentially with water and ethanol. **Figure 9.2** shows the energy dispersion X-ray (EDX) spectrum of the purified PT. No element other than carbon and oxygen could be detected, suggesting that PT is free of impurities, such as metal ions and polyanions. The purified PT was then soaked into a solution with ammonium molybdate tetrahydrate (AMT) and thiourea. This mixture was then hydrothermally treated at 180 °C for 24 h to form $MoS_2$. Large-size freestanding $MoS_2$-loaded PT was obtained after hydrothermal treatment (**Figure 9.3**). In the final step, the product was calcined at 800 °C in Ar atmosphere, during which the PT was transformed into carbon paper, finally generating free standing $MoS_2$@C (**Figure 9.4**). The XRD pattern shown in **Figure 9.1b** suggests that the 2H phase of $MoS_2$ (2H-$MoS_2$) was produced after the hydrothermal treatment and subsequent annealing. As depicted in **Figure 9.1c**, the calculated interlayer distance of 2H-$MoS_2$ is 0.62 nm, according to XRD. **Figure 9.1d s**hows the thermogravimetric analysis (TGA) curves of bare $MoS_2$ and $MoS_2$@C composites. The 10% weight loss of bare $MoS_2$ at 350-430 $^oC$ suggests the oxidation of $MoS_2$ to $MoO_3$ in air.[400] Based on the 14.4% weight loss of $MoS_2$@C composites, the $MoS_2$ loading ratio in the composite is determined to be 95.1%.

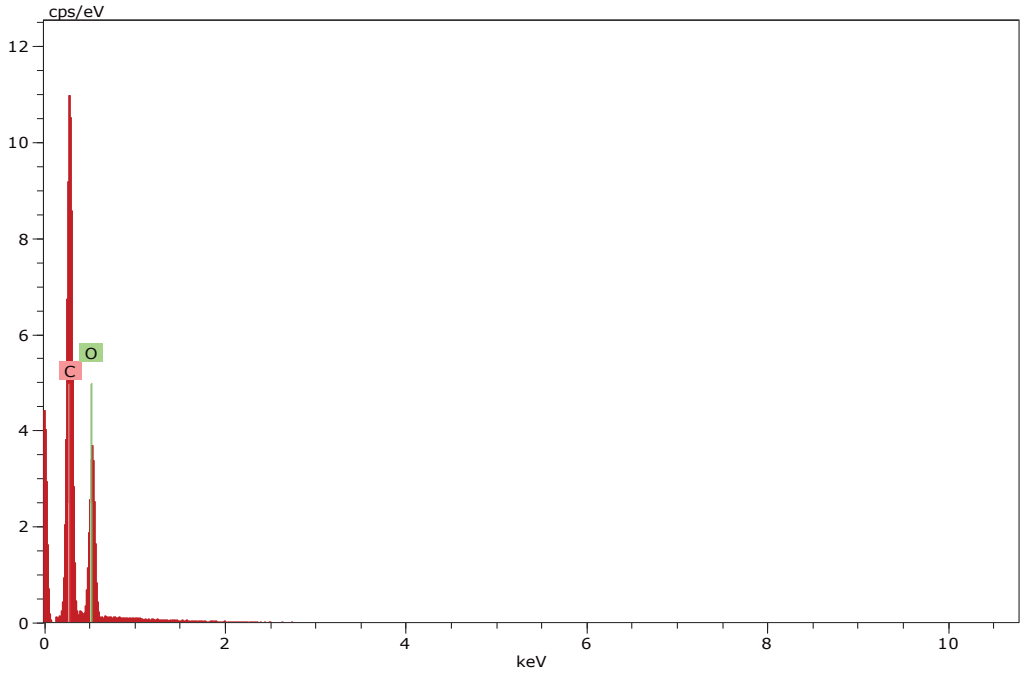


**Figure 9.2** Energy dispersive X-ray (EDX) spectrum of the purified paper towel.

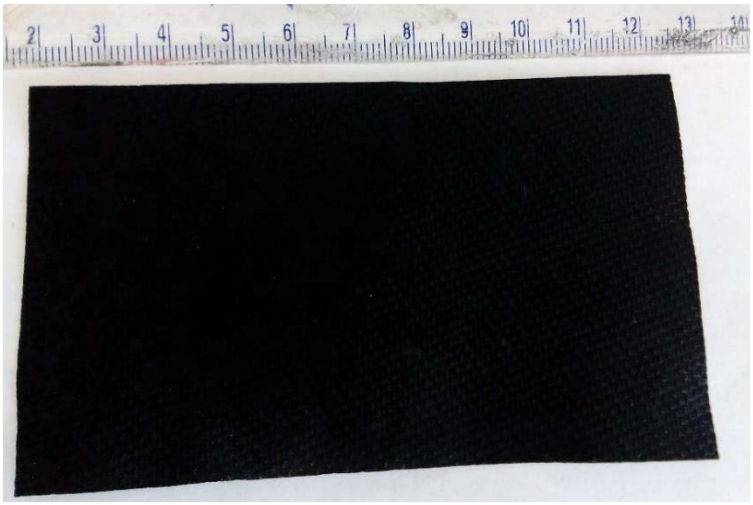

**Figure 9.3** Digital photo of a $MoS_2$ loaded paper towel.

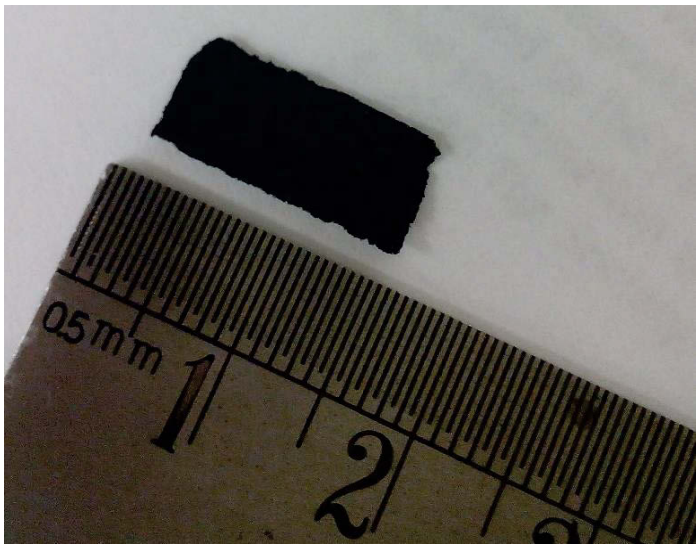


**Figure 9.4** Digital photo of a freestanding $MoS_2$@C paper.

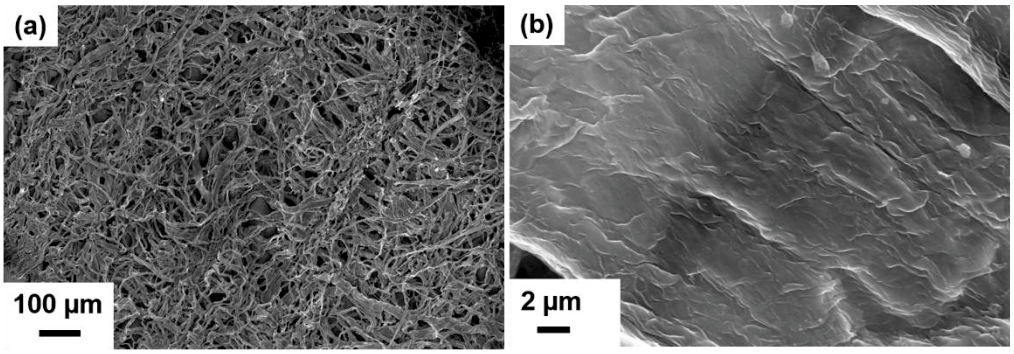


**Figure 9.5** SEM images of carbon paper derived from paper towel.

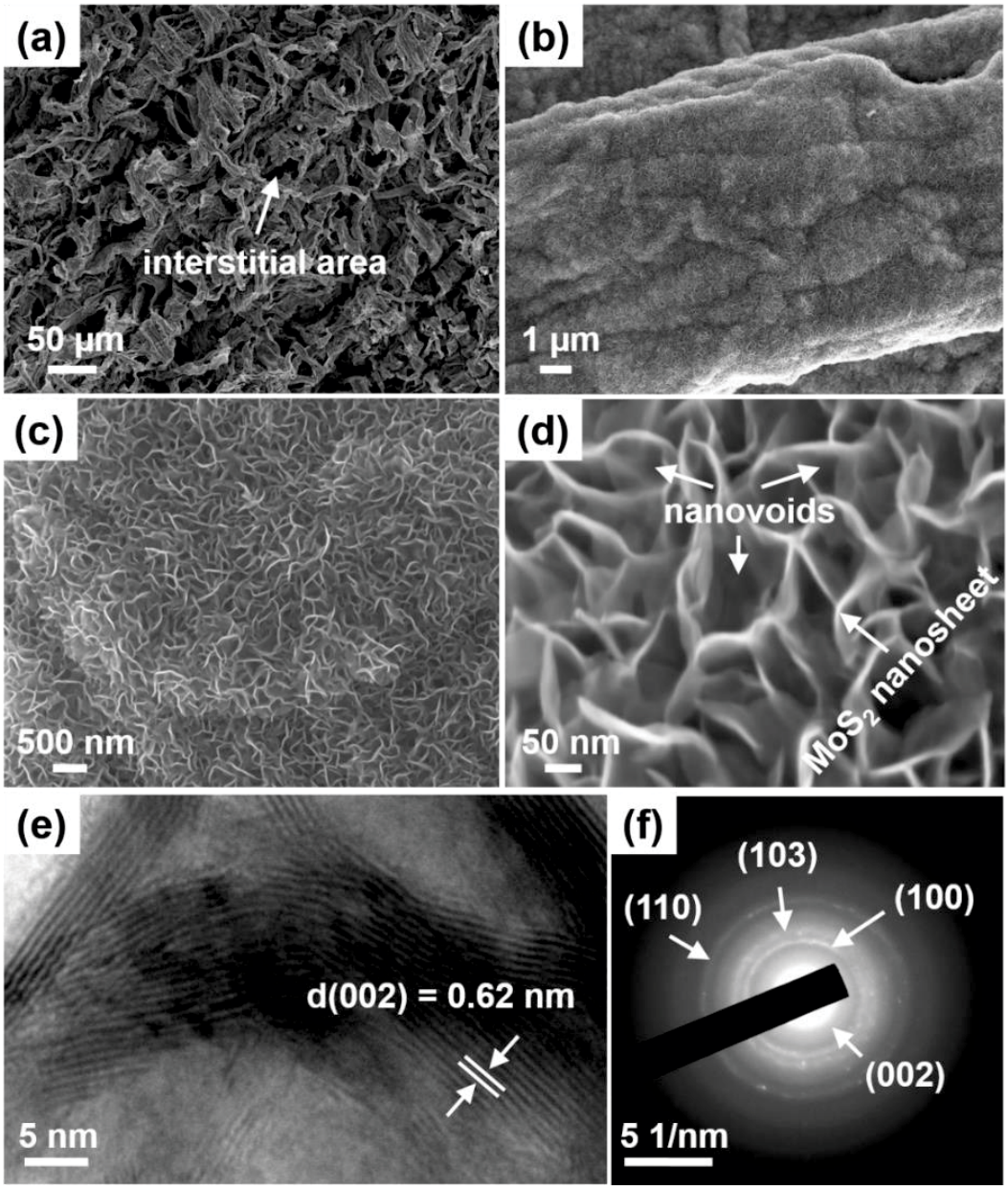


**Figure 9.6** (a-d) SEM images of the as-prepared freestanding $MoS_2$@C. (e) High-magnification TEM image and (f) SAED pattern of $MoS_2$@C.

The porous carbon paper derived from commercial PT consists of carbon fibers with smooth surfaces, which are interwoven into a three-dimensional (3D) open network structure (**Figure 9.5**). As shown in the low-magnification scanning electron microscopy (SEM) image in **Figure 9.6a**, $MoS_2$@C maintains the interwoven structure after $MoS_2$ grafting. The large

interstitial areas formed between carbon fibers are beneficial for the electrolyte penetration, thereby facilitating sodiation/de-sodiation processes. **Figure 9.6b** shows a SEM image collected from typical areas of the as-prepared $MoS_2$@C composites, which suggests the uniform and dense deposition of $MoS_2$ on a large scale. It can be observed in the high-magnification SEM images of $MoS_2$@C shown in **Figure 9.6c and d** that the $MoS_2$ nanosheets are densely packed and aligned vertically, forming a heterostructured microforest. The spatially dispersed $MoS_2$ nanosheets construct nanovoids on the quasi one-dimensional (1D) microfiber, which in turn favors electrode/electrolyte interaction. In this 3D architecture, $MoS_2$ nanosheets are electronically connected to carbon fibers, ensuring efficient electron transfer. The high-resolution transmission electron microscopy (HRTEM) image in **Figure 9.6e** shows a typical edge view of $MoS_2$ nanosheets with clear lattice fringes. The interlayer spacing is measured to be 0.62 nm, corresponding to the (002) plane of 2H-$MoS_2$. It is consistent with the result calculated from XRD. The selected area electron diffraction (SAED) pattern (**Figure 9.6f**) shows clear diffraction rings, indicating the polycrystalline nature of $MoS_2$. These diffraction rings can be well indexed to the (002), (100), (103) and (110) planes of 2H-$MoS_2$.

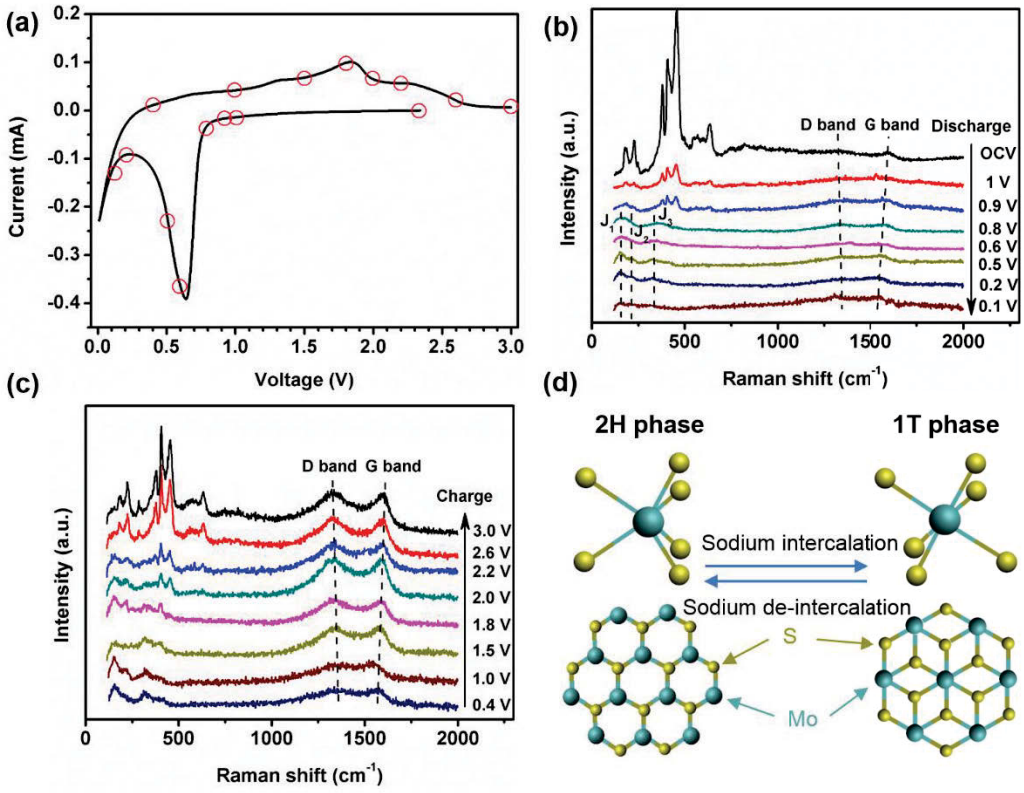


**Figure 9.7** (a) CV curve of the as-prepared $MoS_2$@C anode for sodium-ion batteries. *In situ* Raman spectra of the $MoS_2$@C electrode at different cut-off voltages during discharge (b) and charge (c) processes. (d) Schematic of the phase transition between 2H-$MoS_2$ and 1T-$MoS_2$ during sodium intercalation/de-intercalation.

The freestanding $MoS_2$@C can be directly used as an electrode for SIBs without further manufacturing processes. The cyclic voltammetry (CV) curve of the freestanding $MoS_2$@C electrode is shown in **Figure 9.7a**. A sharp reduction peak located at 0.65 V can be observed. In the following reduction process, a pronounced peak starting from 0.2 V appears. In the charge process, an oxidation peak at ~1.8 V is discernable. As can be seen from **Figure 9.8**, $MoS_2$@C showed a broad reduction peak between 1.1 V and 0.4 V (cathodic sodiation) and an oxidation peak starting from 1.2 V (anodic de-sodiation) from the second cycle. To fully understand the corresponding potential-dependent sodiation/de-sodiation reactions related to

the reduction/oxidation peaks during the discharge/charge, we performed *in situ* Raman spectroscopy in a specially-designed coin-cell. **Figure 9.7b** shows the *in situ* Raman spectra collected at various cut-off potentials (marked by red circles in **Figure 9.7a**) during the first discharge process. Therein, the Raman spectrum of the $MoS_2$@C electrode at open circuit voltage (OCV) displays fingerprint peaks of 2H-$MoS_2$ in the range of 100-750 $cm^{-1}$, in which Raman peaks at 379 and 405 $cm^{-1}$ can be attributed to in-plane $E^1_{2g}$ and out-of-plane $A_{1g}$ modes of 2H-$MoS_2$ nanosheets, respectively.[401] Additionally, two small peaks at 1327 and 1594 $cm^{-1}$ can be observed, which are ascribed to the D- and G-bands of C, respectively. Discharging the cell to 0.9 V results in the continuous attenuation of 2H-$MoS_2$ Raman peaks without emergence of any new peaks, suggesting the presence of a 2H-phase in the sodiated $MoS_2$. In concert with the disappearance of 2H-$MoS_2$ Raman peaks, three new peaks at 156, 218, and 327 $cm^{-1}$ appear at 0.9 V. These peaks, previously referred to as $J_1$, $J_2$, and $J_3$, become more pronounced when the battery is further discharged to 0.5 V. They correspond to the modes that are active in the 1T-$MoS_2$ with octahedral coordination but forbidden in the 2H-$MoS_2$ which has a trigonal prism coordination.[402, 403] These distinct changes indicate 2H-1T phase transitions of $MoS_2$ when more $Na^+$ ions are intercalated to form $Na_yMoS_2$ (1T-$Na_yMoS_2$). The *ex situ* SEM images shown in **Figure 9.9a and b** suggest that 1T-$Na_yMoS_2$ maintains the sheet-like morphology of 2H-$MoS_2$. The intensities of 1T-$Na_yMoS_2$ Raman peaks decrease when the cell was discharged from 0.2 V to 0.1 V, which can be ascribed to the decomposition of 1T-$Na_yMoS_2$ into Mo and $Na_yS$.[233] In addition, the blue-shift of the D-band and the red-shift of the G-band can be observed during the discharge process due to the intercalation of $Na^+$.[404] From the *ex situ* SEM images shown in **Figure 9.9c and d** it can be seen that the original $MoS_2$ nanosheets are converted into well-dispersed nanoparticles after

the discharge process. **Figure 9.7c** presents the Raman spectra collected during charging. It can be seen that the phase transition from 1T-$Na_yMoS_2$ to 2H-$MoS_2$ occurs from 1.5 V and 2H-$MoS_2$ can be recovered at 3.0 V, indicating the reversible phase transition between 1T-$Na_yMoS_2$ to 2H-$MoS_2$ (**Figure 9.7d**). Structurally, 2H-$MoS_2$ has a hexagonal lattice with 3-fold symmetry and shows the atomic stacking sequence (S-Mo-S) of ABA, while the 1T-$MoS_2$ shows the atomic stacking sequence (S-Mo-S') of ABC where the bottom S' plane occupies the hollow center of the 2H hexagonal lattice. Previous investigations suggest that these two phases can easily convert to each other by a glide of the intralayer atomic planes, which involves a transversal displacement of one of the sulfur planes.[233, 405] The hierarchical architecture with vertically aligned $MoS_2$ nanosheets is recovered at 3.0 V (**Figure 9.9e and f**).

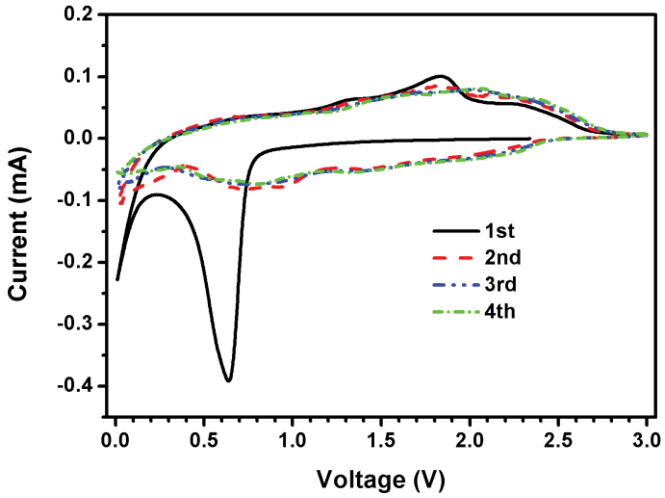


**Figure 9.8** CV curves of the as-prepared $MoS_2$@C anode for sodium-ion batteries in the first 4 cycles at a scan rate of 0.1 mV $s^{-1}$.

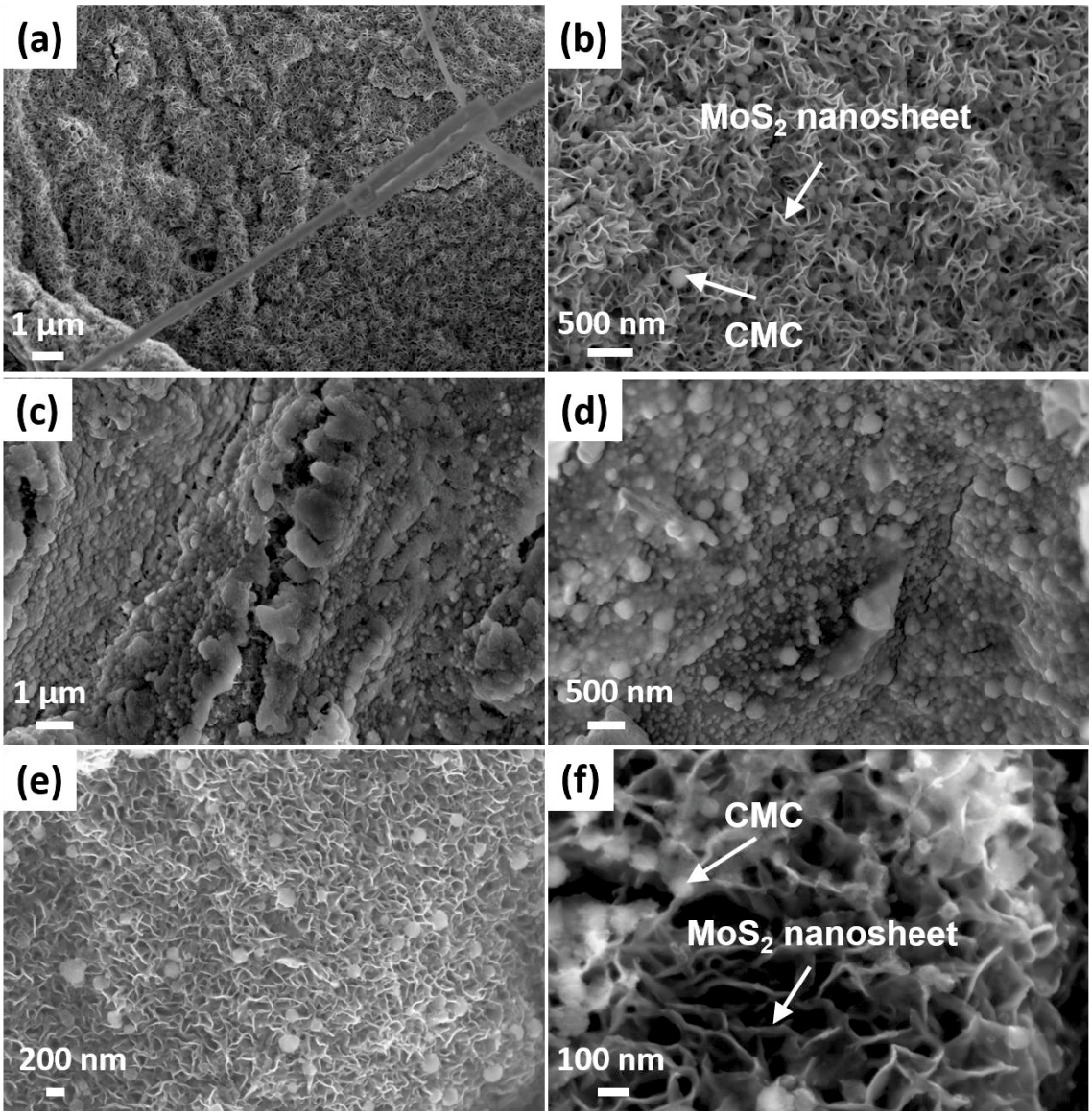


**Figure 9.9** *Ex situ* SEM images of $MoS_2$@C-CMC electrode discharged to 0.5 V (a and b), 0.01 V (c and d) and charged to 3.0 V (e and f).

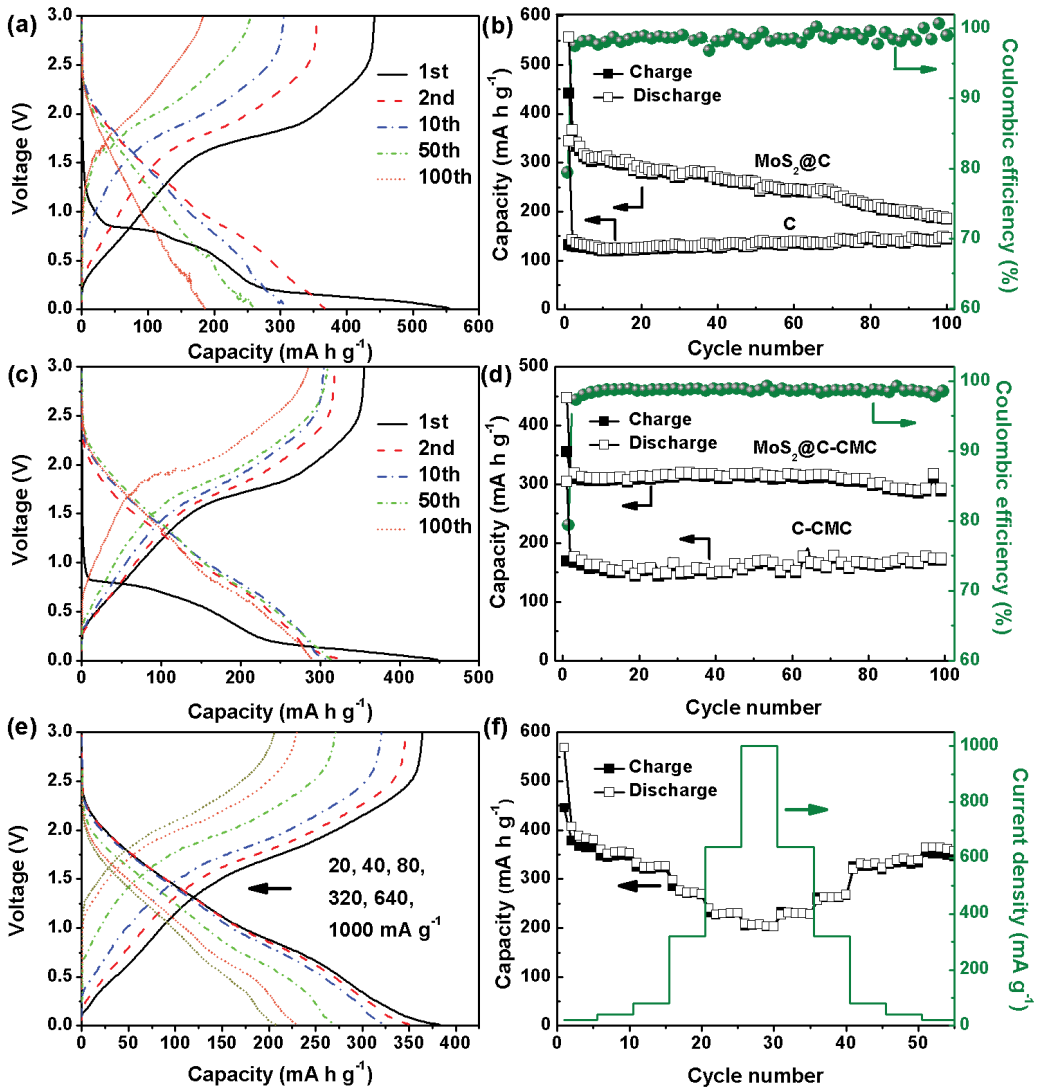


**Figure 9.10** (a) Charge-discharge curves of the as-prepared $MoS_2$@C paper electrode at a current density of 80 mA $g^{-1}$. (b) Cycling performance and the corresponding Coulombic efficiencies of the $MoS_2$@C paper electrode at 80 mA $g^{-1}$. The cycling performance of bare carbon paper is also presented for comparison. (c) Charge-discharge curves of CMC coated $MoS_2$@C electrode ($MoS_2$@C-CMC) at a current density of 80 mA $g^{-1}$. (d) Cycling performance and the corresponding Coulombic efficiencies of the $MoS_2$@C-CMC paper electrode at 80 mA $g^{-1}$ and the cycling performance of the CMC-coated carbon paper electrode (C-CMC). (e) Charge-discharge curves of $MoS_2$@C-CMC at different current densities. (f) Rate-performance of the $MoS_2$@C-CMC electrode.

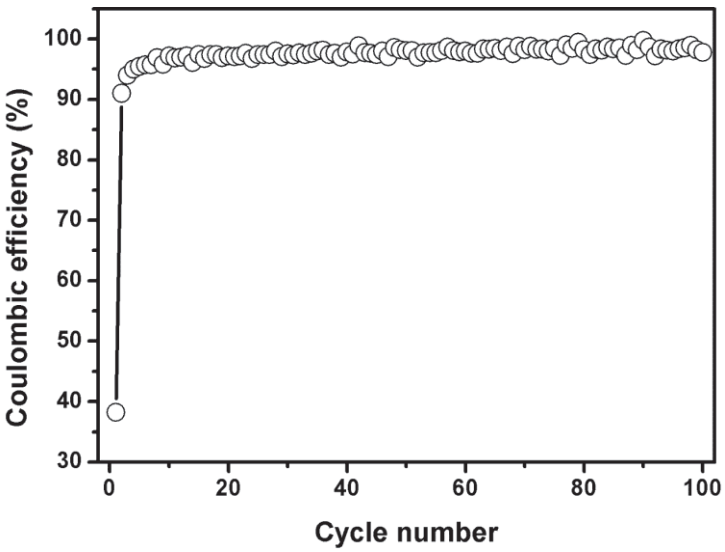


**Figure 9.11** Coulombic efficiency of bare carbon paper electrode as a function of cycle number at a current density of 80 mA $g^{-1}$.

**Figure 9.10a** shows the galvanostatic charge-discharge profiles of the as-prepared freestanding $MoS_2$@C electrode at a current density of 80 mA $g^{-1}$. In the initial discharge curve, a plateau at around 0.7 V appears, which agrees with the CV results and corresponds to the insertion of $Na^+$ in the interlayer of $MoS_2$. The plateau is followed by a sloping curve ranging from 0.7 V to 0.2 V. Another sloping segment observed at potentials < 0.2 V originates from the decomposition of 1T-$Na_yMoS_2$ according to the *in situ* Raman results. At a current density of 80 mA $g^{-1}$, $MoS_2$@C electrodes deliver initial discharge and charge capacities of 556 mA h $g^{-1}$ and 442 mA h $g^{-1}$, respectively, which are higher than that of bare carbon paper (345 and 132 mA h $g^{-1}$, correspondingly). It is worth noting that $MoS_2$@C electrode shows a high ICE of 79.5%, as opposed to that of bare carbon paper (38.3%) as can be seen from **Figure 9.11**. This high ICE stems from the surface coating of carbon fibers by $MoS_2$ in the designed 3D architecture. Owing to the dense coverage of carbon fibers by $MoS_2$, interactions between C and electrolyte are minimized. Consequently, unwanted and

irreversible side reactions associated with carbon, such as the irreversible electrochemical absorption of sodium ions (non-SEI related), are depressed.[406] The Coulombic efficiency of $MoS_2$@C then quickly stabilizes at around 98% in the following cycles (**Figure 9.10b**). As can be seen from **Figure 9.10b**, after cycling for 100 cycles at 80 mA $g^{-1}$, the as-prepared $MoS_2$@C electrode delivers a charge capacity of 184 mA h $g^{-1}$, which is higher than that of bare carbon paper electrode (143 mA h $g^{-1}$).

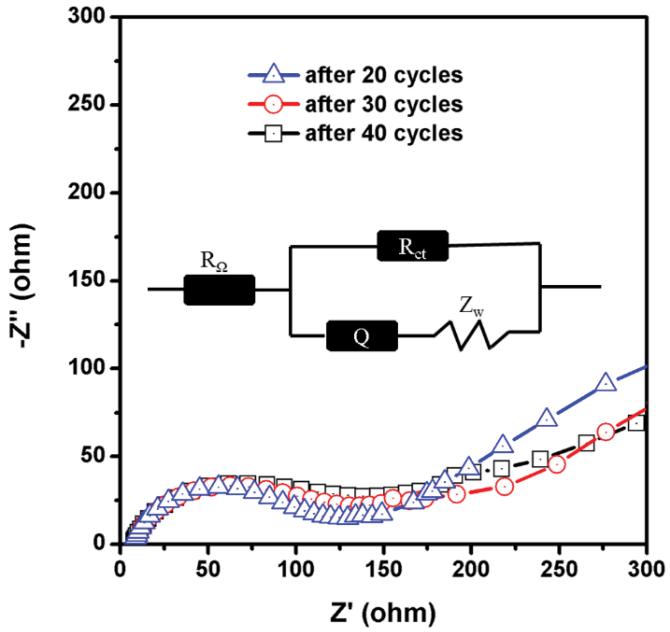


**Figure 9.12** Change of impedance spectra of $MoS_2$@C-CMC electrode during cycling. The inset shows the modeled equivalent circuit. $R_\Omega$ is the electrolyte resistance, Q represents constant phase element, $R_{ct}$ is the charge-transfer resistance, and $Z_w$ is the Warburg impedance.

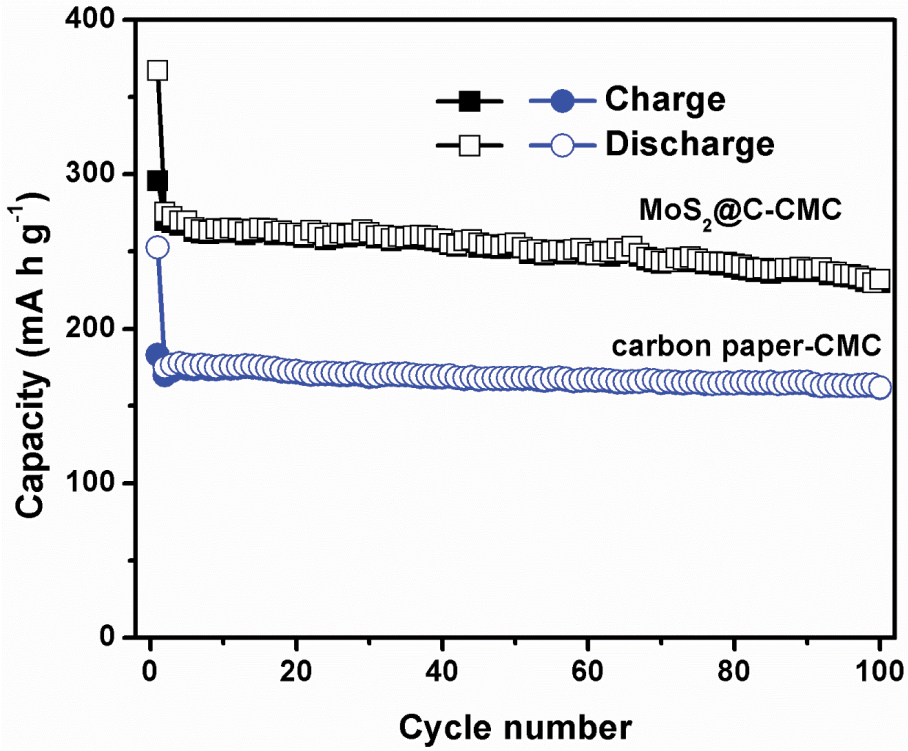


**Figure 9.13** Cycling performance of the $MoS_2$@C-CMC electrode and carbon paper-CMC electrode at a current density of 160 mA $g^{-1}$.

To improve the cycling performance of the freestanding $MoS_2$@C electrode, an efficient one-step carboxymethylcellulose sodium salt (CMC)-coating approach was employed. CMC was deposited on $MoS_2$@C to form CMC-coated $MoS_2$@C ($MoS_2$@C-CMC) by a dip-coating method. The electrochemical impedance spectroscopy (EIS) (**Figure 9.12**) reveals an increase in resistance of the $MoS_2$@C-CMC electrode, leading to the increased polarization as shown in **Figure 9.10c**. As can be seen from **Figure 9.10d**, $MoS_2$@C-CMC electrode shows a high ICE of 79.4%. The Coulombic efficiency increases beyond 98% in the following cycles. **Figure 9.10d** also plots the specific capacity versus cycle number of the $MoS_2$@C-CMC electrode and carbon paper electrode coated with CMC (C-CMC). $MoS_2$@C-CMC electrode exhibits stable cycling performance when cycled at a current

density of 80 mA $g^{-1}$. After 100 cycles, a high charge capacity of 286 mA h $g^{-1}$ can be maintained, which is higher than that of the C-CMC electrode (172 mA h $g^{-1}$), suggesting the promising application of $MoS_2$@C for highly reversible SIBs. The $MoS_2$@C-CMC electrode also shows good cycling performance at a higher current density of 160 mA $g^{-1}$ (**Figure 9.13**). After 100 cycles, it delivers a charge capacity of 230 mA h $g^{-1}$, which is superior to the C-CMC electrode (160 mA h $g^{-1}$). The improved cycling performance by CMC-coating can be ascribed to the ability of CMC to accommodate a large volume change of $MoS_2$ during repeated sodiation/de-sodiation processes.[238, 249, 257]

**Figure 9.10e** shows the charge-discharge voltage profiles of the $MoS_2$@C-CMC electrode in the voltage window of 0.01-3.0 V at different current densities. $MoS_2$@C-CMC electrodes exhibit stable charge-discharge voltage profiles when the current density is increased from 20 to 1000 mA $g^{-1}$. The designed $MoS_2$@C-CMC electrode also demonstrates good rate capability, which is presented in **Figure 9.10f**. At a current density of 20 mA $g^{-1}$, a high reversible capacity of 446 mA h $g^{-1}$ can be achieved. This value is much higher than that of other reported $MoS_2$-based freestanding electrodes for SIBs, such as $MoS_2$/graphene film (338 mA h $g^{-1}$)[292] and membrane-like electrospun $MoS_2$@carbon nanofibres (401 mA h $g^{-1}$)[240]. As the current density is gradually increased to 40, 80, 320, 640, and 1000 mA $g^{-1}$, the $MoS_2$@C-CMC electrode delivers reversible capacities of 348, 321, 271, 230, and 205 mA h $g^{-1}$, respectively. Therefore the $MoS_2$@C-CMC composites demonstrated a high-rate capability for Na-ion storage.

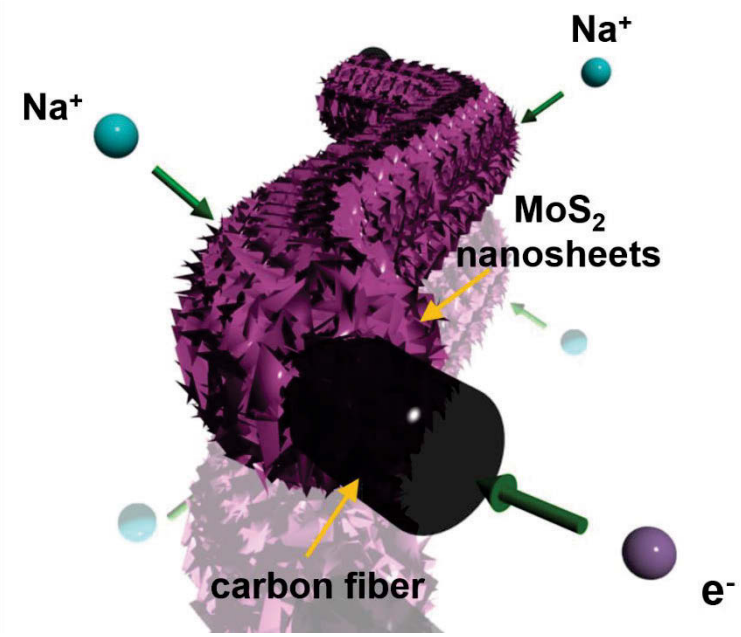


**Figure 9.14** Schematic illustration showing paths for sodium-ion diffusion and electron conduction in the $MoS_2$@C electrode.

This promising electrochemical performances can be ascribed to the hierarchical structure of the $MoS_2$@C hybrid. As illustrated in **Figure 9.14**, the advantages of such a 3D electrode are three-fold. Firstly, the high surface-to-volume ratio of the nested structure with nano-reservoirs between adjacent $MoS_2$ nanosheets favors the interaction between $MoS_2$ and electrolyte. This provides shortened ionic diffusion pathways, thereby helping reduce the mass-transfer limitation for the electrochemical $MoS_2$-$Na^+$ reaction. Secondly, $MoS_2$ layers coated on carbon fibers diminish the carbon-electrolyte interaction and reduce side reactions responsible for irreversible capacity. This endows $MoS_2$@C electrodes with high ICE. Thirdly, in the coaxial structure, $MoS_2$ nanosheets are connected with conductive carbon fibers, thus affording good current collector/active material electrical contacts and low charge transfer resistance. Moreover, carbon paper mats of randomly-woven 1D carbon fibers offer 3D conducting networks that facilitate electron transport. $MoS_2$ nanosheets vertically aligned

on the carbon paper matrix in a manner that concurrently constructs efficient ionic and electronic transfer pathways, overcoming the kinetic limitations. Therefore, $MoS_2$@C composites deliver high reversible capacities and exhibit promising rate performance for Na-ion storage.

### 9.4 Conclusions

$MoS_2$@C composites have been rationally designed as freestanding electrodes for sodium-ion batteries. The $MoS_2$@C electrodes were successfully fabricated by a hydrothermal method and subsequent annealing, utilizing carbonization of paper towel (biomass precursor for carbon paper) and deposition of $MoS_2$ nanosheets. The as-prepared $MoS_2$@C composites feature a 3D hierarchical structure, in which $MoS_2$ nanosheets are vertically aligned on carbon scaffolds. Dip-coating with carboxy methyl cellulose sodium salt improved the cycling performance of the as-prepared $MoS_2$@C electrode. After 100 cycles at a current density of 80 mA $g^{-1}$, a high reversible capacity of 286 mA h $g^{-1}$ was achieved. Benefiting from the unique 3D architecture, the as-prepared electrodes exhibited a high reversible capacity of 446 mA h $g^{-1}$ at 20 mA $g^{-1}$, high ICE (79.5%), and promising rate capability. Even at a high current density of 1000 mA $g^{-1}$, a reversible capacity of 205 mA h $g^{-1}$ was maintained. The reversible phase transition from 2H-$MoS_2$ to 1T-$MoS_2$ was observed during sodium-ion intercalation/de-intercalation process by *in situ* Raman electro-spectroscopy. The technique developed in this research can be extended to deposit other electro-active compounds such as SnS, $SnS_2$, and $WS_2$ for high performance SIBs.

# Chapter 10 Porous Heterostructured MXene/Carbon Nanotube Composite Paper with High Volumetric Capacity for Sodium-Based Energy Storage Devices

## 10.1 Introduction

Compared to $Li^+$, $Na^+$ has a larger ionic radius and different ionic coordination preference (sodium ions prefer to coordinate at prismatic or octahedral sites), resulting in much slower solid-state diffusion of $Na^+$ and decreased kinetics of sodium-insertion/extraction reactions within electrode materials.[407] Nanostructured materials have been widely investigated for electrochemical energy storage (EES) due to their abilities to shorten diffusion paths for $Na^+$ and increase the electrode/electrolyte interactions, thereby increasing the sodium-ion storage capacity.[408] For example, carbon materials,[186, 282, 409, 410] alloying anodes (P,[285, 411-416] Sn,[247, 385, 417, 418] or Sb [287, 288, 291, 419-421]), two-dimensional (2D) transition metal sulfides,[233, 237, 292, 332, 333, 405, 422, 423] and titanium-based oxides [197, 424-426] with controllable nanostructures have been reported. In most cases, the gravimetric capacity has been the focus for evaluating the performance of electrode materials. The volumetric capacity becomes the most relevant figure-of-merit critical for applications where size matters, such as portable or wearable electronics, automotive batteries, or when the storage devices are integrated with energy generating systems such as solar panels or triboelectric power generators.[427] However, the use of nanostructured electrode materials reported so far often leads to a low density of electrodes. Besides, current collectors, conductive agents and polymeric binders are additionally required for device manufacturing, leading to seriously compromised volumetric capacities.

2D transition metal carbides MXenes are formulated as $M_{n+1}X_nT_x$, where M is an early transition metal such as Ti, V, Cr, Nb, Mo, or Ta, X is C and/or N, T is a surface termination - OH, F and/or O, and n is 1-3.[209, 428, 429] MXenes with a combination of metallic conductivity and hydrophilicity are emerging as a promising, versatile platform for applications such as supercapacitors,[214, 430] Li-ion batteries,[209, 212, 431, 432] Li-S batteries,[433] catalysis,[434, 435] sensors,[436, 437] $H_2$ storage,[438] and selective ion sieving[439]. Their performance is highlighted by high volumetric capacitance for supercapacitors.[214, 430, 440] MXenes are also expected to be superior for Na-ion storage. Computational results showed that MXenes have a low diffusion barrier for $Na^+$ on their surfaces (0.1-0.2 eV),[219, 441] which is favorable for fast charging/discharging. Modeling and experimental investigations suggest that two layers of $Na^+$ can intercalate between MXene layers.[217, 218] These characteristics make MXenes attractive candidates for Na-ion storage. Yamada *et al.* reported that multilayered $Ti_2CT_x$ as a negative electrode showed a capacity of 175 mA h $g^{-1}$ and good rate capability.[442] Multilayered $Ti_3C_2T_x$ has also been tested as a negative electrode for Na-ion storage and exhibited a capacity around 100 mA h $g^{-1}$.[217, 218] The Na-ion insertion potentials of MXenes can be tuned by changing the transition metal and surface functional groups.[219, 220] Another MXene, $V_2CT_x$, was successfully used for positive electrodes, paired with hard carbon to assemble full cells delivering a maximum cell voltage of 3.5 V and a cell capacity of 50 mA h $g^{-1}$.[221] The electrochemical performance of MXenes is expected to be further improved by delaminating the multilayered MXenes into few-layered flakes, which can be fabricated as freestanding electrodes directly without using conductive agents, polymeric binders or metal current collectors. This processing technique allows for the reduction of the dead volume and an increase in cell volumetric capacity. However, aggregation and restacking of MXene sheets *via* van der Waals interactions and hydrogen bonds cause limitations in the material's

performance and impede ion access to the active materials.[443, 444] By alternating filtration, carbon nanomaterials have been utilized as spacers to design sandwich-like MXene/carbon composite papers, which showed an improved electrochemical performance compared to that of pure MXene.[443] However, an effective strategy to prevent restacking of MXene nanosheets and construct open channels for ionic transport is highly desirable, and yet to be fully realized.

Herein, porous MXene/CNT films were prepared by self-assembly of negatively charged, metallic $Ti_3C_2T_x$ MXene flakes and positively charged CNTs as spacers. We also fabricated 2D/2D MXene/graphene composite films for comparison. Compared to the 2D/2D integrations of the latter composite, the 2D/1D hybridization between MXene nanosheets and CNTs reduced stacking of nanosheets more efficiently and produced hierarchical films with a porous structure, thereby improving the accessibility of MXene nanosheets to the electrolyte. When directly applied as freestanding electrodes for sodium-ion storage, the porous MXene/CNT papers exhibited a high volumetric capacity, good rate capability and long cycling performance.

## 10.2 Experimental Section

### 10.2.1 Preparation of delaminated $Ti_3C_2T_x$ suspension

$Ti_3AlC_2$ with a particle size of < 38 μm was prepared as described previously.[440] Multilayered $Ti_3C_2T_x$ was synthesized by etching 3 g of $Ti_3AlC_2$ powders in a mixture of lithium fluoride, LiF, (3g, Alfa Aesar) and 9 M hydrochloric acid, HCl, (30 mL, Fisher Scientific) for 24 h at 35 $^oC$. The etched $Ti_3C_2T_x$ powder was washed with deionized water and then centrifuged until the pH of the supernatant was above 5, then vacuum filtered. In order to delaminate $Ti_3C_2T_x$, 1 g of the multilayered $Ti_3C_2T_x$ powder was added in 250 mL deionized water and

sonicated for 1 h under Ar flow. After centrifugation for 1 h at 3500 rpm, the dark green supernatant was collected, confirming the delamination of $Ti_3C_2T_x$. The concentration of the delaminated $Ti_3C_2T_x$ was determined by filtering a known volume of the delaminated $Ti_3C_2T_x$ suspension through a Celgard membrane and measuring the weight of the film after vacuum drying.

### 10.2.2 Fabrication of freestanding $Ti_3C_2T_x$ and its composite films

To prepare cetyltrimethylammonium bromide (CTAB)-grafted CNTs, CTAB (>99%, SigmaAldrich) was dissolved in deionized water (0.1 wt.%), and then CNTs, which were prepared through a floating catalyst chemical vapor deposition (CVD) method [445], were dispersed in the CTAB solution by probe sonication to get a CNTs concentration of 0.5 mg $mL^{-1}$. Porous $Ti_3C_2T_x$/CNTs composite films were prepared by a self-assembly process. Typically, 3.1 mL of the CTAB-grafted CNTs solution was added dropwise to $Ti_3C_2T_x$ suspension (0.4 mg $mL^{-1}$, 35 mL). The mixture was probe sonicated for 10 min and then filtered using a Celgard membrane. Porous self-assembled $Ti_3C_2T_x$/CNTs (denoted as $Ti_3C_2T_x$/CNT-SA) composite film was obtained after washing with copious deionized water and vacuum drying. $Ti_3C_2T_x$/CNT-SDS film was prepared in a similar way but sodium dodecylsulphate (SDS, 99.5%, Fisher Scientific, Fair Lawn, NJ, USA) instead of CTAB was used to modify CNTs. Pure $Ti_3C_2T_x$ film was prepared by vacuum-filtrating 35 mL of $Ti_3C_2T_x$ suspension (0.4 mg $mL^{-1}$). $Ti_3C_2T_x$/rGO-SA films were prepared by a similar self-assembly method, but rGO solution was added.

### 10.2.3 Characterizations

The $Ti_3C_2T_x$-based films were characterized by XRD on a Rigaku Smart Lab (Tokyo, Japan) diffractometer using Cu Kα radiation (40 KV and 44 mA) and step scan 0.02°, 3°-60° 2 theta range and step time of 0.5 s. The morphology of the samples was characterized using a scanning electron microscope (SEM) (Zeiss Supra 50VP, Germany) and a transmission electron microscope (TEM) (JEOL JEM-2100, Japan) using an accelerating voltage of 200 kV. The ζ-potential measurements were conducted using a Zetasizer Nano ZS apparatus from Malvern Instruments. Nitrogen sorption measurements were conducted on a Quadrasorb instrument (Quantachrome, USA) at 77 K using liquid nitrogen to determine the specific surface area and pore size distribution. The pore size distributions were calculated by the non-local density functional theory (NLDFT) method.

### 10.2.4 Electrochemical tests

The three-electrode electrochemical performance was tested in Swagelok cells, where the freestanding $Ti_3C_2T_x$/CNT-SA papers served directly as the working electrodes, over-capacitive activated carbon films prepared by mixing 5 wt.% polytetrafluoroethylene binder (60 wt.% in $H_2O$, Aldrich) to 95 wt.% of YP50 (Kuraray, Japan) were used as the counter electrode, and Na served as the reference electrode. Polypropylene membranes were employed as the separators. The electrolyte solution was 1 M $NaClO_4$ dissolved in a mixture of ethylene carbonate (EC) and propylene carbonate (PC) with a volume ratio of 1:1, in which 5 vol.% fluoroethylene carbonate (FEC) was added as electrolyte additive. FEC is a popular film-forming electrolyte additive for sodium-ion batteries, which is able to stablize the electrochemical performances by reducing the decomposition rate of PC [384, 446]. The cells were assembled and tested in an argon-filled glovebox. For two-electrode tests, CR2032-type coin cells were assembled in an argon-filled glove box. The as-obtained electrode was cut

into ~0.6 × 0.6 $cm^2$ and directly used as self-supported electrode. A photo of the paper electrode was taken with a background providing a scale bar and the precise area was measured by ImageJ computer software. In combination with the thicknesses determined from the cross-sectional SEM images, the volume of the electrode was determined. Na foil was used as the counter and reference electrode. The positive and negative electrodes were electronically separated by glass microfiber (Whatman) saturated with electrolyte. The charge-discharge measurements were performed at different current densities in the voltage range from 0.01 to 3.0 V *vs.* $Na^+$/Na using an Arbin system (Arbin BT-2143-11U, College Station, TX, USA). Cyclic voltammetry (CV), galvanostatic charging/discharging of Swagelok cells, and electrochemical impedance spectroscopy (EIS) were conducted by using a VMP3 potentiostat (Biologic, France). CV curves were measured between 0.01 and 3.0 V *vs.* $Na^+$/Na. The EIS measurements were performed at charged state with a 10 mV amplitude, and frequencies that ranged from 10 mHz to 200 kHz.

### 10.2.5 Assembly of $Na_{0.44}MnO_2$//$Ti_3C_2T_x$/CNT-SA full cells

A coin cell (CR2032) was assembled for full cell testing. $Na_{0.44}MnO_2$ was prepared according to a previous report [447]. Briefly, $MnCO_3$ and $Na_2CO_3$ were manually mixing in a mortar and pestle and then pressed into a pellet. The pellet was heat treated at 300 °C in air for 24 h and then thoroughly ground and pressed into a pellet again. A second heat treatment of 48 h at 800 °C was performed on the repressed material, resulting in a black $Na_{0.44}MnO_2$ powder. The cathodes were prepared by dispersing the as-prepared $Na_{0.44}MnO_2$ (70 wt%), carbon black (20 wt%), and poly (vinylidene fluoride) binder (PVDF, 10 wt%) in *N*-methyl-2-pyrrolidone (NMP) to form a slurry. The resultant slurry was pasted onto Al foil and dried in a vacuum oven for 12 h. $Ti_3C_2T_x$/CNT-SA electrodes were precycled in $Ti_3C_2T_x$/CNT-

SA//Na cells and stopped at a voltage of 1.5 V first, which were then disassembled and paired with $Na_{0.44}MnO_2$ cathodes. The mass ratio between $Na_{0.44}MnO_2$ and $Ti_3C_2T_x$/CNT-SA was 3:1. The same electrolyte and Whatman glass microfiber separators as in the half-cell testing were used in full cells. Galvanostatic charge/discharge experiments were conducted on an Arbin system between 0.01 and 4.0 V.

### 10.3 Results and Discussions

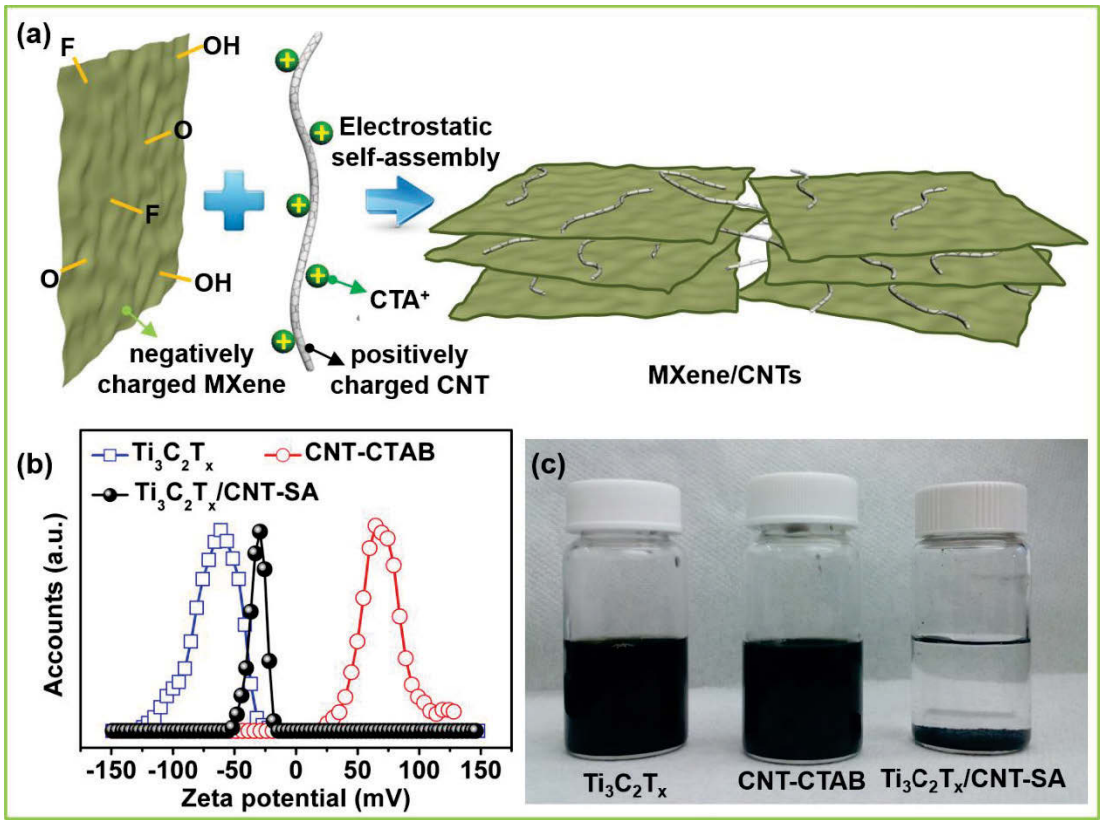


**Figure 10.1** (a) Schematic showing preparation of the porous MXene/CNT electrode by the self-assembly method. The MXene nanosheets are negatively charged due to their functional groups, and the CTAB-grafted CNTs are positively charged. (b) Zeta potential of $Ti_3C_2T_x$ nanosheets, CTAB-grafted CNTs (CNT-CTAB), and self-assembled $Ti_3C_2T_x$/CNT-CTAB ($Ti_3C_2T_x$/CNT-SA). (c) Digital photographs of $Ti_3C_2T_x$ suspension, CNT-CTAB in water, and $Ti_3C_2T_x$/CNT-SA composites.

**Figure 10.1a** illustrates the preparation of porous MXene/CNT composite paper by the self-assembly method. MXene nanosheets are negatively charged and hydrophilic due to their surface functional groups (*e.g.* -O, -OH, and -F). Taking $Ti_3C_2T_x$ for example, the zeta potential of the as-produced $Ti_3C_2T_x$ was measured to be -63.3 mV (**Figure 10.1b**). Due to the hydrophilic surface and the repulsion force between $Ti_3C_2T_x$ nanosheets, $Ti_3C_2T_x$ suspensions are very stable in water (Figure 10.1c, left) and contain primarily single-layer MXene flakes.[440] Positively charged CNTs with a zeta potential of +74.8 mV (**Figure 10.1b**) were prepared by grafting a cationic surfactant cetyltrimethylammonium bromide (CTAB) (**Figure 10.1c**, middle). When CTAB-grafted CNTs (CNT-CTAB) were added to the $Ti_3C_2T_x$ suspension, CNTs were attracted on the surface of $Ti_3C_2T_x$ nanosheets and the negative charges of $Ti_3C_2T_x$ are screened (**Figure 10.1b**). As a result, aggregations appeared and a clear supernatant could be observed (**Figure 10.1c**, right). This suggests the successful self-assembly between $Ti_3C_2T_x$ and CNT-CTAB. The mixture was then vacuum-filtrated to prepare freestanding and flexible self-assembled $Ti_3C_2T_x$/CNTs ($Ti_3C_2T_x$/CNT-SA) paper (**Figure 10.2**). The as-prepared $Ti_3C_2T_x$/CNT-SA papers have a density of 2.4 g $cm^{-3}$, which is lower than pure $Ti_3C_2T_x$ (3.2 g $cm^{-3}$). As a comparison experiment, an anionic surfactant sodium dodecyl sulfate (SDS) was used instead of CTAB to modify CNTs, resulting in negatively charged CNTs (CNT-SDS). The mixture of CNT-SDS and $Ti_3C_2T_x$ led to stable $Ti_3C_2T_x$/CNT-SDS aqueous suspension and no precipitation was observed (**Figure 10.3**), indicating the importance of electrostatic force for the self-assembly process. The weight ratio of CNTs in $Ti_3C_2T_x$/CNT composites was fixed at 10 wt.% in all composites, based on previous experience with MXene/CNT composites.[443]

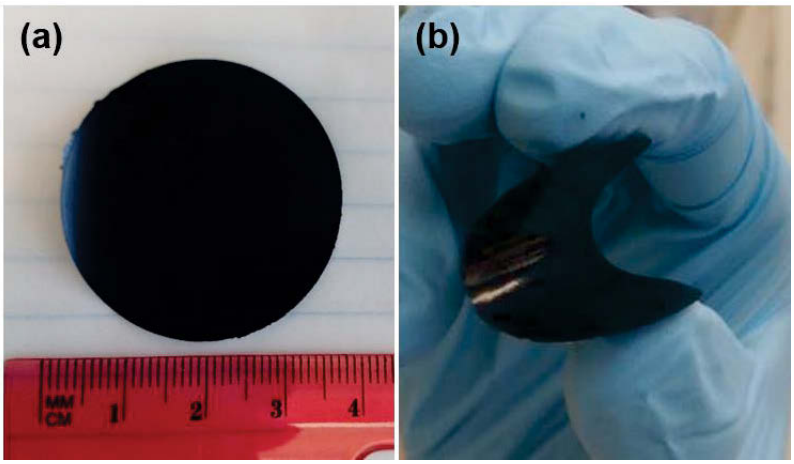


**Figure 10.2** Digital photographs of the as-prepared freestanding $Ti_3C_2T_x$/CNT-SA film.

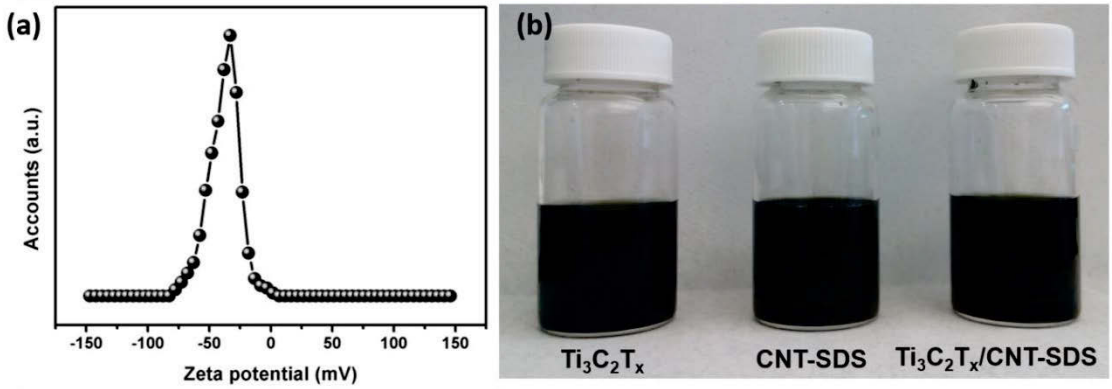


**Figure 10.3** (a) Zeta potential of a colloidal solution of CNT-SDS. (b) Digital photographs of $Ti_3C_2T_x$ suspension, CNT-SDS, and a $Ti_3C_2T_x$/CNT-SDS mixture.

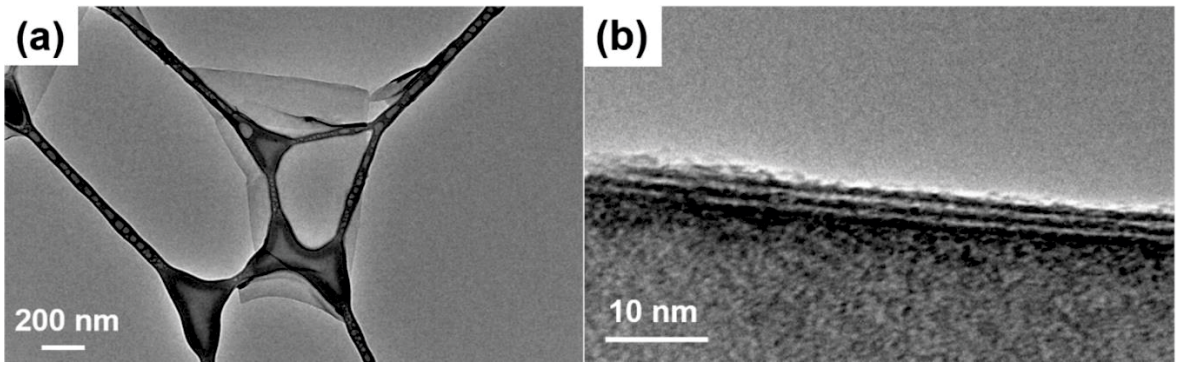


**Figure 10.4** TEM images of $Ti_3C_2T_x$ nanosheet. (a) in plane, (b) cross-section.

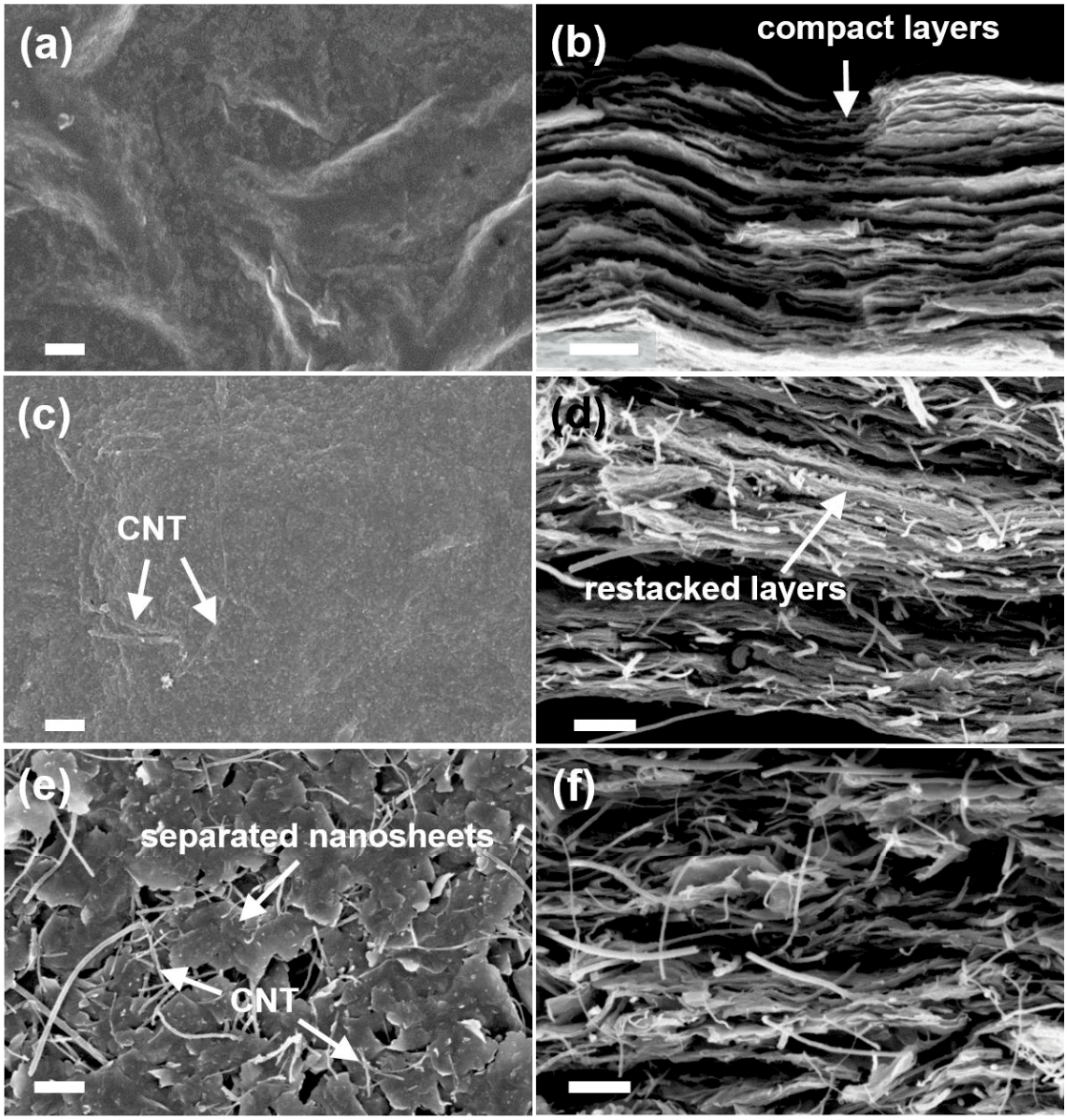


**Figure 10.5** Top view (left panels) and cross-sectional (right panels) SEM images of pure $Ti_3C_2T_x$ (a and b), $Ti_3C_2T_x$/CNT-SDS (c and d) and porous $Ti_3C_2T_x$/CNT-SA (e and f). Scale bars: 1 μm.

The lateral dimensions of $Ti_3C_2T_x$ nanosheets ranged from hundreds of nanometers to several micrometers as shown by transmission electron microscope (TEM) image in **Figure 10.4**. Upon filtration, the directional flow guided assembly of $Ti_3C_2T_x$ nanosheets leads to their layer-by-layer stacking, forming pure $Ti_3C_2T_x$ film. Figure 10.5a and b present the top-view

and cross-sectional scanning electron microscopy (SEM) images of a pure $Ti_3C_2T_x$ paper. Without CNT as spacers, pure $Ti_3C_2T_x$ nanosheets restacked compactly and the film had dense and continuous surface with no visible porosity. A similar surface morphology was observed for the $Ti_3C_2T_x$/CNT-SDS composite paper (**Figure 10.5c**). This is because the $Ti_3C_2T_x$ nanosheets and CNT-SDS were randomly mixed in the suspension, without strong interaction, and deposited separately from each other. As a result, they were deposited individually on the filter paper during filtration and the compact stacking of $Ti_3C_2T_x$ nanosheets could not be fully avoided. As shown in **Figure 10.5d**, although a large amount of CNTs were observed in cross-section, the majority of $Ti_3C_2T_x$ nanosheets were still densely restacked in the $Ti_3C_2T_x$/CNT-SDS film. In contrast, when applying the self-assembly method to hybridize $Ti_3C_2T_x$ with CNTs, $Ti_3C_2T_x$ nanosheets are effectively separated, yet still connected enough to form a conductive network (**Figure 10.5e**). It is also worth noting that pores are formed between adjacent $Ti_3C_2T_x$ nanosheets due to the interruption of the restacking by CNTs. The full advantage of the role of CNTs as spacers was achieved through electrostatic attractions between $Ti_3C_2T_x$ and CNTs, as evidenced by the cross-sectional SEM image of $Ti_3C_2T_x$/CNT-SA. The as-prepared composite film has an open sheet arrangement and CNTs can be seen sandwiched between $Ti_3C_2T_x$ sheets, indicating the successful placement of CNTs as spacers in the $Ti_3C_2T_x$ paper (**Figure 10.5f**).

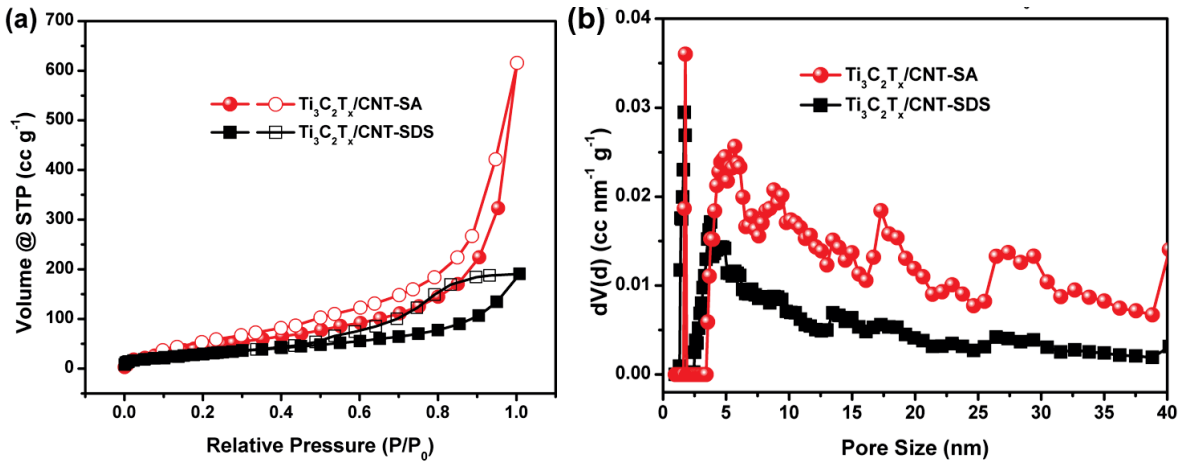


**Figure 10.6** $N_2$ adsorption-desorption isotherms (a) and pore size distribution curves (b) of $Ti_3C_2T_x$/CNT-SDS and porous $Ti_3C_2T_x$/CNT-SA.

The microstructure and exposed surface area of the as-produced composite films were further investigated by $N_2$ sorption/desorption measurements. **Figure 10.6a** presents the $N_2$ sorption isotherms of $Ti_3C_2T_x$/CNT-SA and $Ti_3C_2T_x$/CNT-SDS, which exhibit a typical type-IV behavior with a distinct hysteresis loop of type H3. The type H3 hoop can be ascribed to the incorporation of CNTs between $Ti_3C_2T_x$ nanosheets giving rise to slit-shaped pores. According to the Brunauer-Emmett-Teller (BET) method, $Ti_3C_2T_x$/CNT-SA and $Ti_3C_2T_x$/CNT-SDS films possessed a surface area of 185.4 and 116.8 $m^2\ g^{-1}$, respectively. On the contrary, pure $Ti_3C_2T_x$ only had a BET surface area of 19.6 $m^2\ g^{-1}$.[432] The increased surface area suggests that the incorporation of CNTs can effectively inhibit the restacking effect and the self-assembly between CNTs and $Ti_3C_2T_x$ nanosheets can maximize the accessibility of $Ti_3C_2T_x$ nanosheets. As shown in the inset in **Figure 10.6b**, the $Ti_3C_2T_x$/CNT-SA had a pore size distribution in the range of 5 to 40 nm. On the contrary, $Ti_3C_2T_x$/CNT-SDS lacked pores in this range. The results of $N_2$ sorption/desorption measurements were in agreement with the SEM images, confirming the porous structure of the as-produced

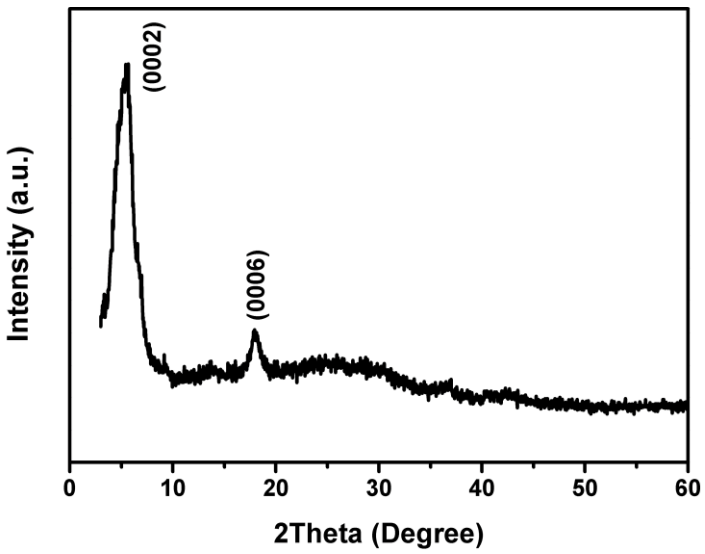


**Figure 10.7** XRD pattern of the as-prepared $Ti_3C_2T_x$/CNT-SA film.

$Ti_3C_2T_x$/CNT-SA films. The X-ray diffraction (XRD) pattern (**Figure 10.7**) of the as-prepared $Ti_3C_2T_x$/CNT-SA paper revealed that the (0002) peak of $Ti_3C_2T_x$ is located at 5.4°, corresponding to a d-spacing of 16.4 Å. The open structure of $Ti_3C_2T_x$/CNT-SA can provide channels for electrolyte transport, thereby increasing the accessibility of $Ti_3C_2T_x$ nanosheets.

The electrochemical kinetics of the freestanding $Ti_3C_2T_x$/CNT-SA paper electrode for sodium-ion storage were investigated by cyclic voltammetry (CV) in $Ti_3C_2T_x$/CNT-SA//Na cells in 1 M $NaClO_4$ dissolved in ethylene carbonate/propylene carbonate with 5 vol.% fluoroethylene carbonate (FEC) as electrolyte additive. **Figure 10.8a** shows the CV curves of a $Ti_3C_2T_x$/CNT-SA electrode at different scan rates from 0.1 to 3.0 mV $s^{-1}$. A pair of broad cathodic/anodic peaks located at around 0.6/1.0 V can be observed, corresponding to $Na^+$ insertion into/extraction from the $Ti_3C_2T_x$/CNT-SA electrode during which the oxidation state of Ti ions changes.[217] The large and broad cathodic/anodic peaks are indicative of a non-diffusion limited mechanism of Na-ion storage at the surface of well-dispersed $Ti_3C_2T_x$

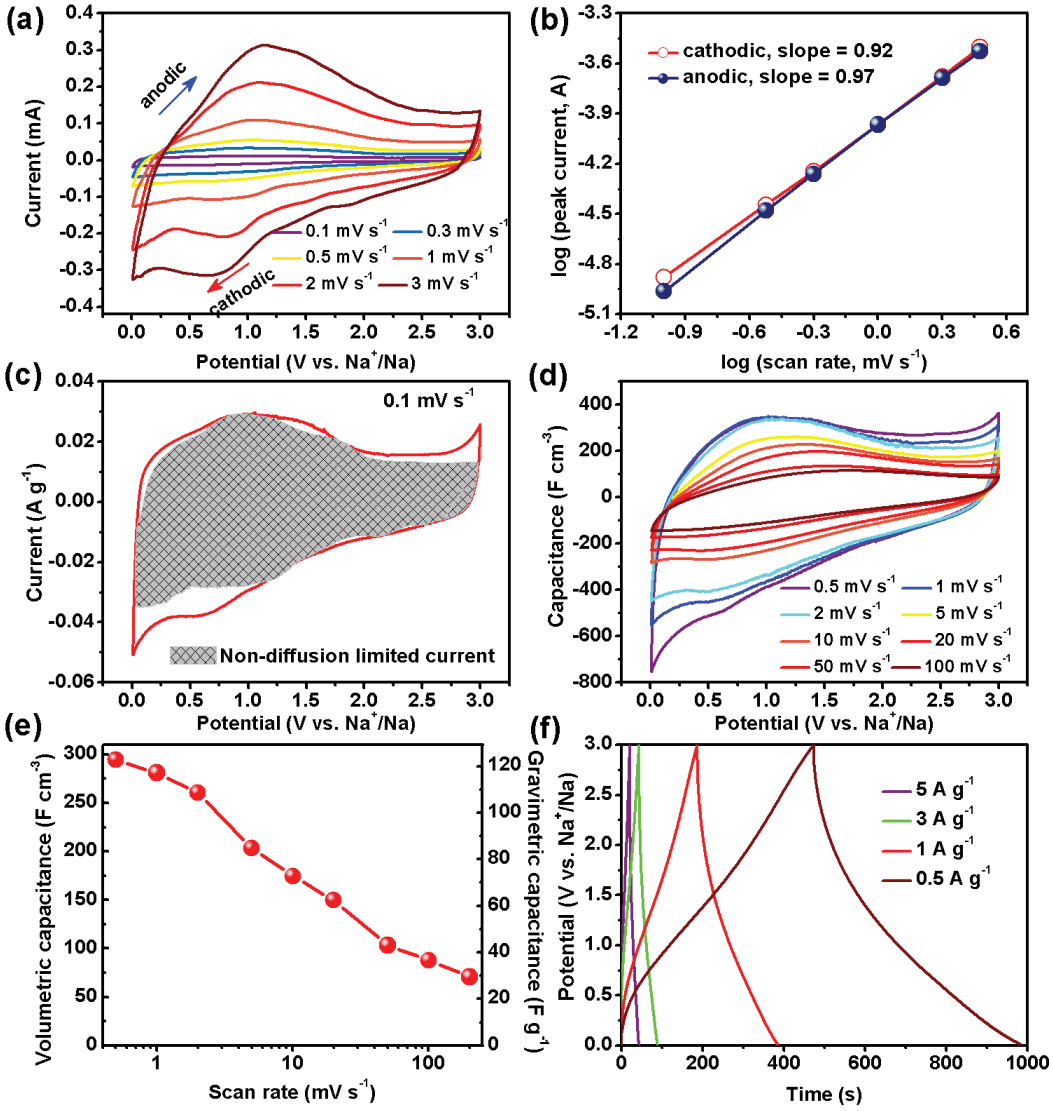


**Figure 10.8** The electrochemical properties of the $Ti_3C_2T_x$/CNT-SA electrode in a two electrode $Ti_3C_2T_x$/CNT-SA//Na cell, where Na foil was used as the counter and reference electrode: (a) cyclic voltammetry (CV) curves of the porous $Ti_3C_2T_x$/CNT-SA electrode at different scan rates from 0.1 to 3 mV $s^{-1}$; (b) the relationship between peak current and scan rate; (c) separation of the non-diffusion limited currents ($k_1v$) in the $Ti_3C_2T_x$/CNT-SA electrode at 0.1 mV $s^{-1}$. Three-electrode tests (overcapacitive activated carbon films and Na work as counter and reference electrodes, respectively): (d) CV curves at different scan rates collected from 0.5 to 100 mV $s^{-1}$; (e) volumetric and gravimetric rate performances; (f) galvanostatic charge-discharge profiles at different current densities.

nanosheets. This is confirmed by plotting log($i$) *versus* log(ν), where $i$ is the measured current and ν is the scan rate. As shown in **Figure 10.8b**, the slope of the log(ν)-log($i$) plots in cathodic and anodic processes are 0.92 and 0.97, respectively, indicating that the current is predominantly non-diffusion limited.[448] According to $i(V) = k_1\nu + k_2\nu^{1/2}$, where $i(V)$, $k_1\nu$, $k_2\nu^{1/2}$ and ν are the current at a fixed potential, non-diffusion limited and diffusion-controlled currents, scan rate, respectively, the quantitative contribution of the non-diffusion limited charge storage at a certain scan rate can be determined by calculating the value of $k_1$. By plotting $\nu^{1/2}$ versus $i/\nu^{1/2}$, $k_1$ can be determined from the slope of a straight line. For example, it is calculated that 88.1% of the total charge is contributed from the non-diffusion limited current at a scan rate of 0.1 mV $s^{-1}$, as shown by the shaded area in **Figure 10.8c**. This can be ascribed to the open structure of the as-prepared $Ti_3C_2T_x$/CNT-SA paper electrode, in which the diffusion of electrolyte is fast. The capacitive performance of the as-prepared $Ti_3C_2T_x$/CNT-SA paper electrodes was tested in a three-electrode configuration against overcapacitive porous carbon electrodes. The corresponding CV curves at different scan rates are plotted in **Figure 10.8d**, which shows a broad cathodic peak at around 0.6 V and an anodic peak located at 1.0 V *versus* $Na^+$/Na. In a voltage window of 0.01-3.0 V versus $Na^+$/Na, the $Ti_3C_2T_x$/CNT-SA electrodes exhibited a high volumetric capacitance of 294 F $cm^{-3}$ at a scan rate of 0.5 mV $s^{-1}$, corresponding to a gravimetric capacitance of 123 F $g^{-1}$ (**Figure 10.8e**). At a scan rate of 200 mV $s^{-1}$, a volumetric capacitance of 71 F $cm^{-3}$ was achieved. The galvanostatic charge-discharge curves had a sloping profile (**Figure 10.8f**), which was closer to the linear charge-discharge of a supercapacitor, with no voltage plateau usual for battery electrodes. The Coulombic efficiency of the electrochemical storage process is close to 100%. At a current density of 0.5 A $g^{-1}$, a volumetric capacitance of 204 F $cm^{-3}$ was obtained. And a volumetric capacitance of 88 F $cm^{-3}$ was retained at 5 A $g^{-1}$.

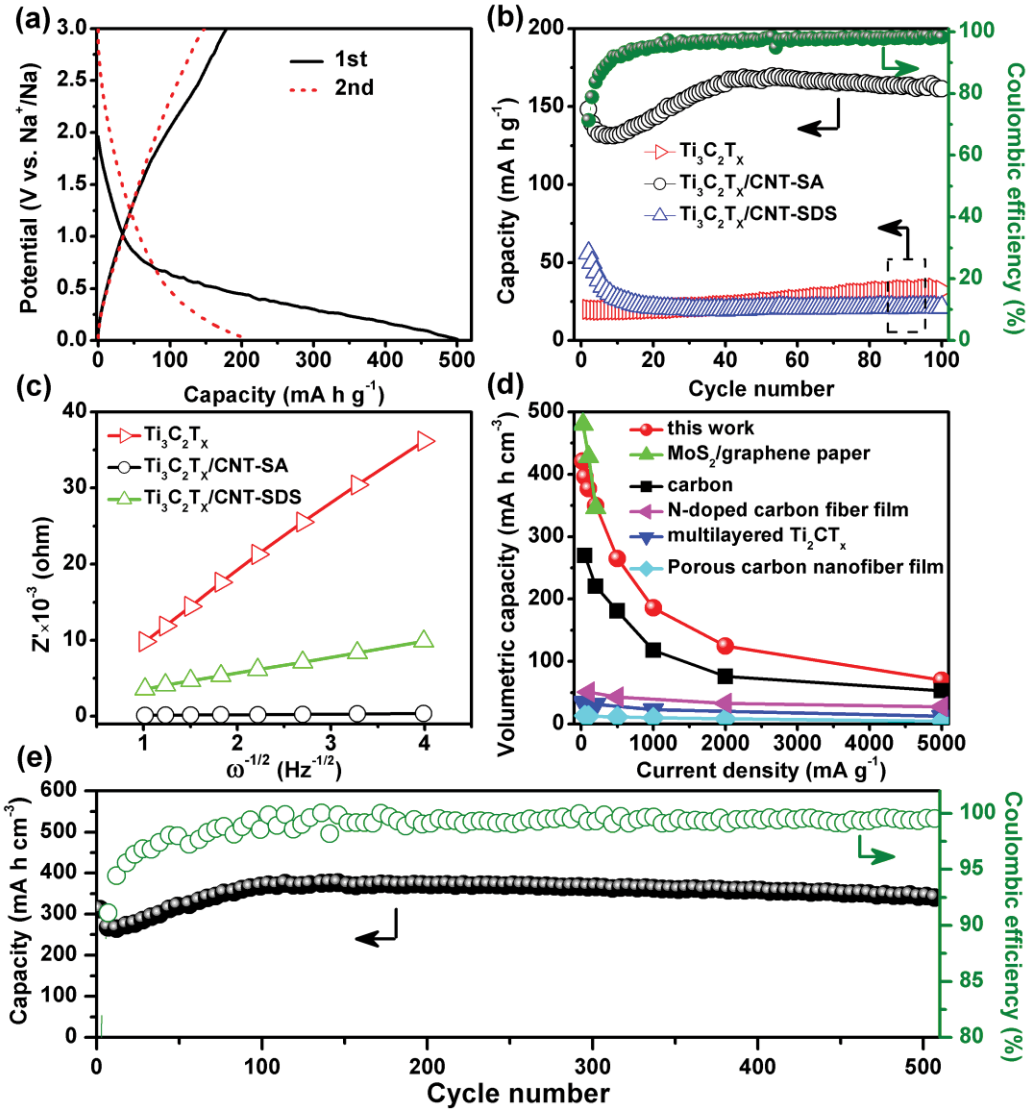


**Figure 10.9** Electrochemical performance of electrodes in a two-electrode cell with Na foil as the counter and reference electrode: (a) charge/discharge curves of $Ti_3C_2T_x$/CNT-SA at 20 mA $g^{-1}$ in the voltage window of 0.01-3.0 V. (b) Cycling performance of pure $Ti_3C_2T_x$, $Ti_3C_2T_x$/CNT-SA, and $Ti_3C_2T_x$/CNT-SDS papers at a current density of 20 mA $g^{-1}$ from the second cycle, the Coulombic efficiencies of $Ti_3C_2T_x$/CNT-SA electrode are also shown. (c) Linear fit of the Warburg impedance of $Ti_3C_2T_x$, $Ti_3C_2T_x$/CNT-SA, and $Ti_3C_2T_x$/CNT-SDS electrodes. (d) Volumetric capacities of $Ti_3C_2T_x$/CNT-SA (this work), carbon,[449] $MoS_2$/graphene paper,[292] multilayered $Ti_2CT_x$ powder,[442] porous carbon nanofiber film,[450]

and N-doped carbon nanofiber film[451]. (e) Reversible capacities and Coulombic efficiencies of $Ti_3C_2T_x$/CNT-SA electrodes at 100 mA $g^{-1}$ from the second cycle.

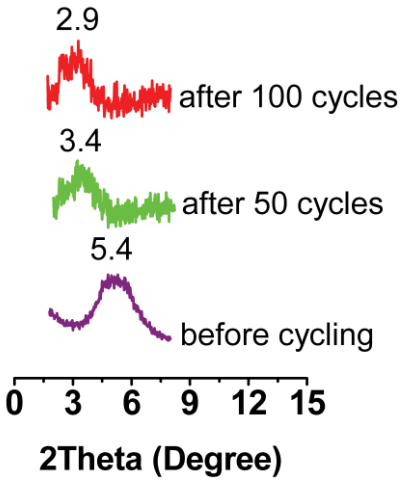


**Figure 10.10** XRD patterns of $Ti_3C_2T_x$/CNT-SA electrodes after different cycles.

The electrochemical performance was further tested in a two-electrode cell with Na foil as the counter and reference electrode. As shown in **Figure 10.9a**, the $Ti_3C_2T_x$/CNT-SA paper electrode showed an initial discharge capacity of 501 mA h $g^{-1}$ with a charge capacity of 179 mA h $g^{-1}$ at a current density of 20 mA $g^{-1}$. The initial irreversible capacity could be due to the formation of a solid electrolyte interface (SEI) as well as the irreversible reaction of Na with the surface functional groups (F, OH, and O) and/or water molecules confined between $Ti_3C_2T_x$ layers.[212, 452] **Figure 10.9b** compares the capacities of pure $Ti_3C_2T_x$, randomly mixed $Ti_3C_2T_x$/CNT-SDS and self-assembled $Ti_3C_2T_x$/CNT-SA composite paper electrodes at 20 mA $g^{-1}$. Both pure $Ti_3C_2T_x$ and $Ti_3C_2T_x$/CNT-SDS delivered very low capacities. The initial reversible capacity increases in the order $Ti_3C_2T_x$ < $Ti_3C_2T_x$/CNT-SDS < $Ti_3C_2T_x$/CNT-SA. A gradual increase in the capacity can be observed in the following cycles for $Ti_3C_2T_x$/CNT-SA electrodes, which could be ascribed to gradually improved Na-ion accessibility to active sites and the increased interlayer spacing during cycling (**Figure 10.10**).[443] The expanded

$Ti_3C_2T_x$ interlayer spacing can be ascribed to $Na^+$ trapping and the swelling effect caused by penetration of the uncoordinated solvent molecules into the interlayer space.[453] The expansion of $Ti_3C_2T_x$ interlayer spacing can significantly decrease sodium diffusion barriers and enhance the storage capacities of $Na^+$.[454] The Coulombic efficiencies of $Ti_3C_2T_x$/CNT-SA electrodes are low in the first few cycles, which result in the decreased capacity. The Coulombic efficiency stabilized at around 99%. After 100 cycles, a capacity of 175 mA h $g^{-1}$ is retained for the $Ti_3C_2T_x$/CNT-SA electrode, which is about 4.6 times higher than that of the pure $Ti_3C_2T_x$ and $Ti_3C_2T_x$/CNT-SDS electrodes. The improved electrochemical performance of the $Ti_3C_2T_x$/CNT-SA electrode can be ascribed to the three-dimensional (3D) open structure, as evidenced by the SEM images (**Figure 10.5e** and **f**) and $N_2$ sorption/desorption measurements results (**Figure 10.6**), which makes $Ti_3C_2T_x$ nanosheets highly accessible for Na-ion storage. Electrochemical impedance spectroscopy (EIS) was used to compare the charge transfer within different electrodes and the Nyquist plots were shown in **Figure 10.11a**. The Nyquist plots can be modeled based on the modified Randles equivalent circuit (**Figure 10.11b**). As shown in **Figure 10.9c** by the relationship between Z' and $\omega^{-1/2}$ ($\omega = 2\pi f$), the $Ti_3C_2T_x$/CNT-SA electrodes have the lowest slope in the low frequency region among the three different electrodes, indicating their best charge transfer kinetics. The good charge transfer kinetics in $Ti_3C_2T_x$/CNT-SA electrodes enables fast charge/discharge processes. The $Ti_3C_2T_x$/CNT-SA electrode exhibited quite respectable volumetric capacities, which range from 421 mA h $cm^{-3}$ at 20 mA $g^{-1}$ to 89 mA h $cm^{-3}$ at 5000 mA $g^{-1}$ (**Figure 10.9d**). The volumetric capacities outperform most of the reported electrode materials for Na-ion storage, such as carbon,[449] multilayered $Ti_2CT_x$ powder,[442] porous carbon nanofiber film,[450] N-doped carbon nanofiber film,[451] and are even comparable to the highest reported values based on $MoS_2$/graphene paper electrodes[292]. Notably, the

$MoS_2$/graphene paper electrode showed stable capacity up to only 20 cycles. However, the $Ti_3C_2T_x$/CNT-SA electrode was much more stable upon cycling, and a volumetric capacity of 345 mA h $cm^{-3}$ was maintained after 500 cycles at a current density of 100 mA $g^{-1}$ (**Figure 10.9e**).

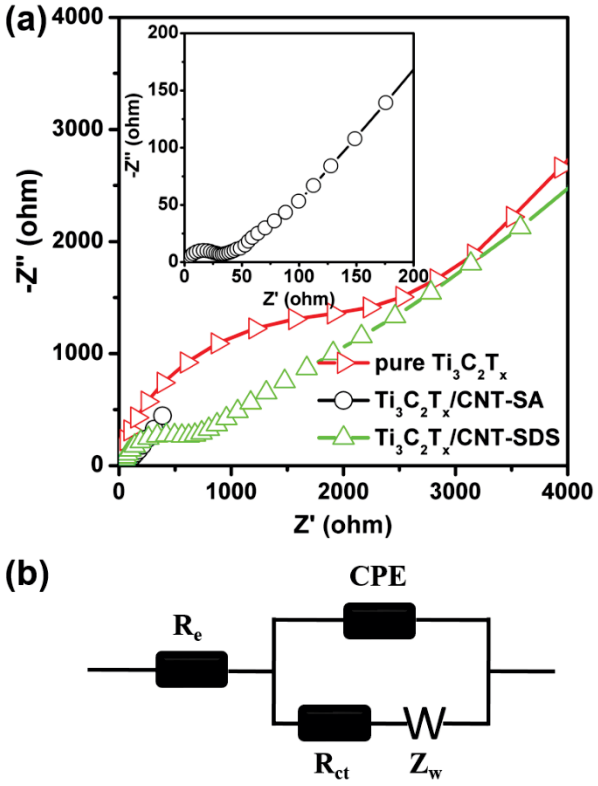


**Figure 10.11** (a) Nyquist plots of pure $Ti_3C_2T_x$, $Ti_3C_2T_x$/CNT-SA and $Ti_3C_2T_x$/CNT-SDS electrodes, the inset is the enlarged Nyquist plots of $Ti_3C_2T_x$/CNT-SA electrode.

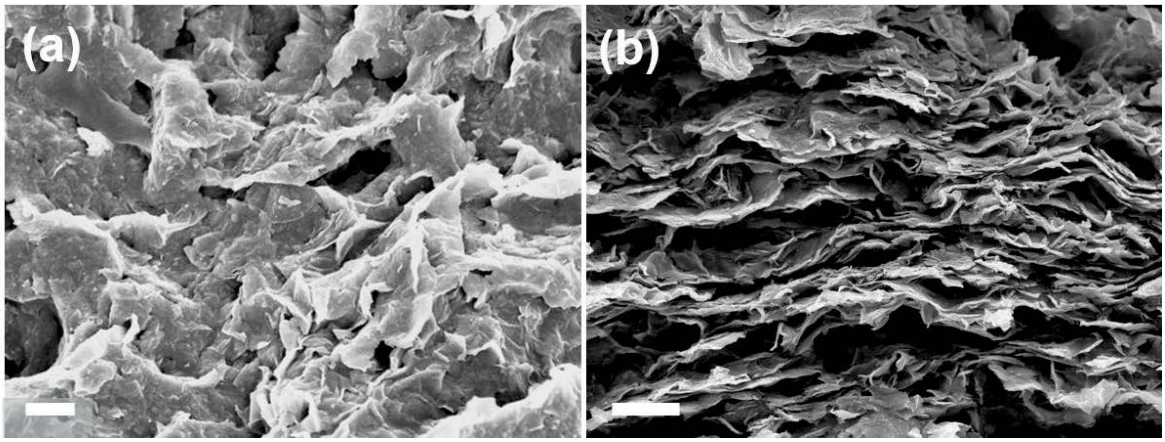


**Figure 10.12** SEM images of the as-produced $Ti_3C_2T_x$/rGO-SA film. (a) Top view, (b) cross-sectional view. Scale bars: 1 μm.

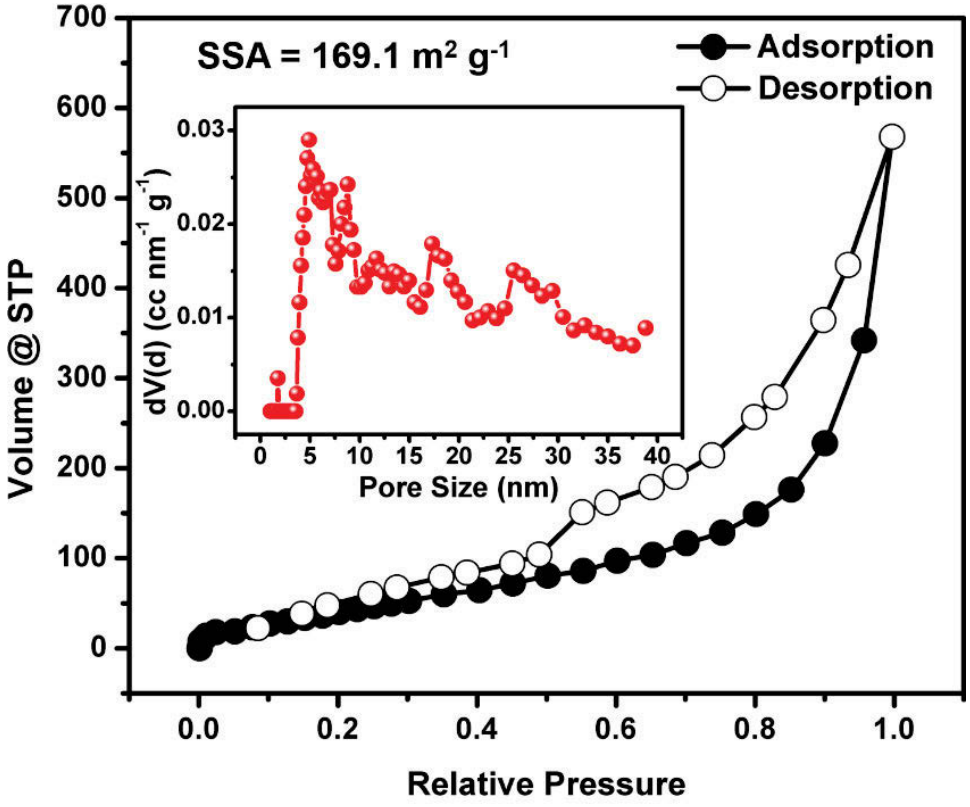


**Figure 10.13** $N_2$ adsorption-desorption isotherm and pore size distribution curve (inset) of $Ti_3C_2T_x$/rGO.

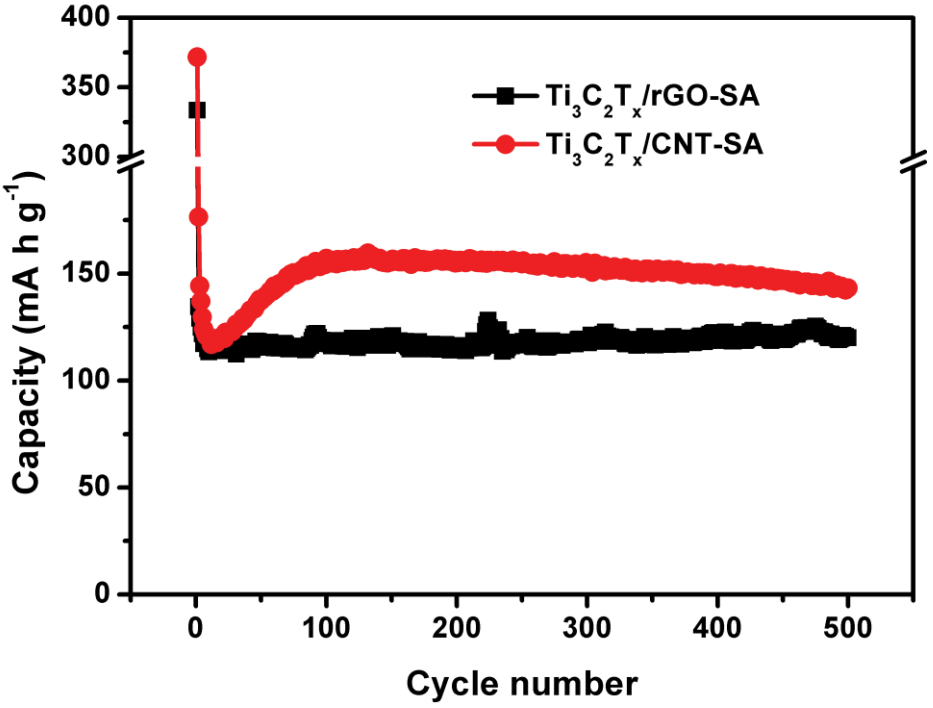


**Figure 10.14** Cycling performances of $Ti_3C_2T_x$/CNT-SA and $Ti_3C_2T_x$/rGO-SA films at a current density of 100 mA $g^{-1}$.

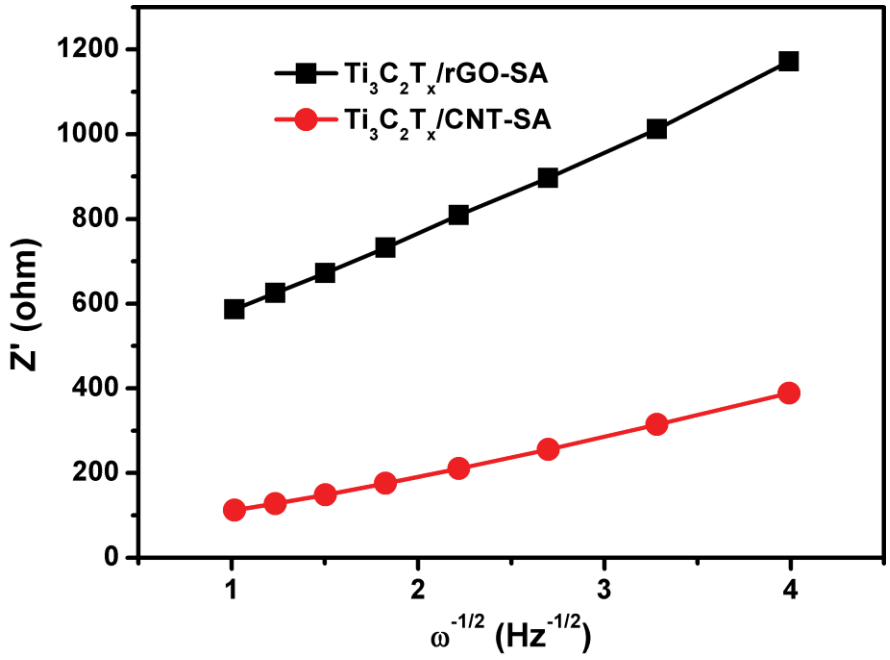


**Figure 10.15** Linear fit of the Warburg impedance of $Ti_3C_2T_x$/CNT-SA and $Ti_3C_2T_x$/rGO-SA electrodes.

The selection of 1D CNTs as spacers is of critical importance to produce $Ti_3C_2T_x$-based porous films with improved electrochemical performance for sodium-ion storage. This is evidenced by the control experiment using 2D reduced graphene oxide (rGO) as conformal spacers in 2D/2D $Ti_3C_2T_x$/rGO composite films ($Ti_3C_2T_x$/rGO-SA) produced by a similar self-assembly method. As shown in the SEM images in **Figure 10.12**, the as-produced $Ti_3C_2T_x$/rGO-SA film was less porous compared to $Ti_3C_2T_x$/CNT-SA. By $N_2$ adsorption-desorption measurement, the BET surface area of the $Ti_3C_2T_x$/rGO-SA film was 169.1 $m^2 g^{-1}$, which is much larger compared to pure MXene, but somewhat smaller than that of $Ti_3C_2T_x$/CNT-SA (**Figure 10.13**). It suggests that $Ti_3C_2T_x$ nanosheets in $Ti_3C_2T_x$/rGO-SA may be less accessible than those in $Ti_3C_2T_x$/CNT-SA. As a result, the electrochemical performance of $Ti_3C_2T_x$/rGO-SA was not as good as $Ti_3C_2T_x$/CNT-SA. After 500 cycles, $Ti_3C_2T_x$/rGO-SA electrodes delivered a capacity of 120 mA h $g^{-1}$ at a current density of 100 mA $g^{-1}$, which is lower than that of $Ti_3C_2T_x$/CNT-SA (**Figure 10.14**) and yet higher than pure $Ti_3C_2T_x$. As can be seen from **Figure 10.15**, the Warburg plot of $Ti_3C_2T_x$/rGO-SA electrodes has a lower slope in the low frequency region than $Ti_3C_2T_x$/CNT-SA, indicating that the charge transfer kinetics in $Ti_3C_2T_x$/rGO-SA is slower than that in $Ti_3C_2T_x$/CNT-SA. It can be concluded that the promising electrochemical performance of the $Ti_3C_2T_x$/CNT-SA critically relies on the construction of a porous 2D/1D heterostructure, which shows superior electrochemical properties compared to the 2D/2D $Ti_3C_2T_x$/rGO-SA.

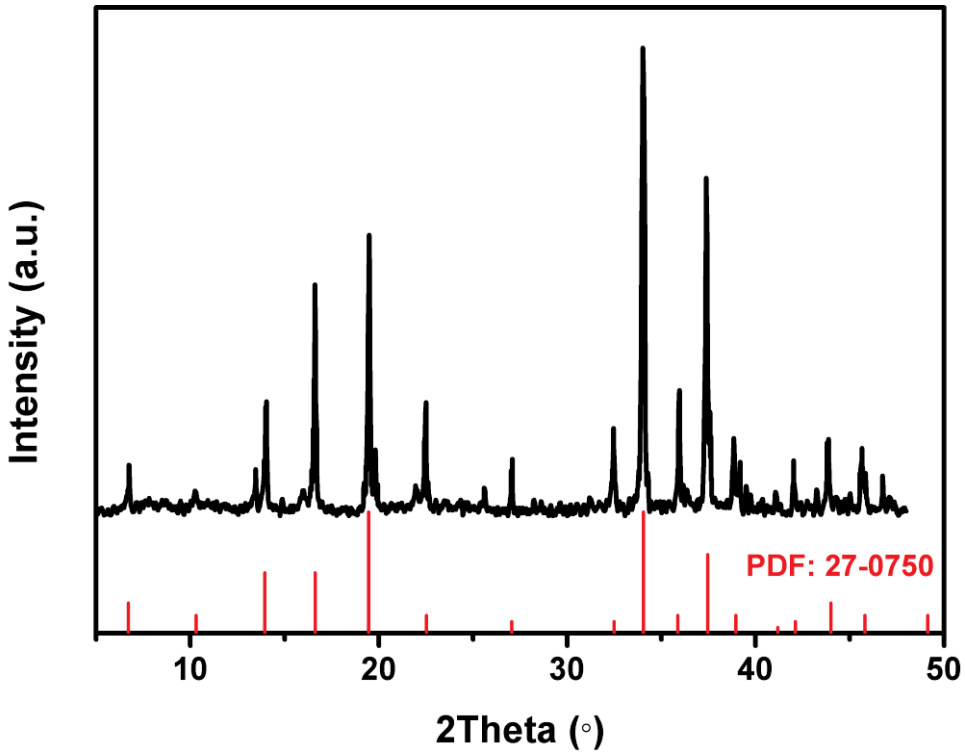


**Figure 10.16** XRD pattern of $Na_{0.44}MnO_2$ powder.

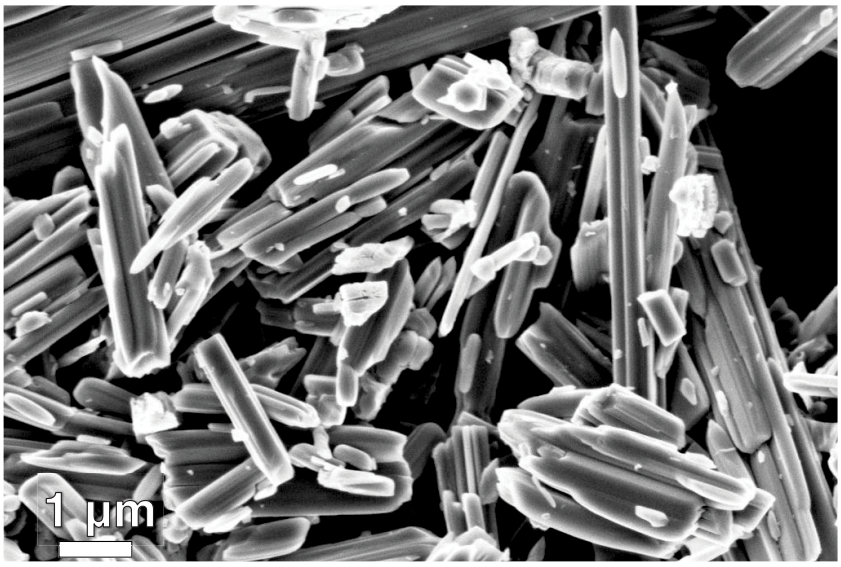


**Figure 10.17** SEM image of $Na_{0.44}MnO_2$ powder.

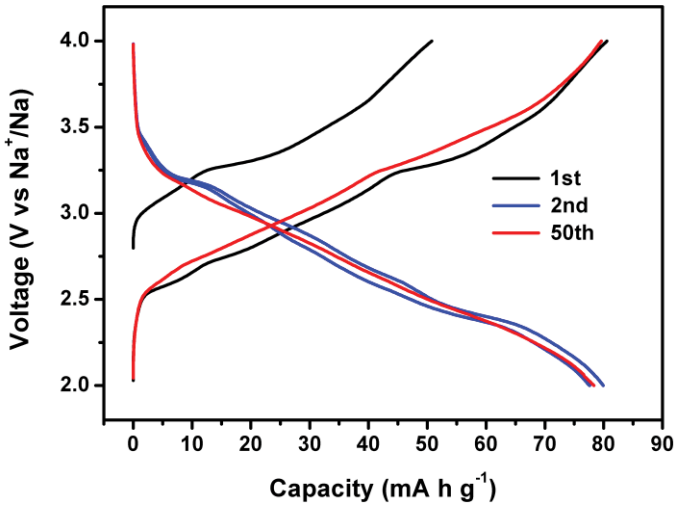


**Figure 10.18** Galvanostatic charge/discharge curves of the $Na_{0.44}MnO_2$ electrode at a current density of 14 mA $g^{-1}$.

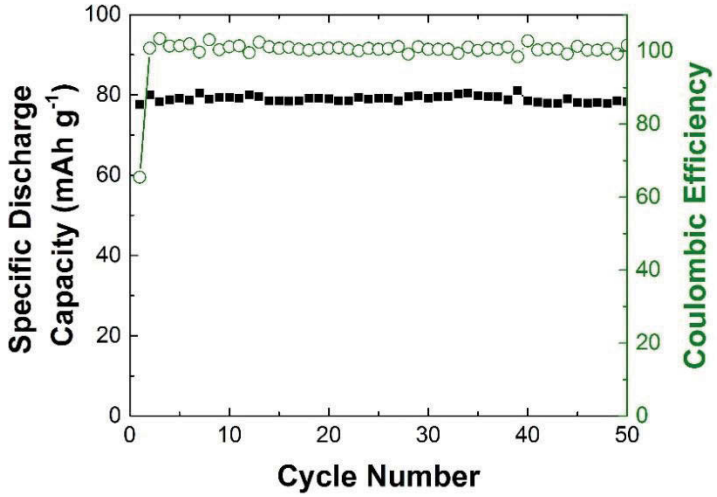


**Figure 10.19** Extended cycling performance of $Na_{0.44}MnO_2$ in a Na-ion half cell at a current density of 14 mA $g^{-1}$.

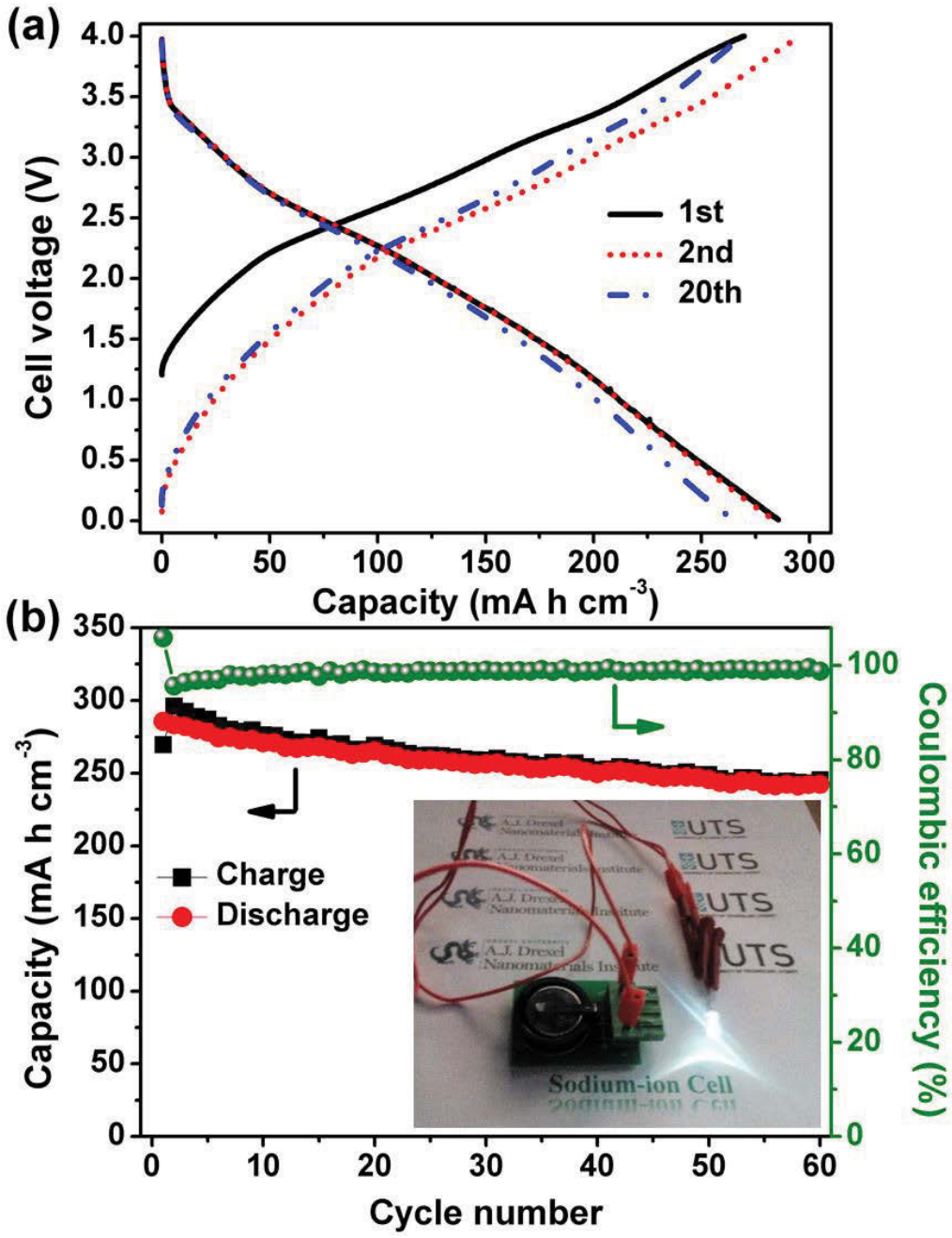


**Figure 10.20** Electrochemical performance of a $Na_{0.44}MnO_2$//$Ti_3C_2T_x$/CNT-SA cell. Charge-discharge curves (a) and cycling performance (b) at a current density of 50 mA (g-$Ti_3C_2T_x$/CNT-SA)$^{-1}$. The inset in b shows that the as-assembled full sodium-ion cell can light up a LED.

To evaluate the performance of the as-produced $Ti_3C_2T_x$/CNT-SA electrodes in a full Na-ion cell, they were coupled with a $Na_{0.44}MnO_2$ cathode and electrochemical performance of this

cell was investigated in a two-electrode configuration. The $Na_{0.44}MnO_2$ phase was chosen for this study based on its stable performance as a Na-ion battery cathode, with previous reports demonstrating excellent cycling stability and good rate performance.[447, 455] Furthermore, the presence of sodium in the crystal structure of this material opens an opportunity to use it as a sodium source and integrate it with sodium-free anode materials in electrochemical cells. The $Na_{0.44}MnO_2$ utilized in this work was prepared *via* a solid state approach following previously reported synthesis technique.[447] XRD analysis (**Figure 10.16**) confirmed that $Na_{0.44}MnO_2$ (PDF# 27-0750) was formed. SEM image (**Figure 10.17**) showed the expected rod-like morphology, in agreement with the previously published literature.[447, 455] When cycled in a Na-ion half cell (**Figure 10.18**), the as-prepared $Na_{0.44}MnO_2$ material exhibited a first charge capacity of 51 mA h $g^{-1}$ at a current density of 14 mA $g^{-1}$, corresponding to extraction of 0.18 $Na^+$ ions. Upon further cycling, a stable capacity of ~80 mA h $g^{-1}$ is achieved (**Figure 10.19)**, in agreement with past results for this material.[447, 455] As the $Na_{0.44}MnO_2$ cathode can accommodate more $Na^+$ than the stoichiometric amount in the pristine material, a partially sodiated $Ti_3C_2T_x$/CNT-SA electrode was used in the full Na-ion cell after precycling in a half cell. The mass ratio between $Na_{0.44}MnO_2$ and $Ti_3C_2T_x$/CNT-SA in full cells was 3:1 based on their specific capacities. As shown in **Figure 10.20a**, the as-assembled full sodium-ion cell exhibited sloping charge-discharge curves in the voltage window of 0.01-4.0 V, in agreement with charge-discharge profiles for $Ti_3C_2T_x$/CNT-SA (**Figure 10.9a**) and $Na_{0.44}MnO_2$ (**Figure 10.18**) half cells. The first charge and discharge capacities for the full cell were 270 and 286 mA h $cm^{-3}$, based on the volume of the $Ti_3C_2T_x$/CNT-SA electrode. The full cell had a high Coulombic efficiency (~99%) and relatively stable cycling performance in the following cycles (**Figure 10.20b**). After 60 cycles at a current density of 50 mA $(g\text{-}Ti_3C_2T_x/CNT\text{-}SA)^{-1}$, a volumetric discharge capacity

of 242 mA h $cm^{-3}$ was retained. As shown in the inset in **Figure 10.20b**, the as-assembled $Na_{0.44}MnO_2$//$Ti_3C_2T_x$/CNT-SA cell could power a 2.5 V light-emitting diode (LED) for approximately 25 minutes, consuming an energy of 0.041 mW h.

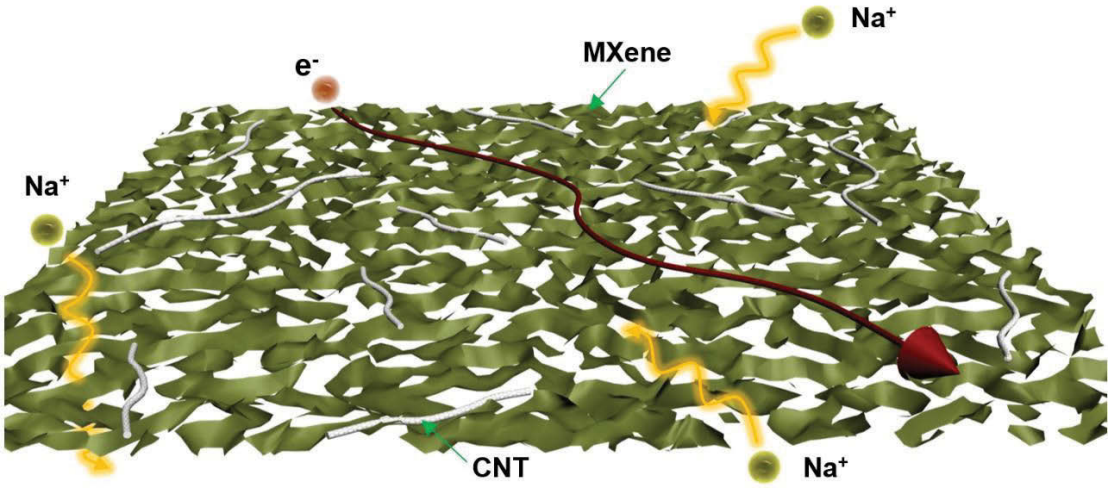


**Figure 10.21** $Na^+$ diffusion and electron transfer within porous MXene/CNT−SA electrodes.

The superior electrochemical performance of $Ti_3C_2T_x$/CNT-SA electrodes can be attributed to the rationally designed structure that is beneficial for both electronic conductivity and ionic transport, as schematically shown in **Figure 10.21**. First, in the self-assembled composites, both $Ti_3C_2T_x$ nanosheets and CNTs are electrically conductive and they form a continuous network, which is favorable for fast electron transfer in plane (along the MXene sheets) and out-of plane (between the sheets). Second, realized by the electrostatic self-assembly, the restacking of $Ti_3C_2T_x$ nanosheets with high surface-to-volume ratio can be effectively inhibited by CNT as spacers, generating porous heterostructured $Ti_3C_2T_x$/CNT composite films, thereby providing multidimensional ion diffusion pathways. Benefiting from these qualities, the good electron conductivity and facile ion diffusion pathways are simultaneously achieved, offering the high performance of $Ti_3C_2T_x$/CNT-SA electrodes for Na-ion storage.

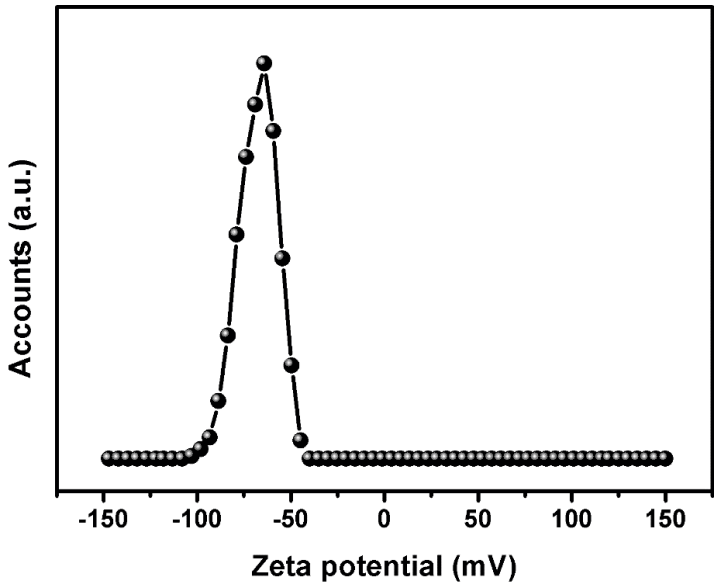


**Figure 10.22** Zeta potential of $Mo_2CT_x$ nanosheets.

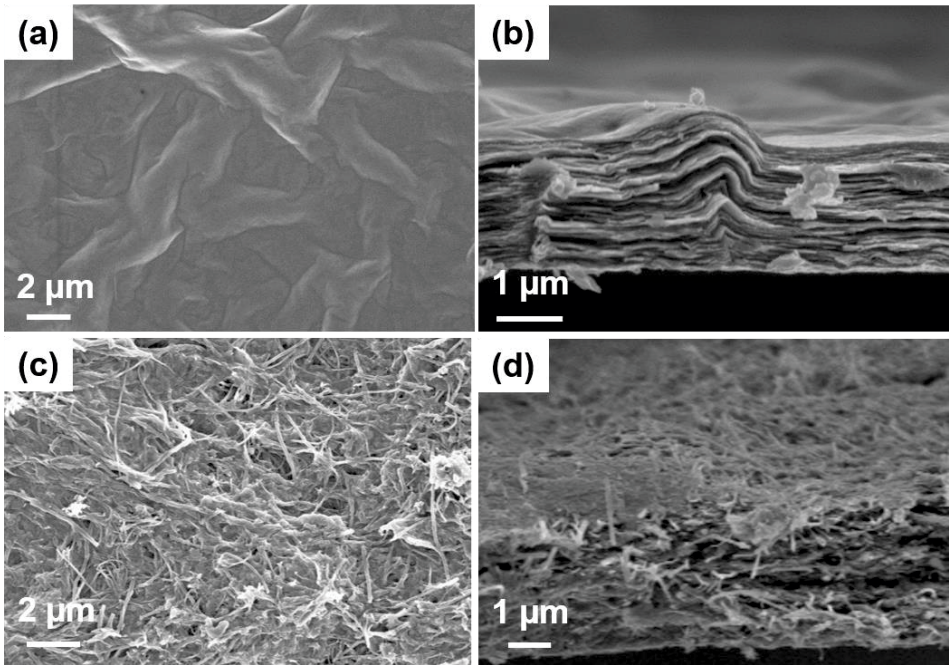


**Figure 10.23** SEM images of pure $Mo_2CT_x$ paper (a and b) and $Mo_2CT_x$/CNT-SA paper (c and d).

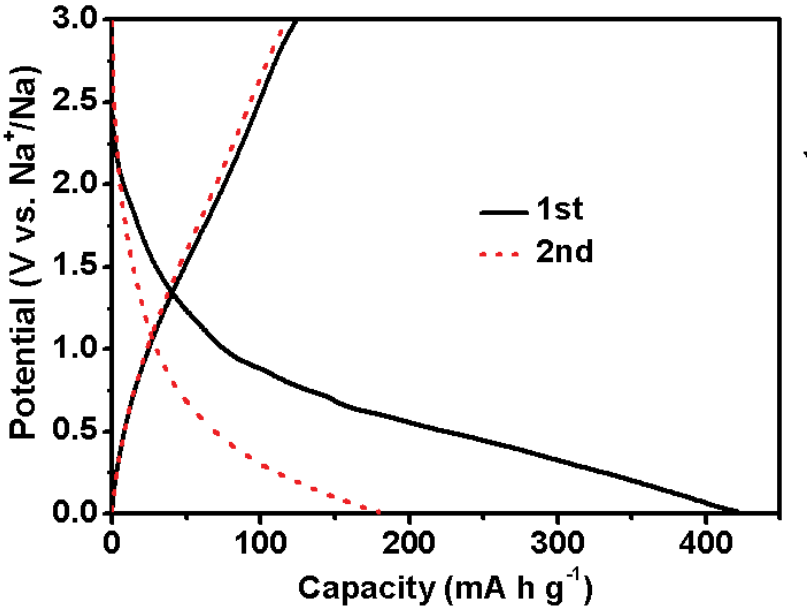


**Figure 10.24** Charge/discharge curves of the $Mo_2CT_x$/CNT-SA//Na cell at 50 mA $g^{-1}$.

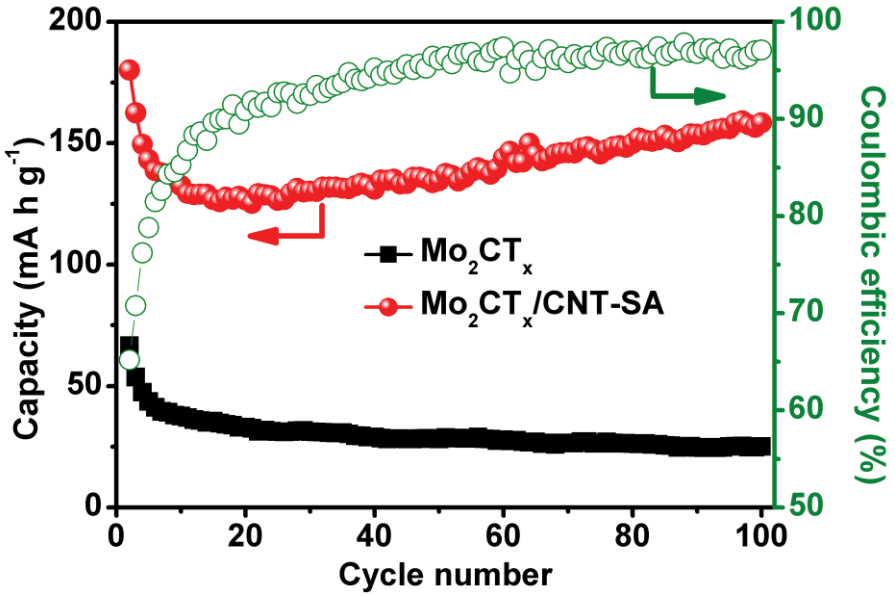


**Figure 10.25** Cycling performance of pure $Mo_2CT_x$ and self-assembled $Mo_2CT_x$/CNTs paper electrodes at 50 mA $g^{-1}$. The Coulombic efficiencies of $Mo_2CT_x$/CNT-SA electrode are also presented.

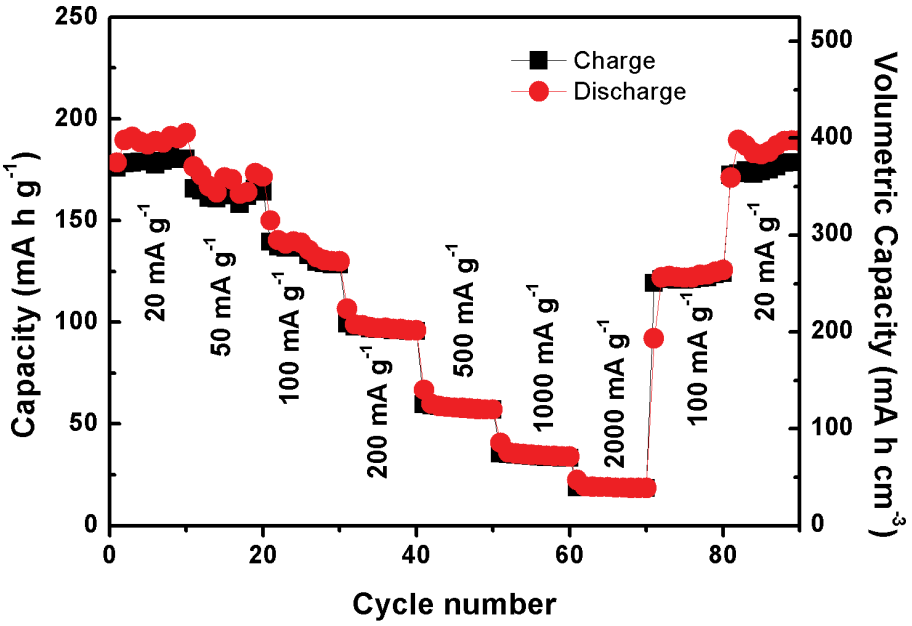


**Figure 10.26** Rate performance of the $Mo_2CT_x$/CNT-SA//Na cell.

To demonstrate the general validity of the proposed self-assembled structure, we further took $Mo_2CT_x$ from the family of MXenes as another example,[456] which has a ζ-potential of -67 mV (**Figure 10.22**). Again, the self-assembly of $Mo_2CT_x$ nanosheets and CNTs effectively hindered the restacking of $Mo_2CT_x$ nanosheets (**Figure 10.23**). The microscopic morphology of the self-assembled $Mo_2CT_x$/CNTs ($Mo_2CT_x$/CNT-SA) paper was analogous to that of $Ti_3C_2T_x$/CNT-SA, featuring a porous structure with well-dispersed $Mo_2CT_x$ nanosheets. At a current density of 50 mA $g^{-1}$, the $Mo_2CT_x$/CNT-SA paper electrode showed an initial discharge capacity of 422 mA h $g^{-1}$ with the corresponding charge capacity of 124 mA h $g^{-1}$ (**Figure 10.24**). The initial Coulombic efficiency of the $Mo_2CT_x$/CNT-SA electrode was 29.3%, which is lower than that of $Ti_3C_2T_x$/CNT-SA electrode (35.7%). This could be due to the smaller molecular weight of $Mo_2C$, resulting in more surface functional groups (F, OH, and O) and/or more trapped water per unit mass. After 100 cycles, the self-assembled $Mo_2CT_x$/CNT-SA electrode delivered a capacity of 164 mA h $g^{-1}$ with Coulombic

efficiencies around 98% at 50 mA $g^{-1}$. The capacity of self-assembled $Mo_2CT_x$/CNT-SA electrodes was 6.6 times higher than that of pure $Mo_2CT_x$ electrode (25 mA h $g^{-1}$) (**Figure 10.25**). At a current density of 20 mA $g^{-1}$, a volumetric capacity of 375 mA h $cm^{-3}$ can be obtained. However, the rate capability of the self-assembled $Mo_2CT_x$/CNT-SA electrode was not as good as that of $Ti_3C_2T_x$/CNT-SA, probably due to the lower conductivity of $Mo_2CT_x$ compared with $Ti_3C_2T_x$ (Figure 10.26) and its semiconducting nature.[456]

## 10.4 Conclusions

In summary, we have demonstrated the preparation of porous MXene/CNT composite paper. Facilitated by a simple self-assembly method, restacking of 2D MXene nanosheets can be impeded *via* the electrostatic incorporation of CNTs as nanoscale spacers. The porous MXene/CNT papers exhibited improved accessibility for electrolyte and showed a good volumetric capacity and rate performance for Na-ion storage. In particular, the self-assembled $Ti_3C_2T_x$/CNT paper achieved a high volumetric capacity of 421 mA h $cm^{-3}$ at 20 mA $g^{-1}$. Even at a current density of 5000 mA $g^{-1}$, a capacity of 89 mA h $cm^{-3}$ was retained. In addition, full sodium-ion cells consisting of $Ti_3C_2T_x$/CNT and $Na_{0.44}MnO_2$ were assembled, which delivered a volumetric discharge capacity of 286 mA h $cm^{-3}$, based on the volume of $Ti_3C_2T_x$/CNT-SA electrodes. The solution processing used in this study offers a simple, yet efficient strategy to improve accessibility of MXenes to liquids or gases, which is expected to promote their applications in supercapacitors, batteries, catalysis, electrochemical hydrogen generators, sensors, etc.

# Chapter 11 Conclusions and Future Perspective

## 11.1 Conclusions

### 11.1.1 $LiMn_2O_4$ nanorods as cathode materials for lithium-ion batteries

Single crystalline spinel $LiMn_2O_4$ nanorods have been successfully synthesized by a template-engaged method. When used as cathode materials for lithium-ion batteries, the spinel $LiMn_2O_4$ nanorods exhibited superior long cycle life owing to the one dimensional nanorod structure and the single crystallinity. $LiMn_2O_4$ nanorods retained 95.6% of the initial capacity after 1000 cycles at 3C rate. In particular, the nanorod morphology of the spinel $LiMn_2O_4$ was well preserved after a long-term cycling, suggesting the ultrahigh structural stability of the single crystalline spinel $LiMn_2O_4$ nanorods. This study sheds light on the long-standing challenge associated with capacity fading of spinel $LiMn_2O_4$ cathode material for lithium-ion batteries.

### 11.1.2 Nanostructured electrode materials for sodium-ion batteries

The work of this doctoral thesis on nanostructured electrode materials for sodium-ion batteries mainly focuses on: 1) understanding the interfacial interactions in graphene-based composite electrode materials; 2) development of built-to-order nanoarchitectured materials for sodium-ion batteries, such as high capacity electrode materials, anodes with high rate capability, and freestanding electrodes.

#### 11.1.2.1 Understanding the interfacial interactions in graphene-based composite electrode materials

A systematic comparison between $SnO_2$/nitrogen-doped graphene nanohybrids and the $SnO_2$/graphene counterpart as anode materials for sodium-ion batteries has been conducted. The results clearly manifest that the improved electron transfer efficiency of $SnO_2$/nitrogen-doped graphene due to nitrogen-doping plays a more important role than the increased electro-active sites within the graphene network in enhancing the electro-activity of $SnO_2$/nitrogen-doped graphene nanohybrids compared to the $SnO_2$/graphene counterpart.

$MoS_2$/reduced graphene oxide (RGO) nanocomposites with intimate two-dimensional heterointerfaces prepared by a facile one-pot hydrothermal method were reported. The two-dimensional $MoS_2$/RGO heterointerfacial area can be effectively tuned by changing the ratio of $MoS_2$ to RGO. When used as anode material for sodium-ion batteries, it is found that the synergistic effect contributing to the enhanced reversible capacity of $MoS_2$/RGO nanocomposites is closely related with the heterointerfacial area. The computational results demonstrate that Na prefers to be adsorbed on $MoS_2$ in the $MoS_2$/RGO heterostructure rather than intercalate into the $MoS_2$/RGO heterointerface. Interestingly, it was found that the $MoS_2$/RGO heterointerfaces can significantly increase the electronic conductivity of $MoS_2$, store more Na-ions, while maintaining the high diffusion mobility of Na-atoms on the $MoS_2$ surface and high electron transfer efficiency from Na to $MoS_2$. This work guides the rational design of layered metal sulfides/graphene composites as high-performance electrode materials for sodium-ion batteries.

#### 11.1.2.2 Development of nanoarchitectured electrode materials for sodium-ion batteries

Inspired by the investigations on the interfacial interactions between $MoS_2$ and graphene, platelet-on-sheet nanostructured $SnS_2$ nanoplatelet@graphene nanocomposites were then

prepared by a morphology-controlled hydrothermal method as anode material with enhanced electrochemical performance for sodium-ion batteries. $SnS_2$/graphene nanosheets achieved a high reversible specific sodium ion storage capacity of 725 mA h $g^{-1}$, and stable cyclability.

The development of high-rate anode materials is highly desirable for sodium-ion batteries. Optimization of mass transport and electron transfer is crucial for discovering electrode materials with good high-rate performances. To this end, 3D interconnected $SnO_2$/graphene aerogels with hierarchically porous structures were synthesized as anode materials for sodium-ion batteries. Such 3D functional architecture not only facilitates the electrode/electrolyte interaction but also provides an efficient electron pathway within the graphene network. When applied as anode material in sodium-ion batteries, the as-prepared $SnO_2$/graphene aerogel exhibited high reversible capacity, improved cycling performance compared to $SnO_2$ and promising high-rate capability. Even at a high current density of 1000 mA $g^{-1}$, the electrode achieved a capacity of 168 mA h $g^{-1}$ after 500 cycles.

Core-sheath structured Sn@CNT nanopillar arrays on carbon paper with a unique 3D hierarchical architecture was developed as freestanding electrode for sodium-ion batteries. The electrode achieved a reversible capacity of 887 μA h $cm^{-2}$ in the first cycle and good cyclability extending to 100 cycles. The electrode also demonstrated a promising rate capability, which is suitable for high power applications. Prototype Na-ion full cells were also assembled, consisting of the as-prepared freestanding Sn@CNT@carbon paper anode and $Na_{0.80}Li_{0.12}Ni_{0.22}Mn_{0.66}O_2$ cathode. The full sodium-ion battery can power LED lights.

Freestanding anode materials for sodium-ion batteries consisting of molybdenum disulfide ($MoS_2$) nanosheets aligned vertically on carbon paper derived from paper towel were

reported. The hierarchical structure enables sufficient electrode/electrolyte interaction and fast electron transportation. Meanwhile, the unique architecture can minimize the excessive interface between carbon and electrolyte, enabling high ICE. The as-prepared $MoS_2$@carbon paper composites as freestanding electrodes for sodium-ion batteries can liberate the traditional electrode manufacturing procedure, thereby reducing the cost of sodium-ion batteries. The freestanding $MoS_2$@carbon paper electrode exhibits a high reversible capacity, high ICE, good cycling performance, and excellent rate capability.

Porous $Ti_3C_2$ MXene/CNT composite paper electrodes for sodium-based energy storage devices were fabricated. The heterostructure formation was realized by electrostatic attraction between negatively charged 2D MXene nanosheets and positively charged 1D CNTs. This method efficiently prevented restacking of MXene nanosheets and produced a well-defined porous structure, thereby facilitating electrolyte transport and access of ions to the electrode and producing functional MXene-based freestanding electrodes for sodium-ion storage. When applied as freestanding electrodes for sodium-ion storage, the built-to-order $Ti_3C_2$ MXene/CNTs porous films showed high volumetric capacity of 421 mA h $cm^{-3}$ at 20 mA $g^{-1}$, good rate performances, and excellent cycling stability. Prototype sodium-ion cells were also assembled using the as-prepared $Ti_3C_2$/CNTs anode and $Na_{0.44}MnO_2$ cathode. The fabrication of porous MXene/CNT composites, using simple self-assembly, opens the door to developing electrode materials with high volumetric capacity for sodium-ion storage.

### 11.2 Future Perspective

We developed $LiMn_2O_4$ nanorods as cathode materials for LIBs with improved cycling stability by designing a homogeneous reaction between Mn and Li precursors, optimizing

the crystallinity and lithium content. These explorations could also be helpful to develop stable spherical $LiMn_2O_4$ cathode materials with high tap density, which is desirable for practical applications to achieve high volumetric energy density. It should also be noted that studies on the effect of morphology and chemical composition on the high temperature stability of $LiMn_2O_4$ cathodes require more efforts.

As promising post-lithium-ion batteries, sodium-ion batteries offer low-cost rechargeable battery technology for energy storage and conversion. To facilitate the implementation of sodium-ion batteries in commercialization, the development of electrode materials is critical, which depends critically on a better understanding of the composition-structure-performance relationship. In this regard, the findings of this doctoral thesis could be useful to rational design electroactive materials and derive advanced electrodes. For example, the fundamental understanding of the interfacial interactions between $MoS_2$ and graphene (Chapter 5) could facilitate the development of high performance 2D metal sulfides/graphene composite anode materials for sodium-ion batteries. The fabrication of composite electrode materials based on 3D graphene aerogel can be extended to construct electrode materials for high-rate applications. Regretfully, the loading of active materials ($SnO_2$ in this doctoral thesis in Chapter 7) is low by current *in situ* synthesis while maintaining the 3D networks of graphene. In contrast, two-step synthesis, i.e., preparing 3D graphene frameworks first and then loading anode materials, could afford to construct 3D graphene-based electrode materials with high loading of electroactive materials with high capacity and high-rate capability for SIBs.

Na metal anodes possess a high theoretical specific capacity of 1166 mA h $g^{-1}$, which is among the highest values. In addition, it has the lowest electrochemical potential (-2.7 V vs. SHE). Consequently, Na metal is considered to be the ideal anode for SIBs. To realize the

potential application of metallic sodium anode, reversibility issues of Na metal should be solved. Optimization of the electrolyte composition (for example, exploring electrolyte additives) that affords the formation of uniform SEI is crucial to solve this problem.

Finally, it should be noted that only by a rational design of electrode materials from a system-level consideration can we develop better rechargeable batteries for energy storage and conversion. The system-level consideration should include but not be limited to the interplay between each component, the electrode/electrolyte interfacial engineering, and the compatibility of the electrolyte. To facilitate the implantation of anode materials such as $SnO_2$/NG, $MoS_2$, $MoS_2$/rGO, and $SnS_2$/rGO, the large irreversible capacity in the initial cycles of the electrode materials should be improved, which depends critically on the deep understanding of the irreversible reactions in the first cycle.

# APPENDIX: NOMENCLATURE

| Abbreviations/Symbols | Full name |
|---|---|
| a.u. | Arbitrary unit |
| Ar | Argon |
| BET | Brunauer-Emmett-Teller |
| BJH | Barrett-Joyner-Halenda |
| CB | Carbon black |
| CNT | carbon nanotube |
| CV | Cyclic Voltammetry |
| C-rate | Current rate |
| DI | de-ionized |
| DMC | Dimethyl carbonate |
| EC | Ethylene carbonate |
| EIS | Electrochemical Impedance Spectroscopy |
| EVs | Electric vehicles |
| FESEM | Field-Emission Scanning Electron Microscopy |
| FTIR | Fourier transform infrared spectroscopy |
| g | Gram |
| GO | Graphene oxide |
| h | Hour |
| Hz | Hertz |
| *I* | Intensity |
| HEVs | Hybrid electric vehicles |

| | |
|---|---|
| HRTEM | High-resolution transmission electronic spectroscopy |
| JCPDS | Joint Committee on Powder Diffraction Standards |
| Li | Lithium |
| LIBs | Lithium-ion Batteries |
| M | Molar concentration |
| mA h $g^{-1}$ | Milli ampere hour per gram |
| min | Minute |
| mm | Millimeter |
| nm | Nanometer |
| NMP | 1-methyl-2-pyrrolidinone |
| PC | Propylene carbonate |
| PVDF | Poly(vinylidene difluoride) |
| $R_{ct}$ | Charge transfer resistance |
| $R_{\Omega}$ | Ohmic resistance |
| SAED | Selected area electron diffraction |
| SEI | Solid Electrolyte Interface |
| SEM | Scanning electron Microscopy |
| SIBs | Sodium-ion Batteries |
| TEM | Transmission electron microscopy |
| TGA | Thermogravimetric analysis |
| XRD | X-ray diffraction |
| ° | Degree |
| Ω | Ohm |

| | |
|---|---|
| °C | Degree Celsius |
| *Z*w | Warburg impedance |

## REFERENCES


1. T. Nagaura and K. Tozawa, *Prog. Batteries Solar Cells*, 1990, **9**, 209-217.
2. P. Roy and S. K. Srivastava, *J. Mater. Chem. A*, 2015, **3**, 2454-2484.
3. Y. Xu, M. Zhou and Y. Lei, *Adv. Energy Mater.*, 2016, 1502514.
4. J. N. Reimers and J. Dahn, *J. Electrochem. Soc.*, 1992, **139**, 2091-2097.
5. J. W. Fergus, *J. Power Sources*, 2010, **195**, 939-954.
6. G. G. Amatucci, J. M. Tarascon and L. C. Klein, *Solid State Ionics*, 1996, **83**, 167-173.
7. G. Amatucci, J. Tarascon and L. Klein, *J. Electrochem. Soc.*, 1996, **143**, 1114-1123.
8. T. Ohzuku and A. Ueda, *J. Electrochem. Soc.*, 1994, **141**, 2972-2977.
9. J. Zhou and P. Notten, *J. Power Sources*, 2008, **177**, 553-560.
10. C. Li, H. P. Zhang, L. J. Fu, H. Liu, Y. P. Wu, E. Rahm, R. Holze and H. Q. Wu, *Electrochim. Acta*, 2006, **51**, 3872-3883.
11. J. Zhang, Y. Xiang, Y. Yu, S. Xie, G. Jiang and C. Chen, *J. Power Sources*, 2004, **132**, 187-194.
12. M. Mladenov, R. Stoyanova, E. Zhecheva and S. Vassilev, *Electrochem. Commun.*, 2001, **3**, 410-416.
13. Z. Wang, L. Liu, L. Chen and X. Huang, *Solid State Ionics*, 2002, **148**, 335-342.
14. Z. Wang, C. Wu, L. Liu, F. Wu, L. Chen and X. Huang, *J. Electrochem. Soc.*, 2002, **149**, A466-A471.
15. H. Zhao, L. Gao, W. Qiu and X. Zhang, *J. Power Sources*, 2004, **132**, 195-200.
16. J. Cho, Y. J. Kim and B. Park, *Chem. Mater.*, 2000, **12**, 3788-3791.

17. J. Cho, Y. J. Kim, T. J. Kim and B. Park, *Angew. Chem. Int. Ed.*, 2001, **40**, 3367-3369.

18. J. Cho, Y. J. Kim and B. Park, *J. Electrochem. Soc.*, 2001, **148**, A1110-A1115.

19. H.-J. Kweon, J. Park, J. Seo, G. Kim, B. Jung and H. S. Lim, *J. Power Sources*, 2004, **126**, 156-162.

20. L. Liu, L. Chen, X. Huang, X.-Q. Yang, W.-S. Yoon, H. Lee and J. McBreen, *J. Electrochem. Soc.*, 2004, **151**, A1344-A1351.

21. S. Oh, J. K. Lee, D. Byun, W. I. Cho and B. W. Cho, *J. Power Sources*, 2004, **132**, 249-255.

22. J. Cho, *J. Power Sources*, 2004, **126**, 186-189.

23. J. Cho, H. Kim and B. Park, *J. Electrochem. Soc.*, 2004, **151**, A1707-A1711.

24. B. Kim, J.-G. Lee, M. Choi, J. Cho and B. Park, *J. Power Sources*, 2004, **126**, 190-192.

25. J.-G. Lee, B. Kim, J. Cho, Y.-W. Kim and B. Park, *J. Electrochem. Soc.*, 2004, **151**, A801-A805.

26. J. Cho and G. Kim, *Electrochem. Solid-State Lett.*, 1999, **2**, 253-255.

27. J. Cho, C. S. Kim and S. I. Yoo, *Electrochem. Solid-State Lett.*, 2000, **3**, 362-365.

28. Y. J. Kim, J. Cho, T.-J. Kim and B. Park, *J. Electrochem. Soc.*, 2003, **150**, A1723-A1725.

29. H. Liu, Y. Wu, E. Rahm, R. Holze and H. Wu, *J. Solid State Electrochem.*, 2004, **8**, 450-466.

30. J. Kim, M. Noh, J. Cho, H. Kim and K.-B. Kim, *J. Electrochem. Soc.*, 2005, **152**, A1142-A1148.

31. H. Takahara, T. Takeuchi, M. Tabuchi, H. Kageyama, Y. Kobayashi, Y. Kurisu, S. Kondo and R. Kanno, *J. Electrochem. Soc.*, 2004, **151**, A1539-A1544.

32. Y. Zhou, C. Shen and H. Li, *Solid State Ionics*, 2002, **146**, 81-86.

33. X. Li, F. Cheng, B. Guo and J. Chen, *J. Phys. Chem. B*, 2005, **109**, 14017-14024.

34. F. Jiao, K. M. Shaju and P. G. Bruce, *Angew. Chem. Int. Ed.*, 2005, **44**, 6550-6553.

35. Y. Koyama, N. Yabuuchi, I. Tanaka, H. Adachi and T. Ohzuku, *J. Electrochem. Soc.*, 2004, **151**, A1545-A1551.

36. N. Yabuuchi, Y. Koyama, N. Nakayama and T. Ohzuku, *J. Electrochem. Soc.*, 2005, **152**, A1434-A1440.

37. G.-H. Kim, S.-T. Myung, H. Bang, J. Prakash and Y.-K. Sun, *Electrochem. Solid-State Lett.*, 2004, **7**, A477-A480.

38. W.-S. Yoon, M. Balasubramanian, X.-Q. Yang, Z. Fu, D. A. Fischer and J. McBreen, *J. Electrochem. Soc.*, 2004, **151**, A246-A251.

39. W.-S. Yoon, C. P. Grey, M. Balasubramanian, X.-Q. Yang, D. A. Fischer and J. McBreen, *Electrochem. Solid-State Lett.*, 2004, **7**, A53-A55.

40. K. Shaju, G. S. Rao and B. Chowdari, *Electrochim. Acta*, 2002, **48**, 145-151.

41. K. Shaju, G. S. Rao and B. Chowdari, *J. Electrochem. Soc.*, 2003, **150**, A1-A13.

42. P. G. Bruce, B. Scrosati and J.-M. Tarascon, *Angew. Chem. Int. Ed.*, 2008, **47**, 2930-2946.

43. M. S. Whittingham, *Chem. Rev.*, 2004, **104**, 4271-4302.

44. R. Amin and J. Maier, *Solid State Ionics*, 2008, **178**, 1831-1836.

45. H.-C. Kang, D.-K. Jun, B. Jin, E. M. Jin, K.-H. Park, H.-B. Gu and K.-W. Kim, *J. Power Sources*, 2008, **179**, 340-346.

46. K. Zaghib, A. Mauger, F. Gendron and C. Julien, *Solid State Ionics*, 2008, **179**, 16-23.

47. N. Ravet, J. Goodenough, S. Besner, M. Simoneau, P. Hovington and M. Armand, *Honolulu, HI*, 1999.

48. G. Wang, L. Yang, Y. Chen, J. Wang, S. Bewlay and H. Liu, *Electrochim. Acta*, 2005, **50**, 4649-4654.

49. Y.-H. Huang and J. B. Goodenough, *Chem. Mater.*, 2008, **20**, 7237-7241.

50. A. Fedorková, A. Nacher-Alejos, P. Gómez-Romero, R. Oriňáková and D. Kaniansky, *Electrochim. Acta*, 2010, **55**, 943-947.

51. C. Delacourt, P. Poizot, S. Levasseur and C. Masquelier, *Electrochem. Solid-State Lett.*, 2006, **9**, A352-A355.

52. F. Jiao, J. Bao, A. H. Hill and P. G. Bruce, *Angew. Chem. Int. Ed.*, 2008, **47**, 9711-9716.

53. F. Cheng, H. Wang, Z. Zhu, Y. Wang, T. Zhang, Z. Tao and J. Chen, *Energy Environ. Sci.*, 2011, **4**, 3668-3675.

54. X. Jia, C. Yan, Z. Chen, R. Wang, Q. Zhang, L. Guo, F. Wei and Y. Lu, *Chem. Commun.*, 2011, **47**, 9669-9671.

55. Y. Xia and M. Yoshio, *J. Electrochem. Soc.*, 1996, **143**, 825-833.

56. R. J. Gummow, A. de Kock and M. M. Thackeray, *Solid State Ionics*, 1994, **69**, 59-67.

57. J. M. Tarascon, W. R. McKinnon, F. Coowar, T. N. Bowmer, G. Amatucci and D. Guyomard, *J. Electrochem. Soc.*, 1994, **141**, 1421-1431.

58. Y. Xia, Y. Zhou and M. Yoshio, *J. Electrochem. Soc.*, 1997, **144**, 2593-2600.

59. D. H. Jang, Y. J. Shin and S. M. Oh, *J. Electrochem. Soc.*, 1996, **143**, 2204-2211.

60. M. M. Thackeray, Y. Shao-Horn, A. J. Kahaian, K. D. Kepler, E. Skinner, J. T. Vaughey and S. A. Hackney, *Electrochem. Solid-State Lett.*, 1998, **1**, 7-9.

61. K. Y. Chung and K.-B. Kim, *J. Electrochem. Soc.*, 2002, **149**, A79-A85.

62. K. Y. Chung, W.-S. Yoon, K.-B. Kim, X.-Q. Yang and S. M. Oh, *J. Electrochem. Soc.*, 2004, **151**, A484-A492.

63. K. Y. Chung, C.-W. Ryu and K.-B. Kim, *J. Electrochem. Soc.*, 2005, **152**, A791-A795.

64. S.-T. Myung, S. Komaba and N. Kumagai, *J. Electrochem. Soc.*, 2001, **148**, A482-A489.

65. K. W. Kim, S.-W. Lee, K.-S. Han, H. J. Chung and S. I. Woo, *Electrochim. Acta*, 2003, **48**, 4223-4231.

66. J.-F. Lee, Y.-W. Tsai, R. Santhanam, B. J. Hwang, M.-H. Yang and D.-G. Liu, *J. Power Sources*, 2003, **119–121**, 721-726.

67. B.-L. He, S.-J. Bao, Y.-Y. Liang, W.-J. Zhou, H. Li and H.-L. Li, *J. Solid State Chem.*, 2005, **178**, 897-901.

68. T. Kakuda, K. Uematsu, K. Toda and M. Sato, *J. Power Sources*, 2007, **167**, 499-503.

69. W.-H. Ryu, J.-Y. Eom, R.-Z. Yin, D.-W. Han, W.-K. Kim and H.-S. Kwon, *J. Mater. Chem.*, 2011, **21**, 15337-15342.

70. P. Aitchison, B. Ammundsen, D. J. Jones, G. Burns and J. Roziere, *J. Mater. Chem.*, 1999, **9**, 3125-3130.

71. J. M. Amarilla, J. L. Martín de Vidales and R. M. Rojas, *Solid State Ionics*, 2000, **127**, 73-81.

72. S. Mandal, R. M. Rojas, J. M. Amarilla, P. Calle, N. V. Kosova, V. F. Anufrienko and J. M. Rojo, *Chem. Mater.*, 2002, **14**, 1598-1605.

73. Y. Yao, Y. Dai, B. Yang, W. Ma and T. Watanabe, *J. Wuhan Univ. Technol.*, 2007, **22**, 307-310.

74. A. Robertson, S. Lu, W. Averill and W. Howard, *J. Electrochem. Soc.*, 1997, **144**, 3500-3505.

75. R. Thirunakaran, B. R. Babu, N. Kalaiselvi, P. Periasamy, T. P. Kumar, N. G. Renganathan, M. Raghavan and N. Muniyandi, *Bull Mater Sci*, 2001, **24**, 51-55.

76. C. Wu, Z. Wang, F. Wu, L. Chen and X. Huang, *Solid State Ionics*, 2001, **144**, 277-285.

77. C. Wu, F. Wu, L. Chen and X. Huang, *Solid State Ionics*, 2002, **152–153**, 335-339.

78. C.-H. Lu, Y. Lin and H.-C. Wang, *J. Mater. Sci. Lett.*, 2003, **22**, 615-618.

79. R. Thirunakaran, K.-T. Kim, Y.-M. Kang, C.-Y. Seo and J. Lee, *Ionics*, 2003, **9**, 266-273.

80. H.-C. Wang and C.-H. Lu, *J. Power Sources*, 2003, **119–121**, 738-742.

81. P. Shen, Y. Huang, L. Liu, D. Jia and Z. Guo, *J Solid State Electrochem*, 2006, **10**, 929-933.

82. R. M. Rojas, K. Petrov, G. Avdeev, J. Amarilla, L. Pascual and J. Rojo, *J. Therm. Anal. Calorim.*, 2007, **90**, 67-72.

83. N. Jayaprakash, N. Kalaiselvi, Gangulibabu and D. Bhuvaneswari, *J Solid State Electrochem*, 2011, **15**, 1243-1251.

84. W. Xu, A. Yuan, L. Tian and Y. Wang, *J. Appl. Electrochem.*, 2011, **41**, 453-460.

85. M. Tabuchi, H. Shigemura, K. Ado, H. Kobayashi, H. Sakaebe, H. Kageyama and R. Kanno, *J. Power Sources*, 2001, **97–98**, 415-419.

86. E. Hosono, T. Kudo, I. Honma, H. Matsuda and H. Zhou, *Nano Lett.*, 2009, **9**, 1045-1051.

87. H.-W. Lee, P. Muralidharan, R. Ruffo, C. M. Mari, Y. Cui and D. K. Kim, *Nano Lett.*, 2010, **10**, 3852-3856.

88. D. K. Kim, P. Muralidharan, H.-W. Lee, R. Ruffo, Y. Yang, C. K. Chan, H. Peng, R. A. Huggins and Y. Cui, *Nano Lett.*, 2008, **8**, 3948-3952.

89. Q. Qu, L. Fu, X. Zhan, D. Samuelis, J. Maier, L. Li, S. Tian, Z. Li and Y. Wu, *Energy Environ. Sci.*, 2011, **4**, 3985-3990.

90. J. Cho, *J. Mater. Chem.*, 2008, **18**, 2257-2261.

91. J.-y. Luo, Y.-g. Wang, H.-m. Xiong and Y.-y. Xia, *Chem. Mater.*, 2007, **19**, 4791-4795.

92. W.-J. Zhang, *J. Power Sources*, 2011, **196**, 13-24.

93. M. Armand and J. M. Tarascon, *Nature*, 2008, **451**, 652-657.

94. J. R. Dahn, T. Zheng, Y. Liu and J. Xue, *Science*, 1995, **270**, 590.

95. F. Leroux, K. Metenier, S. Gautier, E. Frackowiak, S. Bonnamy and F. Beguin, *J. Power Sources*, 1999, **81**, 317-322.

96. A. S. Claye, J. E. Fischer, C. B. Huffman, A. G. Rinzler and R. E. Smalley, *J. Electrochem. Soc.*, 2000, **147**, 2845-2852.

97. S.-H. Yoon, C.-W. Park, H. Yang, Y. Korai, I. Mochida, R. Baker and N. M. Rodriguez, *Carbon*, 2004, **42**, 21-32.

98. G. Wang, J. Yang, J. Park, X. Gou, B. Wang, H. Liu and J. Yao, *J. Phys. Chem. C*, 2008, **112**, 8192-8195.

99. G. Wang, X. Shen, J. Yao and J. Park, *Carbon*, 2009, **47**, 2049-2053.

100. D. Fattakhova and P. Krtil, *J. Electrochem. Soc.*, 2002, **149**, A1224-A1229.

101. J. Huang and Z. Jiang, *Electrochim. Acta*, 2008, **53**, 7756-7759.

102. P. Krtil and D. Fattakhova, *J. Electrochem. Soc.*, 2001, **148**, A1045-A1050.

103. A. Robertson, L. Trevino, H. Tukamoto and J. Irvine, *J. Power Sources*, 1999, **81**, 352-357.

104. C. Chen, J. Vaughey, A. Jansen, D. Dees, A. Kahaian, T. Goacher and M. Thackeray, *J. Electrochem. Soc.*, 2001, **148**, A102-A104.

105. P. Kubiak, A. Garcia, M. Womes, L. Aldon, J. Olivier-Fourcade, P.-E. Lippens and J.-C. Jumas, *J. Power Sources*, 2003, **119**, 626-630.

106. K. Mukai, K. Ariyoshi and T. Ohzuku, *J. Power Sources*, 2005, **146**, 213-216.

107. H.-G. Jung, S.-T. Myung, C. S. Yoon, S.-B. Son, K. H. Oh, K. Amine, B. Scrosati and Y.-K. Sun, *Energy Environ. Sci.*, 2011, **4**, 1345-1351.

108. L. Zhao, Y. S. Hu, H. Li, Z. Wang and L. Chen, *Adv. Mater.*, 2011, **23**, 1385-1388.

109. L. Shen, X. Zhang, E. Uchaker, C. Yuan and G. Cao, *Adv. Energy Mater.*, 2012, **2**, 691-698.

110. S. H. Yu, S. H. Lee, D. J. Lee, Y. E. Sung and T. Hyeon, *Small*, 2015.

111. P. Poizot, S. Laruelle, S. Grugeon, L. Dupont and J. Tarascon, *Nature*, 2000, **407**, 496-499.

112. N. Godshall, I. Raistrick and R. Huggins, *Materials Research Bulletin*, 1980, **15**, 561-570.

113. J. Cabana, L. Monconduit, D. Larcher and M. R. Palacin, *Adv. Mater.*, 2010, **22**.

114. M. Reddy, G. Subba Rao and B. Chowdari, *Chem. Rev.*, 2013, **113**, 5364-5457.

115. D. Larcher, G. Sudant, J. Leriche, Y. Chabre and J. Tarascon, *J. Electrochem. Soc.*, 2002, **149**, A234-A241.

116. X. W. Lou, D. Deng, J. Y. Lee, J. Feng and L. A. Archer, *Adv. Mater.*, 2008, **20**, 258-262.

117. B. Guo, C. Li and Z.-Y. Yuan, *J. Phys. Chem. C*, 2010, **114**, 12805-12817.

118. H. Guan, X. Wang, H. Li, C. Zhi, T. Zhai, Y. Bando and D. Golberg, *Chem. Commun.*, 2012, **48**, 4878-4880.

119. J. C. Park, J. Kim, H. Kwon and H. Song, *Adv. Mater.*, 2009, **21**, 803-807.

120. S. Bijani, M. Gabas, G. Subias, J. Garcia, L. Sanchez, J. Morales, L. Martinez and J. Ramos-Barrado, *J. Mater. Chem.*, 2011, **21**, 5368-5377.

121. F. Lin, D. Nordlund, T.-C. Weng, Y. Zhu, C. Ban, R. M. Richards and H. L. Xin, *Nat. Commun.*, 2014, **5**.

122. M. F. Hassan, Z. Guo, Z. Chen and H. Liu, *J. Power Sources*, 2010, **195**, 2372-2376.

123. P. Meduri, E. Clark, J. H. Kim, E. Dayalan, G. U. Sumanasekera and M. K. Sunkara, *Nano Lett.*, 2012, **12**, 1784-1788.

124. A. Kushima, X. H. Liu, G. Zhu, Z. L. Wang, J. Y. Huang and J. Li, *Nano Lett.*, 2011, **11**, 4535-4541.

125. P. Balaya, H. Li, L. Kienle and J. Maier, *Adv. Funct. Mater.*, 2003, **13**, 621-625.

126. K. E. Gregorczyk, Y. Liu, J. P. Sullivan and G. W. Rubloff, *ACS Nano*, 2013, **7**, 6354-6360.

127. Y.-Y. Hu, Z. Liu, K.-W. Nam, O. J. Borkiewicz, J. Cheng, X. Hua, M. T. Dunstan, X. Yu, K. M. Wiaderek and L.-S. Du, *Nat. Mater.*, 2013, **12**, 1130-1136.

128. J. Hu, H. Li and X. Huang, *Electrochem. Solid-State Lett.*, 2005, **8**, A66-A69.

129. J. Hu, H. Li, X. Huang and L. Chen, *Solid State Ionics*, 2006, **177**, 2791-2799.

130. S. Yoon, C. Jo, S. Y. Noh, C. W. Lee, J. H. Song and J. Lee, *Phys. Chem. Chem. Phys.*, 2011, **13**, 11060-11066.

131. M. Sasidharan, N. Gunawardhana, M. Yoshio and K. Nakashima, *Nano Energy*, 2012, **1**, 503-508.

132. D.-M. Kim, S.-J. Kim, Y.-W. Lee, D.-H. Kwak, H.-C. Park, M.-C. Kim, B.-M. Hwang, S. Lee, J.-H. Choi and S. Hong, *Electrochim. Acta*, 2015, **163**, 132-139.

133. A. S. Arico, P. Bruce, B. Scrosati, J.-M. Tarascon and W. van Schalkwijk, *Nat. Mater.*, 2005, **4**, 366-377.

134. R. Mukherjee, R. Krishnan, T.-M. Lu and N. Koratkar, *Nano Energy*, 2012, **1**, 518-533.

135. L. Ji, Z. Lin, M. Alcoutlabi and X. Zhang, *Energy Environ. Sci.*, 2011, **4**, 2682-2699.

136. T.-J. Kim, C. Kim, D. Son, M. Choi and B. Park, *J. Power Sources*, 2007, **167**, 529-535.

137. K. Chang and W. Chen, *ACS Nano*, 2011, **5**, 4720-4728.

138. Q. Wang, L. Jiao, Y. Han, H. Du, W. Peng, Q. Huan, D. Song, Y. Si, Y. Wang and H. Yuan, *J. Phys. Chem. C*, 2011, **115**, 8300-8304.

139. N. Mahmood, C. Zhang and Y. Hou, *Small*, 2013, **9**, 1321-1328.

140. F. Gillot, S. Boyanov, L. Dupont, M. L. Doublet, M. Morcrette, L. Monconduit and J. M. Tarascon, *Chem. Mater.*, 2005, **17**, 6327-6337.

141. Y. Kim, H. Hwang, C. S. Yoon, M. G. Kim and J. Cho, *Adv. Mater.*, 2007, **19**, 92-96.

142. S. Boyanov, K. Annou, C. Villevieille, M. Pelosi, D. Zitoun and L. Monconduit, *Ionics*, 2008, **14**, 183-190.

143. S. W. Kim, D. H. Seo, H. Gwon, J. Kim and K. Kang, *Adv. Mater.*, 2010, **22**, 5260-5264.

144. F. Wang, R. Robert, N. A. Chernova, N. Pereira, F. Omenya, F. Badway, X. Hua, M. Ruotolo, R. Zhang and L. Wu, *J. Am. Chem. Soc.*, 2011, **133**, 18828-18836.

145. U. Kasavajjula, C. Wang and A. J. Appleby, *J. Power Sources*, 2007, **163**, 1003-1039.

146. M. Winter and J. O. Besenhard, *Electrochim. Acta*, 1999, **45**, 31-50.

147. H.-Y. Lee and S.-M. Lee, *Electrochem. Commun.*, 2004, **6**, 465-469.

148. H.-Y. Lee, Y.-L. Kim, M.-K. Hong and S.-M. Lee, *J. Power Sources*, 2005, **141**, 159-162.

149. M. Wachtler, J. O. Besenhard and M. Winter, *J. Power Sources*, 2001, **94**, 189-193.

150. H. Kim, J. Choi, H. J. Sohn and T. Kang, *J. Electrochem. Soc.*, 1999, **146**, 4401-4405.

151. J. Yan, H. Huang, J. Zhang and Y. Yang, *J. Power Sources*, 2008, **175**, 547-552.

152. J. Yang, M. Winter and J. Besenhard, *Solid State Ionics*, 1996, **90**, 281-287.

153. J. Yang, M. Wachtler, M. Winter and J. O. Besenhard, *Electrochem. Solid-State Lett.*, 1999, **2**, 161-163.

154. M. Obrovac, L. Christensen, D. B. Le and J. Dahn, *J. Electrochem. Soc.*, 2007, **154**, A849-A855.

155. J. T. Vaughey, L. Fransson, H. A. Swinger, K. Edström and M. M. Thackeray, *J. Power Sources*, 2003, **119–121**, 64-68.

156. S. S. Zhang, *J. Power Sources*, 2006, **162**, 1379-1394.

157. M. Sawicki and L. L. Shaw, *RSC Adv.*, 2015, **5**, 53129-53154.

158. J. W. Choi and D. Aurbach, *Nat. Rev. Mater.*, 2016, **1**, 16013.

159. M. D. Slater, D. Kim, E. Lee and C. S. Johnson, *Adv. Funct. Mater.*, 2013, **23**, 947-958.

160. H. Pan, Y.-S. Hu and L. Chen, *Energy Environ. Sci.*, 2013, **6**, 2338-2360.

161. C. Delmas, C. Fouassier and P. Hagenmuller, *Physica B+ C*, 1980, **99**, 81-85.

162. R. Kanno, Y. Takeda, T. Ichikawa, K. Nakanishi and O. Yamamoto, *J. Power Sources*, 1989, **26**, 535-543.

163. N. Yabuuchi, K. Kubota, M. Dahbi and S. Komaba, *Chem. Rev.*, 2014, **114**, 11636-11682.

164. X. Ma, H. Chen and G. Ceder, *J. Electrochem. Soc.*, 2011, **158**, A1307-A1312.

165. N. Yabuuchi, M. Kajiyama, J. Iwatate, H. Nishikawa, S. Hitomi, R. Okuyama, R. Usui, Y. Yamada and S. Komaba, *Nat. Mater.*, 2012, **11**, 512-517.

166. J. Xu, D. H. Lee, R. J. Clément, X. Yu, M. Leskes, A. J. Pell, G. Pintacuda, X.-Q. Yang, C. P. Grey and Y. S. Meng, *Chem. Mater.*, 2014, **26**, 1260-1269.

167. J. Billaud, G. Singh, A. R. Armstrong, E. Gonzalo, V. Roddatis, M. Armand, T. Rojo and P. G. Bruce, *Energy Environ. Sci.*, 2014, **7**, 1387-1391.

168. X. Wang, G. Liu, T. Iwao, M. Okubo and A. Yamada, *J. Phys. Chem. C*, 2014, **118**, 2970-2976.

169. Z. Lu and J. Dahn, *Chem. Mater.*, 2001, **13**, 1252-1257.

170. D. Buchholz, L. G. Chagas, C. Vaalma, L. Wu and S. Passerini, *J. Mater. Chem. A*, 2014, **2**, 13415-13421.

171. D. Kundu, E. Talaie, V. Duffort and L. F. Nazar, *Angew. Chem. Int. Ed.*, 2015, **54**, 3431-3448.

172. K. T. Lee, T. Ramesh, F. Nan, G. Botton and L. F. Nazar, *Chem. Mater.*, 2011, **23**, 3593-3600.

173. P. P. Prosini, C. Cento, A. Masci and M. Carewska, *Solid State Ionics*, 2014, **263**, 1-8.

174. S.-M. Oh, S.-T. Myung, J. Hassoun, B. Scrosati and Y.-K. Sun, *Electrochem. Commun.*, 2012, **22**, 149-152.

175. K. Saravanan, C. W. Mason, A. Rudola, K. H. Wong and P. Balaya, *Adv. Energy Mater.*, 2013, **3**, 444-450.

176. C. Zhu, K. Song, P. A. van Aken, J. Maier and Y. Yu, *Nano Lett.*, 2014, **14**, 2175-2180.

177. R. Shakoor, D.-H. Seo, H. Kim, Y.-U. Park, J. Kim, S.-W. Kim, H. Gwon, S. Lee and K. Kang, *J. Mater. Chem.*, 2012, **22**, 20535-20541.

178. B. Ellis, W. Makahnouk, Y. Makimura, K. Toghill and L. Nazar, *Nat. Mater.*, 2007, **6**, 749-753.

179. Y.-U. Park, D.-H. Seo, H.-S. Kwon, B. Kim, J. Kim, H. Kim, I. Kim, H.-I. Yoo and K. Kang, *J. Am. Chem. Soc.*, 2013, **135**, 13870-13878.

180. P. Barpanda, J.-N. Chotard, N. Recham, C. Delacourt, M. Ati, L. Dupont, M. Armand and J.-M. Tarascon, *Inorg. Chem.*, 2010, **49**, 7401-7413.

181. P. Barpanda, G. Oyama, C. D. Ling and A. Yamada, *Chem. Mater.*, 2014, **26**, 1297-1299.

182. P. Barpanda, G. Oyama, S.-i. Nishimura, S.-C. Chung and A. Yamada, *Nat. Commun.*, 2014, **5**, 4358.

183. Y. Lu, L. Wang, J. Cheng and J. B. Goodenough, *Chem. Commun.*, 2012, **48**, 6544-6546.

184. P. Ge and M. Fouletier, *Solid State Ionics*, 1988, **28**, 1172-1175.

185. D. A. Stevens and J. R. Dahn, *J. Electrochem. Soc.*, 2001, **148**, A803-A811.

186. B. Jache and P. Adelhelm, *Angew. Chem. Int. Ed.*, 2014, **53**, 10169-10173.

187. H. Kim, J. Hong, Y.-U. Park, J. Kim, I. Hwang and K. Kang, *Adv. Funct. Mater.*, 2014, 534-541.

188. H. Kim, J. Hong, G. Yoon, H. Kim, K.-Y. Park, M.-S. Park, W.-S. Yoon and K. Kang, *Energy Environ. Sci.*, 2015, **8**, 2963-2969.

189. M. M. Doeff, Y. Ma, S. J. Visco and L. C. De Jonghe, *J. Electrochem. Soc.*, 1993, **140**, L169-L170.

190. D. Stevens and J. Dahn, *J. Electrochem. Soc.*, 2000, **147**, 1271-1273.

191. C. Bommier, T. W. Surta, M. Dolgos and X. Ji, *Nano Lett.*, 2015, **15**, 5888-5892.

192. P.-c. Tsai, S.-C. Chung, S.-k. Lin and A. Yamada, *J. Mater. Chem. A*, 2015, **3**, 9763-9768.

193. K. Gotoh, T. Ishikawa, S. Shimadzu, N. Yabuuchi, S. Komaba, K. Takeda, A. Goto, K. Deguchi, S. Ohki and K. Hashi, *J. Power Sources*, 2013, **225**, 137-140.

194. H.-G. Wang, S. Yuan, D.-L. Ma, X.-B. Zhang and J.-M. Yan, *Energy Environ. Sci.*, 2015, **8**, 1660-1681.

195. H.-G. Wang, Z. Wu , F.-L. Meng , D.-L. Ma , X.-L. Huang , L.-M. Wang and X.-B. Zhang, *ChemSusChem*, 2013, **6**, 56-60.

196. L. Qie, W. Chen, X. Xiong, C. Hu, F. Zou, P. Hu and Y. Huang, *Advanced Science*, 2015, **2**, 1500195.

197. H. Xiong, M. D. Slater, M. Balasubramanian, C. S. Johnson and T. Rajh, *J. Phys. Chem. Lett.*, 2011, **2**, 2560-2565.

198. K.-T. Kim, G. Ali, K. Y. Chung, C. S. Yoon, H. Yashiro, Y.-K. Sun, J. Lu, K. Amine and S.-T. Myung, *Nano Lett.*, 2014, **14**, 416-422.

199. L. Wu, D. Bresser, D. Buchholz, G. A. Giffin, C. R. Castro, A. Ochel and S. Passerini, *Adv. Energy Mater.*, 2015, **5**.

200. Y. Sun, L. Zhao, H. Pan, X. Lu, L. Gu, Y.-S. Hu, H. Li, M. Armand, Y. Ikuhara, L. Chen and X. Huang, *Nat. Commun.*, 2013, **4**, 1870.

201. J. Liu, K. Tang, K. Song, P. A. van Aken, Y. Yu and J. Maier, *Phys. Chem. Chem. Phys.*, 2013, **15**, 20813-20818.

202. P. Senguttuvan, G. Rousse, V. Seznec, J.-M. Tarascon and M. R. Palacín, *Chem. Mater.*, 2011, **23**, 4109-4111.

203. J.-Y. Liao and A. Manthiram, *Nano Energy*, 2015, **18**, 20-27.

204. D. Wu, X. Li, B. Xu, N. Twu, L. Liu and G. Ceder, *Energy Environ. Sci.*, 2015, **8**, 195-202.

205. A. Rudola, K. Saravanan, S. Devaraj, H. Gong and P. Balaya, *Chem. Commun.*, 2013, **49**, 7451-7453.

206. H. Li, H. Fei, X. Liu, J. Yang and M. Wei, *Chem. Commun.*, 2015, **51**, 9298-9300.

207. P. Eklund, M. Beckers, U. Jansson, H. Högberg and L. Hultman, *Thin Solid Films*, 2010, **518**, 1851-1878.

208. M. Naguib, M. Kurtoglu, V. Presser, J. Lu, J. Niu, M. Heon, L. Hultman, Y. Gogotsi and M. W. Barsoum, *Adv. Mater.*, 2011, **23**, 4248-4253.

209. B. Anasori, Y. Xie, M. Beidaghi, J. Lu, B. C. Hosler, L. Hultman, P. R. C. Kent, Y. Gogotsi and M. W. Barsoum, *ACS Nano*, 2015, **9**, 9507-9516.

210. M. Naguib, O. Mashtalir, J. Carle, V. Presser, J. Lu, L. Hultman, Y. Gogotsi and M. W. Barsoum, *ACS Nano*, 2012, **6**, 1322-1331.

211. P. Urbankowski, B. Anasori, T. Makaryan, D. Er, S. Kota, P. L. Walsh, M. Zhao, V. B. Shenoy, M. W. Barsoum and Y. Gogotsi, *Nanoscale*, 2016, **8**, 11385-11391.

212. M. Naguib, J. Halim, J. Lu, K. M. Cook, L. Hultman, Y. Gogotsi and M. W. Barsoum, *J. Am. Chem. Soc.*, 2013, **135**, 15966-15969.

213. M. Ghidiu, M. R. Lukatskaya, M.-Q. Zhao, Y. Gogotsi and M. W. Barsoum, *Nature*, 2014, **516**, 78-81.

214. M. R. Lukatskaya, O. Mashtalir, C. E. Ren, Y. Dall'Agnese, P. Rozier, P. L. Taberna, M. Naguib, P. Simon, M. W. Barsoum and Y. Gogotsi, *Science*, 2013, **341**, 1502-1505.

215. O. Mashtalir, M. Naguib, V. N. Mochalin, Y. Dall'Agnese, M. Heon, M. W. Barsoum and Y. Gogotsi, *Nat. Commun.*, 2013, **4**, 1716.

216. O. Mashtalir, M. R. Lukatskaya, M. Q. Zhao, M. W. Barsoum and Y. Gogotsi, *Adv. Mater.*, 2015, **27**, 3501-3506.

217. X. Wang, X. Shen, Y. Gao, Z. Wang, R. Yu and L. Chen, *J. Am. Chem. Soc.*, 2015, **137**, 2715-2721.

218. Y. Xie, Y. Dall'Agnese, M. Naguib, Y. Gogotsi, M. W. Barsoum, H. L. Zhuang and P. R. C. Kent, *ACS Nano*, 2014, **8**, 9606-9615.

219. E. Yang, H. Ji, J. Kim, H. Kim and Y. Jung, *Phys. Chem. Chem. Phys.*, 2015, **17**, 5000-5005.

220. C. Eames and M. S. Islam, *J. Am. Chem. Soc.*, 2014, **136**, 16270-16276.

221. Y. Dall'Agnese, P.-L. Taberna, Y. Gogotsi and P. Simon, *J. Phys. Chem. Lett.*, 2015, **6**, 2305-2309.

222. S. Hariharan, K. Saravanan, V. Ramar and P. Balaya, *Phys. Chem. Chem. Phys.*, 2013, **15**, 2945-2953.

223. B. Huang, K. Tai, M. Zhang, Y. Xiao and S. J. Dillon, *Electrochim. Acta*, 2014, **118**, 143-149.

224. P. R. Kumar, Y. H. Jung, K. K. Bharathi, C. H. Lim and D. K. Kim, *Electrochim. Acta*, 2014, **146**, 503-510.

225. D.-Y. Park and S.-T. Myung, *ACS Appl. Mater. Interfaces*, 2014, **6**, 11749-11757.

226. B. Philippe, M. Valvo, F. Lindgren, H. k. Rensmo and K. Edström, *Chem. Mater.*, 2014, **26**, 5028-5041.

227. M. Valvo, F. Lindgren, U. Lafont, F. Björefors and K. Edström, *J. Power Sources*, 2014, **245**, 967-978.

228. X. Liu, T. Chen, H. Chu, L. Niu, Z. Sun, L. Pan and C. Q. Sun, *Electrochim. Acta*, 2015, **166**, 12-16.

229. S. Liu, Y. Wang, Y. Dong, Z. Zhao, Z. Wang and J. Qiu, *ChemElectroChem*, 2016, **3**, 38-44.

230. Y. Jiang, M. Hu, D. Zhang, T. Yuan, W. Sun, B. Xu and M. Yan, *Nano Energy*, 2014, **5**, 60-66.

231. F. Klein, B. Jache, A. Bhide and P. Adelhelm, *Phys. Chem. Chem. Phys.*, 2013, **15**, 15876-15887.

232. H. Liu, F. Cao, H. Zheng, H. Sheng, L. Li, S. Wu, C. Liu and J. Wang, *Chem. Commun.*, 2015, **51**, 10443-10446.

233. X. Wang, X. Shen, Z. Wang, R. Yu and L. Chen, *ACS Nano*, 2014, **8**, 11394-11400.

234. Y.-X. Wang, S.-L. Chou, D. Wexler, H.-K. Liu and S.-X. Dou, *Chem. — Eur. J.*, 2014, **20**, 9607-9612.

235. S. Zhang, X. Yu, H. Yu, Y. Chen, P. Gao, C. Li and C. Zhu, *ACS Appl. Mater. Interfaces*, 2014, **6**, 21880-21885.

236. F. Zhou, S. Xin, H.-W. Liang, L.-T. Song and S.-H. Yu, *Angew. Chem. Int. Ed.*, 2014, **53**, 11552-11556.

237. C. Zhu, X. Mu, P. A. van Aken, Y. Yu and J. Maier, *Angew. Chem. Int. Ed.*, 2014, **53**, 2152-2156.

238. S. H. Choi, Y. N. Ko, J.-K. Lee and Y. C. Kang, *Adv. Funct. Mater.*, 2015, **25**, 1780-1788.

239. J. Wang, C. Luo, T. Gao, A. Langrock, A. C. Mignerey and C. Wang, *Small*, 2015, **11**, 473-481.

240. X. Xiong, W. Luo, X. Hu, C. Chen, L. Qie, D. Hou and Y. Huang, *Sci. Rep.*, 2015, **5**, 9254.

241. B. Qu, C. Ma, G. Ji, C. Xu, J. Xu, Y. S. Meng, T. Wang and J. Y. Lee, *Adv. Mater.*, 2014, **26**, 3854-3859.

242. P. V. Prikhodchenko, D. Y. W. Yu, S. K. Batabyal, V. Uvarov, J. Gun, S. Sladkevich, A. A. Mikhaylov, A. G. Medvedev and O. Lev, *J. Mater. Chem. A*, 2014, **2**, 8431-8437.

243. Y. Liu, H. Kang, L. Jiao, C. Chen, K. Cao, Y. Wang and H. Yuan, *Nanoscale*, 2015, **7**, 1325-1332.

244. C. Ma, J. Xu, J. Alvarado, B. Qu, J. Somerville, J. Y. Lee and Y. S. Meng, *Chem. Mater.*, 2015, **27**, 5633-5640.

245. W. Xu, K. Zhao, L. Zhang, Z. Xie, Z. Cai and Y. Wang, *J. Alloys Compd.*, 2016, **654**, 357-362.

246. Z. Li, J. Ding and D. Mitlin, *Acc. Chem. Res.*, 2015, **48**, 1657-1665.

247. H. Zhu, Z. Jia, Y. Chen, N. Weadock, J. Wan, O. Vaaland, X. Han, T. Li and L. Hu, *Nano Lett.*, 2013, 3093-3100.

248. Y. Liu, Y. Xu, Y. Zhu, J. N. Culver, C. A. Lundgren, K. Xu and C. Wang, *ACS Nano*, 2013, **7**, 3627-3634.

249. Y. Xu, Y. Zhu, Y. Liu and C. Wang, *Adv. Energy Mater.*, 2013, **3**, 128-133.

250. Y.-X. Wang, Y.-G. Lim, M.-S. Park, S.-L. Chou, J. H. Kim, H.-K. Liu, S.-X. Dou and Y.-J. Kim, *J. Mater. Chem. A*, 2014, **2**, 529-534.

251. S. Li, Y. Wang, J. Qiu, M. Ling, H. Wang, W. Martens and S. Zhang, *RSC Adv.*, 2014, **4**, 50148-50152.

252. L. Pei, Q. Jin, Z. Zhu, Q. Zhao, J. Liang and J. Chen, *Nano Res.*, 2015, **8**, 184-192.

253. D. Andre, M. Meiler, K. Steiner, C. Wimmer, T. Soczka-Guth and D. U. Sauer, *J. Power Sources*, 2011, **196**, 5334-5341.

254. A.-M. Cao, J.-S. Hu, H.-P. Liang and L.-J. Wan, *Angew. Chem. Int. Ed.*, 2005, **44**, 4391-4395.

255. J. Maier, *Nat. Mater.*, 2005, **4**, 805-815.

256. H. Li, Z. Wang, L. Chen and X. Huang, *Adv. Mater.*, 2009, **21**, 4593-4607.

257. W. Li, S.-L. Chou, J.-Z. Wang, J. H. Kim, H.-K. Liu and S.-X. Dou, *Adv. Mater.*, 2014, **26**, 4037-4042.

258. J. Qian, Y. Xiong, Y. Cao, X. Ai and H. Yang, *Nano Lett.*, 2014, **14**, 1865-1869.

259. G. Amatucci and J.-M. Tarascon, *J. Electrochem. Soc.*, 2002, **149**, K31-K46.

260. H. Jiang, Y. Fu, Y. Hu, C. Yan, L. Zhang, P. S. Lee and C. Li, *Small*, 2014, **10**, 1096-1100.

261. J. Xu, Y. Hu, T. liu and X. Wu, *Nano Energy*, 2014, **5**, 67-73.

262. D. Su, C. Wang, H. Ahn and G. Wang, *Phys. Chem. Chem. Phys.*, 2013, **15**, 12543-12550.

263. T.-F. Yi, Y.-R. Zhu, X.-D. Zhu, J. Shu, C.-B. Yue and A.-N. Zhou, *Ionics*, 2009, **15**, 779-784.

264. J.-Y. Luo, H.-M. Xiong and Y.-Y. Xia, *J. Phys. Chem. C*, 2008, **112**, 12051-12057.

265. Y.-L. Ding, J. Xie, G.-S. Cao, T.-J. Zhu, H.-M. Yu and X.-B. Zhao, *Adv. Funct. Mater.*, 2011, **21**, 348-355.

266. D. Guyomard and J. M. Tarascon, *J. Electrochem. Soc.*, 1992, **139**, 937-948.

267. H. Kanoh, Q. Feng, Y. Miyai and K. Ooi, *J. Electrochem. Soc.*, 1995, **142**, 702-707.

268. K. Dokko, M. Nishizawa, M. Mohamedi, M. Umeda, I. Uchida, J. Akimoto, Y. Takahashi, Y. Gotoh and S. Mizuta, *Electrochem. Solid-State Lett.*, 2001, **4**, A151-A153.

269. W. Tang, X. Yang, Z. Liu, S. Kasaishi and K. Ooi, *J. Mater. Chem.*, 2002, **12**, 2991-2997.

270. A. R. Armstrong, G. Armstrong, J. Canales and P. G. Bruce, *Angew. Chem. Int. Ed.*, 2004, **43**, 2286-2288.

271. C. K. Chan, H. Peng, G. Liu, K. McIlwrath, X. F. Zhang, R. A. Huggins and Y. Cui, *Nat. Nanotechnol.*, 2008, **3**, 31-35.

272. Y. Huang, J. Li and D. Jia, *J. Nanopart. Res.*, 2004, **6**, 533-538.

273. Z. Bai, N. Fan, Z. Ju, C. Sun and Y. Qian, *Mater. Lett.*, 2012, **76**, 124-126.

274. H. Liu and L. Tan, *J. Nanopart. Res.*, 2010, **12**, 301-305.

275. D. Zhan, Q. Zhang, X. Hu, G. Zhu and T. Peng, *Solid State Ionics*, 2013, **239**, 8-14.

276. D. Su, H.-J. Ahn and G. Wang, *J. Mater. Chem. A*, 2013, **1**, 4845-4850.

277. Y. Xia, T. Sakai, T. Fujieda, X. Q. Yang, X. Sun, Z. F. Ma, J. McBreen and M. Yoshio, *J. Electrochem. Soc.*, 2001, **148**, A723-A729.

278. A. Blyr, C. Sigala, G. Amatucci, D. Guyomard, Y. Chabre and J. M. Tarascon, *J. Electrochem. Soc.*, 1998, **145**, 194-209.

279. S. S. Zhang, M. H. Ervin, D. L. Foster, K. Xu and T. R. Jow, *J. Solid State Electrochem.*, 2005, **9**, 77-82.

280. H. W. Chan, J. G. Duh and S. R. Sheen, *J. Power Sources*, 2003, **115**, 110-118.

281. S. Komaba, W. Murata, T. Ishikawa, N. Yabuuchi, T. Ozeki, T. Nakayama, A. Ogata, K. Gotoh and K. Fujiwara, *Adv. Funct. Mater.*, 2011, **21**, 3859-3867.

282. Y. Cao, L. Xiao, M. L. Sushko, W. Wang, B. Schwenzer, J. Xiao, Z. Nie, L. V. Saraf, Z. Yang and J. Liu, *Nano Lett.*, 2012, **12**, 3783-3787.

283. P. Nie, Y. Zhu, L. Shen, G. Pang, G. Xu, S. Dong, H. Dou and X. Zhang, *J. Mater. Chem. A*, 2014, **2**, 18606-18612.

284. Y. Kim, K.-H. Ha, S. M. Oh and K. T. Lee, *Chem. — Eur. J.*, 2014, **20**, 11980-11992.

285. J. Qian, X. Wu, Y. Cao, X. Ai and H. Yang, *Angew. Chem. Int. Ed.*, 2013, **52**, 4633-4636.

286. H. Zhu, Z. Jia, Y. Chen, N. Weadock, J. Wan, O. Vaaland, X. Han, T. Li and L. Hu, *Nano Lett.*, 2013, 3093–3100.

287. J. Qian, Y. Chen, L. Wu, Y. Cao, X. Ai and H. Yang, *Chem. Commun.*, 2012, **48**, 7070-7072.

288. Y. Zhu, X. Han, Y. Xu, Y. Liu, S. Zheng, K. Xu, L. Hu and C. Wang, *ACS Nano*, 2013, **7**, 6378-6386.

289. X. Xie, D. Su, S. Chen, J. Zhang, S. Dou and G. Wang, *Chem. — Asian J.*, 2014, **9**, 1611-1617.

290. T. Zhou, W. K. Pang, C. Zhang, J. Yang, Z. Chen, H. K. Liu and Z. Guo, *ACS Nano*, 2014, **8**, 8323-8333.

291. D. Y. W. Yu, P. V. Prikhodchenko, C. W. Mason, S. K. Batabyal, J. Gun, S. Sladkevich, A. G. Medvedev and O. Lev, *Nat. Commun.*, 2013, **4**, 2922.

292. L. David, R. Bhandavat and G. Singh, *ACS Nano*, 2014, **8**, 1759-1770.

293. M.-Q. Yang, N. Zhang, M. Pagliaro and Y.-J. Xu, *Chem. Soc. Rev.*, 2014, **43**, 8240-8254.

294. Y. Zhang, Z.-R. Tang, X. Fu and Y.-J. Xu, *ACS Nano*, 2011, **5**, 7426-7435.

295. N. Zhang, Y. Zhang and Y.-J. Xu, *Nanoscale*, 2012, **4**, 5792-5813.

296. M.-Q. Yang and Y.-J. Xu, *Phys. Chem. Chem. Phys.*, 2013, **15**, 19102-19118.

297. N. Zhang, M.-Q. Yang, Z.-R. Tang and Y.-J. Xu, *ACS nano*, 2014, **8**, 623-633.

298. A. L. M. Reddy, A. Srivastava, S. R. Gowda, H. Gullapalli, M. Dubey and P. M. Ajayan, *ACS Nano*, 2010, **4**, 6337-6342.

299. D. Usachov, O. Vilkov, A. Grüneis, D. Haberer, A. Fedorov, V. K. Adamchuk, A. B. Preobrajenski, P. Dudin, A. Barinov, M. Oehzelt, C. Laubschat and D. V. Vyalikh, *Nano Lett.*, 2011, **11**, 5401-5407.

300. Z.-S. Wu, W. Ren, L. Xu, F. Li and H.-M. Cheng, *ACS Nano*, 2011, **5**, 5463-5471.

301. Z.-R. Tang, Y. Zhang, N. Zhang and Y.-J. Xu, *Nanoscale*, 2015, **7**, 7030-7034.

302. H. A. Cha, H. M. Jeong and J. K. Kang, *J. Mater. Chem. A*, 2014, **2**, 5182-5186.

303. G. Qin, X. Zhang and C. Wang, *J. Mater. Chem. A*, 2014, **2**, 12449-12458.

304. Z. Wang, L. Qie, L. Yuan, W. Zhang, X. Hu and Y. Huang, *Carbon*, 2013, **55**, 328-334.

305. W. S. Hummers and R. E. Offeman, *J. Am. Chem. Soc.*, 1958, **80**, 1339.

306. L. Sun, L. Wang, C. Tian, T. Tan, Y. Xie, K. Shi, M. Li and H. Fu, *RSC Adv.*, 2012, **2**, 4498-4506.

307. X. Xie, J. Long, J. Xu, L. Chen, Y. Wang, Z. Zhang and X. Wang, *RSC Adv.*, 2012, **2**, 12438-12446.

308. J. Duan, S. Chen, S. Dai and S. Z. Qiao, *Adv. Funct. Mater.*, 2014, **24**, 2072-2078.

309. K. S. W. Sing, D. H. Everett, R. A. W. Haul, L. Moscou, R. A. Pierotti, J. Rouquérol and T. Siemieniewska, *Pure Appl. Chem.*, 1985, **57**, 603-619.

310. X. Meng, H. Cui, J. Dong, J. Zheng, Y. Zhu, Z. Wang, J. Zhang, S. Jia, J. Zhao and Z. Zhu, *J. Mater. Chem. A*, 2013, 9469-9476.

311. J. Casanovas, J. M. Ricart, J. Rubio, F. Illas and J. M. Jiménez-Mateos, *J. Am. Chem. Soc.*, 1996, **118**, 8071-8076.

312. B. Guo, Q. Liu, E. Chen, H. Zhu, L. Fang and J. R. Gong, *Nano Lett.*, 2010, **10**, 4975-4980.

313. J. Jin, X. Fu, Q. Liu, Y. Liu, Z. Wei, K. Niu and J. Zhang, *ACS Nano*, 2013, 4764–4773.

314. Y. Jiao, Y. Zheng, M. Jaroniec and S. Z. Qiao, *J. Am. Chem. Soc.*, 2014, **136**, 4394-4403.

315. Y. Zheng, Y. Jiao, Y. Zhu, L. H. Li, Y. Han, Y. Chen, A. Du, M. Jaroniec and S. Z. Qiao, *Nat. Commun.*, 2014, **5**, 3783.

316. S. D. Gardner, C. S. K. Singamsetty, G. L. Booth, G.-R. He and C. U. Pittman Jr, *Carbon*, 1995, **33**, 587-595.

317. W. Lv, D.-M. Tang, Y.-B. He, C.-H. You, Z.-Q. Shi, X.-C. Chen, C.-M. Chen, P.-X. Hou, C. Liu and Q.-H. Yang, *ACS Nano*, 2009, **3**, 3730-3736.

318. G. Zhou, D.-W. Wang, L.-C. Yin, N. Li, F. Li and H.-M. Cheng, *ACS Nano*, 2012, **6**, 3214-3223.

319. M. Gu, A. Kushima, Y. Shao, J.-G. Zhang, J. Liu, N. D. Browning, J. Li and C. Wang, *Nano Lett.*, 2013, **13**, 5203-5211.

320. Y.-X. Wang, S.-L. Chou, H.-K. Liu and S.-X. Dou, *Carbon*, 2013, **57**, 202-208.

321. Y. Marcus, *Pure Appl. Chem.*, 1985, **57**, 1129-1132.

322. K. Tang, L. Fu, R. J. White, L. Yu, M.-M. Titirici, M. Antonietti and J. Maier, *Adv. Energy Mater.*, 2012, **2**, 873-877.

323. J. Dahn, T. Zheng, Y. Liu and J. Xue, *Science*, 1995, **270**, 590-593.

324. P. Poizot, S. Laruelle, S. Grugeon and J.-M. Tarascon, *J. Electrochem. Soc.*, 2002, **149**, A1212-A1217.

325. K. Edström, T. Gustafsson and J. O. Thomas, *Electrochim. Acta*, 2004, **50**, 397-403.

326. X. Li, D. Geng, Y. Zhang, X. Meng, R. Li and X. Sun, *Electrochem. Commun.*, 2011, **13**, 822-825.

327. X. Wang, X. Cao, L. Bourgeois, H. Guan, S. Chen, Y. Zhong, D.-M. Tang, H. Li, T. Zhai, L. Li, Y. Bando and D. Golberg, *Adv. Funct. Mater.*, 2012, **22**, 2682-2690.

328. X. Wang, W. Tian, D. Liu, C. Zhi, Y. Bando and D. Golberg, *Nano Energy*, 2013, **2**, 257-267.

329. X. Wang, Q. Weng, X. Liu, X. Wang, D.-M. Tang, W. Tian, C. Zhang, W. Yi, D. Liu, Y. Bando and D. Golberg, *Nano Lett.*, 2014, **14**, 1164-1171.

330. F. Zheng, Y. Yang and Q. Chen, *Nat. Commun.*, 2014, **5**, 5261.

331. L. Fu, K. Tang, K. Song, P. A. van Aken, Y. Yu and J. Maier, *Nanoscale*, 2014, **6**, 1384-1389.

332. J. Park, J.-S. Kim, J.-W. Park, T.-H. Nam, K.-W. Kim, J.-H. Ahn, G. Wang and H.-J. Ahn, *Electrochim. Acta*, 2013, **92**, 427-432.

333. Z. Hu, L. Wang, K. Zhang, J. Wang, F. Cheng, Z. Tao and J. Chen, *Angew. Chem. Int. Ed.*, 2014, **53**, 12794-12798.

334. D. Su, S. Dou and G. Wang, *Chem. Commun.*, 2014, **50**, 4192-4195.

335. P. K. Dutta, U. K. Sen and S. Mitra, *RSC Adv.*, 2014, **4**, 43155-43159.

336. C. N. R. Rao, A. K. Sood, K. S. Subrahmanyam and A. Govindaraj, *Angew. Chem. Int. Ed.*, 2009, **48**, 7752-7777.

337. P.-p. Wang, H. Sun, Y. Ji, W. Li and X. Wang, *Adv. Mater.*, 2014, **26**, 964-969.

338. L. Britnell, R. Gorbachev, R. Jalil, B. Belle, F. Schedin, A. Mishchenko, T. Georgiou, M. Katsnelson, L. Eaves and S. Morozov, *Science*, 2012, **335**, 947-950.

339. L. Britnell, R. Ribeiro, A. Eckmann, R. Jalil, B. Belle, A. Mishchenko, Y.-J. Kim, R. Gorbachev, T. Georgiou and S. Morozov, *Science*, 2013, **340**, 1311-1314.

340. B. Hunt, J. D. Sanchez-Yamagishi, A. F. Young, M. Yankowitz, B. J. LeRoy, K. Watanabe, T. Taniguchi, P. Moon, M. Koshino, P. Jarillo-Herrero and R. C. Ashoori, *Science*, 2013, **340**, 1427-1430.

341. K. Roy, M. Padmanabhan, S. Goswami, T. P. Sai, G. Ramalingam, S. Raghavan and A. Ghosh, *Nat. Nanotechnol.*, 2013, **8**, 826-830.

342. M. Sup Choi, G.-H. Lee, Y.-J. Yu, D.-Y. Lee, S. Hwan Lee, P. Kim, J. Hone and W. Jong Yoo, *Nat. Commun.*, 2013, **4**, 1624.

343. L. Wang, I. Meric, P. Y. Huang, Q. Gao, Y. Gao, H. Tran, T. Taniguchi, K. Watanabe, L. M. Campos, D. A. Muller, J. Guo, P. Kim, J. Hone, K. L. Shepard and C. R. Dean, *Science*, 2013, **342**, 614-617.

344. Z.-G. Chen, Z. Shi, W. Yang, X. Lu, Y. Lai, H. Yan, F. Wang, G. Zhang and Z. Li, *Nat. Commun.*, 2014, **5**.

345. H. Fang, C. Battaglia, C. Carraro, S. Nemsak, B. Ozdol, J. S. Kang, H. A. Bechtel, S. B. Desai, F. Kronast, A. A. Unal, G. Conti, C. Conlon, G. K. Palsson, M. C. Martin, A. M. Minor, C. S. Fadley, E. Yablonovitch, R. Maboudian and A. Javey, *Proc. Natl. Acad. Sci.*, 2014, **111**, 6198-6202.

346. J. Y. Kwak, J. Hwang, B. Calderon, H. Alsalman, N. Munoz, B. Schutter and M. G. Spencer, *Nano Lett.*, 2014, **14**, 4511-4516.

347. R. Chen, T. Zhao, W. Wu, F. Wu, L. Li, J. Qian, R. Xu, H. Wu, H. M. Albishri, A. S. Al-Bogami, D. A. El-Hady, J. Lu and K. Amine, *Nano Lett.*, 2014, **14**, 5899-5904.

348. A. Geim and I. Grigorieva, *Nature*, 2013, **499**, 419-425.

349. K. Zhang, F. L. Yap, K. Li, C. T. Ng, L. J. Li and K. P. Loh, *Adv. Funct. Mater.*, 2014, **24**, 731-738.

350. J. Lu, L. C. Gomes, R. W. Nunes, A. H. Castro Neto and K. P. Loh, *Nano Lett.*, 2014, **14**, 5133-5139.

351. B. Delley, *J. Chem. Phys.*, 2000, **113**, 7756-7764.

352. J. P. Perdew, K. Burke and M. Ernzerhof, *Phys. Rev. Lett.*, 1996, **77**, 3865-3868.

353. S. Grimme, *J. Comput. Chem.*, 2006, **27**, 1787-1799.

354. Y. Li, H. Wang, L. Xie, Y. Liang, G. Hong and H. Dai, *J. Am. Chem. Soc.*, 2011, **133**, 7296-7299.

355. K. Chang, W.-x. Chen, H. Li and H. Li, *Electrochim. Acta*, 2011, **56**, 2856-2861.

356. C. N. R. Rao and A. Nag, *Eur. J. Inorg. Chem.*, 2010, **2010**, 4244-4250.

357. K. Chang and W. Chen, *Chem. Commun.*, 2011, **47**, 4252-4254.

358. L. Xiao, Y. Cao, J. Xiao, W. Wang, L. Kovarik, Z. Nie and J. Liu, *Chem. Commun.*, 2012, **48**, 3321-3323.

359. L. David and G. Singh, *J. Phys. Chem. C*, 2014, **118**, 28401-28408.

360. R. H. Miwa and W. L. Scopel, *J. Phys.: Condens. Matter.*, 2013, **25**, 445301.

361. Y. Li, D. Wu, Z. Zhou, C. R. Cabrera and Z. Chen, *J. Phys. Chem. Lett.*, 2012, **3**, 2221-2227.

362. Y. Ma, Y. Dai, M. Guo, C. Niu and B. Huang, *Nanoscale*, 2011, **3**, 3883-3887.

363. L. D. Ellis, T. D. Hatchard and M. N. Obrovac, *J. Electrochem. Soc.*, 2012, **159**, A1801-A1805.

364. S. Komaba, Y. Matsuura, T. Ishikawa, N. Yabuuchi, W. Murata and S. Kuze, *Electrochem. Commun.*, 2012, **21**, 65-68.

365. J. W. Wang, X. H. Liu, S. X. Mao and J. Y. Huang, *Nano Lett.*, 2012, **12**, 5897-5902.

366. M. K. Datta, R. Epur, P. Saha, K. Kadakia, S. K. Park and P. N. Kumta, *J. Power Sources*, 2013, **225**, 316-322.

367. D. Su, H.-J. Ahn and G. Wang, *Chem. Commun.*, 2013, **49**, 3131-3133.

368. Y. Wang, D. Su, C. Wang and G. Wang, *Electrochem. Commun.*, 2013, **29**, 8-11.

369. B. Luo, Y. Fang, B. Wang, J. Zhou, H. Song and L. Zhi, *Energy Environ. Sci.*, 2012, **5**, 5226-5230.

370. S. Xin, Y.-G. Guo and L.-J. Wan, *Acc. Chem. Res.*, 2012, **45**, 1759-1769.

371. X.-L. Wu, Y.-G. Guo and L.-J. Wan, *Chem. — Asian J.*, 2013, **8**, 1948-1958.

372. Z. Jiang, C. Wang, G. Du, Y. J. Zhong and J. Z. Jiang, *J. Mater. Chem.*, 2012, **22**, 9494-9496.

373. A. Smith, P. Meek and W. Liang, *J. Phys. C*, 1977, **10**, 1321.

374. Z. Ni, Y. Wang, T. Yu and Z. Shen, *Nano Res.*, 2008, **1**, 273-291.

375. A. C. Ferrari and D. M. Basko, *Nat. Nanotechnol.*, 2013, **8**, 235-246.

376. C. Zhai, N. Du, H. Zhang, J. Yu and D. Yang, *ACS Appl. Mater. Interfaces*, 2011, **3**, 4067-4074.

377. K. S. Novoselov, A. K. Geim, S. V. Morozov, D. Jiang, Y. Zhang, S. V. Dubonos, I. V. Grigorieva and A. A. Firsov, *Science*, 2004, **306**, 666-669.

378. M. V. Reddy, S. Madhavi, G. V. Subba Rao and B. V. R. Chowdari, *J. Power Sources*, 2006, **162**, 1312-1321.

379. M. V. Reddy, T. Yu, C. H. Sow, Z. X. Shen, C. T. Lim, G. V. Subba Rao and B. V. R. Chowdari, *Adv. Funct. Mater.*, 2007, **17**, 2792-2799.

380. Y. Zhang, J. Xie, S. Zhang, P. Zhu, G. Cao and X. Zhao, *Electrochim. Acta*, 2015, **151**, 8-15.

381. D. Li, M. B. Muller, S. Gilje, R. B. Kaner and G. G. Wallace, *Nat. Nanotechnol.*, 2008, **3**, 101-105.

382. H. Bai, C. Li, X. Wang and G. Shi, *J. Phys. Chem. C*, 2011, **115**, 5545-5551.

383. Y. Zhou, Q. Bao, L. A. L. Tang, Y. Zhong and K. P. Loh, *Chem. Mater.*, 2009, **21**, 2950-2956.

384. S. Komaba, T. Ishikawa, N. Yabuuchi, W. Murata, A. Ito and Y. Ohsawa, *ACS Appl. Mater. Interfaces*, 2011, **3**, 4165-4168.

385. V. L. Chevrier and G. Ceder, *J. Electrochem. Soc.*, 2011, **158**, A1011-A1014.

386. Y. Liu, N. Zhang, L. Jiao, Z. Tao and J. Chen, *Adv. Funct. Mater.*, 2015, **25**, 214-220.

387. B. Wang, B. Luo, X. Li and L. Zhi, *Materials Today*, 2012, **15**, 544-552.

388. D. Su, X. Xie and G. Wang, *Chem. — Eur. J.*, 2014, **20**, 3192-3197.

389. H. C. Shin and M. Liu, *Adv. Funct. Mater.*, 2005, **15**, 582-586.

390. J. Hassoun, S. Panero, P. Simon, P. L. Taberna and B. Scrosati, *Adv. Mater.*, 2007, **19**, 1632-1635.

391. P. L. Taberna, S. Mitra, P. Poizot, P. Simon and J. M. Tarascon, *Nat. Mater.*, 2006, **5**, 567-573.

392. L.-F. Cui, L. Hu, J. W. Choi and Y. Cui, *ACS Nano*, 2010, **4**, 3671-3678.

393. J. W. Long, B. Dunn, D. R. Rolison and H. S. White, *Chem. Rev.*, 2004, **104**, 4463-4492.

394. H. Zhang, X. Yu and P. V. Braun, *Nat. Nanotechnol.*, 2011, **6**, 277-281.

395. R. Li, X. Sun, X. Zhou, M. Cai and X. Sun, *J. Phys. Chem. C*, 2007, **111**, 9130-9135.

396. J. Qin, C. He, N. Zhao, Z. Wang, C. Shi, E.-Z. Liu and J. Li, *ACS Nano*, 2014, **8**, 1728-1738.

397. X. Xie, D. Su, J. Zhang, S. Chen, A. K. Mondal and G. Wang, *Nanoscale*, 2015, **7**, 3164-3172.

398. W.-M. Zhang, J.-S. Hu, Y.-G. Guo, S.-F. Zheng, L.-S. Zhong, W.-G. Song and L.-J. Wan, *Adv. Mater.*, 2008, **20**, 1160-1165.

399. Y. Zou and Y. Wang, *ACS Nano*, 2011, **5**, 8108-8114.

400. X. Xie, Z. Ao, D. Su, J. Zhang and G. Wang, *Adv. Funct. Mater.*, 2015, **25**, 1393-1403.

401. H. Li, Q. Zhang, C. C. R. Yap, B. K. Tay, T. H. T. Edwin, A. Olivier and D. Baillargeat, *Adv. Funct. Mater.*, 2012, **22**, 1385-1390.

402. S. Jiménez Sandoval, D. Yang, R. F. Frindt and J. C. Irwin, *Phys. Rev. B*, 1991, **44**, 3955-3962.

403. X. Fan, P. Xu, D. Zhou, Y. Sun, Y. C. Li, M. A. T. Nguyen, M. Terrones and T. E. Mallouk, *Nano Lett.*, 2015, **15**, 5956-5960.

404. L. J. Hardwick, P. W. Ruch, M. Hahn, W. Scheifele, R. Kötz and P. Novák, *J. Phys. Chem. Solids*, 2008, **69**, 1232-1237.

405. Y.-C. Lin, D. O. Dumcenco, Y.-S. Huang and K. Suenaga, *Nat. Nanotechnol.*, 2014, **9**, 391-396.

406. E. Memarzadeh, P. Kalisvaart, A. Kohandehghan and D. Mitlin, *J. Mater. Chem. A*, 2014, **2**, 19685-19695.

407. S.-W. Kim, D.-H. Seo, X. Ma, G. Ceder and K. Kang, *Adv. Energy Mater.*, 2012, **2**, 710-721.

408. Y. Gogotsi, *ACS Nano*, 2014, **8**, 5369-5371.

409. J. Sangster, *J. Phace Equilib. Diff.*, 2007, **28**, 571-579.

410. Y. Wen, K. He, Y. Zhu, F. Han, Y. Xu, I. Matsuda, Y. Ishii, J. Cumings and C. Wang, *Nat. Commun.*, 2014, **5**, 4033.

411. Y. Kim, Y. Park, A. Choi, N.-S. Choi, J. Kim, J. Lee, J. H. Ryu, S. M. Oh and K. T. Lee, *Adv. Mater.*, 2013, **25**, 3045-3049.

412. J. Song, Z. Yu, M. L. Gordin, S. Hu, R. Yi, D. Tang, T. Walter, M. Regula, D. Choi, X. Li, A. Manivannan and D. Wang, *Nano Lett.*, 2014, **14**, 6329-6335.

413. J. Sun, H.-W. Lee, M. Pasta, H. Yuan, G. Zheng, Y. Sun, Y. Li and Y. Cui, *Nat. Nanotechnol.*, 2015, **10**, 980-985.

414. N. Wu, H.-R. Yao, Y.-X. Yin and Y.-G. Guo, *J. Mater. Chem. A*, 2015, **3**, 24221-24225.

415. J. Sun, H.-W. Lee, M. Pasta, Y. Sun, W. Liu, Y. Li, H. R. Lee, N. Liu and Y. Cui, *Energy Storage Mater.*, 2016, **4**, 130-136.

416. M. Mayo, K. J. Griffith, C. J. Pickard and A. J. Morris, *Chem. Mater.*, 2016, **28**, 2011-2021.

417. X. Xie, K. Kretschmer, J. Zhang, B. Sun, D. Su and G. Wang, *Nano Energy*, 2015, **13**, 208-217.

418. X. Xie, S. Chen, B. Sun, C. Wang and G. Wang, *ChemSusChem*, 2015, **8**, 2948–2955.

419. A. Darwiche, C. Marino, M. T. Sougrati, B. Fraisse, L. Stievano and L. Monconduit, *J. Am. Chem. Soc.*, 2012, **134**, 20805-20811.

420. L. Wu, X. Hu, J. Qian, F. Pei, F. Wu, R. Mao, X. Ai, H. Yang and Y. Cao, *Energy Environ. Sci.*, 2014, **7**, 323-328.

421. J. Liu, Z. Yang, J. Wang, L. Gu, J. Maier and Y. Yu, *Nano Energy*, 2015, **16**, 389-398.

422. X. Wang, Z. Guan, Y. Li, Z. Wang and L. Chen, *Nanoscale*, 2015, **7**, 637-641.

423. X. Xie, T. Makaryan, M. Zhao, K. L. Van Aken, Y. Gogotsi and G. Wang, *Adv. Energy Mater.*, 2016, **6**, 1502161.

424. K.-T. Kim, G. Ali, K. Y. Chung, C. S. Yoon, H. Yashiro, Y.-K. Sun, J. Lu, K. Amine and S.-T. Myung, *Nano Lett.*, 2014, **14**, 416–422.

425. Y. Wang, X. Yu, S. Xu, J. Bai, R. Xiao, Y.-S. Hu, H. Li, X.-Q. Yang, L. Chen and X. Huang, *Nat. Commun.*, 2013, **4**, 2365.

426. X. Wang, Y. Li, Y. Gao, Z. Wang and L. Chen, *Nano Energy*, 2015, **13**, 687-692.

427. Y. Gogotsi and P. Simon, *Science*, 2012, **335**, 167-167.

428. M. Naguib, V. N. Mochalin, M. W. Barsoum and Y. Gogotsi, *Adv. Mater.*, 2014, **26**, 992-1005.

429. M. Naguib and Y. Gogotsi, *Acc. Chem. Res.*, 2015, **48**, 128-135.

430. M. Boota, B. Anasori, C. Voigt, M.-Q. Zhao, M. W. Barsoum and Y. Gogotsi, *Adv. Mater.*, 2015, **28**, 1517-1522.

431. Q. Tang, Z. Zhou and P. Shen, *J. Am. Chem. Soc.*, 2012, **134**, 16909-16916.

432. C. E. Ren, M. Zhao, T. Makaryan, J. Halim, M. Boota, S. Kota, B. Anasori, M. W. Barsoum and Y. Gogotsi, *ChemElectroChem*, 2016, **3**, 1-6.

433. X. Liang, A. Garsuch and L. F. Nazar, *Angew. Chem. Int. Ed.*, 2015, **54**, 3907-3911.

434. O. Mashtalir, K. M. Cook, V. N. Mochalin, M. Crowe, M. W. Barsoum and Y. Gogotsi, *J. Mater. Chem. A*, 2014, **2**, 14334-14338.

435. X. Li, G. Fan and C. Zeng, *Int. J. Hydrogen Energy*, 2014, **39**, 14927-14934.

436. F. Wang, C. Yang, C. Duan, D. Xiao, Y. Tang and J. Zhu, *J. Electrochem. Soc.*, 2015, **162**, B16-B21.

437. X.-F. Yu, Y.-C. Li, J.-B. Cheng, Z.-B. Liu, Q.-Z. Li, W.-Z. Li, X. Yang and B. Xiao, *ACS Appl. Mater. Interfaces*, 2015, **7**, 13707-13713.

438. Y. Liu, H. Du, X. Zhang, Y. Yang, M. Gao and H. Pan, *Chem. Commun.*, 2016, **52**, 705-708.

439. C. E. Ren, K. B. Hatzell, M. Alhabeb, Z. Ling, K. A. Mahmoud and Y. Gogotsi, *J. Phys. Chem. Lett.*, 2015, **6**, 4026-4031.

440. M. Ghidiu, M. R. Lukatskaya, M.-Q. Zhao, Y. Gogotsi and M. W. Barsoum, *Nature*, 2014, **516**, 78-81.

441. D. Er, J. Li, M. Naguib, Y. Gogotsi and V. B. Shenoy, *ACS Appl. Mater. Interfaces*, 2014, **6**, 11173-11179.

442. X. Wang, S. Kajiyama, H. Iinuma, E. Hosono, S. Oro, I. Moriguchi, M. Okubo and A. Yamada, *Nat. Commun.*, 2015, **6**, 6544.

443. M.-Q. Zhao, C. E. Ren, Z. Ling, M. R. Lukatskaya, C. Zhang, K. L. Van Aken, M. W. Barsoum and Y. Gogotsi, *Adv. Mater.*, 2015, **27**, 339-345.

444. H.-W. Wang, M. Naguib, K. Page, D. J. Wesolowski and Y. Gogotsi, *Chem. Mater.*, 2016, **28**, 349-359.

445. Q. Zhang, J.-Q. Huang, M.-Q. Zhao, W.-Z. Qian, Y. Wang and F. Wei, *Carbon*, 2008, **46**, 1152-1158.

446. L. O. Vogt, M. El Kazzi, E. Jämstorp Berg, S. Pérez Villar, P. Novák and C. Villevieille, *Chem. Mater.*, 2015, **27**, 1210-1216.

447. F. Sauvage, L. Laffont, J. M. Tarascon and E. Baudrin, *Inorg. Chem.*, 2007, **46**, 3289-3294.

448. J. Wang, J. Polleux, J. Lim and B. Dunn, *J. Phys. Chem. C*, 2007, **111**, 14925-14931.

449. E. M. Lotfabad, J. Ding, K. Cui, A. Kohandehghan, W. P. Kalisvaart, M. Hazelton and D. Mitlin, *ACS Nano*, 2014, **8**, 7115-7129.

450. W. Li, L. Zeng, Z. Yang, L. Gu, J. Wang, X. Liu, J. Cheng and Y. Yu, *Nanoscale*, 2014, **6**, 693-698.

451. S. Wang, L. Xia, L. Yu, L. Zhang, H. Wang and X. W. Lou, *Adv. Energy Mater.*, 2016, **6**, 1502217.

452. Y. Xie, M. Naguib, V. N. Mochalin, M. W. Barsoum, Y. Gogotsi, X. Yu, K.-W. Nam, X.-Q. Yang, A. I. Kolesnikov and P. R. C. Kent, *J. Am. Chem. Soc.*, 2014, **136**, 6385-6394.

453. S. Kajiyama, L. Szabova, K. Sodeyama, H. Iinuma, R. Morita, K. Gotoh, Y. Tateyama, M. Okubo and A. Yamada, *ACS Nano*, 2016, **10**, 3334-3341.

454. Y.-X. Yu, *J. Phys. Chem. C*, 2016, **120**, 5288-5296.

455. P. Zhan, S. Wang, Y. Yuan, K. Jiao and S. Jiao, *J. Electrochem. Soc.*, 2015, **162**, A1028-A1032.

456. J. Halim, S. Kota, M. R. Lukatskaya, M. Naguib, M.-Q. Zhao, E. J. Moon, J. Pitock, J. Nanda, S. J. May, Y. Gogotsi and M. W. Barsoum, *Adv. Funct. Mater.*, 2016, **26**, 3118–3127.